UNIVERSITÀ DI BOLOGNA

Dipartimento di Scienze della Terra
e Geologico-Ambientali (GEO/02)

DOTTORATO DI RICERCA
IN SCIENZE DELLA TERRA - XIX CICLO
Coordinatore: Prof. William Cavazza

Elaborato di Tesi

Depositi di movimenti in massa in margini continentali mediterranei

---

Mass-transport deposits on Mediterranean continental margins

Dottorando
Dott. Daniel Minisini

Relatore
Dott. Fabio Trincardi

Co-relatore
Prof. Corrado Venturini

PREFACE

This Ph.D. thesis summarizes three years of effort in acquiring data, analysing and interpreting them to better understand submarine mass-transport deposits, geomorphologies and processes, key elements in the evolution of continental margins. During the thesis, I partecipated to 7 scientific cruises and presented preliminary results in 11 conferences, which help understand the state-of-the-art in mass movements. The time span dedicated to the Ph.D. thesis allowed approach a method of scientific research and partecipate in the whole course of "making science": proposal writing, work planning, data acquisition, data processing, interpretation, report writing and scientific publication. Therefore, the Ph.D. thesis offered a broad view of Research, also comparing among international standards. Because all of this, I am fully indebt to my tutor. At last, the Ph.D. student status has proved to be a unique possibility to experience life: as a sphere with no buoyancy that stays wherever is left in the sea water column.

The thesis layout introduces the main theme of this study with a background setting and short paragraphs that tackle overarching questions in mass-transport products and processes. The core of the the Ph.D. thesis is exposed through six articles submitted to international journals: article 1 gives a bird's eye view of the South Adriatic Margin documenting the broad extent and recurrence of mass-transport deposits; article 2 focuses on the onset of a submarine canyon in the South Adriatic; article 3 examine interaction between mass-transport and along-slope currents in maintaining the canyon; article 4 describes two peculiar slides in the Sicily Channel; article 5 further discusses timing and processes of previous slides; article 6 is an outcrop-scale study of a fossil fluid-migration system, as modern analogue of key predisposing factor for sediment instability. Conclusions summarize main discoveries and ideas occurred during the Ph.D. thesis.

INDEX

ABSTRACT

Extensive mass transport deposits and multiple slide scars testify widespread and recurrent submarine sediment failures occurring during the late Quaternary on the SW-Adriatic and SE-Sicilian margins. These mass movements and their consequences contributed to shape the continental slopes and fill the basins with characteristic signatures. Geomorphological, seismo-stratigraphic, sedimentological and biostratigraphic data provide clues to: 1) define distinct failure mechanisms investigating on factors that determine dissimilar organization of coeval displaced masses, 2) reconstruct successive phases of failure stressing on the same location where slide scars crosscut and mass-transport deposits overlap, 3) analyze regional setting and indicate the most suitable place where to calculate mass wasting frequency. Discussions on the role of fluid flow, currents activity and tectonic deformation determine a wider view on the construction of the studied continental margins.

- - -

Depositi di movimento in massa estesi e molteplici scarpate di frane testimoniano la diffusa e frequente instabiltà dei versanti sottomarini, durante il tardo Quaternario, dei margini sud-occidentale adriatico e sud-orientale siculo. Queste destabilizzazioni e le conseguenze che ne derivano modellano le scarpate continentali e riempiono i bacini sedimentari determinando l'evoluzione dei margini. Dati relativi a geomorfologia, sismica stratigrafica, sedimentologia e biostratigrafia fanno luce su: 1) l'ampia varietà di meccanismi di franemento individuando i fattori che determinano diverse geomorfologie esterne e strutture interne in corpi di frana coevi; 2) la cronologia di franamenti multipli verificatisi in una stessa area dove le scarpate di frana si fagocitano e i relativi depositi si sovrappongono; 3) l'individuazione dell'area fisiografica più adatta per calcolare la frequenza dei movimenti in massa e il conseguente rischio di destabilizzazione dei versanti. La trattazione di tematiche riguardanti risalita di fluidi, correnti di fondo e deformazioni tettoniche coadiuvano la comprensione dell'evoluzione dei margini continentali in relazione al ruolo dei movimenti in massa.

INTRODUCTION

Slope failures occur worldwide throughout continental margins and impact a broad range of environments like: fjords, deltas, flanks of volcanic islands and canyons. Most of these environments are characterized by thick bodies of rapidly-deposited soft sediment, steep slopes and high environmental loads (Hampton et al, 1996; Mulder & Cochonat, 1996).

The sedimentary strata forming on continental margins contain an especially rich record of Earth history, because they are impacted by a complex set of processes within the atmosphere, the lithosphere and the biosphere. In particular, the continental slope receives sediment from land and temporary stored in shallow parts of the continental margin, creating the ocean's largest repository for sediment mass (Kennett, 1982), thus creating the potential for resolving signals of slope failure imparted over a range of time scales (e.g., signals of river floods, of sea-level changes, Wilson's cycles). However, waves, tides, bottom currents and slope failures themselves represent powerful agents capable of erasing sedimentary records. As a result, a complex mix of sediment deposition and failure events impacts the archive of Earth history on the continental slope. Therefore, reading this archive requires a fundamental understanding for translating stratigraphic and geomorphological elements into a record of failure processes.

Continental slope sediment builds its strength as it consolidates, but failure can occur and lead to sediment redistribution through processes ranging from mud flows to blocky slides. These processes create distinctive morphological and stratigraphic features that give shape to the seascape and internal architecture of ocean margins. These geomorphological and stratigraphic elements are key to study the development, timing and recurrence of failures processes.

Submarine slope failures occur when the downslope driving forces acting on the material composing the seafloor and the subsurface are greater than the forces acting to resist the deformations. Slope failures occur either from an increase in the environmental loads or a decrease in the strength of the sediment (or a combination of both) (Hampton et al., 1996). Generally, the more buried the sediment, the higher its consolidation and shear strength. On one hand, sediment can result strengthened

(over-consolidation) by erosion (removal of part of the sediment column – Skempton, 1970), bioturbation (aggregation of sediments by feeding and burrowing organisms - Perret et al., 1995), cementation (bounding of sediment grains by precipitated minerals) and repeated seismic loading (that settles sediment grains and reduces pore water – Boulanger et al., 1998). On the other hand, sediment weakens with the increase of pore-water pressure that, in turn, depends on several factors as, among others, (a) gas charging and (b) rapid sedimentation (Sangrey, 1977). (a) Biogenic and thermogenic gas creating fluid migration systems are common on continental slopes (Kvenvolden & Field, 1981; Schwartz et al., 2003) and depict fluid escape structures observed both at seafloor (i.e., pockmarks) and in the subsurface (i.e., wipe-outs). Some of these migration systems may include clastic intrusions, chemosynthetic fauna and authigenic carbonates (see art. 6), and can be responsible for failures as they pressurize pore water, especially when sea-level fall reduces hydrostatic pressure on the seabed (Rothwell et al., 1998). (b) When rapid sedimentation occur new load is carried by pressure in pore water; sediment cannot increase its load-carrying-capacity without compressing and compression cannot occur instantaneously in a saturated medium, hence sediment has to dewater in order to compress, but if sediment has low permeability water takes considerable time to flow out and consequently pressure in pore water builds up (Esrig and Kirby, 1977).

An increase in pore-water pressure along a defined layer of the stratigraphic section weaken that layer giving rise to the concept of “weak layers”. Weak layers may coincide with unconformities or other key surfaces (onlaps, downlaps and erosional surfaces), ooze horizons, tephra layers, key surfaces in sediment drifts. This reflects the importance of pre-failure architecture and sedimentology of deposits in understanding slope stability along continental margins.

Following slope failure, the displaced mass moves downslope under the influence of gravity and evolves through one or more transport mechanisms (Middleton and Hampton, 1976): a slide mass can break in smaller blocks, as an avalanche, and become a mass flow as the failed sediment progressively disintegrates and moves downslope. Further disintegration and dilution of slide material and mass flows can generate turbidity currents (Morgenstern, 1967; Hampton 1972). Some failures don’t evolve. Some others may generate concurrent slide, mass flow and turbidity current when rupture occurs.

Failures with rigid movement may generate sudden, catastrophic and largerly unpredictable consequences for coastal regions and human infrastructures; in fact, these failures together with offshore earthquakes represent the main mechanism capable to generate tsunami (Synolakis et al., 1997) (see art. 1). In some cases, tsunami are known to occur in response to sediment failure only, in the lack of a concurrent seismic shock. Typically, tsunami caused by mass failure impact on geographically confined areas and may result more devastating compared to those generated by most earthquakes (Schwab et al., 1993; Lee et al., 2003).

A relevant aspect of slope failures is their ability to transport quickly large masses of sediment at depth transferring a conspicuous sediment budget to the basin (see art. 1). Slope failures may also represent a longer-lived means transferring sediment to the basin, in fact they can act as catalysts to headward erosion, a mechanism that contributes to submarine canyon formation (see art. 2). Canyons, in turn, capture downslope and/or along-slope bottom currents and convey their water masses and suspended sediment to the basin (see art. 3).

Late-Quaternary continental margins that show evidence of stacked mass-transport deposits represent areas recurrently impacted by failure and are therefore an ideal site to discuss the origin of failures and the differences in the resulting mass-transport deposits (see art. 4). Most failures occur in a succession of multi-events and recognition of successive phases is critical when they: a) occur very close to each other in time, b) enlarge the head region hampering a precise definition of the previous headscarps, c) remobilize mass-transport deposits produced during previous phases. In all these cases morphologic and stratigraphic reconstructions are complementary keys to understand, respectively, the cross-cutting relationship among successive headscarps and stratal relationships among overlapping failed masses (see art. 5).

When do submarine slope failures occur?

Submarine slope failures occur when the downslope driving forces acting on the seafloor and the subsurface are greater than the forces acting to resist the deformations. Slope failures occur either from an increase in the environmental loads or a decrease in the strength of the sediment (or by a combination of both factors) (Hampton et al., 1996).

Where do slope failures occur?

Slope failures occur throughout the oceans margins of the world and tend to happen most often in fjords, deltas, flanks of volcanic islands, continental slopes, canyons and deep-sea trenches. Common elements to most of these environments are: 1) thick bodies of soft sediment, 2) steep slopes, 3) high environmental loads (Hampton et al, 1996). They can also be quite local in nature, such as those that form on lakes, on lava deltas, on the flanks of steep structural highs, salt domes or mud volcanoes, or on the inner and outer flanks of turbidity-flow channel levees (Posamentier and Kolla, 2003).

Ever seen a slope failure?

Slope failure events have never been observed directly because of the hostile environment for observations (depth, darkness, detection of occurrence-site). What we observe are the products of the failure events that remain recorded in the sediment section. From these elements researchers characterize the failure through deductive inference and back analysis. Laboratory experiments, data imaging of failed areas, recovery of sediment samples accompanied by stratigraphic and geotechnical analyses on them represent the bases to study slope failures, determining their mechanism and downslope propagation, identifying their predisposing factors and triggers.

Ever wonder how to get images of seafloor and subsurface?

Echo sounding is the key method to map the seafloor and the subbottom. The technique uses sound waves bounced off the ocean bottom (and underlying layers), and was first used in the mid 20s' for oceanographic studies during the epic German expedition in the South Atlantic aboard the Meteor. However, modern oceanographic tools really appear less than 60 years ago, during World War II, when the U.S. Navy wanted to learn more about the oceans to gain fighting advantages, especially in submarine warfare. Huge efforts began to develop SONAR (an acronym for "sound" "navigation" and "ranging"). Interestingly, the very first development of sonar helped avoid icebergs after the Titanic sank.

Today, many different types of sophisticated sonars exist. They tell us not only about seafloor depths, but also about the structure of the ocean floor and even about currents and life in the ocean. Main sonars aboard ships (echo sounders) have components called transducers that both transmit and receive sound waves. Transducers send a beam of sound waves down to the seafloor which reflects back to the ship. Then, this echo is amplified electronically and recorded graphically. The time taken for the sound to travel through the ocean and back is then used to calculate water depths. Echo sounders repeatedly "ping" the seafloor as a ship moves along the seafloor, producing a continuous line showing water depths directly beneath the ship. Echo sounders use different frequencies of sound to find out different things about the seafloor.

Echo sounders that transmit sound at 3.5 kiloHertz (kHz) define how far down the seafloor lies and also how layers of sediments accumulated beneath it (geometry, thickness, facies). We call these graphic records "seismic profiles". During the last decades, echo sounders evolved in new instruments that use several arrays of 50 kHz transducers generating a "multibeam bathymetry", based on the simple fact that more beams are better than one. In this way, ships can produce a swath, rather than a line, of water depth information. The processed data produce what we call a "swath bathymetry". Side-scan sonars are yet another kind of sonar transmits sound at 30 kHz and provides information on morphology and sediment composition at the seafloor (texture, grain size, lithification…). High backscatter indicates boulders, gravel, or sandy sediment; low backscatter indicates fine-grained sediments or shadows behind

positive topographic features. Sonographs generated by this tool produce a “side-scan sonar mosaic image”.
Multibeam and side-scan sonar are collected along overlapping paths that cover the survey area. During acquisition, the optimal ship speed depends on water depth and instrument ping rate. Precise positioning, correction of ship movements (roll, pitch, yaw, heave), tide data and velocity of sound in water are essential parameters to take care of.

The track-lines of the “seismic profiles” are geo-referenced and overlain on the seafloor images. In this way, an individual feature seen on the sea bottom can be analyzed also vertically, looking at its internal structure and through the sediments accumulated below the feature itself. Also, seafloor features can be emphasized by overlaying a “side-scan sonar mosaic image” on the “swath bathymetry” of the same area. The integration of these products allow recreate a sort of 3D view of the earth’s inner space, down in the ocean depths.

How do slope-failure products look like?

Slope-failures products possess two essential characters: a failure surface and a displaced mass of sediment (Hampton et al. 1996). The failure surface is where failure took place and downslope movement originated; the displaced mass is the mass-transport deposit that traveled downslope, part of which commonly rests on the failure surface, but in some instances may move completely beyond it. The displaced mass can be recognized seismically by certain morphologic as well as stratigraphic distinguishing characteristics:

1) surfaces underlying displaced masses are either smooth and featureless as a decollement surface or irregular and locally characterized by extensive scours formed by the erosion of ploughing blocks at the base of the mass-transport deposits;

2) the upper bounding surface commonly is characterized by irregular to hummocky relief and can be bounded laterally by steep to gentle flanks;

3) in section view, seismic reflections show transparent to chaotic facies because mass-transport deposits commonly amalgamate, unless underfomed blocks maintaining the original stratigraphy are involved in the failure;

4) the morphology of displaced masses can be channel or lobe form, in some instances these lobes are characterized by extensive low-angle thrust faults associated with compression, commonly at their termini.

Additional elements distinguishing slope-failure products are: the headscarp (upper part of failure surface vacated by the displaced mass), tension cracks (within marginally stable material upslope from the headscarp), minor scarps (within the displaced mass itself), the toe (downslope terminus of the displaced mass).

A slope failure occurs. What goes next?

Following slope failure, the displaced mass moves downslope under the influence of gravity. A movement of mainly rigid and internally undeformed mass generates a slide. If the moving mass is a viscous fluid with considerable internal deformation a mass flow takes place. Mass flows may consist of heterogeneous sediment (debris flows) or predominantly muddy sediment (mud flows). The displaced mass gives rise to a turbidity current if a relatively dilute suspension of sediment grains are supported by an upward component of fluid turbolence.

Evolution of a slope failure?

Slope failures may evolve changing the downslope transport mechanisms. A slide mass can break in smaller blocks, as an avalanche, and become a mass flow as the failed sediment progressively disintegrates and continued downslope movement occurs. Further disintegration and dilution of slides and mass flows can generate turbidity

currents (Mulder and Cochonat, 1996). Some failures just don't evolve. Some others generate slide, mass flow and turbidity current at the same time when rupture occurs.
Slide evolves to mass flow when the displaced mass change from solid to fluid behavior. Mass flow evolves to turbidity current above a sediment concentration threshold, but this threshold has never been firmly established, yet (Pratson and Marr, 2005).

Which are the predisposing factors of slope failures?

Predisposing factors of failures are those which decrease the shear strength of the sediment (Locat and Lee, 2002). The shear strength of the sediment is its ability to resist to shear stresses, these latter mainly caused by gravity. Shear strength is influenced by loading and stress history of sediment.
Loading. If loading is applied rapidly water cannot leave the sediment framework and the loading condition is termed "undrained" (typical of clays). Viceversa, if loading is applied slowly condition is termed "drained" (typical of sands). The loading conditions influence the shear strength: generally undrained shear strength is inferior to drained shear strength.
Stress history. Sediment particles are deposited on the seafloor and gradually become buried to greater depths in the sediment column. The stress on the sediment particles increases almost linearly with subsurface depth while the sediment compacts and dewaters (consolidation). The more buried the sediment, the higher its consolidation and shear strength. Sediment can become densified and strenghtened (over-consolidation) by erosion (removal of part of the sediment column), bioturbation (disruption of sediments by feeding and burrowing organisms), cementation (bounding of sediment grains by precipitated minerals) and repeated seismic loading (that settles the sediment grains and reduces the voids).

The influence of tectonics on slope instability.

The occurrence of structural highs with steep or oversteepened flanks reduces the shear strength of the sediments. Folds plunging perpendicular to the continental slope

determine potential failure units within sinclines and constrain the downslope movement between anticlines. Faults both active and quiescent determine areas of sediment instability. Quiescent faults act as weak surfaces that can dictate depth and shape of the failure. Active faults and related earthquakes may represent the triggers of slope failures.

Slope failures and pressure in pore water: what relationship?

Pressure in pore water strongly impacts the sediment shear strength and thus the ability of the sediment to resist to downslope driving forces (Lee and Edwards, 1986). When pressure in pore water increases, shear strength decreases and slope failures are more likely to occur. Pressure in pore water, in turn, depends on several factors such as: rapid sedimentation (rapid new load is carried by pressure in pore water; sediment cannot increase its load-carrying-capacity without compressing and compression cannot occur instantaneously in a saturated medium, hence sediment has to dewater in order to compress, but if sediment has low permeability water takes considerable time to flow out and pressure in pore water builds up), gas charging (decay of organic matter or dissociation of gas hydrates produce expanding bubbles that pressurize water around them), groundwater seepage (when water table is below sea level it flows out from the seafloor), waves and earthquakes (whose alternating crest and troughs increase and decrease the pressure in pore water and can affect sediment grains until they become mobile), rapid sea level rise (in the order of 120 m in 20,000 years, when substantial buildup of pressure occurs in pore water).

An increase pressure in pore water along a defined layer of the stratigraphic column weaken that layer and gives rise to the concept of “weak layer”. Weak layers may coincide with the unconformities of architectural stratigraphy (onlaps, downlaps and erosional surfaces), ooze horizons, tephra layers, key surfaces of sediment drifts…

Slope failures occur both during sea level rise and fall, why?

Failures during intervals of sea level low stands occur because of decreasing pore-water pressure generated by the sea level drop, and because of action of waves along the upper

slope where sea level stops (Posamentier and Vail, 1988). Moreover, the high steepness typical of the upper slope contributes to sediment instability. Also the increasing sediment accumulation rate, related to the new shoreline is a key factor for failure. Failures during intervals of rapid sea level rise (in the order of 120 m in 20,000 years) are smaller but increasingly recognized and would be caused by the substantial buildup in pore pressure (Trincardi et al., 2003).

Nomenclature, why such a Babel?

Confusion is generated by the interchange of failure-process (e.g., slump, mass flow) and failure-product (e.g., slump deposit, mass-flow deposit). In addition the misuse of the term “slide” increases this confusion. In fact, in literature, all forms of failures processes (from rigid to plastic) and related products (from blocky to liquefied) are occasionally referred to as “slides” s.l.

Lee et al. (in press) try to set up the nomenclature. When motion of the displaced mass is translational it is termed “slide”. “Slide” s.s. is therefore a movement of essentially rigid, internally undeformed masses, slightly to highly deformed or broken up into distinct blocks; the resulting deposit is termed “slide deposit”. In this case, the failure surface may appear more or less planar due to the fact that mechanical inhomogeneities, such as bedding planes, control the failure. When motion of the displaced mass is rotational it is termed “slump” (the failure product is termed “slump deposit”), and the failure surface, particularly in mechanically homogeneous material, appears concave upward. If the displaced mass takes a form that resembles a viscous fluid, where the moving sediment completely disintegrates, the process is termed “mass flow” (and the product mass-flow deposit).

When a failed mass generates other significant ruptures in the neighbouring areas the failure is termed “complex”; ruptures that occur serially as numerous adjacent failures that progress upslope are “retrogressive”; when they progress downslope are “progressive” or “domino-like”. In each failure type (simple or complex slides, slumps, mass flows…) movement can be rapid or slow, when movement is extremely slow the process is termed “creep”. A main distinction between “rapid” and “slow” movement is the generation of wavelengths by the seafloor vertical movement that, in turn, excitates

a tsunami (only wavelengths that exceed three times the water depth contribute much to tsunami – Ward, 2001).

Who is interested in slope failures?

Exploitation of offshore resources, development of communication and transport corridors, fishing habitat safeguard, and protection of coastal communities, have contributed to growing interest in improved understanding of slope failures and their consequences (Solheim et al., 2005).

Geologists care. Slope failures evacuate sediment from small confined areas and spread it into broad areas, transferring conspicuous amounts of material from the slope to the basin. Widespread distribution and high frequency of submarine slope failures make them important geological features that can form a dominant depositional style on continental slopes and basins, thus controlling the long-term evolution of a margin.

Engineers care. When failures occur near shore they assume increasing practical interest, in fact failures can cut back across the shoreline in a populated area or can destabilize the foundation of marine engineered structures as ports and platforms. Submarine slopes often fail along “weak” layers, which can be very thin; the identification of such layers and the extraction of geotechnical and engineering information is therefore important.

Biologists care. Submarine slide scars may offer peculiar niches to chemosynthetic biological communities when supported by methane and hydrogen sulfide that diffuse out of fresh exposed seafloor.

Politicians care. Slope failures represent a geohazard and a main threat because of their potential in damaging seafloor installations and for generating devastating tsunami, such as the 1998 Papua New Guinea event responsible for more than 2000 deaths. Tsunami constitute a serious natural hazard for the populations in coastal exposed areas, thus, one of the future challenges is the development of more advanced numerical tsunami models, generated by slope failures, for early warning and mitigation planning.

Oil industry cares. Another challenge is to model the huge runout distances that occur on small slope gradients (i.e., Storegga Slide deposit, in the Norwegian margin, has been found as far as 450 km from the source area, along a section sloping less than one degree). This is of great importance for the oil industry that often locate offshore structures in continental slope settings. The consequences of a slide-triggered accident offshore, in terms of loss of life and damage to the environment could be catastrophic.

Culture cares. In the *XVIII* century, geohazards as earthquakes and associated slope failures disentangle a new philosophical point of view, as it happened with Voltaire's writings. In particular, "Candid" written in the aftermath of the Lisbon earthquake of 1755, attacks the metaphysical optimism believing that the world created by God is the best one possible. If, as Voltaire writes, "Everything is for the best in the best of all

possible worlds", how does one go about explaining the devastating effects of the Lisbon earthquake and tsunami, where approximately 20,000 lives were lost…?

How does risk management work?

RISK = HAZARD x VULNERABILITY x VALUE,

where HAZARD is the probability of disaster events, VULNERABILITY takes into account the presence of buildings and equipment, VALUE refers to the financial value of those buildings and equipment. This empirical formula is the most used both by governments and insurances to make decisions about risk management (Smolka, 2005).

When managing the risk from extreme natural hazards, the great challenge is to find the right balance between preparing adequately for more frequent typical disasters (as windstorms, floods, earthquakes…) and making due allowance for the occurrence of very rare, extreme natural hazards like submarine slides, volcanic eruptions or tsunami. Submarine slides are potential generators of tsunami and assessing the risk emanating from slide generated tsunami in comparison to other causative hazards (as earthquakes, volcanic collapses, meteorites) is still needed.

Slope failures. State of the art.

In the last few years, the broad array of knowledge gathered by the marine geology community generated a progress in the understanding of submarine slope failures that has been impressive. Progress has been made as a result of the growing interest in the field (due to rare natural events as the Papua New Guinea landslide tsunami of 1998 and the Indian Ocean tsunami of 2004) and the expansion of technology (in particular, multibeam bathymetry). New organizations and challenging projects hosted the debates about slope failures (e.g., COSTA, EUROstrataform).

Expansion of mapping over the oceans and production of clear images of their seafloors improved the knowledge about the environments for slope failures and about their morphologies and structures; all elements that lead to the understanding of processes and effects of failures. Also remotely operated vehicles (ROV) and moorings (with traps and currentometres) helped to improve the state of knowledge.

The 3D geophysical data greatly improved the studies of the subbottom (e.g., giant grooves at the base of slides), but these data are limited to commercial companies and still has to reach the accademic community.

Modelling of failure motions is under study, and even if a better groundtruthing is needed, its contribution to the understanding of failure processes is important (e.g., hydroplanning).

Stratigraphy has highlighted the importance of determined layers that weaken under stressed circumstances and generate slip planes on which mass-transport deposits move (e.g., downlap surfaces or coarse grained sediments horizons).

The sense of chronology and repetitivity of failure events has raisen, but, still, dating of failure products need to be improved.

Incorporation of new communities in the field of slope failure (as tsunami modellers, oceanographers, biologists…) has bloomed into an integration of data with new interesting applications. For instance, the potential for landslide-tsunami has become a recognized geohazard to coastal development.

With the consciousness that the state of the art is based on limited investigated areas, future directions need to better integrate geology, geotechnics and geophysics. Also, a deeper communication among researchers, as well as between industry and accademia, is wished.

Next steps should include a better understanding of transition from slides to plastic flows and from plastic flows to turbidite currents. The role of earthquakes, gas hydrates and sea level fluctuations need to change from speculative to deterministic. As well as triggers have still to be well-recognized.

A new world has still to be discovered in the subbottom where, by now, only thick irregular bodies are indicated as mass-transport deposits, most of them without any related evacuated zone. Longer cores are needed to study buried failed masses. More efforts should be made to couple the acoustic facies of failed masses with their sedimentologic and geotechnical characteristics. Also the assessment of in-situ

effective stress and pore pressure conditions of the sediment should be more solid in order to better indicate the threshold for slope failure. These latter together with an improvement of dating and estimations of failures recurrences would help the risk assessment and management.

Another factor to take into account for risk management is the trend of slope instability (e.g., an incision with lateral collapses will have distinct security factors depending if the incision itself is being eroded or filled).

REFERENCES

Boulanger, E., Konrad, J.-M., Locat, J., and **Lee, H.J.** (1998) Cyclic behavior of Eel River sediments: a possible explanation for the paucity of submarine landslide features. Amer. Geophys. Union, San Francisco, *EOS*, Abstract.

Esrig, M.I. and **Kirby, R.C**. (1977) Implications of gas content for predicting the stability of submarine slopes. *Mar. Geotech.*, **2**, 81-100.

Hampton, M. (1972) The role of subaqueous debris flow in generating turbidity currents. *Jour. Sed. Petr.*, **42**, 775-993.

Hampton, M., A., Lee, H.J., and **Locat, J.** (1996) Submarine landslides. *Rev. of Geophys.*, **34**, 33-59.

Kennett, J.P. (1982) Marine Geology, Prentice-Hall, Englewood Cliffs, pp. 813.

Kvenvolden, K.A. and Field, M.E. (1981) Thermogenic hydrocarbons in unconsolidated sediments of the Eel River Basin, offshore northern California. Am. Assoc. Petrol. Geol. Bull. 65, 1642-1646.

Lee, H.J. and **Edwards, B.D.** (1986) Regional method to assess offshore slope stability. *Jour. of Geotech. Eng.*, ASCE, **112**, 489-509.

Lee, H. J., Kayen, R. E., Gardner, J. V., and **Locat, J**. (2003) Characteristic of several tsunamogenic submarine landslides, in: Submarine Mass Movements and their Consequences, edited by: Locat, J. and Mienert, J., Kluver Acad. Publ., Dordrecht, The Netherlands, 357–366.

Lee, H.J., J. Locat, P. Desgagnes, J.D. Parsons, B.G. McAdoo, D.L. Orange, P. Puig, F.L. Wong, P. Dartnell, and **E. Boulanger** (in press), Submarine Mass Movements on Continental Margins, *in* Continental-Margin Sedimentation: from Sediment Transport to Sequence Stratigraphy, *IAS special publication*, **vol. 37**, edited by C.A. Nittrouer, J.A. Austin, M.E. Field, J.H. Kravitz, J.P.M. Syvitski, and P.L.

Wibergeds, Blackwell Publishing Ltd., Oxford.

Locat, J., and **Lee, H.J.**, (2002) Submarine landslides: advances and challenges. *Can. Geotech. Jour.*, **39**, 193-212.

Middleton G. V. and **Hampton, M. A**. (1976) Subaqueous sediment transport and deposition by sediment gravity flows, in Stanley, D. J., and Swift, D.J.P., editors, Marine sediment transport and environmental management, New York, Wiley, 197-218.

Morgenstern, N.R. (1967) Submarine slumping and the initiation of turbidity currents. In: *Marine Geotechnique* (A.F. Richards, Ed.), University of Illinois Press, Urbana, Ill., p. 189-210.

Mulder, T., and **Cochonat, P**. (1996) Classification of offshore mass movements. *Jour. Sed. Res.*, **66**, 43-57.

Perret, D., Locat, J., and **Leroueil, S.** (1995) Strength development with burial in fine-grained sediments from the Saguenay Fjord, Québec. *Can. Geotech. Jour.*, **32**, 247-262.

Pratson, L. F., and **Marr, J.** (2005) Debris flows, turbidity currents and the transitional flows that lie between them. *2nd. International Conference on Submarine Mass Movements and Their Consequences*, Oslo, Norway, September 5-7, p. 72.

Posamentier, H. W. and **Vail, P. R**. (1988) Eustatic control on clastic deposition, II-sequence and systems trast models, in: Sea-Level Changes – An integrated Approach, edited by: Wilgus, C. K., Hastings, B. S., Kendall, C. G. S. C., et al., *Soc. Economic Paleontologists and Mineralogists*, Spec. Publ., **42**, 125–154.

Posamentier, H. W. and **Kolla, V.** (2003) Seismic geomorphology and stratigraphy of depositional elements in deep-water settings. *Journal of Sedimentary Research*, **73**-3, 367-388.

Rothwell, R. G., Thomson, J., and **Kahler, G.** (1998) Low-sea-level emplacement of a very large Late Pleistocene 'megaturbidite' in the western Mediterranean Sea, *Nature*, **392**, 377–380.

Sangrey, D. (1977) Marine geotechnology—state of the art., *Mar. Geotech.*, **2**, 45-80.

Schwab W. C., Lee H. J., and **Twichell D. C**. (1993) Submarine landslides; selected studies in the U.S. Exclusive Economic Zone, *USGS Bull*., **2002**, pp. 204.

Schwartz, H., Sample J., Weberling K. D., Minisini D., and **Moore, J. C.** (2003) An ancient linked fluid migration system: Cold-seep deposits and sandstone intrusions in the Panoche Hills, California, U.S.A. *Geo-Marine Letters*, **23**, 3–4, 340–350.

Skempton, A.W. (1970) The consolidation of clays by gravitational compaction. Quart. Jour. Geol. Soc., 125, 373-411.

Smolka, A. (2005) Natural catastrophes: causes, trends and risk management. The challange of submarine mass movements. *2nd. International Conference on Submarine Mass Movements and Their Consequences*, Oslo, September 5-7, p. 78-79.

Solheim, A., Bhasin R., De Blasio F. V., and **other 22 authors** (2005) International Centre for Geohazards (ICG): Assessment, prevention and mitigation of geohazards, *Norwegian Journal of Geology*, **85**(1-2), 45-62.

Synolakis, C. E., Liu, P., Carrier, G., and **Yeh, H.** (1997) Tsunamigenic seafloor deformation, *Science*, **278**, 598–600.

Trincardi, F., Cattaneo, A., Correggiari, A., Mongardi, S., Breda, A., and **Asioli, A**. (2003) Submarine slides during sea level rise: two exemples from the eastern Tyrrhenian margin, in: Submarine Mass Movements and their Consequences, edited by: Locat, J. and Mienert, J., Kluver Acad. Publ., The Netherlands, 469–478.

Ward, S. N. (2001) Landslide tsunami, *J. Geophys. Res.*, **106**, B6, 11 201–11 216.

CHAPTER 1

This chapter consists of an article titled “Evidence of slope instability in the Southwestern Adriatic Margin” by Minisini D., Trincardi F., Asioli A., published in “Natural Hazards and Earth System Sciences”.

Natural Hazards and Earth System Sciences, 6, 1–20, 2006
SRef-ID: 1684-9981/nhess/2006-6-1
European Geosciences Union

Natural Hazards and Earth System Sciences

Evidence of slope instability in the Southwestern Adriatic Margin

D. Minisini[1,2], **F. Trincardi**[1], **and A. Asioli**[3]

[1]Istituto di Scienze del Mare, ISMAR-CNR, Via Gobetti 101, 40129 Bologna, Italy
[2]Dipartimento di Scienze della Terra e Geologico-Ambientali, Univ. di Bologna, Via Zamboni 67, 40127 Bologna, Italy
[3]Istituto di Geoscienze e Georisorse, IGG-CNR, C.so Garibaldi 37, 35137 Padova, Italy

Received: 29 August 2005 – Revised: 15 November 2005 – Accepted: 16 November 2005 – Published: 2 January 2006

Part of Special Issue "Tsunami hazard from slope instability"

Abstract. The Southwestern Adriatic Margin (SAM) shows evidence of widespread failure events that generated slide scars up to 10 km wide and extensive slide deposits with run out distances greater than 50 km. Chirp-sonar profiles, side-scan sonar mosaics, multibeam bathymetry and sediment cores document that the entire slope area underwent repeated failures along a stretch of 150 km and that mass-transport deposits, covering an area of 3320 km^2, are highly variable ranging from blocky slides to turbidites, and lay on the lower slope and in the basin. The SAM slope between 300–700 m is impacted by southward bottom currents shaping sediment drifts (partly affected by failure) and areas of dominant erosion of the seafloor. When slide deposits occur in areas swept by bottom currents their fresh appearence and their location at seafloor may give the misleading impression of a very young age. Seismic-stratigraphic correlation of these deposits to the basin floor, however, allow a more reliable age estimate through sediment coring of the post-slide unit. Multiple buried failed masses overlap each other in the lower slope and below the basin floor; the most widespread of these mass-transport deposits occurred during the MIS 2-glacial interval on a combined area of 2670 km^2. Displacements affecting Holocene deposits suggest recent failure events during or after the last phases of the last post-glacial eustatic rise. Differences in sediment accumulation rates at the base or within the sediment drifts and presence of downlap surfaces along the slope and further in the basin may provide one or multiple potential weak layers above which widespread collapses take place. Neotectonic activity and seismicity, together with the presence of a steep slope, represent additional elements conducive to sediment instability and failure along the SAM. Evidence of large areas still prone to failure provides elements of tsunamogenic hazard.

Correspondence to: D. Minisini
(daniel.minisini@ismar.cnr.it)

1 Introduction

Offshore earthquakes and submarine mass failures represent the main mechanism capable to generate tsunami that constitute potential hazards to coastal communities (Synolakis et al., 1997). In some cases it proves difficult to differentiate tsunami that are generated by earthquakes from those generated by mass-failure events (Hasegawa and Kanamori, 1987; Julian et al., 1998; Geist, 2000). However, submarine mass failure is widely recognized as a complementary mechanism in the generation of tsunami (Tappin et al., 2001). Well-known catastrophic events, such as the 1946 tsunami in the Aleutians Islands, are generated by earthquakes but appear much larger than expected solely on the basis of the seismic event; this evidence supports the notion that tsunami can result also or be amplified by earthquake-triggered landslides rather than pure seismic shocks (Tappin et al., 1999; Fryer at al., 2004). In these cases, submarine failure may provide a mechanism to enhance the tsunami wave with respect to what would be generated solely by pure co-seismic dislocation (Tappin et al., 2001; Synolakis et al., 2002). In some cases, tsunami are known to occur in response to sediment failure only, in the lack of a concurrent seismic shock (Malinverno et al., 1988; Gardner, 2001).

Typically, tsunami caused by mass failure impact on geographically more confined areas, even though they may result more devastating compared to those generated by earthquakes (Schwab et al., 1993; Tappin et al., 2001; Lee et al., 2003). The latter mechanism results in tsunami of typically greater wavelengths and longer periods (Tappin et al., 2001). The Papua New Guinea event in 1998, is one of the best documented examples of tsunami related to mass failure, and emphasizes how submarine mass failures can amplify the impact of earthquakes of relatively moderate size (Tappin et al., 2001; Synolakis et al., 2002). Submarine failures occur preferentially in areas of high sediment accumulation such as fjords, deltas, volcanic islands, submarine canyons and continental slopes (Hampton et al., 1996).

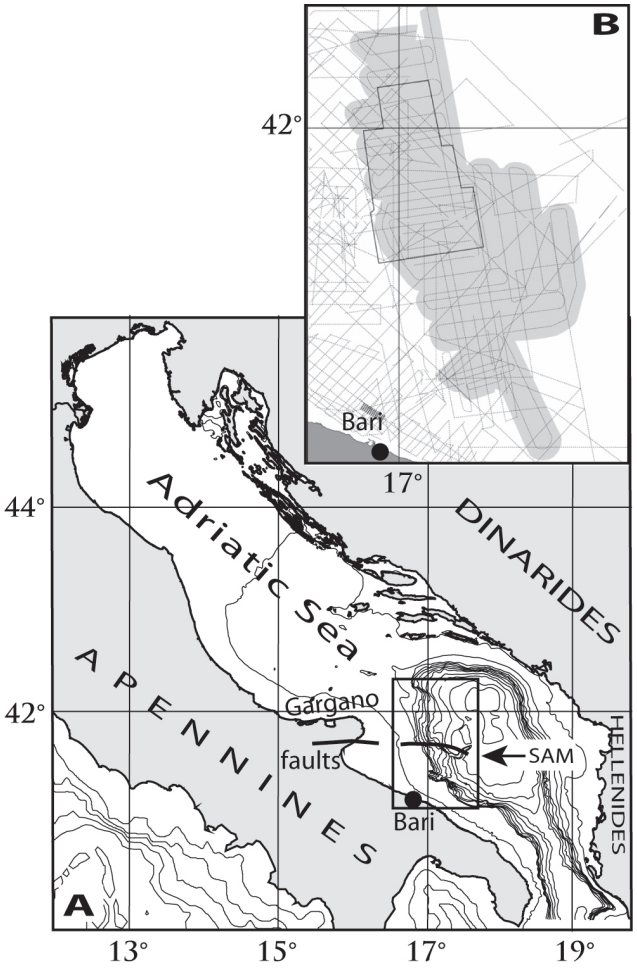

Fig. 1. (A): location of the Sothwestern Adriatic Margin (SAM) in the Adriatic Sea, Central Mediterranean Sea (bathymetric contour intervals are every 100 m). **(B)**: data base: Chirp-sonar profiles (dashed lines), TOBI side-scan sonar mosaic (grey pattern) and multibeam swath bathymetry (solid black box). B represents the SAM area shown in Fig. 2.

The Southwestern Adriatic Margin (SAM), in southern Italy (Fig. 1a), is a seismically active area repeatedly impacted by large tsunami in historical times (Tinti et al., 1995) where new multibeam bathymetric data, TOBI side-scan-sonar mosaics, Chirp-sonar profiles and sediment cores reveal widespread slope instability and mass-transport features suggesting several generations of failures and involving distinct mechanisms of sediment transport. Here we discuss the sedimentary processes that are believed to shape the SAM, their predisposing factors and triggers, and propose a chronology of these events. In addition, we try to ascertain if, and where, this area of high sediment instability is still prone to failure. If this is the case, the SAM may represent a potential tsunamigenic area also in the future.

2 Setting

2.1 Geologic setting

The Adriatic Sea is a foreland domain between the Southern Alps, the Apennines and the Dinarids-Hellenids fold-and-thrust belts (D'Argenio and Horvath, 1984; Ricci Lucchi, 1986; Ori et al., 1986) (Fig. 1a). The mainland region adjacent to the SAM includes the emerging sectors of the Apennine foreland and provides significant structural differentiation (de Alteriis, 1995). The segmented structure of this region reflects lateral variations of the lithospheric thickness of the westward dipping Adriatic plate and gives rise to areas of more intense or more recurrent seismicity (Royden et al., 1987; Doglioni et al., 1994).

The evolution of the SAM during the Cenozoic reflects the re-activation and inversion of inherited Mesozoic extensional faults (Argnani et al., 1993). The main deformational zone, known as the south Gargano system (Colantoni et al., 1990; Tramontana et al., 1995) extends both on land, with the Monte Santangelo-Mattinata fault (Ortolani and Pagliuca, 1987), and offshore with the Gondola deformation belt (Finetti et al., 1987) (Fig. 1a). During the Quaternary, the SAM was affected by uplift and deformation (Doglioni et al., 1994). During the last 500 ky, the SAM has built through the deposition of a composite stack of regressive depositional (progradational) sequences, formed mainly through prolonged intervals of sea level fall, and bounded at the top by shelf wide erosion surfaces (Ridente and Trincardi, 2002a). Each of these sequences records a 100–120 ky-glacio-eustatic cycle (Trincardi and Correggiari 2000). Along the SAM these sequences form a composite progradational wedge with an overall forestepping architecture and a progressive seaward shift of the landward pinchout, in response to the seaward tilt of the margin (Ridente and Trincardi, 2002a). Active tectonic deformation on the continental margin generated a suite of gentle anticlines and vertical offsets that affect superficial deposits, particularly along the E-W-trending Gondola deformation belt (Fig. 2). These features indicate that tectonic deformation is occurring up to recent times (Tramontana et al., 1995; Ridente and Trincardi, 2002b), even if the interpretation of the kinematic of these tectonic features remains controversial (Colantoni et al., 1990; Argnagni et al., 1993; de Alteriis, 1995).

2.2 Seismicity

The SAM is a seismically active area where earthquakes are well documented both from historical catalogues over the last ten centuries and from modern registrations over the last few decades (Tinti and Armigliato, 2003). Seismic activity appears to cluster along the main tectonic structures described above, with shallow earthquakes reaching magnitudes typically between 5 and 6 on Richter scale (Tinti et al., 1995; Tinti and Armigliato, 2003). In particular, earthquakes located offshore the Gargano Promontory (Fig. 1a) reach higher energy releases with peaks greater than 6.6 on Richter

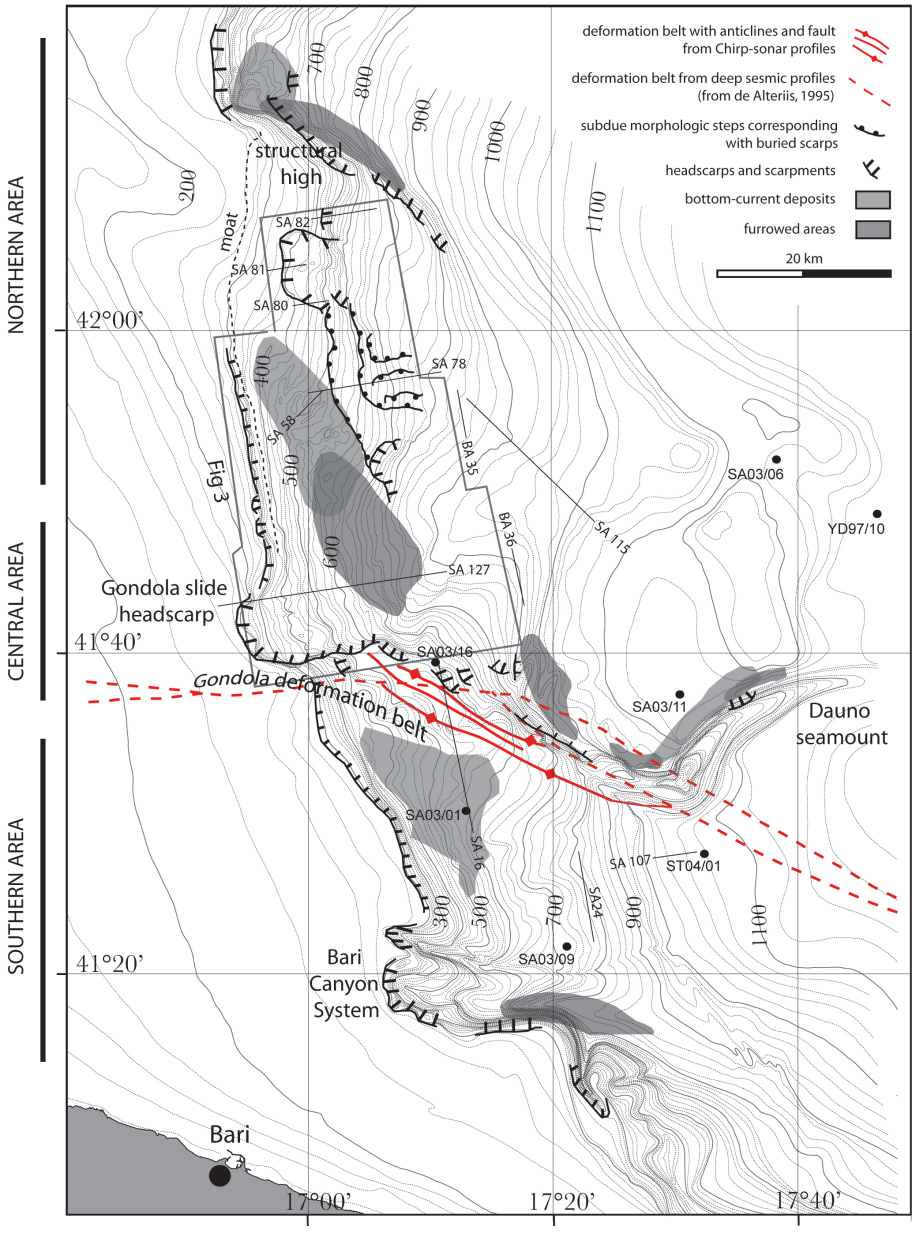

Fig. 2. Detailed bathymetry of the Southwestern Adriatic Margin (SAM) with contour intervals of 20 m and location of Chirp-sonar profiles and cores shown in the following figures.

scale (Tinti et al., 1995). The south Adriatic was also affected by large tsunami particularly well documented in historical times (Tinti et al., 1995), the largest of which occurred in 1627 destructing several coastal villages and killing more than 5000 people (Postpischl, 1985); this event, in particular, may have been triggered by the intense seismic activity offshore but it is difficult to explain why distructive waves hit simultaneously the coast both north and south of the Gargano Promontory, as documented by Tinti and Armigliato (2003).

2.3 Oceanographic setting

Two main bottom water masses impact on the SAM (Artegiani et al., 1997): the Levantine Intermediate Water (LIW) layer in a water depth of 200–700 m (Orlic et al., 1992), and the bottom layer represented by the North Adriatic Dense Water (NAdDW) (Cushman-Roisin et al., 2001). These two bottom currents flow southward along the SAM and result in current velocities exceeding 60 cm/s along the slope (Miserocchi, personal communication). This current circulation regime may have undergone significant changes in intensity in the recent geologic past, particularly through glacial periods, when the north Adriatic shelf was subaerial and major rearrangements affected the overall Mediterranean circulation (Myers et al., 1998, Verdicchio et al., 2005).

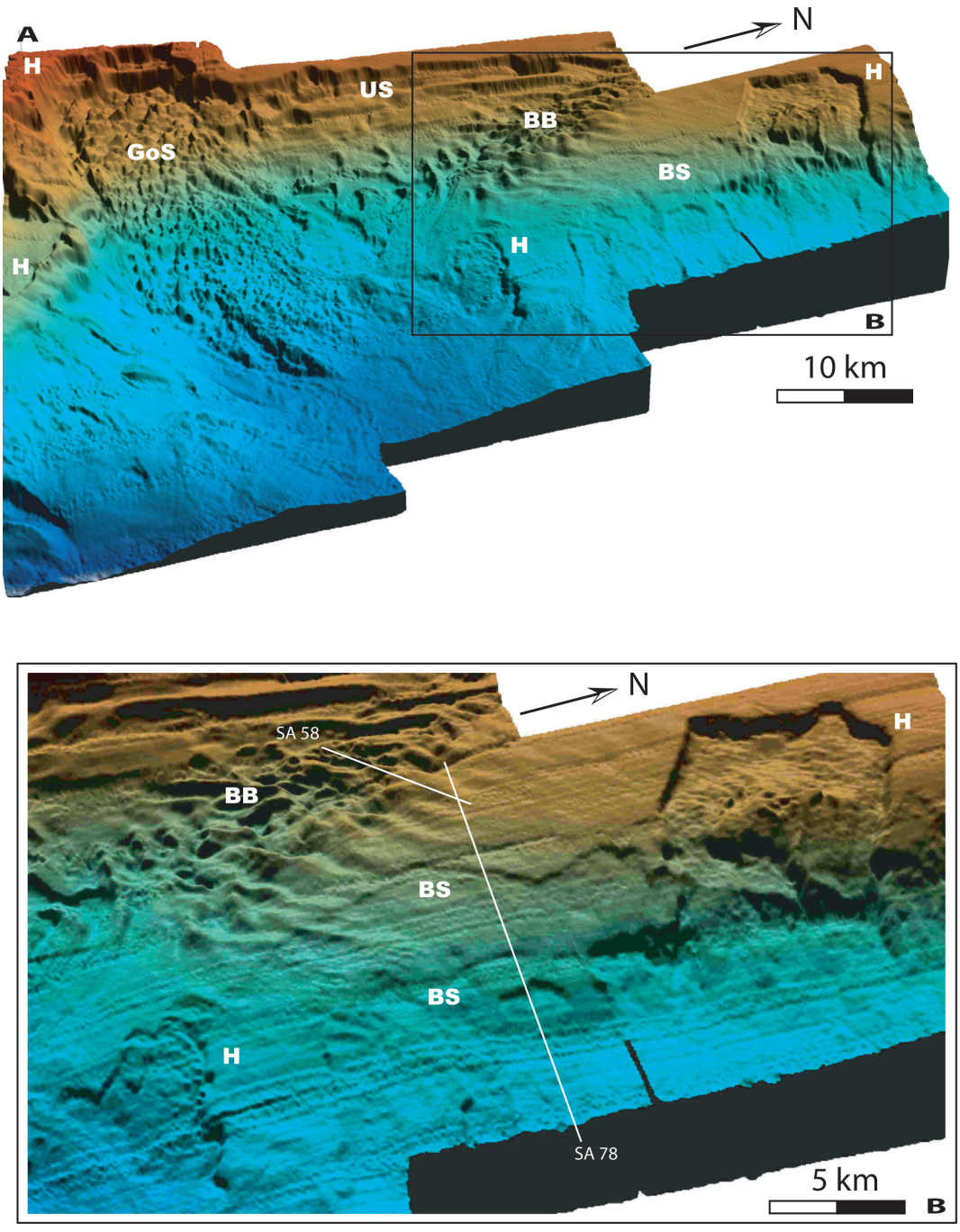

Fig. 3. (A): EM-300 multibeam bathymetry showing upper slope (US), Gondola Slide deposit (GoS), bottom-current bedforms (BB), slide headscarps (H), traces of buried scarps (BS); vertical exaggeration 5x, artificial sun angle from N, red is 150 m, dark blue is 1000 m. Close up **(B)** evidences arcuate lineations corresponding to buried scarps (BS); artificial sun angle from W; profiles SA78 and SA58 are shown in Fig. 7.

3 Data and methods

The data set for this study has been collected by ISMAR-CNR (Bologna) during three cruises on board R/V Urania (2003 and 2004) and R/V Odin Finder (2005) (Fig. 1b). The main data set includes a dense network of Chirp-sonar profiles. Chirp-sonar profiles use a 2–7 kHz sweep-modulated band width, equivalent to a 3.5 kHz profiler fired from 16 transducers, and have a 500–2000 ms recording length, depending on water depth. In the northern half of the study area, high-resolution bathymetric data were gathered using a 50-kHz EM-300 multibeam and reduced to a 5×5 m grid. The remaining slope and basin area are covered by conventional bathymetric data that are anyhow sufficient to

identify the morphologic expression of mass-transport deposits. A 30-kHz TOBI side-scan-sonar mosaic offers information about the seafloor back-scatter and macro morphology, side-scan-sonar data were processed at the "National Oceanographic Center, Southampton" following the methods defined by Le Bas et al. (1995). Sediment cores were collected using a piston corer with variable barrel lengths (5–20 m), for a maximum core recovery of circa 16 m. In addition, a light-coring device (SW104) with a 1.35-m barrel was employed to collect large-diameter undisturbed core tops (Magagnoli and Mengoli, 1995). Track-line positioning was based on D-GPS navigation, assuring a position accuracy of circa 10 m, and transformed to geographic coordinates referred to the ED-50 datum.

4 Results

4.1 Morphology

4.1.1 The upper slope

The new bathymetric map evidences a markedly erosive upper slope dipping 1° to 8° and reaching a maximum of 30°, in the southern area (Figs. 2, 3). Where the upper slope is steeper than the bedding planes of the underlying strata, Pleistocene progradational sequences are variably exposed (Fig. 4). The relative age of the exposed sequences can be defined through seismic correlation to the shelf area (Ridente and Trincardi, 2002a).

Prominent features of the upper slope are: 1) the headscarp of Gondola Slide that has an extent of about 10 km along the slope, a relief up to 250 m and indents the shelf edge for 5 km truncating several stratigraphic units including, atop, a progradational sequence that postdates 120 ky BP (Ridente and Trincardi, 2002a) (Figs. 2, 3, 4a); 2) the head of the Bari Canyon System that breaches the outer shelf over 12 km and presents multiple heads separated by a set of gentle anticlines whose axes intersect the shelf break and plunge eastward (Figs. 2, 5); the Bari Canyon System is East-West and dissects the slope for about 30 km; 3) an erosional moat developing for 46 km at the toe of the upper slope in the northern area (Fig. 2). Additional evidence of past failures are the 10–20 m-high buried scars in the outer shelf area affecting the Pleistocene progradational sequences; these scars occur both landward of the Bari canyon head and of Gondola Slide headscarp, in both cases affecting regressive progradational sequences older than the last interglacial.

4.1.2 The lower slope

The lower slope of the SAM is gentler than the upper slope but, overall, shows a greater morphologic variability that likely reflects local tectonic deformation, the presence of slide headscarps, mass-transport deposits and the growth of bottom-current sediment drifts and bedforms (Verdicchio et al., 2005) (Figs. 2, 3, 7a). On the lower slope, wavy-stratified deposits are quite variable in thickness and external morphology: they display short distance changes in thickness where reflectors are undulated and converge away from the depocentres, and show local seafloor or subsurface erosion; these deposits record the activity of bottom currents (Figs. 2, 7a, b). Seaward of this area, evidence of sediment instability is widespread along the slope: the seafloor is locally dissected by detachment surfaces and gentle depressions (Fig. 3), often accompanied by broad areas of exposed acoustically-transparent deposits with high back-scatter (Figs. 5, 6) and/or multiple stacked acoustically-transparent deposits in the subsurface (Fig. 7b).

Major morphologic elements of the lower slope are: 1) furrowed areas particularly developed on the N or NE dipping flank of the main structural features intersecting the slope (Figs. 2, 5, 6a); 2) arcuate lineations extending over 20 km across the slope corresponding to buried scarps that define the upslope limit of buried failed deposits (Figs. 2, 3, 7b); 3) subtle depressions and offsets of otherwise undisturbed sedimentary units located landward of slide scarps, indicating short and narrow linear features and/or small pockmarks (Fig. 8); these subtle depressions appear either at the seafloor or buried, but they never extend below the reflector that correlates to the mobilization surface in the nearby failure zone; these depressions likely indicate potential landward mobilization; 4) a suite of anticlines and faults affecting shallow deposits along the Gondola deformation belt, and adjacent to slide headscarps (Fig. 7a) and well documented on side-scan sonar mosaics (Fig. 5)

4.1.3 The basin area

East of the SAM a 1200-m deep basin is divided in two parts by the Dauno seamount that connects with the Gondola deformation belt and reaches about 400 m above the adjacent basin floor (Fig. 2). Both parts of the basin are filled by buried acoustically-transparent deposits and mantled by a well stratified unit with great reflector continuity. North of Dauno seamount the basin floor displays additional local reliefs related to the presence of buried anticlines. The well-stratified uppermost seismic unit extends also across these features.

4.2 Mass-transport features

On the SAM, multiple and overlaying mass-transport deposits extending over 3320 km^2 encompass most of the margin, between 400 and 1100 m, and record a succession of distinct failures (Figs. 9, 10). Locally, elementary mass-transport deposits overlap and coalesce so that individual deposits cannot be discerned; in this case acoustic penetration is often not sufficient to detect the base of the oldest failed unit and, consequently, the total thickness of the units involved. The mass-transport deposits are mapped individually where separated by layered stratigrafic units of variable thickness (Fig. 7b), where a high-amplitude reflector indicates stacked mass-transport units within the otherwise acoustically-transparent deposit, (Fig. 11a) and where

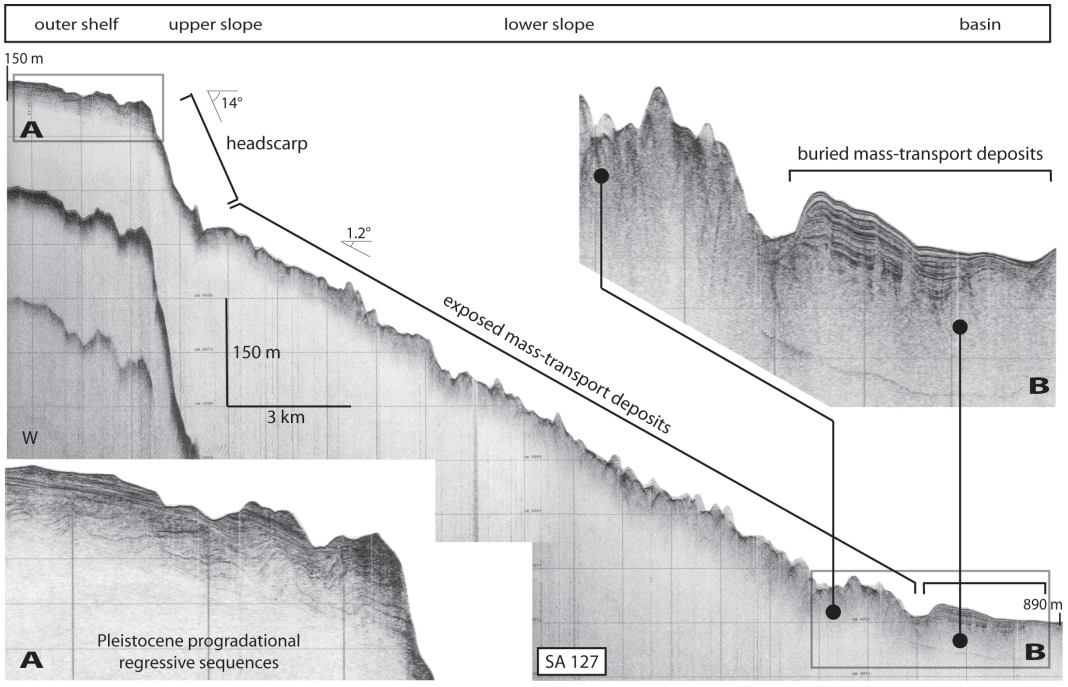

Fig. 4. Chirp-sonar profile across the Gondola Slide deposit (location in Figs. 2, 9, 10). Close-up **(A)** shows Pleistocene progradational regressive sequences truncated by the Gondola Slide headscarp. Close-up **(B)** shows the physical continuity of the exposed mass-transport deposit on the slope and the buried correlative in the basin, evidencing that bottom currents determine extensive erosion and enhanced deposition in adjacent areas.

a shallow-buried mass-transport deposit thins and allow define the underlying older failed masses (Fig. 11b); elsewhere mass-transport deposits are mapped as a whole. The uppermost buried failed deposit (indicated as GS) represents the main failure event and affects the SAM north and south of the Dauno seamount (Fig. 10).

Mass-transport deposits are either exposed at the seafloor or buried below a draped sedimentary unit. In some cases, seismic-stratigraphic correlation proves that the same mass-transport deposit can be buried in the basin area and exposed on the slope where bottom currents are active and prevent burial (Figs. 4, 7a, 11c). In other cases, several distinct failed masses superimpose displaying substantial overlaps that make it difficult to define their relative timing of deposition (Fig. 11d).

4.2.1 Northern area

Arcuate lineations at the seafloor, accompanied by subdue morphologic steps, extend over 20 km and define the upslope limit of buried failure deposits (Figs. 2, 7b, 8a). The longest and most prominent of these lineations connects the headscarps of two recent failures (Fig. 3b). These two headscarps, as many others, occur at the seafloor and are not draped by younger units, as documented on Chirp-sonar profiles (Fig. 8b). Sediment cores recovered a thin veneer of muddy bioclastic sand above some of the mass-transport deposits that are spatially associated to these headscarps. Nowhere slide scars are entirely evacuated and the basal slip surfaces are never exposed. The failed deposits have a locally-erosional base and a hummocky top, both indicative of deposition through mass-transport processes. The largest of these headscarps is 7 km-wide and 35 m-high (Figs. 3, 6b) and rims acoustically-transparent deposits or areas where deposits are characterized by folded and disrupted reflectors exposed at the seafloor (Fig. 8b). In a similar and adjacent failure zone, the mass-transport deposits genetically linked to the headscarp are exposed at the seafloor, proximally, and organized in several stacked units, more distally (Fig. 11d); in proximal areas, the acoustically-transparent deposits failed along a common basal layer. Because older mass-transport deposits do not extent upslope of the youngest headscarp, it is conceivable that in this area failures propagated upslope in a retrogressive style, in a fashion similar to that described by Twichell and Roberts (1982), Farre et al. (1983), and Pratson and Coakley (1996).

4.2.2 Central area

The central area corresponds to Gondola Slide that is part of the largest mass failure deposit (GS) on the SAM (Figs. 3, 6a). Gondola Slide is 10 km wide on the slope, up to 35 m thick and has a total run out greater than 50 km (Fig. 10). The evacuation zone includes a crescent-shaped headscarp located at the shelf edge with a maximum height of 250 m with several subparallel secondary scarps and a complex escarpment along the regional E-W structural lineation (Figs. 3, 4, 6a). On the slope, mass-transport deposits are at the seafloor

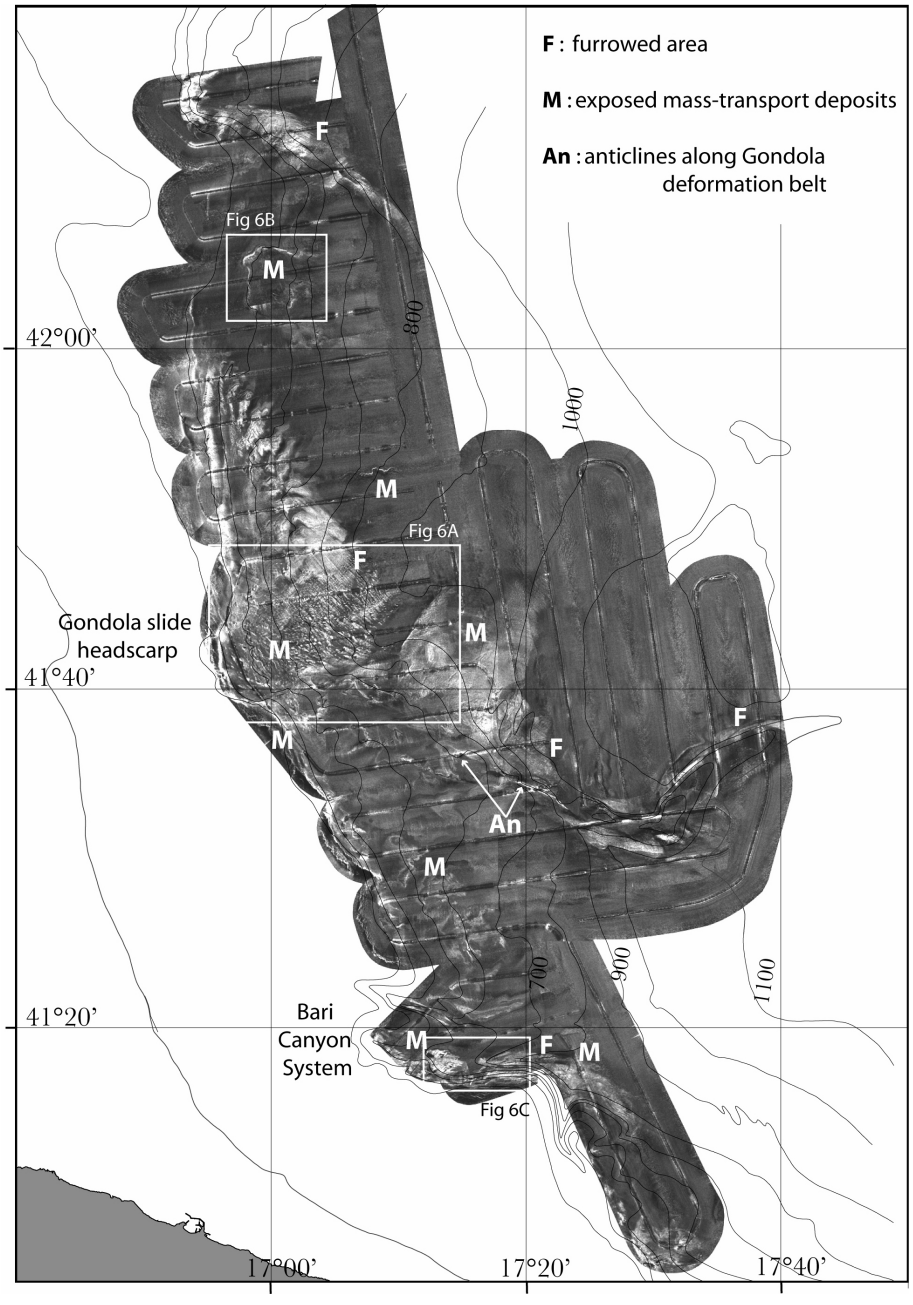

Fig. 5. TOBI side-scan-sonar image; high back-scatter (light tones) correspond to failed masses exposed at the seafloor or erosional areas, including eroded flanks of anticlines.

and correspond to a very irregular area of reduced acoustic-signal penetration accompanied by diffraction hyperbolae on Chirp-sonar profiles (Fig. 4). On side-scan-sonar images, the exposed accumulation zones are characterized either by a broad area of high back-scatter with multiple low-relief steps that appear rather irregular in plane view (Fig. 5), or by high-back-scatter polygonal reliefs, up to 500 m wide, accompanied by longitudinal stripes of alternating low and intermediate back-scatter (Fig. 6a). These stripes are interpreted as furrows (Flood, 1983) parallel to the main flow of the bottom currents (Verdicchio et al., 2005). The resulting morphologic pattern reflects the interaction between the complex relief created by down-slope gravity flows and along-slope bottom currents. On the lower slope and beneath the basin floor, acoustically-transparent deposits are generally buried under a stratified unit, locally affected by faint or disrupted reflectors (Figs. 4b, 11e). Where detectable, the base of the mass-transport deposits is erosional at the base of the slope and the top is irregular over the entire accumulation zone but with decreasing relief distally (Figs. 11c, e). A limited number of cores penetrating the slide top on the slope collected disaggregated sandy sediment encasing irregular clay chips (Fig. 7a).

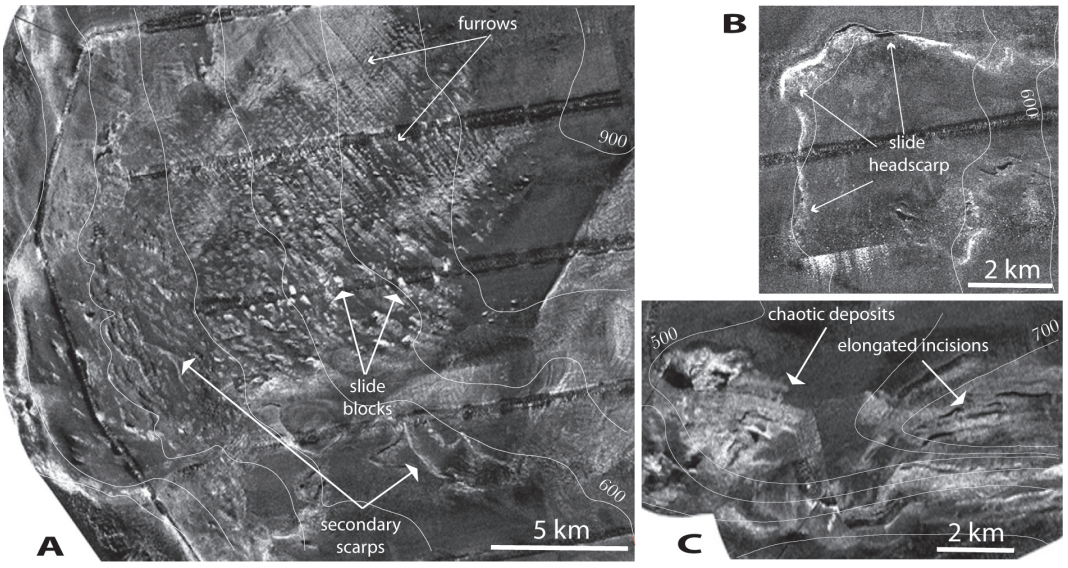

Fig. 6. Close ups of TOBI side-scan-sonar image of Fig. 5. **(A)**: secondary scarps and blocks of the Gondola Slide, and furrows parallel to the southward flow of bottom currents; **(B)**: 35 m-high headscarp of a recent failure; **(C)**: elongated incisions on the Bari canyon walls and chaotic deposit at the seafloor with high back-scatter.

4.2.3 Southern area

The southern area records three distinct failure events (I, II, III) predating the most extensive mass-transport deposit (GS) (Figs. 9, 10). Buried failed masses lay on irregular surfaces of pre-existing structural reliefs, are locally ponded and extend up to the erosional upper slope (Figs. 9, 11f). This 200 m-high, 30-km long, erosional upper slope, together with the region head of the Bari Canyon System, represents the most likely source area for I, II, III mass-transport deposits (Fig. 9). At the seafloor, several 10–20 m deep incisions dissect stratified units perpendicular or slightly oblique to the regional slope defining the flanks of folds related to the Gondola deformation belt (Fig. 7a) and recording a high back-scatter signature on side-scan-sonar mosaics (Fig. 5). Erosional surfaces separate also mounded layered deposits reflecting bottom-current activity and, in some cases, mark the top of old but exposed mass-transport deposits (Fig. 7a). Recent mass wasting in the southern area occurs along the steep walls of structural highs and, particulary, along the Bari Canyon System that develops between 150 and 1100 m water depth. Elongated incisions on the Bari canyon walls and chaotic deposit at the seafloor with high back-scatter suggest that the canyon is impacted by mass-transport events in recent times (Figs. 5, 6c).

4.3 Slope and basin floor stratified unit

A plane-parallel 10–16 m-thick stratified unit mantles the basin floor and shows great reflector continuity (Fig. 11f); approaching the base of the slope this unit thins and drapes areas of pre-existing irregular seafloor (Fig. 7b). Locally, in this area, the top of the stratified unit displays a diffused fine-scale roughness and the otherwise uniform reflectors are interrupted by a pattern of closely spaced sub-vertical disturbances with small vertical offsets, occasionally accompanied by diffraction hyperbolae, and folded reflectors (Figs. 7b, 11b). This seismic-reflector geometry is most evident where the seafloor morphology reflects the presence of shallow-buried mass-transport deposits (Fig. 11e). Indeed, this unit is irregular along the slope, everywhere the underlying topography is irregular. This draped unit, however, is no longer detectable in the slope areas directly impacted by bottom currents causing sediment winnowing or erosion and in areas where more recent failure has occurred (Figs. 4, 11e). Based on the internal seismic facies and on the structure of the top surface, the acoustical anomalies of the slope and basin floor stratified unit can be ascribed to fluid escape from the thick mass-transport deposit underneath (Trincardi et al., 2004). Upslope of the buried transparent deposits the layered unit and its base correlate, respectively, to a stratigraphic unit shaped in bottom current deposits and to one of their typical internal erosional surfaces (Fig. 7b).

4.4 Cores and stratigraphy

Seismic-stratigraphic correlation documents that the Gondola Slide deposit is coeval with buried mass-transport deposits in the northern basin area (Figs. 10, 11e). However, the roughly E-W lineament formed by the Gondola deformation belt (Fig. 7a) and the Dauno seamount (Fig. 10) hampers seismic-stratigraphic correlation toward the south, where mass-transport deposits occupy a similar stratigraphic position (compare Figs. 7b and 11a).

Sediment cores collected north and south of the Dauno seamount document that the slope and basin floor stratified unit is essentially a clay unit with rare interbedded silt-rich clayey horizons, thin bioclastic sandy layers and

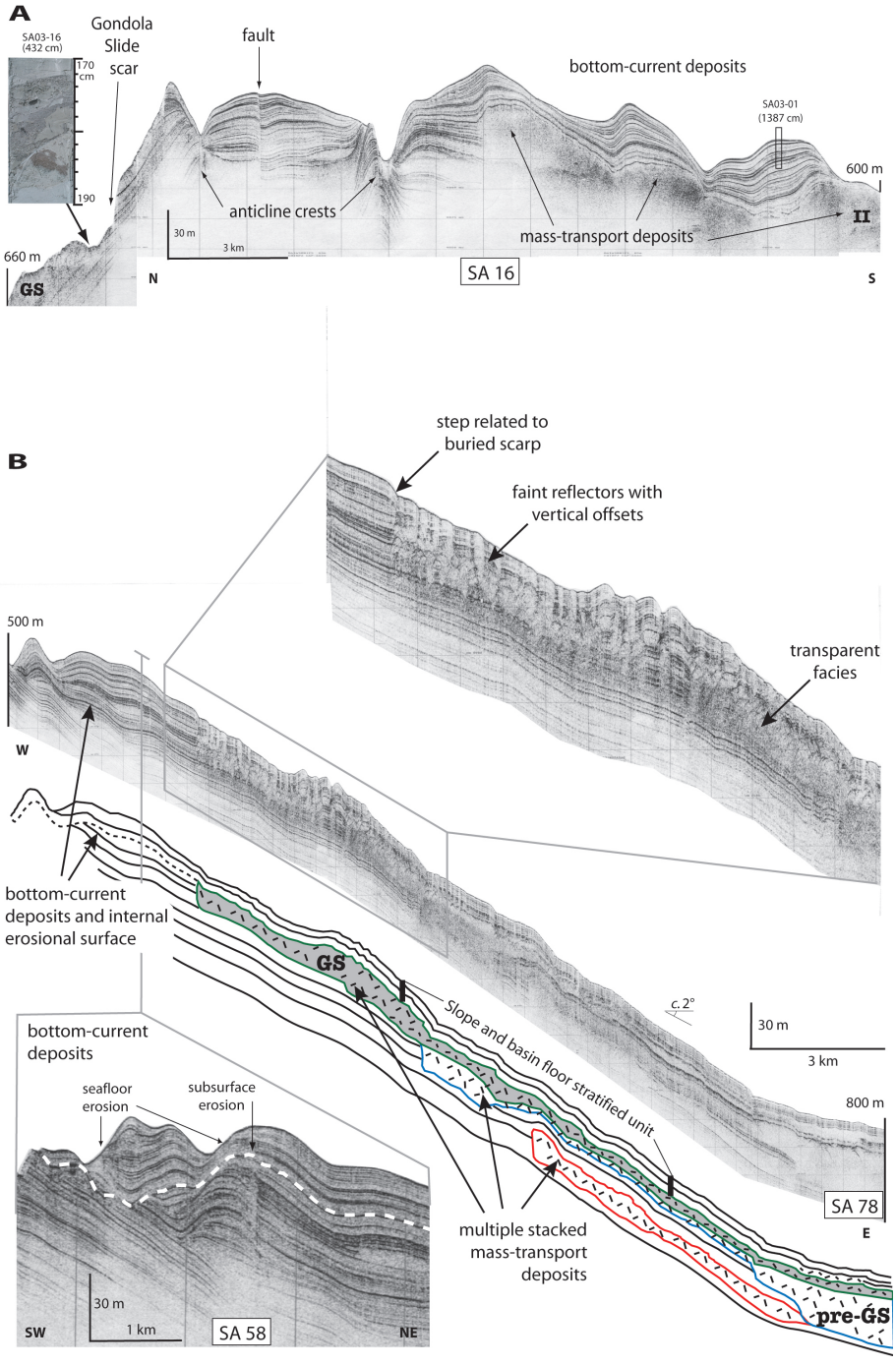

Fig. 7. **(A)**: Chirp-sonar profile (location in Figs. 2, 9, 10) crossing the Gondola deformation belt showing a fault and two anticlines whose flanks are dissected by deep incisions; the acoustically-transparent deposits on the rigth are mass-transport deposits, partly buried by asymmetric and mounded bottom-current deposits. Core SA03-01 is discussed in Fig. 12. On the left, bedding planes steeply dip to the north providing potential slip surfaces for Gondola Slide. Core SA03-16 from Gondola Slide deposits retrieved remolded silty mud deposits. **(B)**: Chirp-sonar profile (location in Figs. 2, 3, 9, 10) and line drawing along the lower slope showing a set of acoustic-transparent mass-transport deposits; note the layered stratigraphic units separating individual mass-transport deposits and the coalescence of mass-transport deposits basinward; a well-stratified unit mantles the seafloor with diffuse roughness and small vertical offsets (upper close-up); bottom-current bedforms (on the left) show seafloor and subbottom erosional surfaces, better imaged in a perpendicular profile (lower close-up).

volcanogenic layers either visible (and up to centimetric thicknesses) or detectable at the microscope only (Fig. 12). Core correlation is mainly based on foraminifera assemblages (see Verdicchio et al., 2005) and magnetic susceptibility curves whose peaks commonly indicate the presence of tephra layers. Ages are ascribed to biozone boundaries

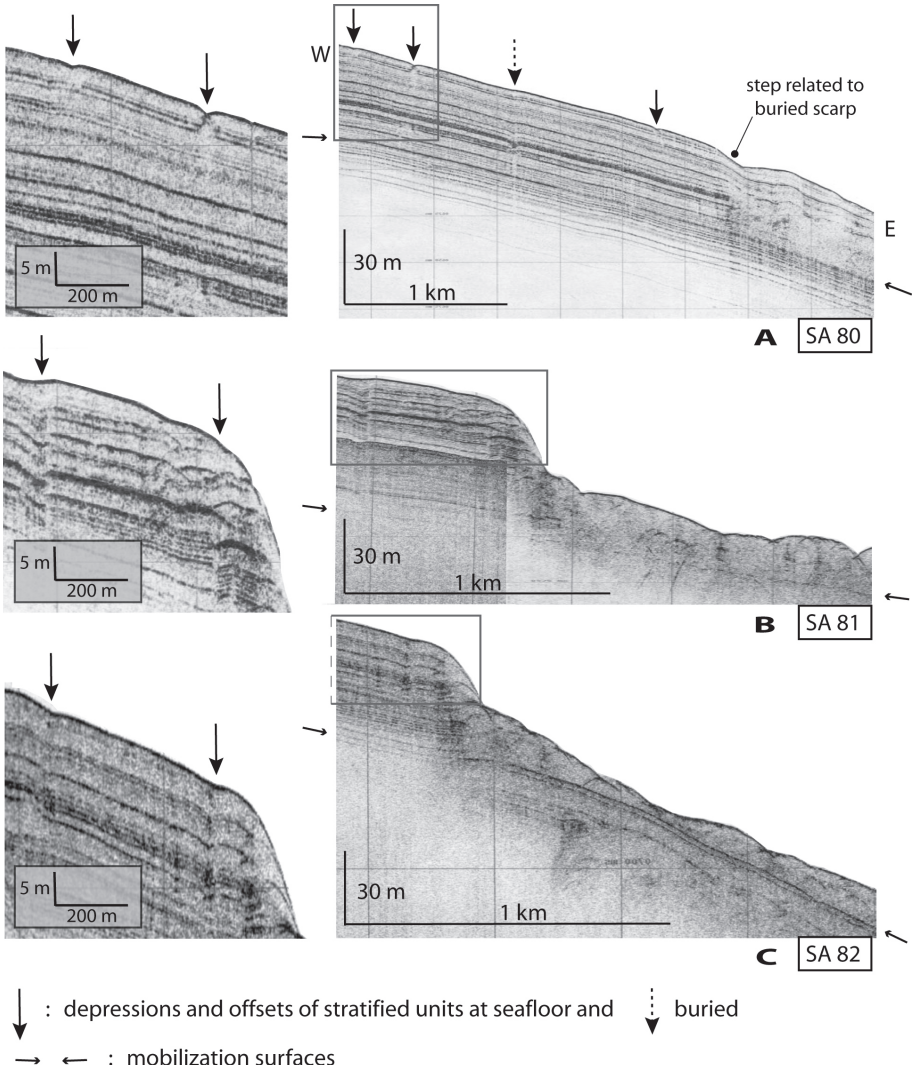

Fig. 8. Chirp-sonar profiles (location in Figs. 2, 9, 10) and close-ups showing subtle depressions and minor reflector offsets of otherwise undisturbed sediment units at the seafloor or buried. Note that these features do not extend below the basal mobilization surfaces. Acoustically-transparent deposits lay at the base of the scarp implying that evacuation was not complete after failure.

based on published literature and framed in a well defined seismic stratigraphic context (Jorissen et al., 1993; Asioli 1996, 1999, 2001; Trincardi et al., 1996; Capotondi et al., 1999; Ariztegui et al., 2000).

The slope and basin floor stratified unit thins across the morphologic high that marks the center of the south Adriatic basin and against which Gondola Slide deposit pinches out (Figs. 10, 12). Beyond this high, piston cores YD97-10 and SA03-6, into undisturbed well-stratified muddy sediment, encountered a graded fine-grained sand bed interpreted as a turbidite deposit (Fig. 12). This bed correlates, on Chirp-sonar profiles, with the acoustically-transparent deposit of Gondola Slide indicating that the mass-transport produced a distal turbidite deposit beyond the failed masses mapped on the basis of Chirp-sonar profiles (Fig. 10).

Figure 12 shows two transects, north and south of the Dauno seamount, defining the age of the largest mass-transport deposit (GS), which includes Gondola Slide. Biostratigraphic information from planktonic foraminifera allow define the post-failure units above this main mass-transport deposit and its distal correlative turbidite deposits. The succession of post-failure units (both N and S of Dauno seamount) includes, from top to bottom: 1) a typically reduced thickness of late-Holocene deposits above the Last Occurrence of *Globorotalia inflata* (Asioli, 1996); 2) a well defined Sapropel S1 interval characterised by large specimens of *Globigerinoides ruber* (pink) with thin and inflated tests; all cores show evidence of a sapropel break as previously observed in the area and marked by the re-appearance of *Globorotalia inflata* and *Globorotalia truncatulinoides* (Rohling et al., 1997; Ariztegui et al., 2000); core ST04-01 lacks biostratigraphic information but displays the typical change in color of the sapropel S1 and its break associated to a minimum in whole-core magnetic susceptibility;

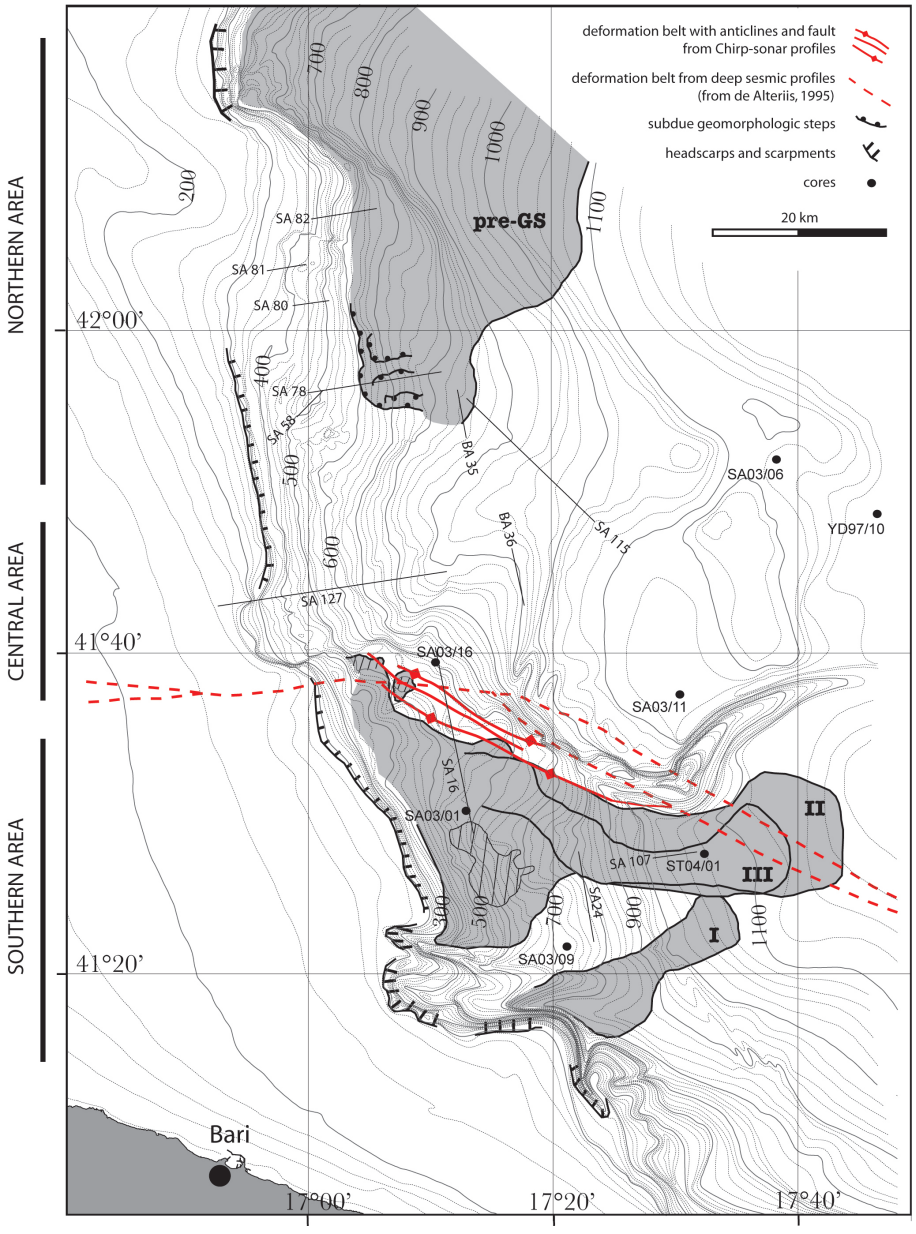

Fig. 9. Distribution of mass-transport deposits pre-dating the largest failure event of the Southwestern Adriatic Margin. Areas not delimited by solid lines correspond to uncertain boundaries. In the northern area individual failed masses coalesce and have been mapped as a whole (pre-GS). In the southern area, relative emplacement of distinct mass-transport deposits is indicated by roman numbers (dashed areas correspond to exposed failed units).

furthermore, all cores include a tephra layer into the sapropel interval corresponding to the Mercato event (Asioli et al., 1996; Calanchi et al., 1998; Siani et al., 2001; Lowe et al., 2005); 3) the pre-Boreal interval, characterised by repeated and short-term oscillations in the relative abundance of species indicative of cold and warm waters; 4) the GS-1 (Younger Dryas) interval marked by a dominant cold-water association with *Globigerina bulloides*, *Neogloboquadrina pachyderma* and *Globorotalia scitula*, and including a tephra layer, known as C1, that corresponds to the Pomici Principali event (Asioli et al., 1996; Calanchi et al., 1998; Siani et al., 2001; Lowe et al., 2005); 5) the GI-1 interval (Bolling/Allerod) marked by a basal peak in the abundance of *Globigerinoides ex gr. ruber* and an oscillatory cooling trend as previously observed in the Central Adriatic (Asioli et al., 1999, 2001); 6) a glacial interval dominated by cold water species like *Globigerina bulloides*, *Neogloboquadrina pachyderma* and *Globorotalia scitula* (indicated as MIS 2 on Fig. 12). The top of the GS-mass-transport deposit in both sub-basins lays within this glacial unit (MIS 2).

Distal cores, in both transects, penetrated the largest slide deposit (GS) or the correlative turbidite deposits and allow

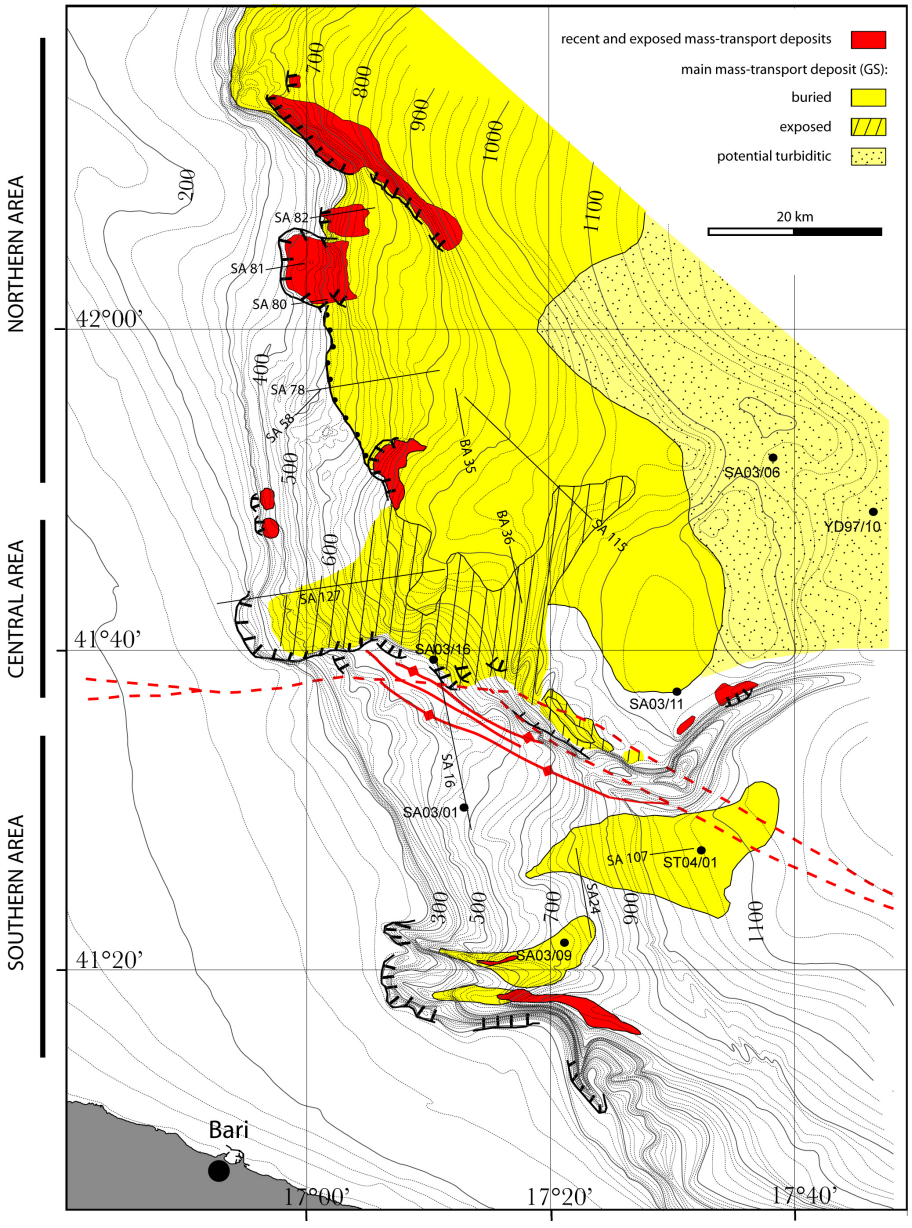

Fig. 10. Distribution of the largest mass-transport deposit (GS) in the Southwestern Adriatic Margin and of recent-most failed masses with geomorphic expression at the seafloor.

define the age of the units immediately beneath, that, in all cases, are consistent with a MIS 2 age, as confirmed also by core YD97-10 where the top of MIS 3 was reached about 3 m below the turbidite. In both transects the age of the mass-transport deposit, and related distal turbidites, appear comparable based on the identical succession of foraminifera associations, rapidly summarised above, and additional data including: 1) whole-core magnetic susceptibility curves; 2) successions of peaks in magnetic susceptibility corresponding to consistent succession of tephra layers (each occurring consistently within the same biostratigraphic association); 3) the presence of a two-phase tephra horizon characterised by a couplet of layers with distinctive colours (Fig. 12). The GS-mass-transport deposit and its distal correlative turbidite deposits are in the order of 20–24 ky cal. BP old, assuming a constant sediment accumulation rate within the glacial unit (MIS 2) where they occur.

In the southern area several mass-transport deposits stack on the slope and not only in the basin area. The correlation above, however, suggests that at least one event in this area is virtually coeval with the main failure event (GS) occurred northward of the Gondola deformation belt indicating a possible common trigger during the MIS 2-glacial interval (Fig. 10).

The younger age of other, overlying, mass-failure deposits is evident where headscarps and displaced masses affect the stratified units recording the post-glacial interval (Figs. 8b, c, 10). Main recent-most failures head in proximity to the

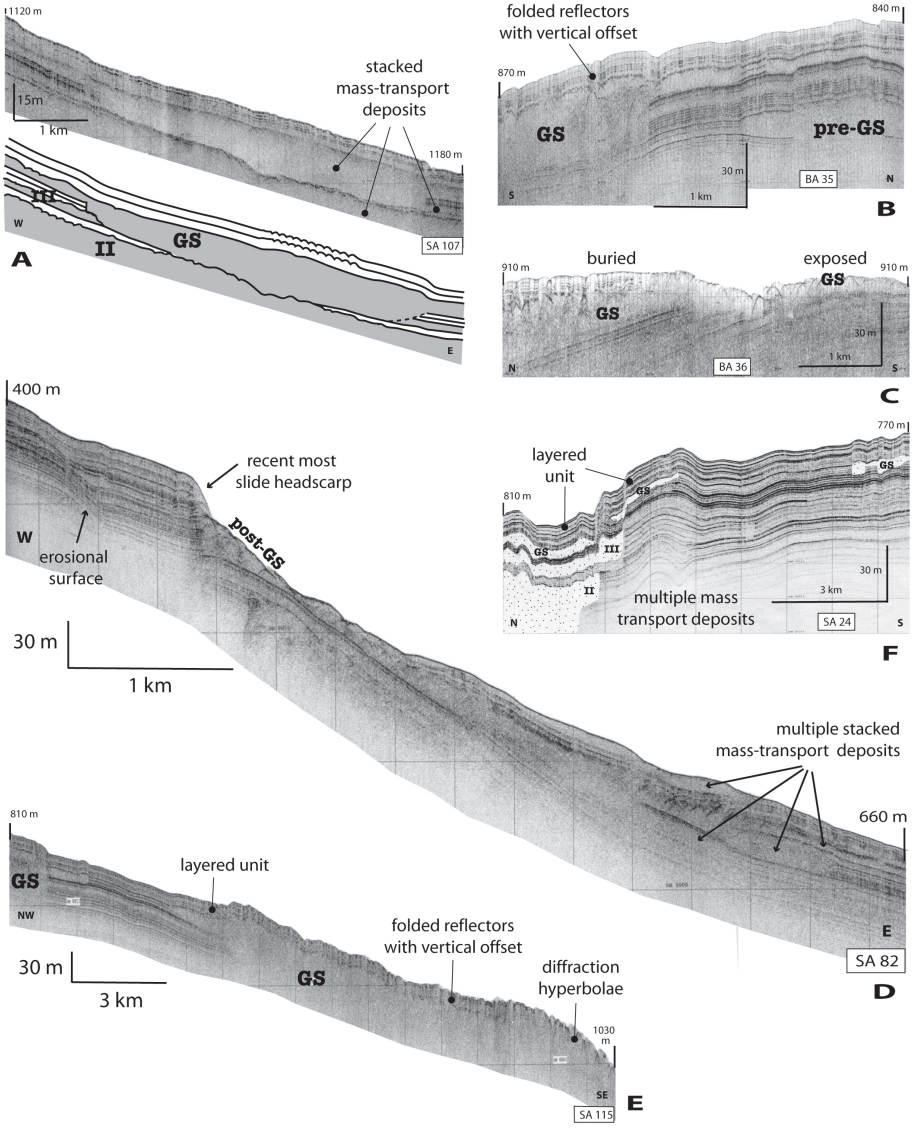

Fig. 11. Chirp sonar profiles located in Figs. 2, 9, 10. **(A)**: coalescence of distinct mass-transport deposits (GS and III), laterally separated by stratified units; note the high-amplitude reflector with hyperbolic defractions that separate two failed masses (GS and II), otherwise undistinguishable. **(B)**: correlation of top of a failed mass (pre-GS) and base of a younger failed mass (GS); the stratified unit that mantles the seefloor presents diffuse fine-scale roughness, sub-vertical disturbances and folded reflectors. **(C)**: physical continuity of the same mass-transport deposit buried and exposed at the seafloor. **(D)**: mass-transport deposits superimposed in an area of recent failure; note that mobilization surface correlates upslope with an erosional surface (arrow). **(E)**: seismo-stratigraphic correlation between Gondola Slide deposits (right) and mass-transport deposits of the northern area (left); the uppermost stratified unit shows vertical acoustic disturbances where the failed deposit beneath is thicker; note that this draped unit is locally affected by erosion and/or failure (rigth). **(F)**: ponded mass-transport deposits (left); uppermost failed deposits are time equivalent and correlate with the main mass-transport deposits (GS) of the Southwestern Adriatic Margin.

buried headscarps or extend further upslope affecting well stratified units. Incipient failure features distribute upslope of the recent-most slide scarps and indicate a potential generation of mass movements over a large area of the SAM, with consequent possibility of tsunamogenic hazard (Fig. 8).

5 Discussion

5.1 Failed units, predisposing factors and triggers

On the outer shelf of the SAM, Pleistocene progradational sequences, are selectively affected by repeated events of sediment failure characterized by limited displacement above downlap surfaces (Trincardi et al., 2004). On the steep upper slope these progradational sequences and the downlap

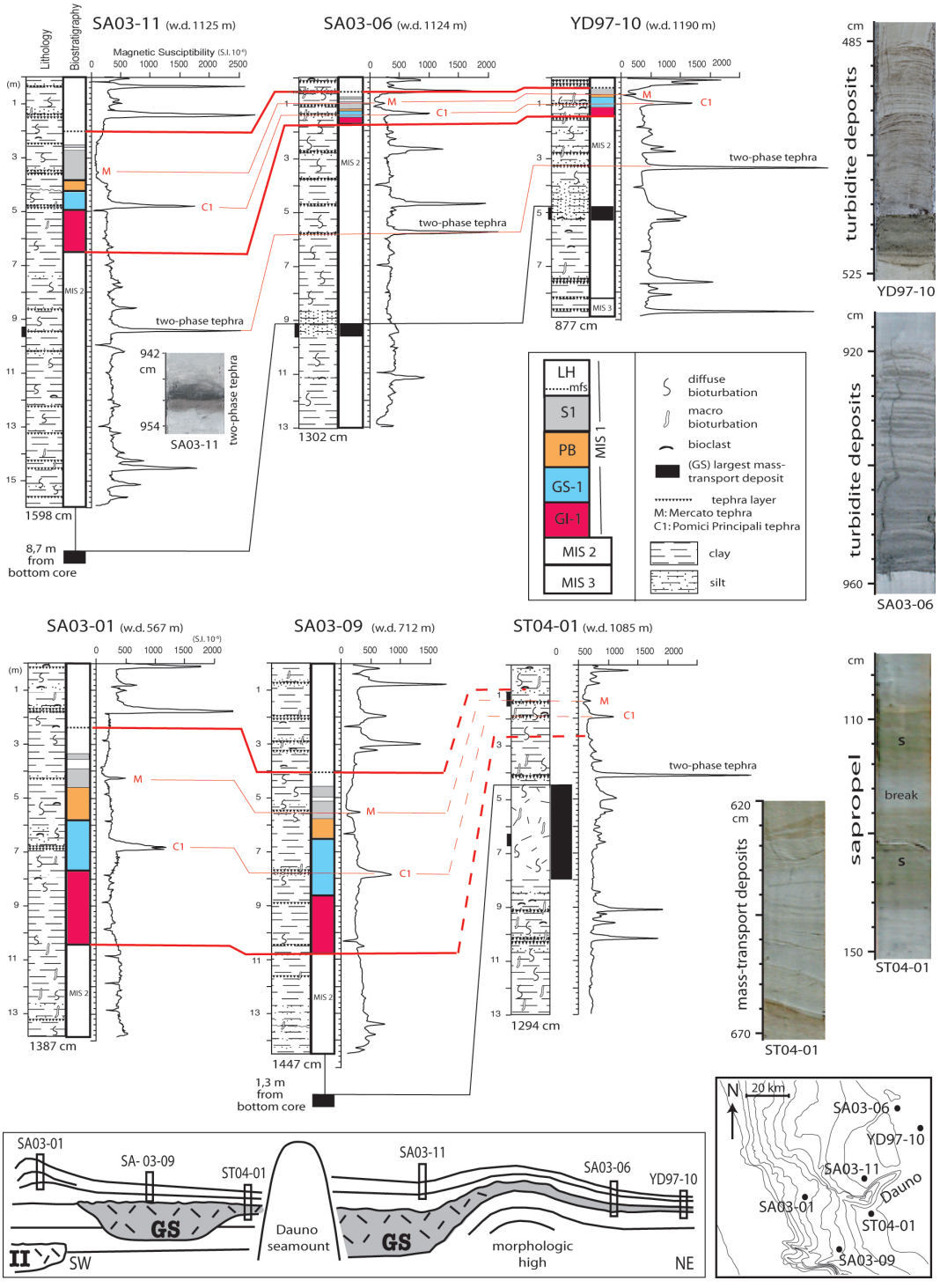

Fig. 12. Stratigraphic correlation between six piston cores, north and south of the Dauno seamount. Bold lines on the scales indicate the photographs locations. LH: late Holocene, mfs: maximum flooding surface (occurred after last sea-level rise), S1: Sapropel 1, PB: pre-Boreal, GS-1: Glacial Stadial 1, GI-1: Glacial Interstadial 1, MIS: Marine Isope Stage. Biostratigraphic subdivisions are based on planktonic foraminifera biozones for the Central Mediterranean region (Asioli et al., 1996, 2001; Verdicchio et al., 2005). The two core transects N and S of Dauno seamount reached, in the most distal cores, either the pinch out of the GS-mass-transport deposit seen on seismic profiles (southern transect, core ST04-01) or a thick turbidite deposit (northern transect) interpreted as the distal equivalent of the GS-mass-transport deposit. In both transects, the undisturbed unit above the GS-mass-transport deposit and turbidite deposits onset during the last glacial interval (MIS 2). The correlation of several stratigraphic markers (including Sapropel S1 and a two-phase tephra) suggests that failure has the same age in the whole study area.

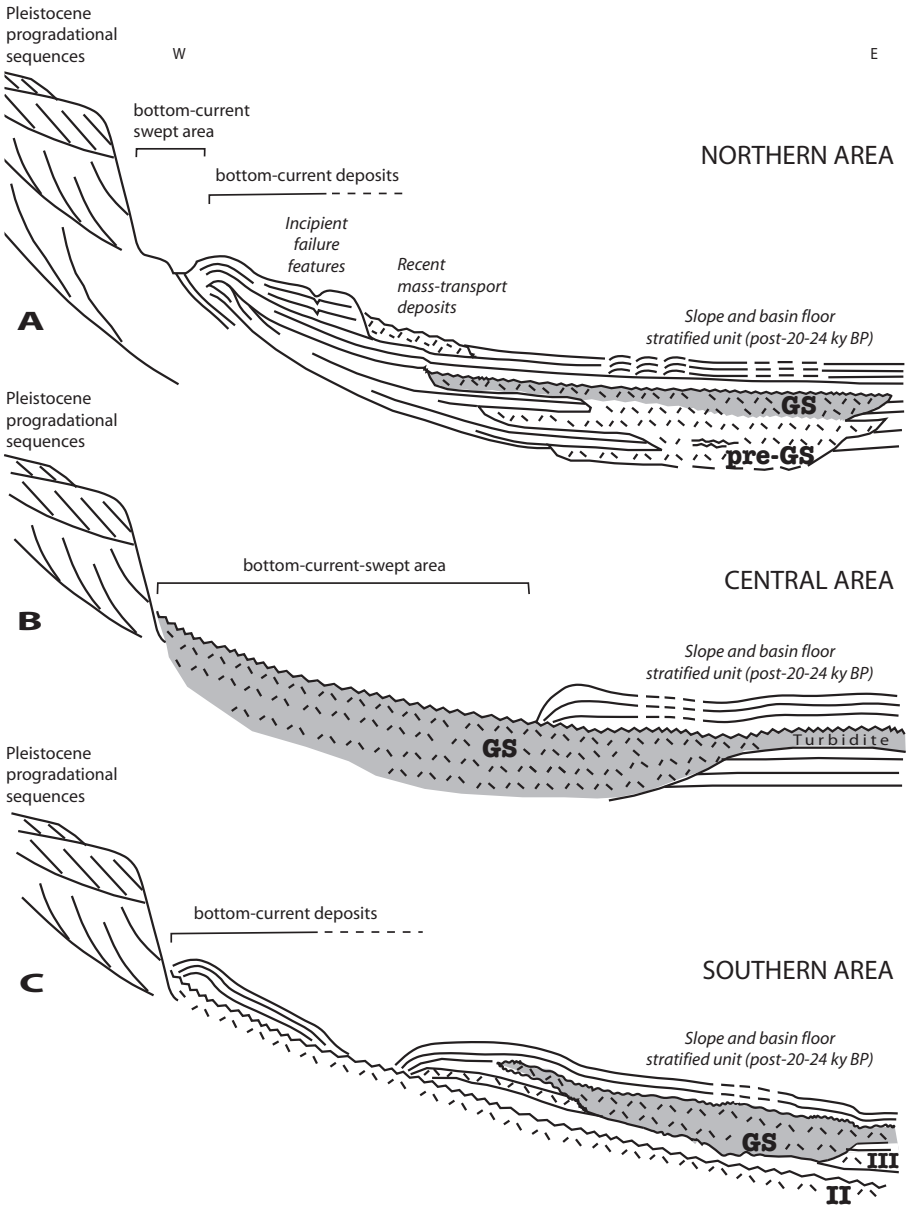

Fig. 13. Simplified stratigraphic scheme of northern, central and southern areas of the Southwestern Adriatic Margin. Note that bottom currents define areas of enhanced deposition or extensive erosion along the slope, making the age determination of the GS-event problematic.

surfaces at their base are variably truncated along the upper-slope escarpment and local slide scars (Figs. 4, 13). On the lower slope, failure affects bottom-current deposits that are dominant in this area and commonly overlay older failed units; both the units affected by failure and the post-failure deposits record a similar depositional environment variably impacted by the activity of bottom currents; therefore, sediment failure did not lead to a change in depositional style in the area (Fig. 13a).

The main predisposing factors conducive to sediment instability on the SAM include: 1) active tectonism leading to local increases of margin steepness; 2) slope erosion or enhanced deposition by bottom currents; 3) occurrence of possible weak layers. Tectonic deformation affected the SAM during the last 500 ky causing the progressive seaward tilt of the margin (Ridente and Trincardi, 2002a) while active tectonic deformation on the margin generated faults and gentle anticlines affecting shallow deposits along the E-W-trending Gondola deformation belt (Tramontana et al., 1995; Ridente and Trincardi, 2002a) (Fig. 7a). The instability of the margin was likely further enhanced through local oversteepening derived from southward erosional currents focused at the toe of the upper slope and structural highs; the incision of erosional moats may undermine the northern upper slope (Fig. 2). Sedimentation and erosion patterns are related to bottom currents whose variable activity, over the area and over time, is recorded by bottom-current deposits and multiple erosion surfaces of variable along- and down-slope extent

both at the seafloor and deeper in the stratigraphic record (Figs. 2, 7b). Seaward of the northern bottom-current bedform field, mass-transport deposits have tops that correlate with buried erosional surfaces within the conturite deposits, thus suggesting that some failures occurred in a dominantly erosional environment where reworking of the mass transport deposit was recurrent and, later, a time-equivalent layer covered both the accumulation zone and the upslope erosional surface (Figs. 7b, 13). Other kinds of slip planes, often marked by acoustically enhanced seismic reflectors, and acting as weak layers, may coincide with buried erosional surfaces (Fig. 11d), with the irregular top of older mass-movement deposits (Fig. 11b) or with comformable layers that mark the abrupt base of the observed vertical acoustic disturbances (Fig. 8). Local tectonic deformation, erosion and sedimentation become crucial factors controlling mass movement location and size on several margins worldwide, including the northern Pacific slope where mass-transport deposits appear somewhat independent from seismicity (McAdoo et al., 2000).

Recurrent seismic activity affects the SAM and likely plays a major role as a trigger for sediment instability. Earthquakes during historical times exceed 6.6 on Richter scale (Tinti et al., 1995). Earthquakes can induce large cyclic loading and remains a plausible triggering mechanism for the observed extensive mass wasting on the SAM, similarly to what has been proposed for other Adriatic areas (Correggiari et al., 2001; Cattaneo et al., 2004; Trincardi et al., 2004).

5.2 Mass-transport styles

The mass–transport features on the SAM slope indicate a succession of failure events involving several distinctive styles of mass movement. A similar degree of complexity has been recurrently observed in several other failure areas worldwide (e.g., Hampton et al., 1996; Mulder and Cochonat, 1996; Canals et al., 2004). On the SAM, the headscarps on the upper slope occur where the underlying progradational strata show the greatest dip seaward, a common predisposing factor also in other slide areas worldwide. In the central and southern area progradational deposits are involved in mass failure deposits, respectively exposed and buried at the base of the slope (Figs. 13b, c), while in the northern area, masses evacuated from progradational units, not imaged on Chirp-sonar profiles, are likely deeper and buried beneath the basin floor (Fig. 13a). A similar scenario is reported from other continental margins that exhibit steep and high-relief headscarps on the upper slope and buried mass wasting deposits beneath the basin floor (e.g., Twichell et al., 1993; Wilson et al., 2003).

On the slope, particularly in the northern area, mass-transport deposits reflect distinct events with un-deformed layered units between failed deposits (Figs. 7b, 13a). Initially, failure occurred in response of slope over-steepening and/or of enhanced erosion driven by the intensification of southward-flowing bottom currents. After the deposition of a layered unit, a new phase of slope instability generated new failed deposits partially overlapping the previous one and locally eroding part of the underlying layered unit. These displaced deposits lack of a well-defined parent headscarp likely because in situ deformation dominated with only a minor component of downslope movement (Figs. 7b, 8a). This interpretation is supported by the evidence in the upslope part of the failed material of faint internal reflectors accompanied by small vertical offsets with little internal remolding, possibly indicating more coherent material within the deformed mass; proceeding basinward, the internal character of the failed deposit changes into a transparent facies with irregular base and top suggesting increased remolding through mass flow (Fig. 7b).

The uppermost of the buried failed deposits (GS) represents the largest failure event that affected the SAM (Fig. 10). While in the northern area this main failure event is related to in situ deformation and mass flow processes, as discussed above, in the central area the same failure is expressed by the Gondola Slide. In this area, the failure event went through significant mechanical transformations over relatively short lateral distances, undergoing changes in rheology during its downslope translation, as noted in the evolution of other failures (Hampton, 1972; Cochonat and Piper, 1995; Mulder and Cochonat, 1996; Hampton et al., 1996; Mulder et al., 1998). In fact, Gondola Slide is here interpreted as a slide transforming into mass flow and consequent further turbidite: crescent-shaped 250 m-high headscarp, secondary scarps and transverse cracks occur in the evacuation zone affected by sliding of relatively coherent masses; the high-back-scatter polygonal areas, on the slope, suggest a break up of the displaced mass into distinct slide blocks; disaggregated sandy sediment supporting irregular clay chips, recovered in the accumulation zone, indicates a further disintegration of the mass-transport deposits. The significant run out distance ($>$50 km) supports the evolution of the failed mass into a flow spreading over a large area. A coarser-grained horizon within a muddy succession, cored beyond the distal pinch-out of the seismically-detectable acoustically-transparent unit, represents a distal turbiditic component of the mass-transport deposit indicating the evolution of the flow into a turbidity current.

Mass-transport style of coeval failed deposits in the southern area is complicated by the irregular pre-existing morphology that divides the GS-failed deposits in distinct ponded units and scattered depocenters (Fig. 11f).

Recent-most failed masses in the SAM are scattered along the margin, both upslope of buried mass-transport deposits and clustered along the steep walls of structural highs and the Bari Canyon System, thus representing upslope extensions or local reactivations of main failure zones (Figs. 3, 10). Some of these recent-most mass-transport deposits moved on a relatively deep weak layer, as noted along other margins (Trincardi and Field, 1992; Field, 1993; Lee at al., 2003). In some cases, these layers relate to pre-existing slip planes that locally coincide with one of the multiple detechment surfaces generated by the largest failure event. The sediment mobilization was thus likely confined to a thin horizon, leading

to the collapse of the sediment above it; folding of beds was possibly brought about by the interaction between downslope transport and shear resistance on the overlying sediment pile (Fig. 8b).

5.3 Timing of failure

Although the evidence of sediment failure is widespread on the SAM slope, dating individual mass-failure events is complicated by the following main factors: 1) the excessive depth of burial of the oldest mass-transport deposits (I, II, III) that prevents sampling by conventional coring; 2) the stacking of multiple mass-transport deposits that prevents precise correlation of some of the oldest units (pre-GS); 3) the lack of post-failure sedimentary units not only in the youngest deposits but also in some areas where bottom currents sweep the seafloor leaving the slide age undetermined (GS). In addition, and more in general, we still lack a sufficient number of sediment cores to allow dating of each individual mass failures on the SAM. However, despite these limitations some basic information on the timing of sediment failure on the SAM comes from seismic-stratigraphic architecture, sea floor morphology, and sediment cores correlation (Fig. 12).

The largest failure event (GS) occurred within the MIS 2-glacial unit (in the order of 20–24 ky cal. BP) as most sequence-stratigraphy models predict during low sea-level intervals (e.g., Posamentier et al., 1988). During low sea-level intervals failed deposits are widely recognized in the deepest areas of the Mediterranean Sea (e.g., Rothwell et al., 1998; Reader et al., 2000; Trincardi et al., 2004).

Interestingly, growing evidence from the study area and other sub-basins in the Mediterranean Sea indicate that failures occurs also during overall sea-level rise conditions (e.g., Trincardi et al., 2003; Canals et al., 2004, and references therein). On the SAM, these more recent failure events result in several mass-transport deposits of small size. Nevertheless, these deposits confirm the unstable nature of the margin.

5.4 Incipient failures and tsunamogenic area

The occurrence of a new large-scale slope failure on the SAM is possible, as the area shows clear-cut scarps that delimit sediment units and disappear on key seaward-dipping reflectors interpreted as possible weak layers. These scarps occur upslope of older mass-transport deposits that are either buried or exposed at the seafloor (Fig. 8). In some cases, subdued morphologic steps are also associated to buried mass-transport deposits (Figs. 3b, 7b), an erosional moat undermining the upper slope (Fig. 2) and subtle depressions accompanied by modest offsets of the underlying seismic reflectors indicating short and narrow linear features and/or small pockmarks (Fig. 8). This evidence characterizes an area of tens of kilometers along the slope. All together these features define areas that are still prone to failure that may occur as part of a longer-term retrogressive trend.

It is also possible that some of the largest failure deposits generated tsunami in the past. In the case of Gondola Slide, this hypothesis is supported by 1) the significant height of the head scarp (as much as 250 m), 2) the initial sliding that presumebly mobilized coherent masses as supported by the presence of relatively large blocks in the proximal area, and 3) the slide scar breaching the shelf break and therefore indicating failure in shallow water, particularly if taking place during the last glacial interval (MIS2) when sea level was 120 m lower than today (Fairbanks, 1989). Together these characters are key in the generation of a tsunami.

6 Conclusions

Multiple slide scars and extensive, buried or exposed, mass-transport deposits testify widespread and recurrent sediment failure events on the Southwestern Adriatic Margin (SAM). A preliminary overview of the margin morphology and stratigraphy supports the following conclusions:

1. Distinctive failure styles range from in situ sediment deformation to sliding and mass transport with run out distances up to more than 50 km and evolving, distally, in turbidity currents.

2. The most widespread failure event affected the SAM during the MIS 2-glacial interval, north and south of the Dauno seamount on a combined area of 2670 km^2.

3. After the main phase of failure, the lower slope and basin floor was progressively buried by a thick and layered unit; the slope shallower than about 700 m, instead, remained exposed to the waxing of bottom currents that prevented deposition or focused sediment to confined areas (Fig. 13). Locally, the resulting bottom-current deposits were affected by additional failure in recent times.

4. The most recent failure areas are several, but appear smaller in extent, and more limited in displacement compared with older events. These most recent failures typically occur on pre-existing seaward dipping slip planes and represent local reactivations or an upslope (retrogressive) propagation of slope failure after the MIS 2-glacial interval.

5. The margin shows elongated steps and clear-cut scarps indicating possible incipient failure further upslope of the areas that failed most recently. This evidence, together with evidence of seismic activity and tectonic deformation, indicates that a large area of the SAM may still be prone to failure. Further studies should define the extent of these failures and their potential in tsunami generation.

Acknowledgements. This study was supported by the European project EUROSTRATAFORM (EC contract no. EVK3-CT-2002-00079). We thank the captains and crews of R/V Urania, R/V Odin Finder, the TOBI team and all participants to campaigns

SAGA-03, STRATA-04 and BARI-05. This is ISMAR-Bologna (CNR) contribution no. 1472.

Edited by: S. Tinti
Reviewed by: H. Haflidason and another referee

References

Argnani, A., Favali, P., Frugoni, F., Gasperini, M., Ligi, M., Marani, M., Mattietti, G., and Mele, G.: Foreland deformational pattern in the southern Adriatic sea, Annali di Geofisica, 36, 229–247, 1993.

Ariztegui, D., Asioli, A., Lowe, J. J., Trincardi, F., Vigliotti, L., Tamburini, F., Chondrogianni, C., Accorsi, C. A., Bandini Mazzanti, M., Mercuri, A. M., van der Kaars, S., McKenzie, J. A., and Oldfield, F.: Palaeoclimate and the formation of sapropel S1; inferences from late Quaternary lacustrine and marine sequences in the central Mediterranean region, Palaeogeography, Palaeoclimatology, Palaeoecology, 158, 215–240, 2000.

Artegiani, A., Bregant, D., Paschini, E., Pinardi, N., Raicich, F., and Russo, A.: The Adriatic Sea general circulation. Part II: Baroclinic circulation structure, J. Phys. Oceanography, 27, 1515–1532, 1997.

Asioli, A.: High resolution foraminifera biostratigraphy in the central Adriatic basin during the last deglaciation: a contribution to the PALICLAS project, Memorie Istituto Italiano Idrobiologia, 55, 197–217, 1996.

Asioli, A., Trincardi, F., Lowe, J. J., and Oldfield, F.: Short-term climate changes during the Last Glacial-Holocene transition: comparison between Mediterranean records and the GRIP event stratigraphy, J. Quaternary Sci., 14, 373–381, 1999.

Asioli, A., Trincardi, F., Lowe, J. J., Ariztegui, D., Langone, L., and Oldfield, F.: Sub-millennial climatic oscillations in the Central Adriatic during the last deglaciation: paleoceanographic implications, Quaternary Science Reviews, 20, 33–53, 2001.

Calanchi, N., Cattaneo, A., Dinelli, E., Gasparotto, G., and Lucchini, F.: Tephra layer in Late Quaternary sediments of the Central Adriatic Sea, Mar. Geology, 149, 191–209, 1998.

Canals, M., Lastras, G., Urgeles, J. L., et al.: Slope failure dynamics and impacts from seafloor and shallow sub-seafloor geophysical data:case studies from the COSTA project, Mar. Geo., 213, 9–72, 2004.

Capotondi, L., Borsetti, A. M., and Morigi C.: Foraminiferal ecozone, a high resolution proxy for the late Quaternari biochronology in the central Mediterranean Sea, Mar. Geology, 153, 253–274, 1999.

Cattaneo, A., Correggiari, A., Marsset, T., Thomas, Y., Marsset, B., and Trincardi, F.: Seafloor undulation pattern on the Adriatic shelf and comparison to deep-water sediment waves, Mar. Geo., 213, 121–148, 2004.

Cochonat, P. and Piper, D. J. W.: Source area of sediments contributing to the “Grand Banks” 1929 turbidity current, in: Atlas of deep water environments; architectural style in turbidite systems, edited by: Pickering, K. T., Hiscott, R. N., Kenyon, N. H., Ricci Lucchi, F., and Smith, R. D. A., Chapman and Hall, London, U.K., 12–13, 1995.

Colantoni, P., Preti, M., and Villani, B.: Sistema deposizionale e linea di riva olocenica sommersi in Adriatico e al largo di Ravenna, Giornale di Geologia, 52, 1–18, 1990.

Correggiari, A., Trincardi, F., Langone, L., and Roveri, M.: Styles of failure in heavily-sedimented highstand prodelta wedges on the Adriatic shelf, J. Sedimentary Res., 71, 218–236, 2001.

Cushman-Roisin, B., Gacic, M., Poulain, P. M., and Artegiani, A.: Physical oceanography of the Adriatic Sea – past, present and future, Kluver Acad. Publ., Dordrecht, The Netherlands, pp. 304, 2001.

D’Argenio, B. and Horvarth, F.: Some remarks on teh deformation history of Adria, from the Mesozoic to the Tertiary, Ann. Geophys., 2, 143–146, 1984.

de Alteriis, G.: Different foreland basins in Italy: examples from the Central and Southern Adriatic Sea, Tectonophysics, 252, 349–373, 1995.

Doglioni, C., Mongelli, F., and Pieri, P.: The Puglia uplift (SE Italy): an anomaly in the foreland of the Apennine subduction due to buckling of a thick continental lithosphere, Tectonics, 13, 1309–1321, 1994.

Fairbanks, R. G.: A 17 000 year glacio-eustatic sea level record: influence of glacial melting rates on the Younger Dryas event and deep-ocean circulation, Nature, 342, 637–642, 1989.

Farre, J. A., McGregor, B. A., Ryan, W. B. F., and Robb, J. M.: Breaching the shelf; Passage from youthful to mature phase in submarine canyon evolution, in: The shelfbreak: Critical interface on continental margins, edited by: Stanley, D. J. and Moore, G. T., Society of Economic Paleontologists and Mineralogists, Spec. Publ., 33, 25–39, 1983.

Field, M. E.: Liquefaction of continental shelf sediment; the Northern California earthquake of 1980, in: Submarine landslides; selected studies in the U.S. Exclusive Economic Zone, edited by: Schwab, W. C., Lee, H. J., and Twichell, D. C., USGS Bull., 2002, 60–68, 1993.

Finetti, I., Bricchi, G., Del Ben, A., Pipan, A., and Xuan, Z.: Geophysical study of the Adria plate, Mem. Soc. Geol. It., 40, 335–344, 1987.

Fryer, G. J., Watts, P., and Pratson L. F.: Source of the great tsunami of 1 April 1946: a landslide in the upper Aleutian forearc, Mar. Geol., 203, 201–218, 2004.

Gardner, J. V., Van den Ameele, E. J., Gelfenbaum, G., Barnhardt, W., Lee, H. J., and Palmer, S.: Mapping southern Puget Sound delta fronts after 2001 earthquake, Eos, Transactions, American Geophysical Union, 82, 485, 488–489, 2001.

Geist, E. L.: Origin of the 17 July 1998 Pappau New Guinea tsunami: earthquake or landslide?, Seismological Res. Lett., 71, 344–355, 2000.

Hampton, M. A.: The role of subaqueous debris flow in generating turbidity currents, J. Sediment. Petrol., 42, 775–793, 1972.

Hampton, M. A, Lee, H. J, and Locat, J.: Submarine landslides, Rev. Geophys., 34, 1, 33–59, 1996.

Hasegawa, H. S. and Kanamori, H.: Source mechanism of the magnitude 7.2 Grand Banks earthquake of November 18, 1929: double-couple or submarine landslide?, Bull. Seism. Soc.Am., 77, 1984–2004, 1987.

Jorissen, F. J., Asioli, A., Borsetti, A. M., Capotondi, L., de Visser, J. P., Hilgen, F. J., Rohling, E. J., van der Borg, K., Vergnaud-Grazzini, C., and Zachariasse, W. J.: Late Quaternary central Mediterranean biochronology, Mar. Micropalaeontology, 21, 169–189, 1993.

Julian, B. R., Miller, A. D., and Foulger, G. R.: Non-double couple earthquakes, 1 Theory, Rev. Geophys., 36, 525–550, 1998.

Le Bas, T. P., Mason, D. C., and Millard, N. W.: TOBI Image Processing – The State of the Art, IEEE J. Oceanic Engineering, 20, 85–93, 1995.

Lee, H. J., Kayen, R. E., Gardner, J. V., and Locat, J.: Characteristic of several tsunamogenic submarine landslides, in: Submarine

Mass Movements and their Consequences, edited by: Locat, J. and Mienert, J., Kluver Acad. Publ., Dordrecht, The Netherlands, 357–366, 2003.

Lowe, J. J., Blockley, S., Trincardi, F., Asioli, A., Cattaneo, A., Matthews, I. P., Pollard, M., and Wulf, S.: Age modelling of late Quaternary marine sequences in the Adriatic: towards improved precision and accuracy using volcanic event stratigraphy, Continental Shelf Research, accepted, 2005.

Magagnoli, A. and Mengoli, M.: Carotiere a gravità SW-104, Rapporto Tecnico CNR, 27, pp. 45, 1995.

Malinverno, A., Ryan, W. B. F., Auffret, G. A., and Pautot, G.: Sonar images of the path of recent failure events on the continental margin off Nice, France, Special Paper – Geological Soc. Amer., 229, 59–75, 1988.

McAdoo, B. G., Pratson, L. F., and Orange, D. L.: Submarine landslide morphology, US continental slope, Mar. Geo., 169, 103–136, 2000.

Mulder, T. and Cochonat, P.: Classification of offshore mass movements, J. Sedimentary Res., 66, 1, 43–57, 1996.

Mulder, T., Savoye, B., Piper, D. J. W., and Syvitski, J. P. M.: The Var submarine sedimentary system; understanding Holocene sediment delivery processes and their importance to the geological record, Geological Soc. Special Publications, 129, 145–166, 1998.

Myers, P. G., Haines, K., and Rohling, E. J.: Modeling the paleocirculation of the Mediterranean: the last glacial maximum and the Holocene with emphasis on the formation of Sapropel S1, Paleoceanography, 13(6), 586–606, 1998.

Ori, G. G., Roveri M., and Vannoni, F.: Plio-Pleistocene sedimentation in the Apenninic-Adriatic foredeep (Central Adriatic sea, Italy), in: Foreland Basins, edited by: Allen, P. A. and Homewood, P., IAS Spec. Publ., 8, 183–198, 1986.

Orlic, M., Gicic, M., and La Violette, P. E.: The currents and circulation of the Adriatic Sea, Oceanologica Acta, 15, 109–122, 1992.

Ortolani, F. and Pagliuca, S.: Tettonica transpressiva nel Gargano e rapporti con le catene Appenninica e Dinarica, Mem. Soc. Geol. It., 38, 205–224, 1987.

Posamentier, H. W. and Vail, P. R.: Eustatic control on clastic deposition, II-sequence and systems trast models, in: Sea-Level Changes – An integrated Approach, edited by: Wilgus, C. K., Hastings, B. S., Kendall, C. G. S. C., et al., Soc. Economic Paleontologists and Mineralogists, Spec. Publ., 42, 125–154, 1988.

Postpischl, D.: Atlas of isoseismal maps of Italian earthquakes, Quaderni de "La ricerca scientifica", 114–2A, CNR, Roma, pp. 164, 1985.

Pratson, L. F. and Coakley, B. J.: A model for the headward erosion of submarine canyons induced by downslope-eroding sediment flows, GSA Bull., 108, 2, 225–234, 1996.

Reeder, M. S., Rothwell, R. G., and Stow, D. A. V.: Influence of sea level and basin physiography on emplacement of the late Pleistocene Herodotus Basin Megaturbidite, SE Mediterraenan Sea, Mar. Petr. Geo., 17, 199–218, 2000.

Ricci Lucchi, F.: The Oligocene to recent foreland basins of the Northern Apennines, in: Foreland Basins, Allen, P. A. and Homewood, P., IAS Spec. Publ., 8, 105–139, 1986.

Ridente, D. and Trincardi, F.: Eustatic and tectonic control on deposition and lateral variability of Quaternary regressive sequences in the Adriatic basin, Mar. Geology, 184, 273–293, 2002a.

Ridente, D. and Trincardi, F.: Late Pleistocene depositional cycles and syn-sedimentary tectonics on the central and south Adriatic shelf, Memorie della Società Geologica Italiana, 57, 516–526, 2002b.

Rohling, E. J., Jorissen, F. J., and De Stigter, H. C: 200 Year interruption of Holocene sapropel formation in the Adriatic Sea, J. Micropalaeontology, 16, 97–108, 1997.

Rothwell, R. G., Thomson, J., and Kähler, G.: Low-sea-level emplacement of a very large Late Pleistocene 'megaturbidite' in the western Mediterranean Sea, Nature, 392, 377–380, 1998.

Royden, L. E., Patacca, E., and Scandone, P.: Segmentation and configuration of subducted lithosphere in Italy: an important control on thrust-belt and foredeep-basin evolution, Geology, 15, 714–717, 1987.

Schwab W. C., Danforth, W. W., and Scanlon, K. M.: Tectonic and stratigraphic control on a giant submarine slope failure: Puerto Rico insular slope, in: Submarine landslides; selected studies in the U.S. Exclusive Economic Zone, edited by: Schwab, W. C., Lee, H. J., and Twichell, D. C., USGS Bull., 2002, 60–68, 1993.

Siani, G., Paterne, M., Michel, E., Sulpizio, R., Sbrana, A., Arnold, M., and Haddad, G.: Mediterranean Sea surface radiocarbon reservoir age changes since the last glacial maximum, Science, 294, 1917–1920, 2001.

Synolakis, C. E., Liu, P., Carrier, G., and Yeh, H.: Tsunamigenic seafloor deformation, Science, 278, 598–600, 1997.

Synolakis, C. E., Bardet, J. P., Borrero, J. C., Davies, H. L., Okal, E. A., Silver, E. A., Sweet, S., and Tappin, D. R.: The slump origin of the 1998 Papua New Guinea tsunami, Proceedings – Royal Society, Mathematical, Physical and Engineering Sciences, 458, 2020, 763–789, 8 April 2002.

Tappin, D. R., Matsumoto, T., Watts, P., et al.: Sediment slump likely caused Papua New Guinea tsunami, Eos (Transactions American Geophysical Union), 80, 329–340, 1999.

Tappin, D. R., Watts, P., McMurtry, G. M., Lafoy, Y., and Matsumoto, T.: The Sissano, Papua New Guinea Tsunami of July 1998 – offshore evidence on the source machanism, Mar. Geol., 175, 1–23, 2001.

Tinti, S. and Armigliato, A.: The use of scenarios to evaluate the tsunami impact southern Italy, Mar. Geology, 199, 221–243, 2003.

Tinti, S., Maramai, A., and Favalli, P.: The Gargano promontory: an important Italian seismogenetic-tsunamigenic area, Mar. Geology, 122, 227–241, 1995.

Tramontana, M., Morelli, D., and Colantoni, P.: Tettonica plioquaternaria del sistema sud-garganico (settore orientale) nel quadro evolutivo dell'Adriatico centro meridionale, Studi Geologici Camerti, 2, 467–473, 1995.

Trincardi, F. and Correggiari, A.: Muddy forced-regression deposits in the Adriatic basin and the composite nature of Quaternary sea level changes, in: Sedimentary Responses to Forced Regressions, edited by: Hunt, D. and Gawthorpe, R. L., Geological Society Spec. Publ., 172, 245–269, 2000.

Trincardi, F. and Field, M. E.: Collapse and flow of lowstand shelf-margin deposits: An example from the eastern Tyrrhenian Sea, Italy, Mar. Geo., 105, 77–94, 1992.

Trincardi, F., Cattaneo, A., Asioli A., Correggiari, A., and Langone, L.: Stratigraphy of the late-Quaternary deposits in the central Adriatic basin and the record of short-term climatic events, Memorie Istituto Italiano di Idrobiologia, 55, 39–70, 1996.

Trincardi, F., Cattaneo, A., Correggiari, A., Mongardi, S., Breda, A., and Asioli, A.: Submarine slides during sea level rise: two exemples from the eastern Tyrrhenian margin, in: Submarine Mass Movements and their Consequences, edited by: Locat, J. and Mienert, J., Kluver Acad. Publ., Dordrecht, The Netherlands, 469–478, 2003.

Trincardi, F., Cattaneo, A., Correggiari, A., and Ridente, D.: Evidence of soft sediment deformation , fluid escape, sediment failure and regional weak layers within the late Quaternary mud deposits of the Adriatic Sea, Mar. Geo., 213, 91–120, 2004.

Twichell, D. C. and Roberts, D. G.: Morphology, distribution, and development of submarine canyons on the United States Atlantic continental slope between Hudson and Baltimore Canyons, Geology, 10, 408–412, 1982.

Twichell, D. C., Valentine, P. C., and Pratson, L. M.: Slope failure of carbonate sediment on the west Florida slope, in: Submarine landslides; selected studies in the U.S. Exclusive Economic Zone, edited by: Schwab W. C., Lee H. J., and Twichell D. C., USGS Bull., 2002, 60–68, 1993.

Verdicchio, G., Trincardi, F., and Asioli, A.: Mediterranean current deposits: an exemple fromk the Southwestern Adriatic Margin, Geological Society of London, Spec. Publ., in press, 2005.

Wilson, C. K., Long, D., and Bulat, J.: The Afen Slide – a multi-staged slope failure in the Faeroe-Shetland Channel, in: Submarine Mass Movements and their Consequences, edited by: Locat, J. and Mienert, J., Kluver Acad. Publ., Dordrecht, The Netherlands, 357–366, 2003.

CHAPTER 2

This chapter consists of an article titled “Shelf-edge erosion, sediment failure and inception of Bari Canyon on the Southwestern Adriatic Margin (Central Mediterranean)” by Ridente D., Foglini F., Minisini D., Trincardi F., Verdicchio G., in press in “Marine Geology”.

ELSEVIER
Marine Geology xx (2007) xxx–xxx
MARINE GEOLOGY
INTERNATIONAL JOURNAL OF MARINE GEOLOGY, GEOCHEMISTRY AND GEOPHYSICS
www.elsevier.com/locate/margeo

Shelf-edge erosion, sediment failure and inception of Bari Canyon on the Southwestern Adriatic Margin (Central Mediterranean)

Domenico Ridente *, Federica Foglini, Daniel Minisini, Fabio Trincardi, Giuseppe Verdicchio

Istituto di Scienze Marine (ISMAR-Geologia Marina), CNR, via Gobetti 101, 40129, Bologna, Italy

Accepted 30 January 2007

Abstract

We investigate the impact of regional tectonic setting and sedimentary dynamics on the onset of Bari Canyon, the main sediment conduit on the Southwestern Adriatic Margin (SAM). Since the Middle Pleistocene, deposition on the SAM, a foreland basin relative to the Southern Apennines, was primarily controlled by glacio-eustatic cycles. However, a number of tectonic structures, active since the early Cenozoic, impacted on the stacking of progradational deposits and on the overall slope setting and stability along the SAM. Four depositional sequences accomplished the progradation of the shelf-margin between ca. 450 kyr BP and the Last Glacial Maximum lowstand (ca. 20 ka BP). These sequences are variably dissected by two large-scale erosional features on the upper slope: 1) Bari Canyon, and 2) Gondola Slide headscarp, further north. The shelf facing these two major erosional structures shows several, smaller-scale incisions that merge with the sequence boundaries between each of the four stacked depositional sequences. The distribution of these erosional features reflects the location of tectonic structures that are still active, suggesting that both the intense erosion and the sediment failure in these areas were enhanced by tectonic deformation. We define the age of these older episodes of shelf-edge erosion and mass wasting that were conducive to the inception of Bari Canyon as we know it today. Moreover, we envisage the following predisposing factors as responsible for the inception and subsequent evolution of Bari Canyon: a) long-term regional uplift and margin tilt, likely controlling the lateral variability in shelf width and shelf-slope profile; b) rapid margin progradational during the deposition of Middle–Late Pleistocene sequences; c) recent tectonic deformation resulting in gentle folds growing during the canyon evolution.

Keywords: Late Quaternary; submarine canyons; adriatic margin; sequence stratigraphy

1. Introduction

Submarine canyons are large-scale incisions (hundreds of metres deep, up to several kilometres wide and hundreds of kilometres long) affecting the morphology of shelf and slope environments on continental margins; they are preferential pathways to the deepest part of sedimentary basins for both river- and shelf-borne sediment (Durrieu de Madron, 1994; Lewis and Barnes, 1999; Mullenbach and Nittrouer, 2000; Schmidt et al., 2001; Canals et al., 2004; Baztan et al., 2005). Pioneering studies focused on the problem of explaining the origin of submarine canyons, and relied on their morphological classification in the attempt to address this problem (Shepard and Dill, 1966). However, submarine canyons

* Corresponding author.
E-mail address: domenico.ridente@bo.ismar.cnr.it (D. Ridente).

0025-3227/$ - see front matter © 2007 Elsevier B.V. All rights reserved.
doi:10.1016/j.margeo.2007.01.014

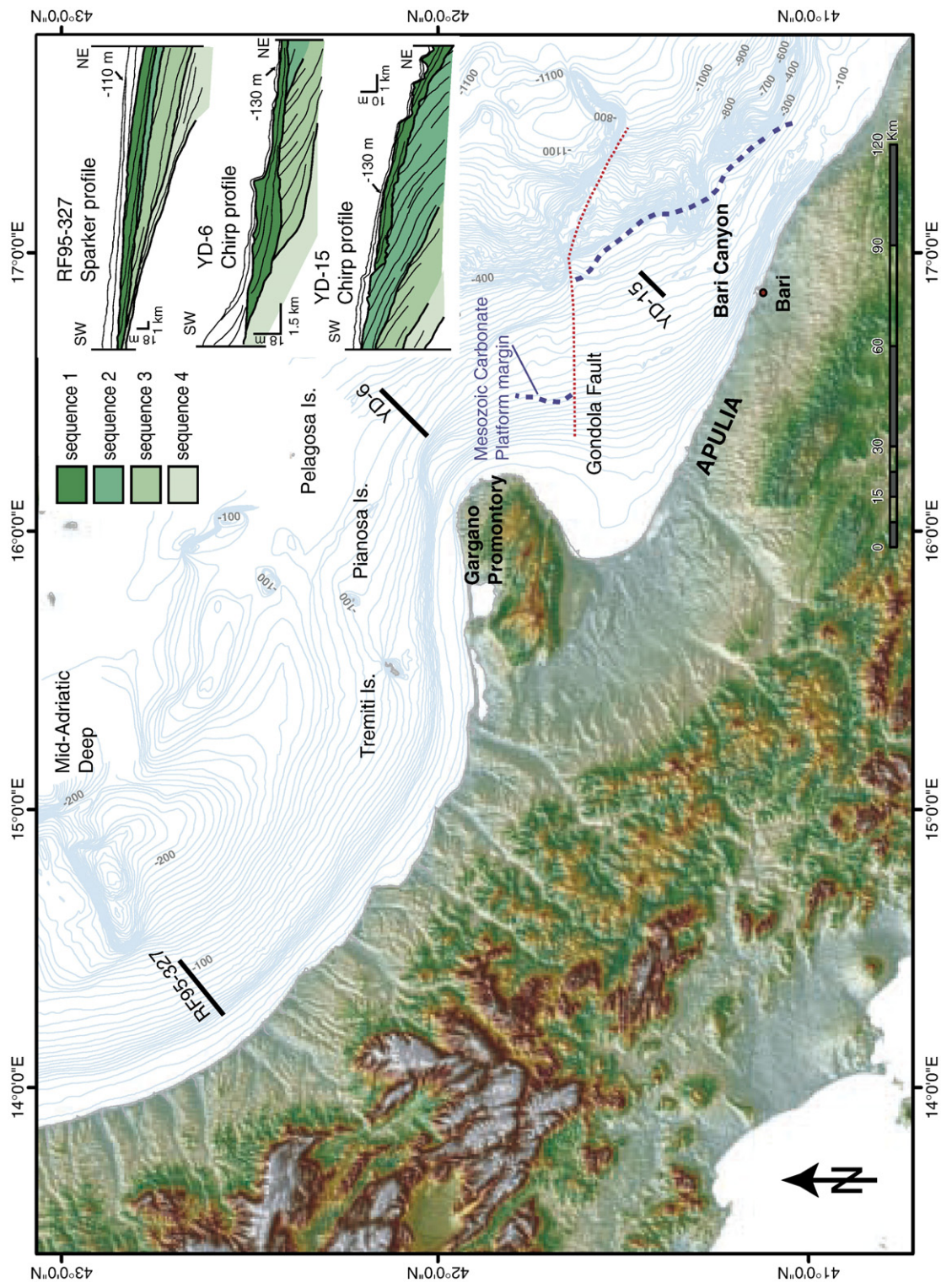

Fig. 1. Location of Bari Canyon in the Adriatic Sea and main tectonic structures on the SAM. The dashed line indicates the position of the Mesozoic Carbonate Platform margin (modified from De' Dominicis and Mazzoldi, 1987). Linedrawing of three seismic profiles evidence increased tectonic tilt affecting the stacking pattern of four Middle–Upper Pleistocene depositional sequences in the area close to Bari Canyon (see text for discussion).

Please cite this article as: Ridente, D. et al. Shelf-edge erosion, sediment failure and inception of Bari Canyon on the Southwestern Adriatic Margin (Central Mediterranean). Mar. Geol. (2007), doi:10.1016/j.margeo.2007.01.014

display internal complexity and variability (e. g., Soh and Tokuyama, 2002) that are unlikely to reflect a straightforward relationship between morphology and inception mechanism.

Moreover, submarine canyons may experience long-term evolution during which new and totally different conditions superimpose on the original geological setting (Shepard, 1981). With this limitation, a primary morpho-genetic distinction among canyon systems on modern continental margins is between "slope-confined" and "shelf-indenting" canyons (Twichell and Roberts, 1982; Farre et al., 1983), the former also referred to as "headless" canyons (Orange et al., 1997).

Shelf-indenting canyons may be closely related to a fluvial system, constituting a more or less detached element of a composite river–sea system (Cutshall et al., 1986; Liu and Lin, 2004). However, a most frequent case on modern continental margins is that in which a great distance separates the river delta and the canyon heads (Monaco et al, 1990; Mullenbach and Nittrouer, 2000; Liu and Lin, 2004). This evidence led early theories to emphasize the importance of sea level lowstands in the onset of submarine canyons, because in these intervals the continental shelves were exposed and sand supply to the shelf-margin increased (Spencer, 1903; Shepard, 1933; Bourcart, 1938). Early investigators also realised that this mechanism may have worked in conjunction with submarine erosion related to turbidity currents (Daly, 1936). In this view, the impact of glacio-eustasy has been considered important, although alternative mechanisms of sea level change, such as mid-oceanic ridge evolution and plate tectonics, have been proposed particularly to explain some long-lived, deeply incised canyons, extending back in time as far as the Mesozoic (Pitman, 1978).

More recently, side-scan sonar imaging and multibeam sounding have shown that slope-confined canyons are common on many continental slopes (e. g., Pratson et al., 1994). Based on 3D-seismic stratigraphy, shelf-confined canyon systems have been recognised also in the subsurface of continental margins (Bertoni and Cartwright, 2005), thus highlighting the significance of this type of canyon system in the stratigraphic record. The influence of fluvial down-cutting and associated turbidites may still be invoked as one possible mechanism contributing to canyon onset and maintenance, particularly in the case of shelf-indented canyons; however, alternative mechanisms are required in the case of slope-confined canyons, headed hundreds of metres below the shelf break and thus beyond the influence of lowstand, shelf-margin valley incision. For instance, special attention was given to retrogressive landslides of variable extent, fluid venting, and tide-driven bottom currents (Galloway et al., 1991; Orange and Breen, 1992; Pratson and Coackley, 1996; McAdoo et al., 1997; Shanmugam, 2003). Faulting and tectonic control is also an important genetic factor that may influence canyon inception in two ways: by determining the *locus* where erosion may focus, or, less directly, by affecting shelf width, slope gradients, and providing a triggering mechanism for mass failure (in seismically-active areas).

In this paper we investigate the impact of regional tectonic setting and Late Pleistocene sedimentary dynamics on the onset of Bari Canyon, on the Southwestern Adriatic Margin (Fig. 1); the activity of Bari Canyon in recent–modern time is described in two companion articles (Trincardi et al., this volume; Turchetto et al., this volume). The Southwestern Adriatic Margin (SAM) is a foreland domain affected by the regional flexural bending of the Adriatic plate and by several

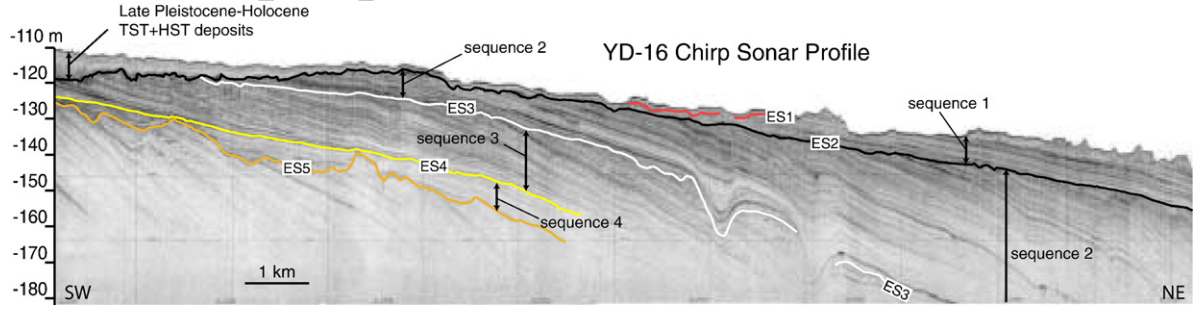

Fig. 2. Four depositional sequences bounded by erosional unconformities on the shelf (E S surfaces) record successive phases of margin progradation, during Quaternary glacio-eustatic cycles. Each sequence is dominantly composed of regressive units recording intervals of sea level fall (e.g. forced-regression deposits). The stacking pattern of the four sequences is offlapping with a seaward down-step and thickening toward the shelf edge. Marked erosion affects the top of sequence 3 (E S3) and of sequence 1 (ES1 at the sea floor). Late Pleistocene–Holocene deposits, recording the last deglacial sea level rise and modern highstand, form a thin mud drape, pinching out in ca. 130 m water depth (see Fig. 3 for location of seismic profile YD-16).

Please cite this article as: Ridente, D. et al. Shelf-edge erosion, sediment failure and inception of Bari Canyon on the Southwestern Adriatic Margin (Central Mediterranean). Mar. Geol. (2007), doi:10.1016/j.margeo.2007.01.014

E–W and NW–SE fault systems (Royden et al., 1987; Doglioni et al., 1994; Morelli, 2002). A succession of four depositional sequences on the SAM (numbered 1 to 4, top-down) records glacio-eustatic cycles during the Middle–Upper Pleistocene (Fig. 2, see also box in Fig. 1). These sequences are dissected by the Bari Canyon, a number of slide headscarps on the upper slope (Minisini et al., 2006), and incisions that are now buried on the outer shelf (Fig. 3). Bari Canyon is a shelf-indenting canyon that appears not related to any fluvial or shelf-margin deltaic system. In order to define how this canyon formed, we focus on the age and origin of the buried erosional features on the outer shelf, interpreted as precursors of the more intense excavation and activity of the modern Bari Canyon.

2. Tectono-sedimentary evolution of the SAM

The Adriatic Sea is part of a foreland domain rimmed by mountain belts of the Mediterranean Orogen (Channell et al., 1979; D'Argenio and Horvath, 1984). The tectono-sedimentary evolution of foreland basins is

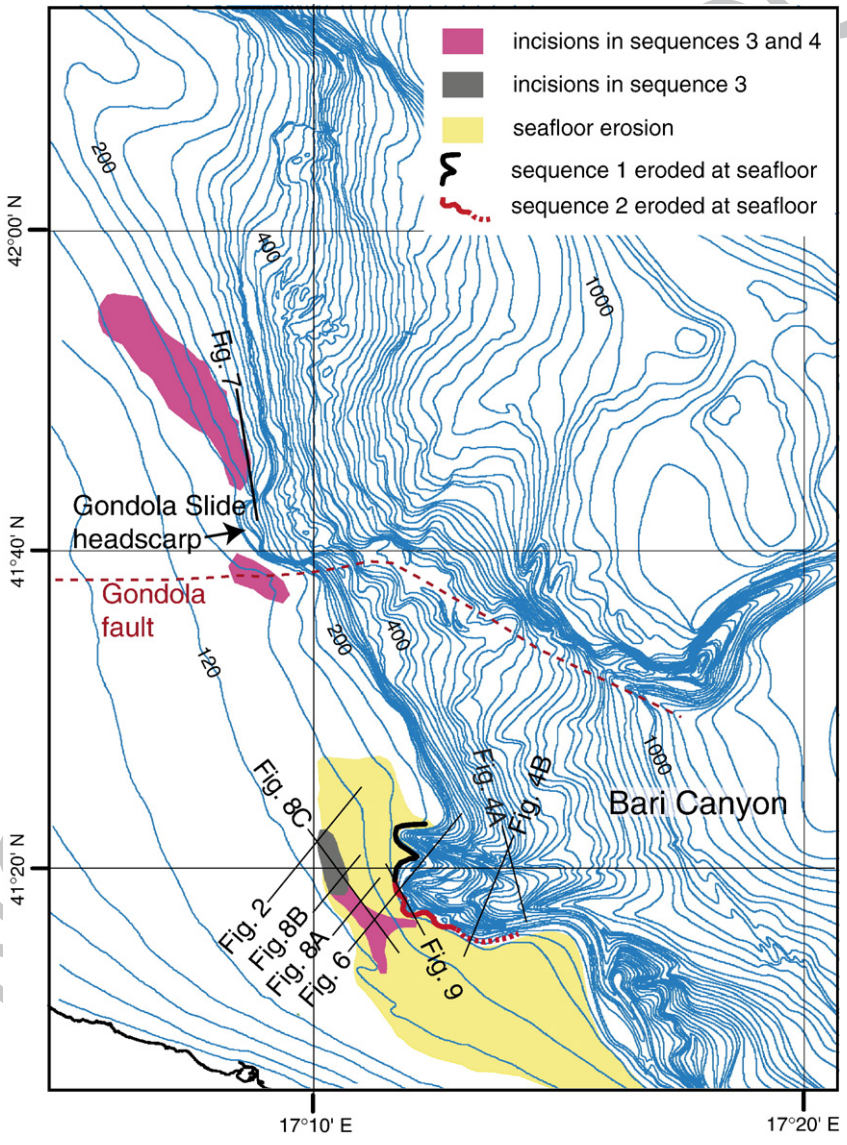

Fig. 3. Bathymetry of the SAM showing the main areas where regressive sequences are affected by phases of intense erosion. Sequences 1 and 2 are alternatively exposed at the seafloor on the shelf edge. In the northern area, marked but confined shelf-edge erosion records the large-scale mass failure of Gondola Slide and represents the most recent stage of margin erosion. To the south, repeated mass wasting and erosion evolved into the modern Bari Canyon.

Please cite this article as: Ridente, D. et al. Shelf-edge erosion, sediment failure and inception of Bari Canyon on the Southwestern Adriatic Margin (Central Mediterranean). Mar. Geol. (2007), doi:10.1016/j.margeo.2007.01.014

influenced by inherited tectonic and stratigraphic features of former passive margins; in turn, these inherited features influence the local and regional response to thrust deformation and loading during the accretion of mountain belts (Zoetemeijer et al., 1992; Waschbusch and Royden, 1992; Bertotti et al., 1999). The structural setting of the Adriatic foreland is the result of a long-term geological evolution encompassing the transition from a rift basin and passive margin, during the early Mesozoic, to a collisional foreland domain during the emplacement of the Alpine–Apennine and Dinarides–Hellenides belts (Eocene–Oligocene to Plio-Pleistocene; Morelli, 2002).

The main structural elements dissecting the modern Adriatic foreland (Fig. 1) experienced several episodes of re-activation during the Meso-Cenozoic collisional and post-collisional phases. In particular, early Mesozoic extensional faults, recording the rifting of the ancient Tethyan margin, are re-activated as compressive and transcurrent deformational features during the Late Cenozoic (Finetti, 1984; Colantoni et al., 1990; Argnani et al., 1993). Several of these fault systems originated since the early Jurassic as border faults separating the Mesozoic Carbonate Platform from adjacent deeper basins (Ortolani and Pagliuca, 1987; Colantoni et al., 1990; Morelli, 2002). These Carbonate Platform units are more than 4 km thick (Santantonio, 1994; Bosellini et al., 1999), and extensively crop out on the Gargano Promontory and Apulia (Ortolani and Pagliuca, 1987). In the South Adriatic, the extent of the Mesozoic Carbonate Platforms controls the lateral variability in shelf width and in dip gradients along the continental slope (De' Dominicis and Mazzoldi, 1987; Fig. 1). The structural setting also influenced the margin construction during the Plio-Quaternary, when several episodes of margin progradation occurred in response to tectonic uplift and sea level change. During the Middle–Upper Pleistocene, margin progradation was accomplished by a succession of four depositional sequences essentially composed of regressive units (Trincardi and Correggiari, 2000; Ridente and Trincardi, 2002a,b). The resulting stacking pattern of these sequences (hereinafter referred to as regressive sequences) is highly variable along the margin, reflecting changes in structural setting (see Fig. 1) and recording tectonic deformation along active tectonic structures (e.g., the Gondola Fault; Ridente and Trincardi, 2006).

3. Data and methods

The seismic data set for this study has been collected by ISMAR-CNR (Bologna) on board R/V Urania, during several cruises between 1997 and 2005. Seismic data have been acquired using a hull-mounted Chirp-Sonar Profiler with 16 transducers, characterised by 2–7 kHz sweep-modulated bandwidth (equivalent to a 3.5 kHz). The penetration obtained was in the order of 50–80 m, with vertical resolution of ca. 0.5 m. A low-frequency multi-channel seismic profile (data acquired by AGIP Oil Company in 1967 and subsequently released by the Italian Ministry of Industry) is also used to provide information on the upper 1000 m of stratigraphic section (Fig. 4). Track-line positioning was based on D-GPS navigation, assuring a position accuracy of ca. 10 m. A detailed bathymetric map of Bari Canyon (Fig. 5) was acquired using a RESON 8160 multibeam echo sounder with nominal sonar frequency of 30 kHz and angular coverage sector of 135 beams per ping at 1°.

Sediment cores collected using a piston corer with variable barrel lengths (5–20 m) and light-coring device (SW104), to assure undisturbed core tops, are discussed in Trincardi et al. (this volume). Unpublished data from a borehole that penetrated the four regressive sequences on the central Adriatic shelf-margin confirm that the four regressive sequences record each a 100 kyr glacio-eustatic cycle (PROMESS 1 European Project- PROfiles across MEditerranean Sedimentary Systems). Dating is based on tephra layers, isotope curves, pollen spectra, ^{14}C analyses, and foraminifera abundance (Trincardi et al., 1996; Asioli, 1996; Asioli et al., 1999, 2001).

4. General morphology of Bari Canyon

Bari Canyon, firstly described by Colantoni and Gallignani (1978), is a composite, ca. 10 km wide erosional feature that incises the continental slope and breaches the shelf edge (Fig. 5). Its two main canyon heads occur in about 200 m water depth, and the related branches reach 800 m water depth (Fig. 6). Bari Canyon is thus a "shelf-indenting" canyon and, given the lack of prograding deltaic deposits on the inner shelf, appears not connected to any shelf-margin delta. The main morphological features of Bari Canyon are: a) two main canyon branches (indicated as N- and S-branch) departing from each canyon head; b) a mounded relief that separates the N-branch and S-branch; c) a slope-confined trough just north of the N-branch (Moat A); d) a channel-levee departing from the middle slope (Canyon B′) and extending on the basal slope (Canyon B″; Fig. 5). A further morphologically relevant feature is the steep southern flank of the S-branch (up to 800 m in relief and up to 35° steep), likely representing a fault-controlled escarpment.

Please cite this article as: Ridente, D. et al. Shelf-edge erosion, sediment failure and inception of Bari Canyon on the Southwestern Adriatic Margin (Central Mediterranean). Mar. Geol. (2007), doi:10.1016/j.margeo.2007.01.014

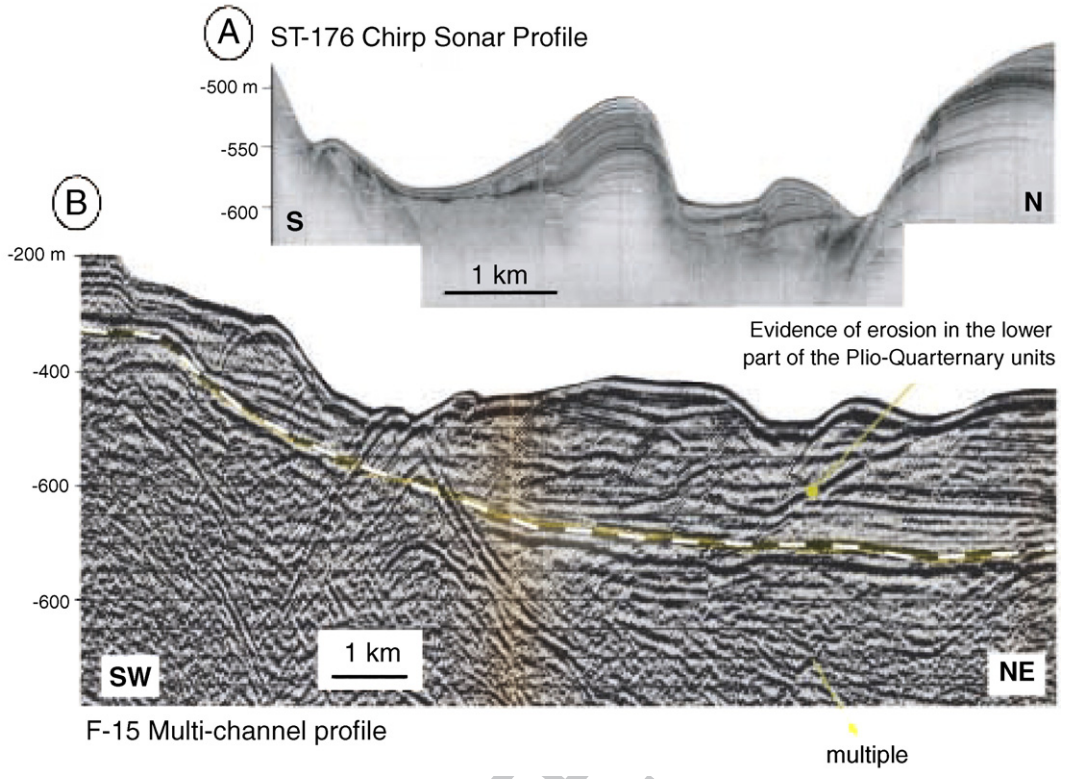

Fig. 4. Sub-parallel Chirp-Sonar (A) and multi-channel (B) seismic profiles along Bari Canyon (location is in Fig. 3). White dashed line in F-15 MC profile indicates the base of the Plio-Quaternary succession. Note that evidence of large-scale erosional features occurs solely above the base of Plio-Pleistocene deposits.

The northern canyon head (Canyon B) is a narrow and symmetric incision, whereas the southern canyon head (Canyon C) is broader, composite and asymmetric. The N-branch has a straight course and a very gentle dip at a depth greater than 400 m, running almost horizontally between 500 m and 600 m; the S-branch is broader, markedly asymmetric, with a steeper flank to the south and a more complex erosional–depositional side to the north. The divide between these two main canyon branches is a mounded relief that plunges seaward with slope gradients as gentle as 0.6° between 450 m and 650 m water depth (Fig. 5). Based on multibeam data, the sea floor morphology on this median relief is characterised by the presence of shallow troughs.

A well developed channel-levee complex (Canyon B″) is between ca. 600 m and 1000 m water depth (Fig. 5). This channel appears as the morphological continuation of the N-branch, and represents the most seaward evidence of a channelized feature within Bari Canyon. The course of this channel-levee complex is rather straight but presents a deviation to the left (north) in ca. 850 m water depth. The right-hand levee of this channel forms a gentle relief that can be traced up-slope, where it merges with a crest separating the N-branch from Moat A (Fig. 5). The left-hand flank of Moat A corresponds to the steepest flank of a large mound resulting from bottom current activity (Verdicchio et al., in press).

5. Margin stratigraphy, shelf-edge erosion and sediment failure

5.1. Sequence stratigraphy of Late Quaternary deposits

The Adriatic Late Quaternary stratigraphy is here summarised based on previous studies (Trincardi et al., 1996; Correggiari et al., 1996; Cattaneo and Trincardi, 1999; Trincardi and Correggiari, 2000; Correggiari et al., 2001; Ridente and Trincardi, 2002a,b; Cattaneo et al; 2003; Ridente and Trincardi, 2005; Piva et al., 2006). Seismic stratigraphy reveals a succession of depositional sequences, each up to few tens of metres thick, separated by shelf-wide erosional surfaces (labelled ES1 to ES5 down-section; see Fig. 2). Based on eco-biostratigraphic and chronologic data, each of these sequences reflects one glacio-eustatic cycle of ca. 100 kyr duration. The amplitude of sea level fluctuation during these cycles

Please cite this article as: Ridente, D. et al. Shelf-edge erosion, sediment failure and inception of Bari Canyon on the Southwestern Adriatic Margin (Central Mediterranean). Mar. Geol. (2007), doi:10.1016/j.margeo.2007.01.014

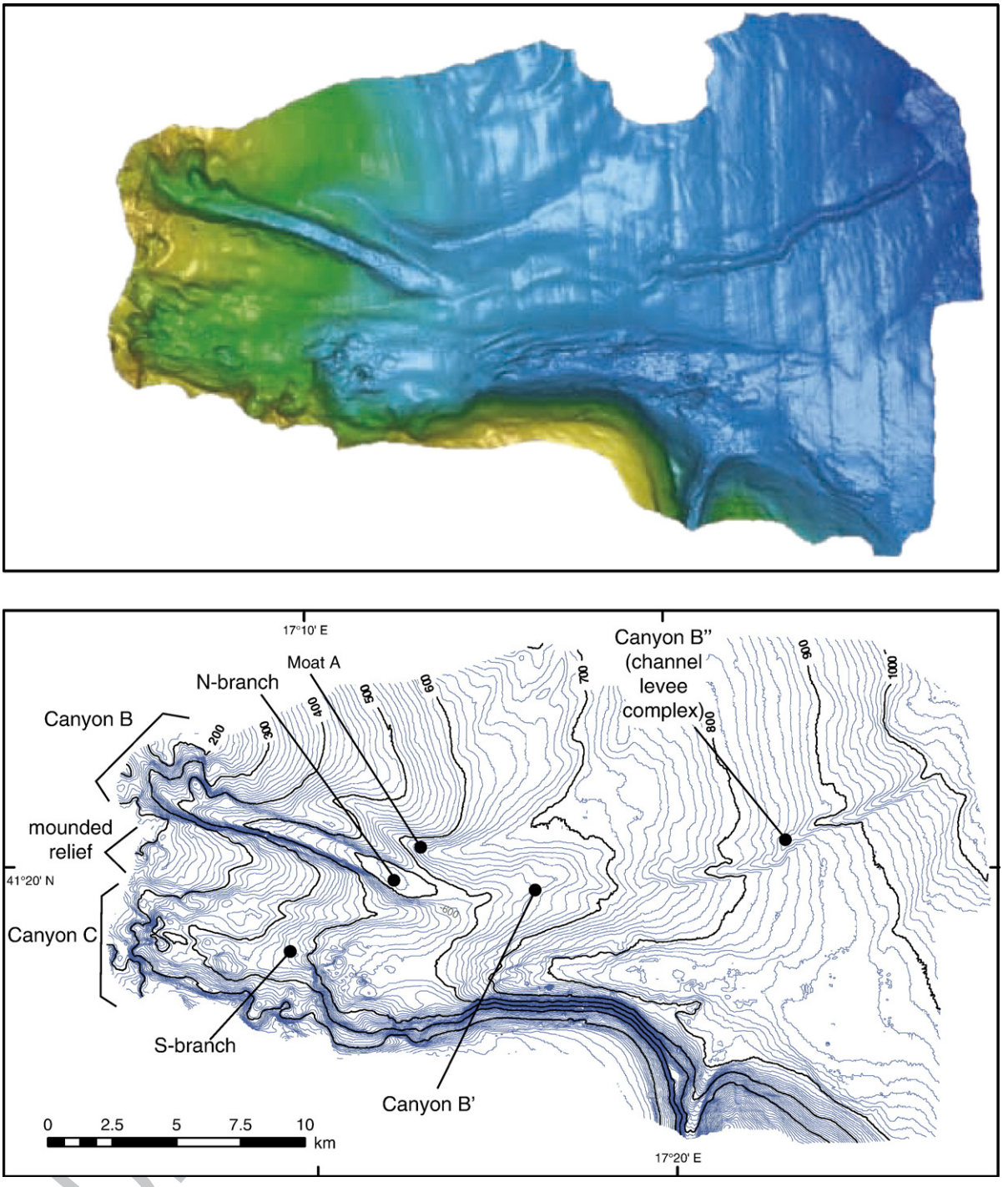

Fig. 5. DTM (above) and multibeam bathymetry (below) evidencing the main morphological elements of Bari Canyon. Contour line spacing is 10 m.

was in the order of 100–120 m (Hays et al., 1976). During the most recent of these cycles, three distinct stratigraphic units deposited: 1) lowstand deposits formed during the Last Glacial Maximum (LST); 2) transgressive units of the subsequent sea level rise (TST); 3) muddy progradational deposits formed after that sea level rise culminated in the modern highstand, ca 5.5 kyr BP (HST). Below the deposits of this cycle, the four regressive sequences represent older glacio-eustatic cycles that occurred between ca. 450 and 20 kyr BP, each

Please cite this article as: Ridente, D. et al. Shelf-edge erosion, sediment failure and inception of Bari Canyon on the Southwestern Adriatic Margin (Central Mediterranean). Mar. Geol. (2007), doi:10.1016/j.margeo.2007.01.014

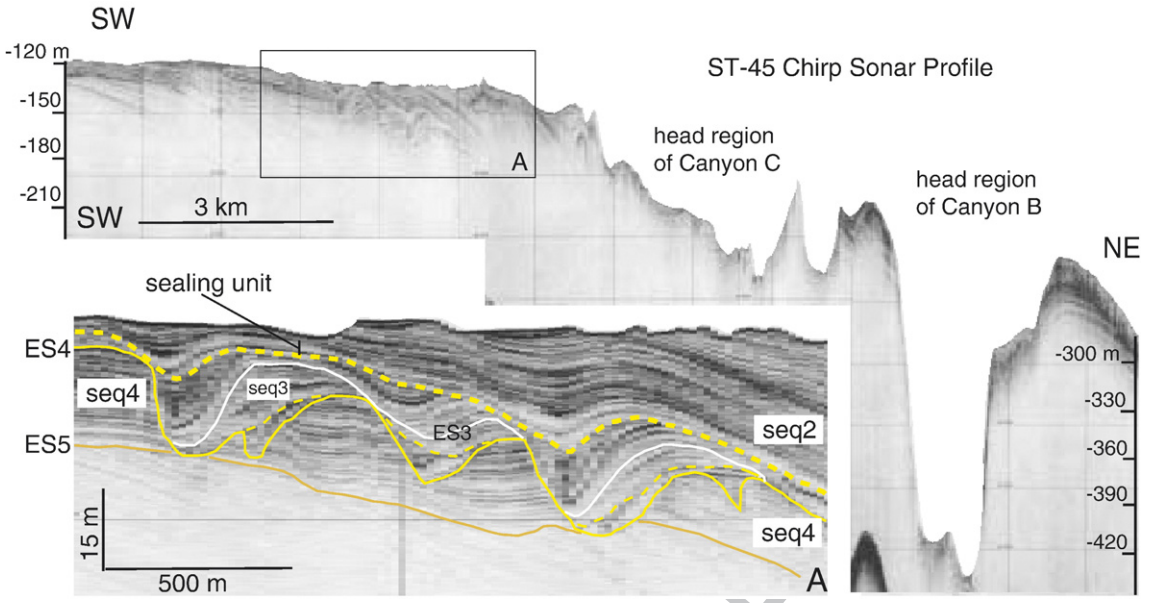

Fig. 6. Marked erosional features buried below sequence 2 on the outer shelf, near the area where Bari Canyon is located (location of seismic profile is in Fig. 3). V-shaped incisions cutting sequence 4 likely form during the sea level fall and lowstand producing erosional surface ES4. Subsequently, these incisions are filled by deposits of sequence 3 and re-incised during the successive sea level fall and lowstand (recorded by ES3). Erosion on top of sequence 3 is filled by deposits of sequence 2 and buried below a thick progradational wedge; the late stages of incision are evidenced by a transparent seismic unit at the base of this thick progradational wedge within sequence 2 (termed sealing unit; see text for explanation).

sequence extending laterally from the mid-Adriatic deep (Fig. 1) to the area offshore Bari.

Internally, the regressive sequences are composed by progressively seaward- and downward-shifted prograding wedges (Fig. 2), encompassing deposits formed between the highstand and the falling phases of each cycle (forced-regression deposits, sensu Plint, 1991). The regional erosion surfaces bounding each sequence (ES in the figures) formed during sub-aerial exposure caused by sea level falls and subsequent transgressive

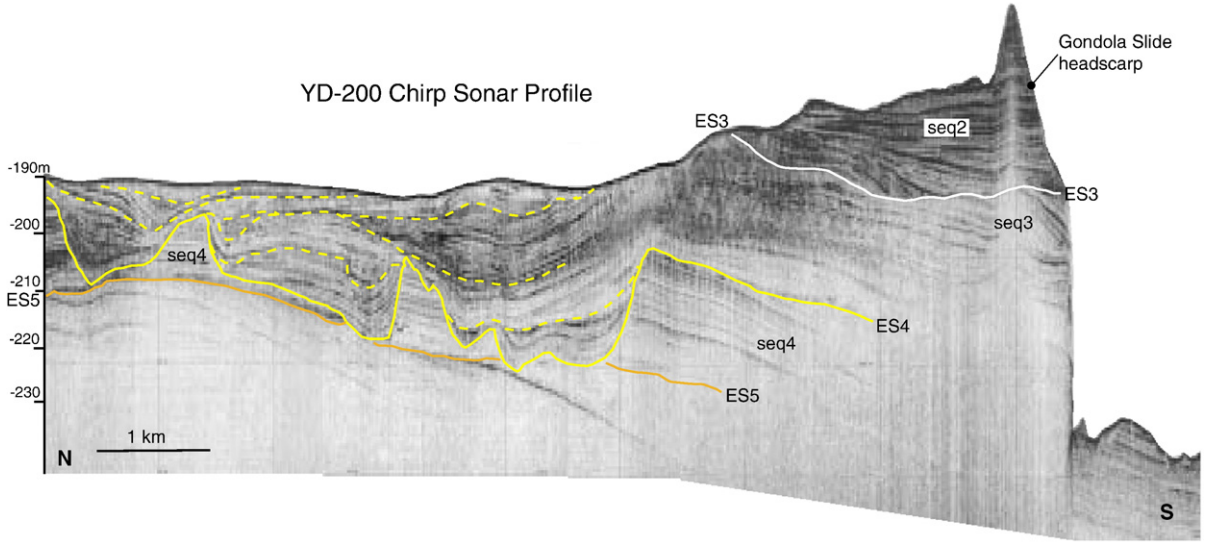

Fig. 7. Erosion of regressive sequences on the shelf edge in an area of the SAM affected by large-scale mass failure. Note the lack of deposits of sequence 1, that, in this area, pinch-out in water depth between 120 and 130 m (location of seismic profiles is in Fig. 3).

Please cite this article as: Ridente, D. et al. Shelf-edge erosion, sediment failure and inception of Bari Canyon on the Southwestern Adriatic Margin (Central Mediterranean). Mar. Geol. (2007), doi:10.1016/j.margeo.2007.01.014

reworking. Towards the upper slope, these sequence boundaries generally become conformable surfaces. On the SAM, however, they maintain an erosional character, likely indicating episodes of enhanced submarine erosion (Fig. 2).

Along-strike, the overall regional trend of depocenters of each sequence constitutes a laterally continuous progradational unit, suggesting a line-source progradation rather than the coalescence of local deltaic apparatuses (Ridente and Trincardi, 2005). North of Bari

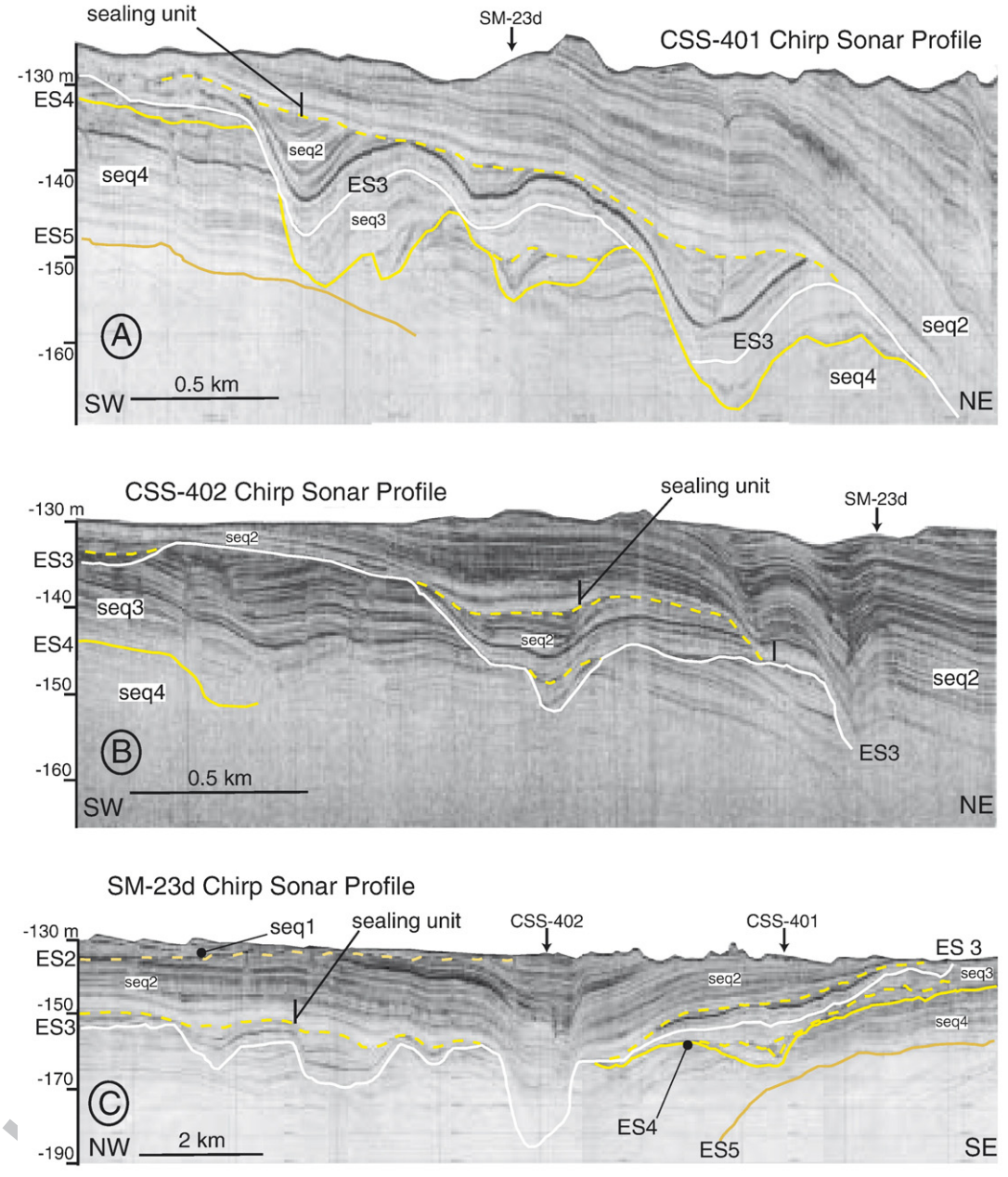

Fig. 8. Three seismic profiles intersecting the shelf edge facing Bari Canyon evidence distinct intervals of erosion from south to north. A) Seismic line CSS-401 shows a pattern of erosion and infilling similar to the one described in Fig. 6, characterised by the onset of marked erosion at the end of deposition of sequence 4, and burial during progradation of sequence 2 (note the same sealing unit at its base). B) To the north, seismic line CSS-402 shows that major erosion occurred mainly on top of sequence 3 and did not affect sequence 4 (see also Fig. 2). C) These two distinct patterns are shown in seismic line SM-23d.

Please cite this article as: Ridente, D. et al. Shelf-edge erosion, sediment failure and inception of Bari Canyon on the Southwestern Adriatic Margin (Central Mediterranean). Mar. Geol. (2007), doi:10.1016/j.margeo.2007.01.014

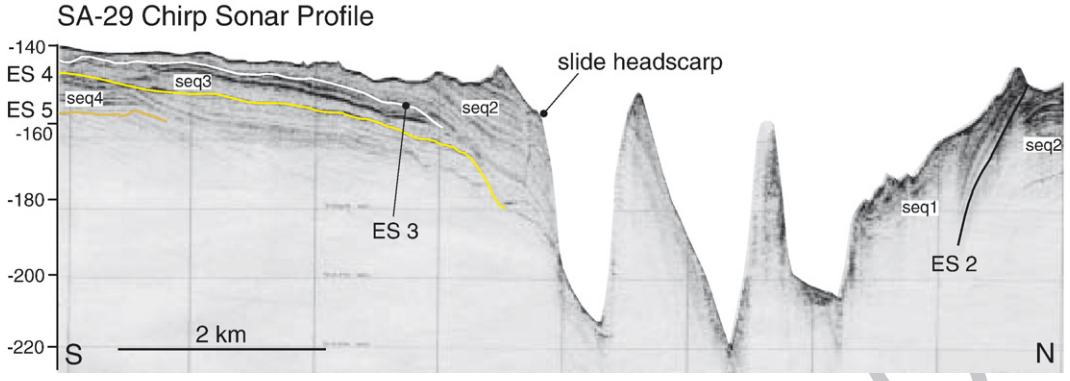

Fig. 9. Deposits of sequence 2 thickening on the shelf edge and likely prone to failure where Bari Canyon breaches the shelf (location of seismic profiles is in Fig. 3).

Canyon, where the shelf is wider (ca. 50 km to day; Fig. 1), sequences 2 and 3 thicken on the outer shelf and upper slope, whereas sequence 1 is reduced on the outer shelf and does not reach the upper slope (Fig. 7). To the south, where shelf width is reduced (Figs. 1 and 3), sequence 1 progrades beyond the shelf edge around Bari Canyon (Fig. 2).

5.2. Shelf-edge erosion and buried incisions around Bari Canyon

Deep-penetration multi-channel seismic profiles show that Bari Canyon cuts into deposits older than the four regressive sequences, remaining above the base of the Plio-Quaternary succession (Fig. 4B). Multiple

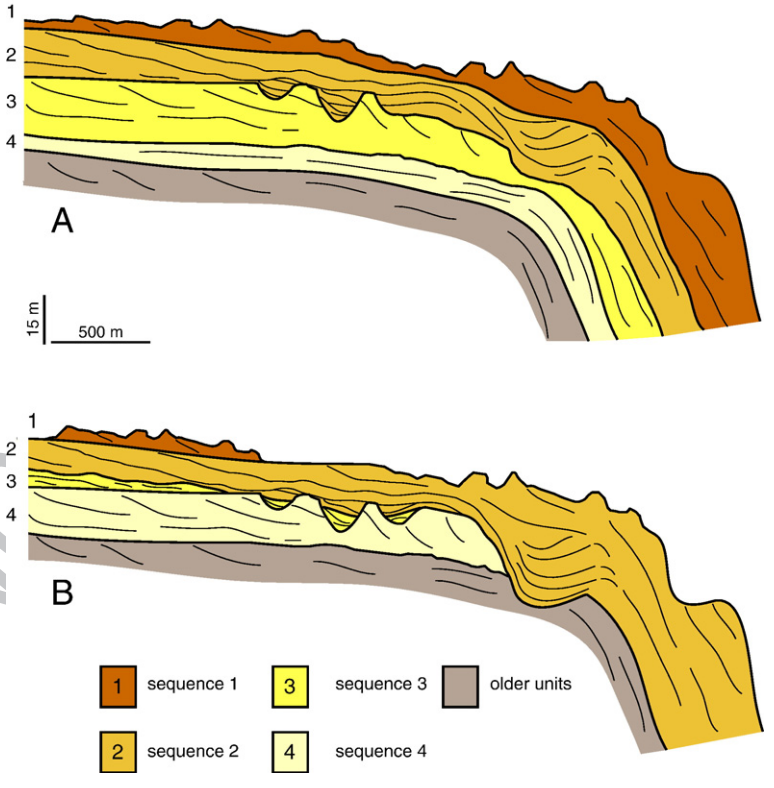

Fig. 10. Schematic reconstruction of margin progradation and progressive erosion at the shelf edge, summarising the pattern of incision, infill, and re-incision observed in seismic profiles. The pattern in (A) is recorded by deposits prograding on the northern flank of Bari Canyon (closer to Canyon B); the pattern in (B) is observed farther south, closer to Canyon C. Note that sequence 1 is preserved down-slope only in (A), and that sequence 4 is incised only in (B).

Please cite this article as: Ridente, D. et al. Shelf-edge erosion, sediment failure and inception of Bari Canyon on the Southwestern Adriatic Margin (Central Mediterranean). Mar. Geol. (2007), doi:10.1016/j.margeo.2007.01.014

generations of incised valleys on the outer shelf surrounding Bari Canyon are V-shaped and vertically stacked (Fig. 3).

Sequence 1 is exposed and incised near the northern flank of Bari Canyon (Fig. 2); instead, sequence 1 is not preserved on the outer shelf (Fig. 8) and upper slope (Fig. 9) near the southern flank of Bari Canyon, where sequence 2 crops out and is incised (Fig. 10). Incisions affect deposits as old as sequence 3 near Canyon B, whereas also sequence 4 is incised along Canyon C (Fig. 10, see also Fig. 8). Average widths of 200–300 m and up to 1.5 km are observed on seismic profiles illustrated in Figs. 6 and 8; flanks of the incisions dip more than 7° and resemble the angles along the heads of the recent canyon (see seismic profile ST-45 in Fig. 6). Infillings display laterally continuous reflectors that onlap or drape the eroded surfaces, and are sealed by a continuous, almost transparent unit (named sealing unit in Figs. 6 and 8). Seismic correlation indicates that this sealing unit is the distal part of a regressive wedge within sequence 2. The sharp basal contact of this sealing unit (dashed line in Figs. 6 and 8) indicates erosion of the sediment units filling older valley incisions. On seismic profiles CSS-401 and CSS-402 (Fig. 8A, B) the base of the sealing unit clearly truncates underlying deposits and merges seaward, towards NE, with erosion surface ES3, forming a deeper incision. This deeper incision is viewed in cross-section on seismic profile SM-23d (Fig. 8C), along the intersection with CSS-402, where the sealing unit becomes a basal deposit within this more seaward incision.

5.3. Predisposing factors to Bari Canyon inception

Evidence of tectonic deformation affecting the regressive sequences is widespread on the SAM, and consists of high-angle faults and gentle folds, with stacked syn-tectonic units that pinch-out against the flanks of the folds (Ridente and Trincardi, 2006); syn-tectonic units are accompanied by tectonically-driven unconformities. For instance, tectonic unconformities can be correlated with outer shelf incision along the eastern termination of the E–W branch of the Gondola Fault (Ridente and Trincardi, 2006); further seaward, the slope appears affected by the Gondola Slide headscarp (Fig. 3), ca. 10 km wide and 250 m in relief (Minisini et al., 2006).

In general, where active faulting and anticline growth affects regressive sequences, erosional features and broad slide scars can be recognised on the outer shelf and upper slope, respectively (Fig. 7). This combined evidence suggests that the recent tectonic growth along tectonic lineaments may have enhanced both outer shelf incision and sediment failure. Based on the absence of fluvial and deltaic deposits on the outer shelf, and given the vicinity of the incisions to active tectonic structures,

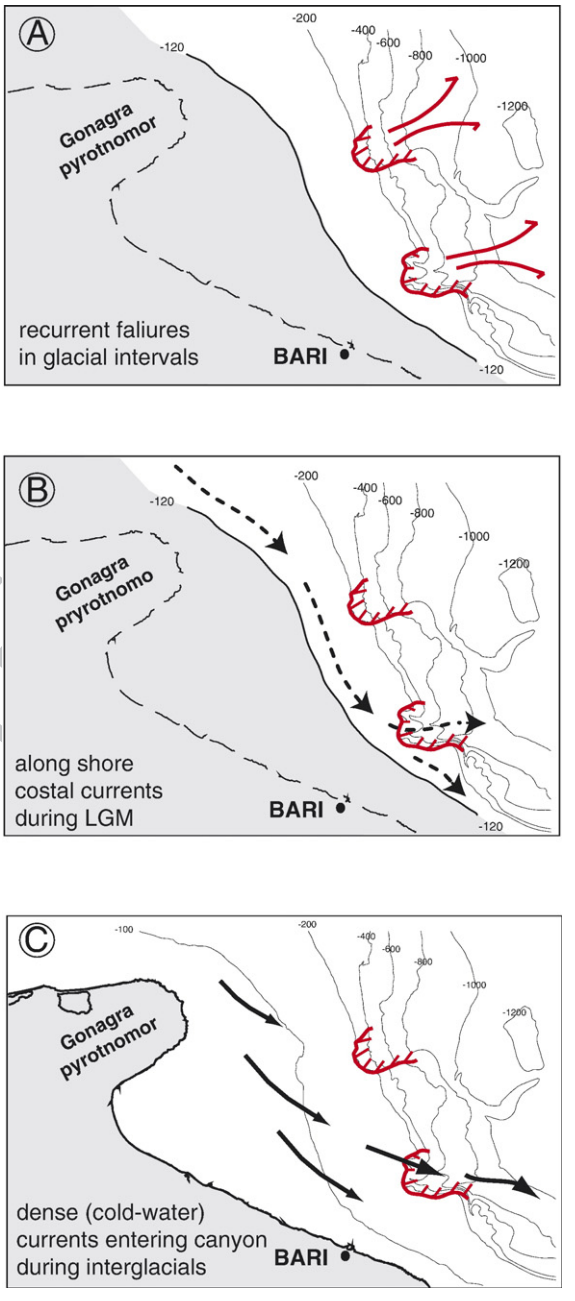

Fig. 11. Schematic model of formation and evolution of Bari Canyon: A) extensive failures affect the margin during lowstands; B) headscarps closer to coast line capture long-shore currents, becoming a preferential conduit for sediment transport to the basin; C) during highstands, activity of the canyon reflects the cold cascading currents flowing southward (Trincardi et al., this volume). Comparable volumes of failed masses to the North do not evolve into canyons as they result offshore with respect to contour-parallel coastal currents.

Please cite this article as: Ridente, D. et al. Shelf-edge erosion, sediment failure and inception of Bari Canyon on the Southwestern Adriatic Margin (Central Mediterranean). Mar. Geol. (2007), doi:10.1016/j.margeo.2007.01.014

we infer that mass wasting during episodes of tectonic growth, rather than fluvial activity, caused the incision on the shelf-margin around Bari Canyon.

The above evidence allows recognition of three main predisposing factors as possible mechanisms of Bari Canyon formation: 1) distribution of inherited tectonic relief, that controls shelf width and slope gradients; 2) shelf-margin progradational into progressively steeper regions; 3) concurrent active deformation along the main tectonic lineaments dissecting the margin. All these factors likely favoured the potential instability of the slope area, leading to the formation of slide headscarps that, subsequently, evolved as a persistent sediment conduit through sediment erosion (Fig. 9, compare with similar features in Fig. 7). The evolution of Bari Canyon was also favoured by the capture of currents entering this area from the north (Turchetto et al., this volume) and capable of eroding sediments on the outer shelf (Fig. 11).

6. Discussion

6.1. Origin of incised erosional surfaces on the SAM

The overall stratigraphic architecture of the Adriatic succession is similar to that on other Quaternary margins where regressive deposits are dominant (Ridente and Trincardi, 2005). These regressive successions develop on continental margins dominated by high supply and high-frequency eustatic cycles during which deposition and preservation prevail over erosion. Based on classical sequence-stratigraphic schemes, areas of intense erosion and sediment bypass generally coincide with the unconformity (i.e. the sequence boundary) that separates the highstand and lowstand systems tracts of successive depositional sequences (Dalrymple et al., 1992; Posamentier and Allen, 1993; Zaitlin et al., 1994). In depositional contexts where forced-regression deposits are preserved between the highstand and lowstand units of successive sequences, valley incisions most likely form on top forced-regression units. However, several Quaternary examples of forced-regression deposits lack of valley incisions on their top. This evidence has been interpreted as reflecting both the relatively slow rate of base level fall and a poor preservation potential during the following transgressive erosion (Trincardi and Field, 1991; Tesson et al., 2000).

In the Adriatic, incisions are uncommon through Middle–Upper Pleistocene forced-regression deposits and restricted to the SAM outer shelf. This area shows multiple evidences of incised erosional surfaces that cluster in two distinct sectors: around the headscarp of Gondola Slide and landward of Bari Canyon (Fig. 3). The infill of these outer shelf incisions consists of stratified deposits with variable dips, sealed by draping units in continuity with the progradational/regressive component of each sequence (Figs. 6 and 8). Acoustically transparent or chaotic reflector packages are uncommon, suggesting that the outer shelf incisions did not result from river down-cutting and did not act as incised valleys connected to a fluvial system. In the head region of Bari Canyon, repeated phases of outer shelf down-cut alternated with phases of substantial margin outbuilding (Fig. 10). Different to what is observed for the outer shelf near the Gondola Slide headscarp, in the north (Fig. 3), the Bari Canyon head became a more persistent route for the export of sediment from the shelf. We infer that this preferential sediment transport relates to the geographic location of the canyon where: a) the shelf edge and the modern shoreline tend to converge southward and the outer shelf becomes markedly erosional or non depositional during each sea level lowstand; b) the outer shelf was swept by coastal currents toward the south and sediment deposited into the canyon, resulting in alternating erosion and deposition (Turchetto et al., this volume); c) the dense currents flowing southward are particularly active during interglacials and also are captured by the canyon, oblique to the contour (Verdicchio and Trincardi, in press; Fig. 11). It is worth noting that the southward narrowing of the shelf reflects a reduced eastward extent and width of the Mesozoic Carbonate Platform margin (Fig. 1, dashed line).

6.2. Evidence for Middle Pleistocene inception of Bari Canyon

In the vicinity of the modern Bari Canyon, seafloor irregularities on the upper slope correspond to the erosional truncation on top of regressive sequences 1 and 2 (just north and south of Bari Canyon, respectively; Figs. 2 and 8); erosional features include broad scours and narrower channel-like incisions. Because both features are devoid of any sediment fill (see also Figs. 2, 6, 8, 9), we infer that they reflect sediment transport and erosion related to canyon activity; at places, sequence 1 has been completely removed and erosion cuts into deposits of sequence 2 (Figs. 8 and 9). A set of older incisions affecting sequences 3 and 4 consists of narrower "V"-shaped erosional features, typically filled by deposits of the successive cycle (Figs. 6 and 8).

Infilling deposits are draped by a continuous, almost transparent unit (e.g., sealing unit in Figs. 6 and 8) that can be traced landward into a regressive wedge within sequence 2. This wedge lays above older progradational wedges recording previous phases of sea level fall

Please cite this article as: Ridente, D. et al. Shelf-edge erosion, sediment failure and inception of Bari Canyon on the Southwestern Adriatic Margin (Central Mediterranean). Mar. Geol. (2007), doi:10.1016/j.margeo.2007.01.014

during deposition of sequence 2, and is truncated by ES2 at ca. 100–110 m below modern sea level. Hence, infilling deposits below the sealing unit formed during an interval between the onset of sea level rise and the early part of the subsequent sea level fall.

The occurrence of older buried incisions, landward of the modern shelf edge (see Figs. 6 and 8), parallels the paleo-shelf-margins during the progradational phases of sequences 4, 3 and 2; by analogy with the marked incisions on the modern shelf-margin and upper slope, we assume that these older and more landward incisions represent earlier episodes of canyon down-cut. Hence, the earliest evidence of canyon activity, likely constraining its inception, can be traced down to the Middle Pleistocene sequence 4. In addition, deeper-penetration multi-channel seismic data show that the erosional profile of Bari Canyon does not cut into the base of the Plio-Quaternary succession (Fig. 4B). We therefore infer that the canyon evolution, although influenced by inherited pre-Quaternary tectonic structures, was controlled by the construction of a progressively steeper margin through the progradation of sequences 4, 3 and 2, during which the predisposing conditions to slope failure and erosion were created and became progressively more relevant.

7. Conclusions

The presence of incised morphologies in the distal part of the Pleistocene regressive sequences records the early phases of Bari Canyon evolution, on the Southwestern Adriatic Margin (SAM). The SAM is a tectonic margin where along-strike changes in the stacking pattern of Pleistocene regressive sequences define areas of prevailing margin tilt and local deformation. In this context, repeated mass wasting and slope failure resulted in the carving of deeply incised scars at the shelf edge (Fig. 11A). Evidence of multiple generations of these shelf-edge scars come in two clusters: one is close to the northern limb of Gondola Fault, and the other is landward of modern Bari Canyon. Only the latter and southernmost area evolved into a canyon (the Bari Canyon), while the former became buried during repeated phases of shelf progradation. Two concurrent factors may explain this evidence: 1) failure in the Bari Canyon area was more recurrent throughout the last 300–400 kyr; 2) the location of Bari Canyon heads is closer to shore (Fig. 11B), and the system is therefore more capable of capturing density currents both at lowstands, when longshore drift dominates, and even during highstands (like the modern one), when dense waters forming in the north Adriatic flow southward, entering and flushing the canyon (Trincardi et al., this volume; Fig. 11C). Indeed, older erosional features around the Bari Canyon heads reflect the impact of currents entering this area from the north and interacting with the irregular topography of the margin created by failure events.

The erosional features observed on the shelf edge clearly cut through deposits of sequences 1 and 2, cropping out at the seafloor respectively north and south of Bari Canyon heads; older incisions in sequences 3 and 4 are filled by deposits of the overlying sequence. Down-cutting of sequence 4 is limited to the area around Canyon C, whereas down-cutting of sequence 3 is widespread on the outer shelf. This scenario suggests that the Bari Canyon area was susceptible to erosion and down-cutting since the end of deposition of sequence 4 (between ca. 450 and 350 kyr BP), and that erosion became more intense and affected a broader area during deposition of sequence 3 (between ca. 350 and 250 kyr BP). However, these older incisions do not connect to the main canyon system. It is possible that these early phases of erosion, now preserved only landward of the canyon head region, ceased during subsequent phases of margin building, with the progradational of a new shelf-margin during deposition of sequences 2 and 1. In these later stages, erosion and incision affected the outer shelf and upper slope in a more seaward position, likely re-establishing the connection with Bari Canyon and leading to the modern stage of canyon activity. In particular, marked erosion and incision atop of sequences 2 and 1 on the slope indicates strong activity of Bari Canyon during the last two phases of sea level fall and lowstand.

The fact that sequence 1 is preserved only on the outer shelf surrounding Canyon B, whereas sequence 2 appears incised at the seafloor along Canyon C, may indicate enhanced erosion and bypass during the last sea level fall and lowstand throughout Canyon C (where a dynamic interaction between currents flowing southward and the steep southern canyon flank is documented; Turchetto et al., this volume). On the SAM, mass failure is the most likely driving mechanisms of canyon inception, in conjunction with high sediment flux and bypass toward the slope.

Acknowledgements

This study was supported by the European Project EUROSTRATAFORM (EVK3-CT-2002–00079). We thank the crew and captain of CNR R/V Urania for their work during several campaigns in the study area. We are grateful to G.J. Weltje and an anonymous referee for greatly improving the manuscript with their review. We would like to thank also C. Bertoni for reading the

Please cite this article as: Ridente, D. et al. Shelf-edge erosion, sediment failure and inception of Bari Canyon on the Southwestern Adriatic Margin (Central Mediterranean). Mar. Geol. (2007), doi:10.1016/j.margeo.2007.01.014

manuscript and providing insightful comments. This is ISMAR-CNR (Bologna) contribution n. 1525.

References

Argnani, A., Favali, P., Frugoni, F., Gasperini, M., Ligi, M., Marani, M., Mattietti, G., Mele, G., 1993. Foreland deformational pattern in the Southern Adriatic Sea. Ann. Geofis. XXXVI (2), 229–247.

Asioli, A., 1996. High-resolution foraminifera biostratigraphy in the central Adriatic basin during the last deglaciation: a contribution to the Paliclas Project. In: Guilizzoni, P., Oldfield, F.L. (Eds.), Palaeoenvironmental Analysis of Italian Crater Lake and Adriatic Sediments (PALICLAS project). Mem. Ist. Ital. Idrobiol., vol. 55, pp. 197–217.

Asioli, A., Trincardi, F., Lowe, J.J., Oldfield, F., 1999. Short-term climate change during the Last Glacial-Holocene transition: comparison between Mediterranean records and grip event stratigraphy. J. Quat. Sci. 14, 373–381.

Asioli, A., Trincardi, F., Lowe, J.J., Ariztegui, D., Langone, L., Oldfield, F., 2001. Sub-millennial climatic oscillations in the Central Adriatic during the last deglaciation: paleoceanographic implications. Quat. Sci. Rev. 20, 33–53.

Baztan, J., Berne, S., Olivet, J., Rabineau, M., Aslanian, D., Gaudin, M., Rehault, J.P., Canals, M., 2005. Axial incision; the key to understand submarine canyon evolution (in the western Gulf of Lion). Mar. Pet. Geol. 22, 805–826.

Bertoni, C., Cartwright, J., 2005. 3 D seismic analysis of slope-confined canyons from the Plio-Pleistocene of the Ebro Continental Margin (Western Mediterranean). Basin Res. 17, 43–62.

Bertotti, G., Casolari, E., Picotti, V., 1999. The Gargano Promontory, a contractional belt in the Adriatic plate. Terranova 11, 168–173.

Bosellini, A., Morsilli, M., Neri, C., 1999. Long-term event stratigraphy of the Apulia Platform Margin (Upper Jurassic to Eocene, Gargano, Southern Italy). J. Sediment. Res. 69 (6), 1241–1252.

Bourcart, J., 1938. Essai sur le regressions et trasgressions marines. Soc. Geol. Fr. Bull. 5, 489–512.

Canals, M., Casamor, J.L., Lastras, G., Monaco, A., Acosta, J., Berné, S., Loubrieu, B., Weaver, P.P.E., Grehan, A., Dennielou, B., 2004. The role of Canyons on strata formation. Oceanography 17 (4), 80–91.

Cattaneo, A., Trincardi, F., 1999. The late-Quaternary transgressive record in the Adriatic Epicontinental Sea: basin widening and facies partitioning. In: Bergman, K., Snedden, J. (Eds.), Isolated Shallow Marine Sand Bodies: Sequence Stratigraphic Analysis and Sedimentologic Interpretation. SEPM, Spec. Publ., vol. 64, pp. 127–146.

Cattaneo, A., Correggiari, A., Langone, L., Trincardi, F., 2003. The late-Holocene Gargano subaqueous delta, Adriatic shelf: sediment pathways and supply fluctuations. Mar. Geol. 193, 61–91.

Channell, J.E.T., D'Argenio, B., Horvath, F., 1979. Adria, the African Promontory, in Mesozoic mediterranean paleogeography. Earth Sci. Rev. 15, 213–292.

Colantoni, P., Gallignani, P., 1978. Quaternary evolution of the continental shelf off the co ast of Bari (South Adriatic Sea): shallow seismic, sedimentological and faunal evidences. Geol. Mediterr. V (3), 327–338.

Colantoni, P., Tramontana, M., Tedeschi, R., 1990. Contributo alla conoscenza dell'avampaese apulo: struttura del Golfo di Manfredonia (Adriatico meridionale). G. Geol. 52 (1–2), 19–32.

Correggiari, A., Roveri, M., Trincardi, F., 1996. Late Pleistocene and Holocene evolution on the North Adriatic Sea. Il Quaternario-Ital. J. Quat. Sci. 9, 697–704.

Correggiari, A., Trincardi, F., Langone, L., Roveri, M., 2001. Styles of failure in late Holocene highstand prodelta wedges on the Adriatic shelf. J. Sediment. Res. 71 (2), 218–236.

Cutshall, N.H., Larsen, I.L., Olsen, C.R., Nittrouer, C.A., DeMaster, D.J., 1986. Columbia River sediment in Quinault Canyon, Washington — evidence from artificial radionuclides. Mar. Geol. 71, 125–136.

Daly, R.A., 1936. Origin of submarine canyons. Am. J. Sci. 31, 401–420.

D'Argenio, B., Horvath, F., 1984. Some remarks on the deformation history of Adria, from the Mesozoic to the Tertiary. Ann. Geophys. 2, 143–146.

De' Dominicis, A., Mazzoldi, G., 1987. Interpretazione geologico-strutturale del margine orientale della Piattaforma apula. Mem. Soc. Geol. Ital. 38, 163–176.

Doglioni, C., Mongelli, F., Pieri, P., 1994. The Puglia uplift (SE Italy): an anomaly in the foreland of the Apennine subduction due to buckling of a thick continental lithosphere. Tectonics 13, 1309–1321.

Dalrymple, R.W., Boyd, R., Zaitlin, B.A., 1992. History of research, types and internal organisation of incised valley systems: introduction to the volume. In: Dalrymple, R.W., Boyd, R., Zaitlin, B.A. (Eds.), Incised-valley Systems: Origin and Sedimentary Sequences. SEPM., Spec. Pub., 51, pp. 3–10.

Durrieu de Madron, X., 1994. Hydrography and nepheloid structures in the Grand-Rhone canyon. Cont. Shelf Res. 14 (5), 457–477.

Farre, J.A., MecGregor, B.A., Ryan, W.B.F., Robb, J.M., 1983. Breaching the shelfbreak: passage from youthful to mature phase in submarine canyon evolution. In: Stanley, D.J., Moore, T.G. (Eds.), The Shelfbreak: Critical Interface on Continental Margins. SEPM, Spec. Publ., 33, pp. 25–39.

Finetti, I., 1984. Struttura ed evoluzione della microplacca Adriatica (structure and evolution of the Adriatic microplate). Boll. Oceanol. Teor. Appl. 2 (2), 115–123.

Galloway, W.E., Dingus, W.F., Paige, R.E., 1991. Seismic and depositional facies of Paleocene–Eocene Wilcox Group submarine canyon fills, Northwest Gulf Coast, U.S.A. In: Weimer, P., Link, M.H. (Eds.), Seismic Facies and Sedimentary Processes of Submarine Fans and Turbidite Systems. Springer-Verlag, pp. 247–271.

Hays, J.D., Imbrie, J., Shackleton, N.J., 1976. Variations in the earth's orbit: pacemaker of the ice ages. Science 194, 1121–1134.

Lewis, K.B., Barnes, P.M., 1999. Kaikoura Canyon, New Zealand: active conduit from nearshore sediment zones to trench-axis channel. Mar. Geol. 162, 39–69.

Liu, J.T., Lin, H., 2004. Sediment dynamics in a submarine canyon: a case of river–sea interaction. Mar. Geol. 207, 55–81.

McAdoo, B.G., Orange, D.L., Screaton, E., Lee, H., Kayen, R., 1997. Slope basins, headless canyons, and submarine palaeoseismology of the Cascadia accretionary complex. Basin Res. 9, 313–324.

Minisini, D., Trincardi, F., Asioli, A., 2006. Evidences of slope instability in the South Adriatic Margin. Nat. Hazard Earth Syst. Sci. 6 (1), 1–20.

Monaco, A., Courp, T., Heussner, S., Carbonne, J., Fowler, S.W., Deniauz, B., 1990. Seasonality and composition of of particulate fluxes during ECOMARGE-1, western Gulf of Lions. Cont. Shelf Res. 10, 959–987.

Morelli, D., 2002. Evoluzione t ettonico-stratigrafica del Margine Adriatico compreso trail Promontorio del Gargano e Brindisi. Mem. Soc. Geol. Ital., Vol. Spec. 57, 343–353.

Mullenbach, B.L., Nittrouer, C.A., 2000. Rapid deposition of fluvial sediment in the Eel Canyon, northern California. Cont. Shelf Res. 20, 2191–2212.

Please cite this article as: Ridente, D. et al. Shelf-edge erosion, sediment failure and inception of Bari Canyon on the Southwestern Adriatic Margin (Central Mediterranean). Mar. Geol. (2007), doi:10.1016/j.margeo.2007.01.014

Orange, D.L., Breen, N.A., 1992. The effects of fluid escape on accretionary wedges 2: seepage force, slope failure, headless submarine canyons, and vents. J. Geophys. Res. 97, 9277–9295.

Orange, D.L., McAdoo, B.G., Moore, J.C., Tobin, H., Screaton, E., Chezar, H., Lee, H., Reid, M., Vail, R., 1997. Headless submarine canyons and fluid flow on the toe of the Cascadia accretionary complex. Basin Res. 9, 303–312.

Ortolani, F., Pagliuca, S., 1987. Tettonica transpressiva nel Gargano e rapporti con le Catene Appenninica e Dinarica. Mem. Soc. Geol. Ital. 38, 205–224.

Pitman Jr., W.C., 1978. Relation between eustasy and stratigraphic sequences of passive margins. Geol. Soc. Amer. Bull. 89, 1389–1403.

Piva, A., Asioli, A., Schneider, R., Andersen, N., Cattaneo, A., Ridente, D., Verosub, K., Vigliotti, L., Trincardi, F., 2006. EC-PROMESS 1 Project: stratigraphic synthesis of the hol e PRAD1–2 (Middle Pleistocene–Holocene of the Central Adriatic). EGU General Assembly, Vienna, Abstract, vol. 8.

Plint, A.G., 1991. High-frequency relative sea-level oscillations in the Upper Cretaceous shelf clastics of the Alberta foreland basin: possible evidence for glacio-eustatic control? In: Macdonald, D.I.M. (Ed.), Sedimentation, Tectonics and Eustasy. International Association of Sedimentologists, Spec. Publ., vol. 12, pp. 409–428.

Posamentier, H.W., Allen, G.P., 1993. Variability of the sequence stratigraphic model: effects of local basin factors. Sediment. Geol. 86, 91–109.

Pratson, L.F., Coackley, B.J., 1996. A model for the headward erosion of submarine canyons induced by downslope-eroding sediment flows. Geol. Soc. Amer. Bull. 108 (2), 225–234.

Pratson, L.F., Ryan, W.B.F., Mountain, G.S., Twichell, D.C., 1994. Submarine canyon initiation by downslope-eroding sediment flows: evidence in late Cenozoic strata on the New Jersey continental slope. Geol. Soc. Amer. Bull. 106, 395–412.

Ridente, D., Trincardi, F., 2002a. Eustatic and tectonic control on deposition and lateral variability of Quaternary regressive sequences in the Adriatic basin. Mar. Geol. 184, 273–293.

Ridente, D., Trincardi, F., 2002b. Late Pleistocene depositional cycles and syn-sedimentary tectonics on the Adriatic shelf. Mem. Soc. Geol. Ital., Vol. Spec. 57, 517–526.

Ridente, D., Trincardi, F., 2005. Pleistocene "muddy" forced-regression deposits on the Adriatic shelf: a comparison with prodelta deposits of the late Holocene highstand mud wedge. Mar. Geol. 222–223, 213–233.

Ridente, D., Trincardi, F., 2006. Active foreland deformation evidenced by shallow folds and faults affecting late Quaternary shelf-slope deposits (Adriatic Sea, Italy). Basin Res. 18 (2), 171–188.

Royden, L.E., Patacca, E., Scandone, P., 1987. Segmentation and configuration of subducted lithosphere in Italy: an important control on thrust-belt and foredeep-basin evolution. Geology 15, 714–717.

Santantonio, M., 1994. Pelagic carbonate platforms in the geologic record: their classification and sedimentary and paleotectonic evolution. AAPG Bull. 78, 122–141.

Schmidt, S., de Strigter, H.C., van Weering, T.C.E., 2001. Enhanced short-term sediment deposition within the Nazare Canyon, North-East Atlantic. Mar. Geol. 173, 55–67.

Shanmugam, G., 2003. Deep-marine tidal bottom currents and their reworked sands in modern and ancient submarine canyons. Mar. Pet. Geol. 20, 471–491.

Shepard, F.P., 1933. Canyons beneath the Seas. Sci. Mon. 37, 31–39.

Shepard, F.P., 1981. Submarine canyons: multiple causes and long-time persistence. AAPG Bull. 65 (6), 1062–1077.

Shepard, F.P., Dill, R.F., 1966. Submarine Canyons and Other Sea Valleys. Rand McNally and Co., Chicago. 381 pp.

Soh, W., Tokuyama, H., 2002. Rejuvination of submarine canyon associated with ridge subduction, Tenryu Canyon, off Tokai, central Japan. Mar. Geol. 187, 203–220.

Spencer, J.W., 1903. Submarine valleys off the American coasts and in the North Atlantic. Geol. Soc. Amer. Bull. 14, 207–226.

Tesson, M., Posamentier, H.W., Gensous, B., 2000. Stratigraphic organization of late Pleistocene deposits of the western part of the Golfe du Lion shelf (Languedoc shelf), western Mediterranean Sea, using high-resolution seismic and core data. AAPG Bull. 84 (1), 119–150.

Trincardi, F., Correggiari, A., 2000. Quaternary forced-regression deposits in the Adriatic basin and the record of co mposite sea-level cycles. In: Hunt, D., Gawthorpe, R. (Eds.), Depositional Response to Forced Regression. Geol. Soc., Spec. Publ., vol. 172, pp. 245–269.

Trincardi, F., Field, M.E., 1991. Geometry, lateral variability, and preservation of downlapping regressive shelf deposits: Eastern Tyrrhenian margin, Italy. J. Sediment. Petrol. 61, 75–90.

Trincardi, F., Asioli, A., Cattaneo, A., Correggiari, A., Langone, L., 1996. Stratigraphy of the late-Quaternary deposits in the Central Adriatic basin and the record of short-term climatic events. In: Guilizzoni, P., Oldfield, F.L. (Eds.), Palaeo environmental analysis of Italian crater lake and Adriatic sediments (PALICLAS project). Mem. Istit. It. Idrob., vol. 55, pp. 39–64.

Trincardi, F, Foglini, F., Verdicchio, G., Asioli, A., Correggiari, A., Minisini, D., Piva, A., Remia, A., Ridente, D., Taviani, M. The impact of cascading currents on the Bari Canyon System, SW-Adriatic Margin (Central Mediterranean). This volume.

Turchetto, M., Boldrin, A., Langone, L, Miserocchi, S., Tesi, T., Foglini, F. Particle transport in the Bari canyon (southern Adriatic Sea). This volume.

Twichell, D.C., Roberts, D.G., 1982. Morphology, distribution, and development of submarine canyons on the United States Atlantic continental slope between Husdon and Baltimore Canyons. Geology 10, 408–412.

Verdicchio, G., Trincardi, F., in press. Short-distance variability in abyssal bed-forms along the Southwestern Adriatic Margin (Central Mediterranean). Marine Geology.

Verdicchio, G., Trincardi, F., Asioli, A., in press. Mediterranean bottom-current deposits: an example from the Southwestern Adriatic Margin. In: Viana, A.R., Rebesco, M. (Eds.) Econo mic and palaeoceanographic importance of Contourite. Geol. Soc. Spec. Pub.

Waschbusch, P.J., Royden, L.H., 1992. Spatial and temporal evolution of foredeep basins: lateral strength variations and inelastic yielding in continental lithosphere. Basin Res. 4, 179–196.

Zaitlin, B.A., Dalrymple, R.W., Boyd, R., 1994. The stratigraphic organization of incesed-valley systems associated with realtive sea-level change. In: Dalrymple, R.W., Boyd, R., Zaitlin, B.A. (Eds.), Incised-valley Systems: Origin and Sedimentary Sequences. SEPM., Spec. Pub., vol. 51, pp. 45–60.

Zoetemeijer, R., Sassi, W., Roure, F., Cloetingh, S., 1992. Stratigraphic and kinematic modeling of thrust evolution, Northern Apennines, Italy. Geology 20, 1035–1038.

Please cite this article as: Ridente, D. et al. Shelf-edge erosion, sediment failure and inception of Bari Canyon on the Southwestern Adriatic Margin (Central Mediterranean). Mar. Geol. (2007), doi:10.1016/j.margeo.2007.01.014

CHAPTER 3

This chapter consists of an article titled “The impact of cascading currents on the Bari Canyon System, SW-Adriatic Margin (Central Mediterranean).” by Trincardi F., Foglini F., Verdicchio G., Asioli A., Correggiari A., Minisini D., Piva A., Remia A., Ridente D., Taviani M., in press in “Marine Geology”.

The impact of cascading currents on the Bari Canyon System, SW-Adriatic Margin (Central Mediterranean).

Trincardi, F.[1], Foglini, F.[1], Verdicchio, G.[1-2], Asioli, A.[3], Correggiari A.[1], Minisini, D.[1-2], Piva, A.[1-2], Remia, A., Ridente, D.[1], Taviani, M.[1]

1 - ISMAR-CNR, Via Gobetti, 101, 40129 Bologna, Italy

2 - Dipartimento Scienze della Terra e Geologico-Ambientali, Università di Bologna, Via Zamboni 67, 40126 Bologna, Italy

3 - IGG-CNR, Corso Garibaldi 37, 35137 Padova, Italy

ABSTRACT

The Bari Canyon System (BCS) is a peculiar erosional-depositional feature characterised by two main, almost parallel, conduits emanating from a broad crescent-shaped upper slope region. When viewed in cross sections parallel to the margin, BCS appears markedly asymmetric with a right hand (southern) flank that is higher and steeper (about 800 m in relief and more than 30° steep). The left-hand side of the canyon is instead much smoother. As a consequence, bottom currents flowing along the slope from the north enter the canyon and interact with its complex topography leading to preferential deposition on the up-current side of pre-existing morphological relief. Where mass-failure deposits generate morphologic relief, outside the canyon, sediment is preferentially deposited up current (N-ward). BCS includes three main EW-oriented sediment conduits: canyon C, to the south, channel B, in the central area, and moat A in the north. Channel B shows a well developed levee deposit on its right-hand side and appears markedly straight and erosional on the upper slope. The deepest portion of channel B is substantially abandoned and draped but still shows a subdued thickening of the draped unit north (and up current) of pre-existing morphologic relief, confirming the impact of along-slope flowing currents. Canyon C is flanked by erosional walls all the way to the basin floor where deep-sea furrows develop with a NW-SE orientation.

Today, dense water formation in the Adriatic is seasonally modulated and displays a significant variability on inter-decadal scales. Dense water formation during glacial intervals was likely different from the modern because most of the North Adriatic shelf was subaerially exposed and the deep water mixing in the south was likely reduced, as suggested by paleoceanographic reconstructions. The growth patterns of

BCS since the LGM are characterised by concurrent erosion of the upper portion of channel B and of the lower portion of canyon C. It is possible that flows through the straight, narrow and steep upper segment of channel B spill over its right hand levee in ca. 600 m water depth, where the relief of levee B on the channel floor is minimal, and enter canyon C, where substantial erosion takes place. In this view, the upper portion of canyon C, where hard grounds and coral colonies are encountered, is flushed by currents characterised by reduced turbidity, while the lower part of canyon C collects additional flows from upper channel B.

1. INTRODUCTION

Active submarine canyons are extensively described worldwide along oceanic margins (e.g., Shepard et al., 1933; 1981; Daly, 1936, Shepard and Dill, 1966, McAdoo et al., 1997) and along continental margins of confined basins, such as the Mediterranean Sea. Mediterranean active canyons are documented along the Gulf of Lion slope (e.g., Droz and Bellaiche, 1985; Batzan et al., 2005), in the Catalan Margin (e.g., Field and Gardner, 1990; Palanques et al., 1994), and in the Tyrrhenian Margin (e.g., Gallignani, 1982; Gamberi and Marani, this vol.). These sediment conduits occur in a broad range of physiographic and geological contexts, presenting an extreme variability in dimensions, morphology and seafloor sediment. The processes that feed canyon heads and transport sediment along their axes are also greatly diversified, depending primarily on the type and amount of sediment that reach the canyon, and on the oceanographic regime impacting the canyon area (Normark, 1970; Farre, 1983; Normark and Piper, 1991). All these factors are commonly considered as

strictly related to the presence of a sediment source close to the canyon head, either a delta or a littoral cell carrying sediment into the canyon (Cutshall et al., 1986). Variations of relative sea level are important in controlling the distance of the canyon head from a river source and the water depth in the outer shelf, in turn controlling its current and wave regime.

Where a canyon head is located on a shallow inner shelf, sediment can be supplied directly from river deltas or long-shore drift; where, instead, the canyon head is more seaward, close to the shelf edge, sediment is fed by shelf currents and/or episodic density currents triggered by the instability of the canyon shoulders. Several Authors have linked the onset of canyons and their activity to sea-level falls and lowstands, when shelves become narrow and fluvial sediment sources may reach directly into the canyon heads, which commonly are situated close to the shelf edge (e.g., Twichell and Roberts, 1982; Carlson and Karl, 1988; Galloway, 1991). Under these conditions, large amounts of sediment are available for remobilization and large-scale slump and turbidity currents may be generated (Mutti, 1985). However, documentation from a great number of canyons described worldwide, indicates that sea-level fall and lowstand are not mandatory requirements for canyon activity. Indeed some canyons have been documented as active during rising and the highstand of sea-level (e.g., Kolla and Perlumutter, 1993; Trincardi et al., 1995).

We focused our attention on the Bari Canyon System (BCS), located along the SW Adriatic Margin, Central Mediterranean. The BCS dissect a relatively steep continental slope far away from river mouths, impacted, at least since the end of the last glacial interval, by very strong bottom currents resulting by the combined flow of the long-lasting contour-parallel slope currents, Levantine Intermediate Water (LIW), and of the episodic slope-transverse cascading currents, North Adriatic Dense Water

(NAdDW) (Verdicchio et al., in press). The peculiar oceanographic context in which BCS developed strongly influences the present day activity and the sedimentary processes inside the canyon. The main interest in studying the recent evolution of the BCS is understanding how cascading and contour currents can be captured within the canyon system defining areas of erosion and increased sediment deposition during periods of sea-level rise and modern sea-level highstand.

2. SETTING

2.1. Geologic setting of the SW Adriatic Margin

The western margin of the Adriatic basin belongs to the Apennine forleand domain (Ricci Lucchi, 1986; Ori et al., 1986, Royden et al., 1987; Doglioni et al., 1996), where the emerged sectors of the Gargano Peninsula and the Apulia region correspond to the flexural bulge (Doglioni et al., 1994; de Alteriis, 1995; Bertotti et al., 1999). Post-Mesozoic tectonic deformation led to the definition of the W-E-trending “Gondola deformation belt” (Fig. 1). The main structural feature of the SW Adriatic Margin, with a clear morphologic expression in the Dauno Seamount (Colantoni et al., 1990; de Alteris and Aiello, 1993; Tramontana et al., 1995). On the Adriatic shelf and upper slope four stacked depositional sequences (termed Sequence 1-4, top down) are separated by shelf-wide unconformities (ES1-ES4) and their correlative conformities; these sequences accumulated during the last ca. 450 kyr (Trincardi and Correggiari, 2000; Ridente and Trincardi, 2002). Each sequence is composed of progradational units (low angle clinoforms passing distally into plane-parallel mud drapes) among which forced regression deposits record phases of sea level fall (Ridente and Trincardi, 2005). These sequences extend along strike over

distances up to 300 km from the Central to the South Adriatic and form a composite shelf wedge with an overall backstepping architecture in the central Adriatic and forestepping stacking pattern north and south of Gargano Peninsula, respectively (Ridente and Trincardi, 2002), where Bari Canyon is located. The distribution and thickness variability of the four sequences suggests how tectonic activity controls sediment preservation. In particular, regressive sequence 2 (ca. 230-140 kyr) appears confined more seaward, along the Adriatic margin, compared to the sequences above and below, possibly reflecting a phase of tectonic deformation of the entire region (Ridente and Trincardi, 2006). Sequence 1 (ca. 140-25 kyr) shows variable thickness along the South Adriatic shelf, reaching a maximum in the shelf-edge region that rims the Northern head of BCS.

2.2. Oceanographic setting

Two main bottom-flowing water masses impact today the SW Adriatic Margin (Cushman-Roisin et al., 2001): the Levantine Intermediate Water (LIW) and the North Adriatic Deep Water (NAdDW; Fig. 1). The LIW forms in the Rhodes permanent cyclonic gyre in the Levantine Basin through evaporation during the summer and cooling during winter (Lascarotos et al. 1999). This salty water mass (29,0 kg/m^3) enters the South Adriatic on the eastern side and flows out southward along the SAM slope in intermediate depths (200-600 m; Orlic et al., 1992, Wust, 1961; Manca et al., 2002; Fig. 1). The NAdDW forms in the North Adriatic shelf and densifies through winter cooling and evaporation associated with local wind forcing (Bora events). This cold and dense water mass (29,8 kg/m^3) moves southward along the Italian cost passing around the Gargano promontory (Cushman-Roisin et al.

2001), and cascading obliquely across the SW-Adriatic slope, where strongly interacts with its topography (Vilibic and Orlic, 2002).

The long-lasting contour parallel LIW and the off-shelf cascading NAdDW have a similar southward flow component, and their dynamical interaction leads formation of several type of bottom-current sedimentary feature along the SW-Adratic Margin (Verdicchio et al., in press, Verdicchio and Trincardi, in press). The rate of formation and the physical properties of both water masses show strong seasonality (Roussenov et al., 1995), as indicated by oceanographic time series over the last few decades. Mooring data in the study area confirm that strong seasonally modulated S-flowing bottom currents, have a down-slope component and reach velocities greater than 60 cm sec^{-1} (Turchetto et al., this vol.). The modern current regime through the canyon, and on the open slope to the north, is discussed by Turchetto et al. (this vol.) and by Verdicchio et al. (in press).

Within the South Adriatic Basin, the South Adriatic Dense Water (ADW) reflects an open ocean formation process preconditioned by the permanent cyclonic South Adriatic Gyre (Pinardi and Masetti, 2000). The ADW flows out the Otranto Strait contributing to the formation of the Eastern Mediterranean Deep Water (Artegiani et al., 1989; Bignami et al., 1990).

2.3. Past Changes in the Adriatic oceanographic regime

The Adriatic physiography and oceanography underwent dramatic rearrangements during Quaternary climatic oscillations and particularly since the last glacial lowstand (Cattaneo and Trincardi, 1999). The north Adriatic shelf, where the NAdDW forms today, was subaereally exposed during the Last Glacial Maximum, when sea level was about 125 m below the modern level (Fairbanks, 1989). At that time, stabilized

stratification of the water column allowed only weak and shallow temperature-driven winter convection, in the deepest parts of the basin (Myers et al., 1998). Likely, therefore, the last-glacial Adriatic was characterized by a low energy bottom current circulation.

Short-lived but important changes of the Adriatic circulation occurred also during intervals of decreased surface water salinity that impacted the whole Mediterranean leading to the deposition of sapropel layers (Vergnaud-Grazzini, 1977; Rohling and Hilgen, 1991; Ariztegui et al., 2000). The formation of a low-salinity surface water layer acted to hinder the potential overturning and deep-water formation limiting the open ocean convection to the upper 300 – 400 m, and resulting in a cold and relatively fresh outflow from the Otranto Strait and a more sluggish deep-water circulation (Rohling, 1994; Myers et al., 1998).

3. METHODS

A new bathymetric map of the BCS (Fig. 1) was acquired using a RESON 8160 multibeam echo sounder with nominal sonar frequency of 30 kHz and angular coverage sector of 135 beams per ping at 1^{o}. Chirp-sonar profiles were gathered using a hull-mounted 16-transducer source with a sweep modulated 2-7-kHz outgoing signal equivalent to a 3.5 kHz profiler. Chirp-sonar profiles allow vertical resolution of 0.5 m or better. A 30 kHz TOBI side scan sonar mosaic was acquired and processed following Le Bas et al. (1995). All data has been collected with differential GPS ship positioning every 5 seconds. Two current-meter moring were located along the main canyon branches and one on the open slope north of it, and are discussed in Turchetto et al. (this vol.). Long piston cores provide basic stratigraphic information

on the evolution of BCS and are complemented by information from dredges on the upper reaches of canyon branches and short cores collected in the mooring sites.

4. RESULTS

4.1. Morphology and backscatter of the Bari Canyon System

A recently acquired multibeam bathymetry on the BCS allows recognize three E-W oriented sub-parallel conduits: the mid slope sinuous moat A, in the northernmost part of the BCS; 2) the channel levee complex B, in the middle part; and 3) the broad and deeply incised Canyon C, to the south (Fig.2).

Moat A is between 500 and 700 m and shows an overall lunate pattern and a substantial downslope broadening. Along the axis of moat A the sea floor displays a prevailing erosional character, as documented by patches of high backscatter on TOBI mosaics (Fig. 2b). The left (Northern) flank of the moat has a relief up to 100m and displays stripes of high and low backscatter sub-parallel to the moat axis, suggesting the presence of erosional steps into units of variable lithology. The right (southern) flank of moat A is characterised by low and more uniform backscatter that suggests the presence of muddy deposits.

Channel B is divided in 3 main parts: 1) down to 620 m the NNW-SSE channel is markedly erosional, narrow, straight and confined by steep walls up to 60-80 m high; 2) further seaward and down to 750 m water depth, the channel (labelled B^{I}) becomes narrower, slightly sinuous and veers along an E-W path; this channel appears somewhat subdued on swath bathymetry but is better recognised on the slope map (Fig. 2c); 3) in greater water depths the system evolves into a well defined channel (called B^{II}) that shows moderate sinuosity, has clear-cut edges and is accompanied by a levee wedge on its right-hand side, to the south (Fig. 2a). The channel disappears in

water depths greater than 1100 m, where a subtle basin-ward bulge of the bathymetric contour is observed (Fig. 2c). The axial gradient of channel B decreases from several degrees in the head region to about 3.5^{o} in 620 m water depth. At the exit of this deeply incised segment the sea floor becomes sub-horizontal before defining an area that dips landward (see bathymetric profile in Fig. 2c). In greater water depths channels B^{I} and B^{II} have axial dips of less than 1^{o} but display well developed inner walls up to 6^{o} steep.

Canyon C is broad (about 4 km) and characterised by a 600 m high southern wall that appears extremely steep (up to 31^{o}). Along its straight axis, canyon C shows a terraced floor with repeated gradient changes accompanied by deep scours located in the flat areas downslope of major morphological steps. Multiple scars have high backscatter on TOBI mosaics in water depths of less than 300 m. Low backscatter is encountered in water depths of about 550 to 600 m in the area where channel B approaches the transition between the upper and lower portion of canyon C. The lower portion of canyon C has a more regular axial gradient, compared to the upper portion, and is characterised by dominantly high backscatter, particularly along the southern wall where abyssal furrows develop and multibeam bathymetry suggests the presence of slide blocks. In this area the left hand flank of canyon C is characterised by discontinuous stripes of high and low backscatter elongated parallel to the canyon axis. These features resemble the stripes observed on the erosional flank of moat A and define possible erosional steps.

4.2. Seismic stratigraphy of the Bari Canyon System

High-resolution seismic profiles document sedimentary bodies that thicken northward both within and outside the Bari Canyon System (Fig. 3) suggesting an active

migration to the north (with a variable upslope component) that is consistent with the impact of the slope parallel current regime of the entire margin (Verdicchio et al., in press). Locally, bottom-current deposits accumulate on the irregular northward-dipping side of mass-transport deposits (Minisini et al., 2006) and on the southern flanks of the canyons, particularly in their upper reaches (Fig. 3, III-V).

4.2.1. Upper slope stratigraphy (ca. 200-600 m)

The head region of BCS is in of about 200 m water depths, seaward of a narrow outer shelf area that remained likely under marine conditions also during the LGM lowstand. North and south of the head region the regressive sequences exposed on the seafloor have different ages: in the south, deposits of Sequence 2 (Marine Isotopic Stage 7 and 6, Ridente and Trincardi, 2002) are truncated at their top by the steep walls of canyon C; in the north progradational deposits toward channel B belong to Sequence 1 and are therefore younger than MIS 6. This observation suggests that the last major phase of canyon down-cut took place during or at the end of the sea level fall that culminated with MIS 6. During the most recent cycle of sea level fluctuation, shelf margin progradation took place mostly north of BCS, impacted on the area of channel B and culminated in a phase of outer shelf and upper slope canyon down cut during the MIS 2 lowstand.

Seismic profiles define areas of dominant sea floor erosion both in canyon C and channel B and on the northern side of moat A (Figs. 2 and 4). The upper straight segment of channel B is characterised by sharp erosional flanks and a narrow relatively flat floor. The uppermost reaches of channel B are sediment barren and show sharply truncated parallel reflectors that belong to gently dipping regressive sequences. Proceeding downslope, the channel floor shows patches of acoustically

transparent deposits with hummocky top. The age and facies of these deposits is poorly constrained but seismic profiles indicate repeated depositional phases (Fig. 4).

Channel B is flanked by asymmetric levee wedges with the right-hand wedge higher and more developed in extent (Fig. 4). In particular, the right-hand levee of channel B advances onto the floor of the adjacent canyon C and pinches out with a low angle downlap onto older acoustically transparent deposits that provide an irregular substrate (Figs. 4, I-III). The southern flank of canyon C is characterised by very low acoustic-signal penetration, likely caused by the steep slope and the presence of cemented materials. Locally, truncated seaward dipping reflectors can be discerned (Fig. 4, IV).

4.2.2. Lower slope stratigraphy (ca. 600-900 m)

A channel-levee complex, below 600 m w.d., corresponds to the narrow channel detected on swath bathymetry seaward of the markedly erosional channel B (Fig.2). This channel-levee complex appears draped by a uniform plane-parallel unit (up to 20 m tick) with a very subtle wedging on the right-hand (southern) levee (Fig. 3, VI). Basinward, the draping unit decreases in thickness and the edges of the narrow channel beneath appear more evident. Concurrently, the right-hand levee becomes progressively more developed. In this sector of the channel-levee complex the base of the narrow channel reaches 40 m below the levee crest. The levee wedge and the underlying units are sharply truncated by canyon C that down cuts the sea floor to about 150 m deeper than the levee crest (Fig. 5). The lower part of canyon C is therefore surrounded by two markedly asymmetric flanks: the steep and high E-W-trending slope to the right (south) and the sharp but smaller erosional flank down cutting the channel levee complex on the left (north). Seismic profiles in figure 3

indicate that the units truncated by the left flank of canyon C are older than the last glacial interval.

4.2.3. Transitional area

Between the two areas described above (in between 600 and 700 m w.d.) channel B^{I} is poorly defined on morpho-bathymetric images compared to the deeply erosional channel B, upslope, and the channel-levee complex B^{II}, further downslope. On seismic profiles, the narrow channel B^{I} is accompanied by a small levee wedge and buried beneath a thick unit characterised by low-angle reflectors converging away from the channel axis. This feature appears down-cut on both sides by moat A, in the north, and Canyon C to the south (Fig. 4).

4.2.4. Mass-transport deposits in the Bari Canyon System

Mass-transport deposits into the BCS reach up to 150 km^2 in extent and 15 m in thickness. Seismic-stratigraphic correlation allows define simultaneous events affecting several sectors of the SW Adriatic Margin. Most mass-wasting deposits within the BCS do not extend to the basin floor and are less thick than elsewhere on the SW Adriatic Margin (Trincardi et al., 2004; Minisini et al., 2006). Within the BCS, mass-wasting deposits are typically buried, have erosional bases, irregular tops and chaotic or acoustically transparent seismic facies (Fig. 6). Seismic stratigraphic correlation indicates that at least one major mass-wasting deposit extends over most of the canyon area and appears coeval to extensive mass-wasting deposits generated along the SAM during the MIS 2 sea level lowstand (Minisini et al., 2006).

4.3. Sediment cores and sea floor samples

4.3.1. Sea floor samples

Surface samples (dredges and box cores) come from the outer shelf just outside the canyon, from the floor and the walls of Canyon C between 300 and 600 m (Tab. 1 and Fig. 7) and from the sites of mooring deployment (Turchetto et al., this volume). Samples recovered from canyon walls include various types of carbonate firm- and hardgrounds, with irregular, somewhat nodular surfaces often patinated by Fe-Mn oxides and affected by bioerosion (Fig. 7a-c). These indurated substrates provide a suitable ecospace to encrusting epifauna, mainly serpulid polychaetes, bryozoans, sponges, solitary corals (*Caryophyllia smithii*) and inarticulated brachiopods (*Neocrania anomala*) some of which still alive when sampled (Fig. 7d). Other lithologies contributing to the canyon stratigraphy include marly sandstones intensely bored by *Pholadidea loscombiana* clams (Fig. 7g), a cold Pleistocene indicator (Colantoni et al., 1975; Malatesta and Zarlenga, 1986) and loose "pipes" resembling fluid escape chimneys (Fig. 7e,f; Kulm and Suess, 1990; Schwartz et al., 2003). Dead but sub-recent (dating in progress) azoxanthellate scleractinian corals (*Desmophyllum dianthus*, *Lophelia pertusa*, *Madrepora oculata*) occur as well in the dredged catch (Fig. 7h). These taxa are known to colonize deep-water firm and hard substrata (Taviani et al., 2005, with references therein), a further indication of communities exploiting the canyon walls since the late Holocene at least. An articulated shell of the sediment-nestling mytilid *Modiolula phaseolina* embedded within a carbonate hardground (Fig. 7i) provided a calibrated AMS- C^{14} age of 50000±3000 years BP (Poznàn Radiocarbon Laboratory). Combined sedimentary and biological data provide evidence of prolonged temporal exposition to seawater under sediment-

starving conditions that promoted submarine lithification and oxide precipitation, and the concurrent and still persistent action of strong currents coupled with trophic regimes capable to sustain sessile filter feeding and micro-carnivore communities.

Samples obtained by coring and dredging from the outer shelf contain shell assemblages dominated by the glacial Pleistocene pectinid *Pseudamussium septemradiatum* associated with other molluscs such as the cold–water faunas *Iothia fulva*, *Buccinum humphreysianum* and *B. undatum*, the bivalves *Venus casina* and *Karnecampia bruei*, large Pleistocene morphotypes of the bryozoan *Turbicellepora coronopus*, the terebratulid brachiopod *Gryphus vitreus*, the solitary scleractinian coral *Caryophyllia smithi* and many other invertebrates (Fig. 7l). These dominantly last glacial assemblages are widely distributed in this area and often still exposed (Colantoni and Gallignani, 1978; Taviani, 1978). Traditional C^{14} dating of *P.septemradiatum* valves provide calibrated ages of 19000±370 and 15350 ±250 years BP (Colantoni et al., 1975), suggesting that post-Last Glacial Maximum communities settled on a silty-muddy middle-outer shelf, characterised by times of sediment starvation as documented by advanced shell bioerosion and epifaunal occupancy (bryozoans, oysters, serpulid polychaetes, corals) of many shells (Fig. 7-l).

4.3.2. Sediment cores and stratigraphic correlations

Figure 8 shows a stratigraphic correlation among core SA03-01, north of the BCS, and two cores collected through the right-hand levee of the upper portion of channel B and outside the left levee of B'. Core correlation is mainly based on foraminifera assemblages and magnetic susceptibility curves whose peaks commonly indicate the presence of tephra layers (Verdicchio et al., in press). Ages are ascribed to biozone boundaries based on published literature (Jorissen et al., 1993; Asioli, 1996; Asioli, et

al., 1999; 2001; Capotondi et al., 1999; Ariztegui et al., 2000). The planktonic foraminifera ecozones defined for the Central Adriatic for the last 20 kyr (Asioli, 1996; Asioli et al., 1999, 2001) correlate to the Southern Adriatic ones. Reference cores in the Central Adriatic are also constrained by oxygen stable isotope stratigraphy, ^{14}C AMS datings, tephrochronology, pollen record, planktic and benthic foraminifera assemblages in a well defined seismic stratigraphic context (Trincardi et al., 1996, 1998; Asioli, 1996; Calanchi et al., 1998; Ariztegui et al., 2000).

In the BCS area core stratigraphy shows from top to bottom: 1) a late-Holocene interval above the Last Occurrence of *Globorotalia inflata* (Asioli, 1996); 2) a well defined Sapropel S1 interval characterised by large specimens of *Globigerinoides ruber* (pink) with thin and inflated tests; all cores show evidence of a marked break of Sapropel 1 characterised by the re-appearance of *Globorotalia inflata* (Rohling et al., 1997; Ariztegui et al., 2000). All cores include a tephra layer into the sapropel sediment likely corresponding to the Mercato event (Calanchi et al., 1998; Siani et al., 2001; Lowe et al., in press); 3) the pre-Boreal interval, characterised by repeated and short-term oscillations in abundance of cold- and warm-water species; 4) the GS-1 (Younger Dryas) interval marked by a dominant cold-water association with *Globigerina bulloides*, *Neogloboquadrina pachyderma* and *Globorotalia scitula*, and including a tephra layer, known as C1, that corresponds to the Pomici Principali event (Asioli, 1996; Calanchi et al., 1998; Lowe et al., in press); 5) the GI-1 interval (Bolling/Allerod) marked by a basal peak in the abundance of *Globigerinoides ex gr. ruber* and an oscillatory cooling trend as previously observed in the Central Adriatic (Asioli et al., 1999, 2001); 6) a glacial interval dominated by cold-water species like *Globigerina bulloides*, *Neogloboquadrina pachyderma* and *Globorotalia scitula* (the interval below the Bolling-Allerod interval on Fig. 8).

In contrast to other Adriatic cores a small percentage of *G.inflata* is present throughout the last 6 kyr interval (HST) in cores SA03-09 and SA03-01 (Fig. 8). Several authors (Jorissen et al., 1993; Asioli, 1996; Capotondi et al., 1999; Ariztegui et al., 2000) have demonstrated that the disappearing of *G. inflata* from the Adriatic circa 6 kyr B.P. is a well documented bio-event, which approximates the achievement of the modern sea level highstand and corresponds to the maximum flooding surface defined on seismic profiles on the shelf (Trincardi et al., 1996; Cattaneo and Trincardi, 1999, Cattaneo et al., 2003). The occurrence of *G. inflata* during the last 6 kyr is ascribed to a component of re-sedimentation and deposition by either slope parallel currents or by sediment shedding from shallower waters. Also south of BCS in 716 m w.d. Jorissen et al. (1993) document the occurrence of a very low percentage of *G. inflata* in a core that recoverd a relatively expanded sequence (ca. 1.20 m) of the last 6 kyr B.P.

The last glacial-interglacial transition was an interval of extreme variability in sediment accumulation rates on the SAM slope (Verdicchio et al., in press; Verdicchio and Trincardi, in press): in the northern portion of the margin, after the late glacial period, sedimentation rates are in the order of 25 cm kyr^{-1}, while in the BCS area sediment accumulation rates are up to about 185 cm kyr^{-1}. The post-LGM sediment accumulation rates likely reflect increased off-shelf sediment transport proceeding to the south. Along most of the SAM slope, deposition decreased during the last 6 kyr, when modern sea level highstand was achieved, with sediment accumulation rates varying between 2 and 35 cm kyr^{-1} (Verdicchio et al., in press). Away from the main erosional pathways, sediment accumulation rates in the BCS reached values between 35 and 70 cm kyr^{-1} during this interval.

4.3.3. Seismic stratigraphic correlation

The cores collected in the BCS allow assign an age to key reflectors and compare how sediment accumulation rates change in time and space. By projecting core SA03-09 on a seismic profile (Fig. 9) we can ascribe ages to key reflectors as follows: 1) the onset of the channel-levee complex predates the LGM and a down-section age extrapolation suggests that the base of the deposit is within the last 120 kyr; 2) the levee wedge was still growing during at least the first half of the post glacial sea level rise; 3) the draped unit that mantles the channel-levee complex B is Holocene (post GS-1) and shows a subtle reflector convergence toward canyon C; 4) all units are down cut by canyon C. In its upper reaches, channel B is deeply down-cut and the levee on its right shows relatively-low accumulation rates since the Younger Dryas suggesting that sediment bypass the area in flows that are mostly confined within the canyon axis (Fig. 9).

5. DISCUSSION

The BCS develops north of a high (up to 800 m) and steep (> 30°) E-W wall on the continental slope, likely reflecting structural control (Ridente et al., this vol.). This morphological wall not only provides a source for mass wasting but also forms a barrier capable of diverting along-slope bottom currents that flow southward reaching velocities greater than 60 cm sec^{-1} (Turchetto et al., this vol.). BCS has a complex history of erosion and deposition that includes major phases of down cut, well documented on the outer shelf, during MIS 8 and 6 (Ridente et al., this vol.), leading to the formation of a broad canyon partially floored by mass-transport deposits beneath the modern C and B conduits (Fig. 10-1). This large canyon was likely

reactivated during falling sea level conditions after MIS 5 and until the LGM. We discuss the stratigraphic evidence that characterises the canyon evolution during and after the LGM.

5.1. Activity of the Bari Canyon System since the LGM lowstand

During the LGM lowstand, the shoreline was located close to the modern 125 m isobath and in the order of 10 km from a rather deep shelf edge (now in ca. 180-200 m; Fig. 10-1). The outer-shelf remained submerged during the LGM and was swept by currents as indicated by the sharp truncation of progradational clinoforms in this area. The direction of progradation of Sequence 1 suggests that circulation was likely southward (Ridente and Trincardi, 2002), as today, and bottom-hugging currents could be captured by the head of BCS located near shore and in very shallow water (40-60 m). During LGM, progradational units were mainly deposited on the NW side of the BCS indicating sustained sediment transport into the canyon. Channel-levee complex B begun to grow during the last sea level cycle and particularly during the LGM lowstand, resulting in a pronounced levee asymmetry (Figs. 9 and 10-2). Seismic profiles (Figs. 5 and 9) show consistently that the right-hand levee of channel B advances onto the floor of canyon C, located just south, that remained sediment starved as documented by the presence of firm- and hard-ground substrates and by a peculiar assemblage of molluscs and corals. This lateral spreading of levee B is consistent with flows that tend to overbank predominantly to the right of the conduit, resulting in a downlap termination or a more gradual pinch out of seismic reflectors in the thalweg of canyon C.

During this phase, channel B evolved down slope into a low-sinuosity submarine channel (B^{I} and B^{II} in Fig. 2) reaching the basin floor but not resulting in significant

depositional relief as observed in most examples of turbidity systems (e.g., Normark and Piper, 1991; Weimer, 1991; Galloway, 1998). The transitional area (B^I) is subdued both on multibeam images and on Chirp-sonar profiles reflecting lateral infill and partial burial by contourite deposits. The lack of a depositional lobe at the channel terminus and the evidence of lateral infill of part of the channel, upslope, indicate that the system has been continuously affected by slope transverse currents able to divert down slope flows and/or rework sediment transported through channel-levee complex B.

Several schemes have been proposed that define possible interactions between turbidity-current deposits and along-slope bottom currents (e.g., Faugères et al., 1999; Stow et al., 2002). Most attention has been directed to the reworking of base-of-slope deposits that become progressively re-organised into contour-parallel, typically mounded, deposits (Normark et al., 1993; Ross et al., 1994). In the BCS an additional effect is the lateral infill of a channel feature (channel B^I, in particular) by the flow of slope-parallel currents against the inner side of the right-hand (and most developed) levee wedge (Fig. 4).

5.2. Recent Activity of the Bari Canyon System

Sediment cores also indicate that channel-levee complex B has been growing well after the end of the LGM (Fig. 8), although the wedging of seismic reflectors across the levee became progressively less pronounced. Today, density-driven bottom currents cascade off shelf and flow both across the open slope and through the BCS, reaching velocities greater than 60 cm sec^{-1} (Turchetto et al., this vol.). At core scale, the upslope portion of levee wedge B does not show typical overbank turbidity current deposits, as observed in many examples of deep sea fans (e.g., Piper and

Savoye, 1993; Migeon et al., 2001). Deposition is instead dominated by hemipelagic sediment and results in a reduced thickness of the Late-Holocene unit compared to cores on the open slope north of BCS (Verdicchio et al., in press). During this interval of reduced deposition, density flows had reduced sediment load and/or remained confined within channel B, which was likely waxed by downslope currents, as indicated by the evidence of steep erosional canyon walls and truncated subsurface reflectors. These observations are consistent with the evidence of limited levee aggradation during the mid-late Holocene.

The upper part of Canyon C is sediment starved and swept by intense but relatively clear bottom currents. In contrast, the lower part becomes gradually more erosional, as documented by the occurrence of truncated reflectors and erosional steps on the left canyon wall (Fig. 5). The lower canyon C down-cuts B^{II} levee wedge including its Holocene drape, indicating substantial erosion during modern interglacial conditions (Fig. 10-3). The steep and high southern wall of BCS acts as a hydrological barrier that confines bottom currents flowing either along slope (LIW) or cascading off the shelf oblique to the slope (NAdDW), possibly favouring their acceleration. This view is consistent with the occurrence of erosional furrows further eastward at the exit of canyon C. The main erosional elements of the BCS are the upper, straight and narrow, portion of channel B, down to about 600 m water depth, and the deepest portion of canyon C, beyond 700m water depth. A possible connection between these two elements corresponds to the area where levee wedge B reaches the minimum elevation and presents elongated erosional steps on its outer-bank side dipping toward canyon C. In contrast, the upper part of canyon C is flushed by turbidity bottom currents while the lower segment of channel B is abandoned. We suggest that after the LGM, and probably in very recent times, density currents started to down cut

substantially the upper portion of channel B. The gradient inversion at the exit of this straight erosional segment may be instrumental in generating flow detachment and spill over into lower canyon C (Figs. 2c and 10-3). Whether this pathway reflects a single major event or recurrent spill over flows is difficult to ascertain with the available data.

5.3 Sediment sources during LST and HST conditions

During the last glacial lowstand the sediment source for channel B was likely long-shore drift, while during higjstands, when the shoreline is further landward, the canyon is impacted by off-shelf density currents (the NAdDW) that cascade along the entire SAM (Fig. 10). Sediment cores through the upper section of levee wedge suggest that deposition took place through diluted flows resulting in the deposition of mottled and structure-less mud. Also in the area outside the left-hand levee of the upper channel B cores do not show sedimentary structures typical of turbidity current deposits, despite downslope transport is proved by the presence of a small but persistent component of recycled benthonic foraminifera from the shelf (Fig. 7). Direct observation from current-meter moorings and sediment traps North of BCS, within channel B and in canyon C define clear episodes of dense waters cascading off the shelf and resulting in net downslope transport at rates that appear similar within and outside the BCS (Turchetto et al., this vol.).

In summary, the BCS is impacted by down slope currents, both during sea level lowstand and modern conditions. In the first case, the growth of channel-levee complex B suggests an activity of mud-laden turbidity currents. In the latter case, down slope flowing water mass is instead driven by density gradients and impacts the entire margin outside BCS. When this water mass is captured by the narrow conduit

of channel B lateral confinement leads to flow acceleration and consequent channel floor erosion. At the exit of this straight conduit, a high momentum down slope flow impacts an area of flat or up-slope dipping sea floor and may result in flow detachment and spill over into the lower canyon C (Fig. 11).

CONCLUSIONS

Bari Canyon System (BCS) is the main active sediment conduit of the SW Adriatic margin since the last glacial interval. During this interval, processes typical of active submarine canyons, such as turbidity currents and mass-transport events, are replaced or overshadowed by intense cascading currents impacting seasonally the entire SW Adriatic margin and accelerating through the canyon. When captured by the BCS, the off-shelf cascading current becomes confined eroding, transporting and depositing fine-grained sediment mimicing a very-dilute turbidity current.

Geomorphological, seismo-stratigraphic, sedimentological and biostratigraphic data support the following conclusions: **1.** BCS is characterised by a marked morphological asymmetry with a high-relief, steep and erosional right hand flank. **2.** The most recent phase of extensive canyon erosion occurred during the lowstand of MIS 6, as part of a long-term history of canyon down-cut over the last ca. 350-400 kyr. **3.** During the last sea level cycle (MIS 5e to present), shelf-margin progradation was particularly active on the Northern side of BCS where the apex of channel B is located. **4.** Channel-levee complex B begun to grow during the last sea level cycle and particularly during the LGM when the levee asymmetry became more pronounced. After the LGM, channel B became abandoned in water depths greater than ca. 700 m but more actively incised in shallower areas. **5.** Today, the cold and dense bottom waters that form on the Adriatic shelf through winter cooling enter the BCS with a reduced sediment load but capable to hug the seafloor and entraining sediment. Since these dense waters can reach velocities greater than 60 cm sec^{-1} it is conceivable that, during modern highstand conditions, they down cut the steep walls and sweep the floor of the upper portion of channel B. In deeper waters, instead, the most actively eroded element is canyon C which down cuts the abandoned levee complex of

channel B. **6.** The evidence of active erosion both on the upper portion of channel B and the lower part of canyon C suggests that cascading currents flushing the upper trunk of B tend to overbank towards the right and spill over into canyon C.

Acknowledgments We thank captains and crews of R/V *Urania* for helping during cruises SA03, ST04 and ST05. The TOBI team at NOC, Southampton, is also acknowledged for their invaluable work on cruise SAGA03 and post-cruise processing. This study is supported by the European projects EUROSTRATAFORM (EC contract n. EVK3-CT-2002-00079), the European Access to Seafloor Survey Systems "EASSS III-TOBI side-scan sonar" (HPRICT199900047) , and the HERMES European project (G0CECT200551112341). This is ISMAR (CNR) contribution number 1514.

Figures list

Figure 1. Location of the Adriatic in the Mediterranean Sea with area of formation and main circulation path of the Levantine Intermediate Waters (upper left). Schematic bathymetry and main current path of the Adriatic basin and areas of formation of the North Adriatic Deep Waters (NAdDW) and Adriatic Deep Waters (ADW) (upper right). Bathymetry of the SW Adriatic Margin showing the Bari Canyon System (BCS) and major slump scars affecting the outer shelf and slope. The Dauno Seamount and the trace of Gondola deformation belt are also reported. Triangles represent mooring locations.

Figure 2. a) Detailed bathymetry of the BCS; b) TOBI mosaic on the same area with simplified bathymerty superimposed for reference; c) map of the slope gradient. Note that the upper and lower portions of channel B (called B and B^{II}, respectively) are best detected on bathymetry data while the intermediate portion of this system (B^{I}) is less evident morphologically, possibly in response to lateral infill. The highest backscatter values are in canyon C, particularly along its southern steep and erosive wall. Other areas of high backscatter are the erosional walls of the upper portion of channel B and the Northern flank of moat A.

Figure 3. Seismic profiles across the BCS document the spatial relationship among the three main conduits from shallower to deeper slope areas. The thalweg of channel B is deeply incised than canyon C in the upper slope (I), viceversa in areas deeper than 650 m where canyon C is actively eroding the levee of channel B (IV). Moat A is visible on the right portion of profiles in intermediate slope depths (II) and disappears downslope (VI). Outside the canyon, bottom-current deposits (star symbol) are asymmetrically distributed on the northern flank of pre-existing sea floor reliefs (IV) and sediment waves (V). All profiles have the same vertical exaggeration. Dashed lines are location of dredges that collected samples showed in figure 7.

Figure 4. Detailed N-S profile along the upper slope showing the morphologic and stratigraphic relationship among canyon C, channel levee complex B and moat A. The channel-levee complex of B is filled by stacked acoustically transparent deposits and downlaps into the adjacent canyon C. The floor of the channel levee complex B and

of canyon C consist of acoustically transparent deposits interpreted as mass transport deposits. Location in Fig. 3.

Figure 5. Evidence of canyon C down-cutting the right-hand levee of channel B and producing elongated erosional steps seen on TOBI (arrows) and on a Chirp sonar profile. The Chirp profile also documents the asymmetric deposition of Holocene deposits north of the pre-existing depositional relief of channel-levee complex B. TOBI mosaic also shows furrows in deeper waters (dashed lines). Location in Fig. 3.

Figure 6. Chirp profile oriented downslope (roughly EW) and positioned in figure 3 through the erosional upper portion of channel B (left) and the floor of moat A (right) where acoustically-transparent mass-transport deposits are partly buried and partly exposed at sea floor. The close-up shows marked erosional truncations of older tilted deposits below and younger depositional units pinching out above the mass-transport deposit. Cores SA03-02 and SA03-09 are positioned and will be discussed later in the text.

Figure 7. Seafloor samples recovered from stations indicated in Fig. 3. a) large slab of carbonate hardground; note irregular nodular surface and localised oxide patination; b) carbonate hardground showing intense epifaunal colonisation by serpulid polychaetes, brachiopods and bryozoans; c) carbonate hardground showing a complete stratigraphy from firm mudstone still including pockets of unlithified sediment to micritised upper surface, micro-bioeroded and encrusted by Recent epifauna; the mudstone retains *in situ* shells (arrow) of the nestling mytilid *Modiolula phaseolina* that provided an age > 50 kyr; d) close-up of a living specimen of the inarticulated brachiopod *Neocrania anomala* (arrow) documenting present sediment-starvation at this site; on the lower left side a serpulid polychaete; e) 'pipe' encrusted by recent epifauna (serpulid polychaetes, brachiopods and bryozoans); note scalloped external surface; f) section of a hollowed 'pipe'; g) articulated shell of the boring clam *Pholadidea loscombiana* (late Pleistocene) still *in situ* within fine sandstones; sample hosted in the Zoological Museum of the University of Bologna (catalog n. MZB44056); h) articulated nestling mytilid *Modiolula phaseolina* embedded in a carbonate concretion; i) deep-water scleractinian corals from the southern wall of Bari Canyon: L= *Lophelia pertusa*, M = *Madrepora oculata*, D = *Desmophyllum*

dianthus; C = *Caryophyllia* sp; l) skeletal assemblage from post-LGM Pleistocene silty-muddy units: P = *Pseudamussium septemradiatum*, V = *Venus casina*, N = *Neopycnodonte cochlear*, C = *Caryophyllia smithii*, T = *Turbicellepora coronopus*, S = serpulid polychaetes, E = echinoid spine; note that most valves are often bioeroded and encrusted by epifaunal organisms also inside the shell.

Figure 8. Core correlation between SA03-2 and SA03-9 within the BCS (location in Figs. 4 and 7) and SA03-1 (location in Fig. 1) just north of it. Quantitative micro-paleotological analysis of core SA03-01 allows identify the last occurrence datum of *G. inflata*, that approximates the base of the highstand deposits. The post-glacial record that accompanies the eustatic rise, includes Sapropel S1 and the Pre-Boreal, both within the Holocene, and the GS-1 and GI-1 intervals, below Holocene. Note that core SA03-02 documents a reduced rate of levee aggradation after MIS2 and, in particular, during the HST (above the L.O of *G. inflata*). During the same interval, both cores SA03-01 and SA03-09, respectively outside and within the BCS, show much higher sediment accumulation rates with a continuous shedding of reworked shelf material also during the modern HST.

Figure 9. Seismic stratigraphic correlation based on biostratigraphic information from cores SA03-02 and SA03-09. Chirp profiles ST179 and ST166 report the seismic reflectors that approximate the top of MIS 2 and the base of the HST thereby bracketing the section that deposited during the eustatic rise and the resulting drowning of the Adriatic shelf.

Figure 10. Cartoons portraying three phases in the late-Quaternary evolution of the BCS (left); fixed schematic profiles of the upper and lower slope show three key intervals of the canyon evolution: 1) lowstand of MIS 6 after a broad erosional valley formed; this valley remained active during the following cycle of sea level fluctuation leading to the lowstand of MIS 2. 2) during the lowstand of MIS2, BCS was fed by alongshore drift and channel-levee complex B developed occupying the northern portion of the pre-existing erosional valley. During this phase channel B was connected, upslope, to the area of rapid progradation of Sequence 1. 3) during modern highstand conditions the canyon is impacted by the same bottom currents as the rest of the slope outside. Currents down flowing through channel B may accelerate,

entraining sediment from the canyon walls and floor, and *jump* into the lower part of canyon C, actively eroded at present.

Figure 11. 3D bathymetry of the BCS viewed from the NE. Arrows denote the path of two main water masses in the area: the LIW flowing along the slope and the NAdDW cascading across the slope outside and within the BCS. During modern highstand conditions the canyon head is not fed directly by river born density flows as it may have been during glacial intervals. NAdDW may however focus into the straight upper segment of channel B, accelerate and possibly *jump* into canyon C, bypassing the area where the relief of the right hand levee of B is minimum. Moat A is also impacted by down slope flows and along slope bottom currents (red arrows denoting the LIW). The upper part of canyon C is also swept by down slope currents but the living faunal assemblage encountered here suggests that flows have a reduced turbidity.

Table 1. Position of dredges and box core samples.

References:

Artegiani, A., Azzolini, R., Salusti, E. 1989. On dense water in the Adriatic Sea. Oceanol. Acta, 12, 151-160.

Ariztegui, D., Asioli, A., Lowe, J. J., Trincardi, F., Vigliotti, L., Tamburini, F., Chondrogianni, C., Accorsi, C. A., Bandini Mazzanti, M., Mercuri, A. M., van der Kaars, S., McKenzie, J. A., Oldfield, F., 2000. Palaeoclimate and the formation of sapropel S1; inferences from late Quaternary lacustrine and marine sequences in the central Mediterranean region. Palaeogeography, Palaeoclimatology, Palaeoecology, 158, 215-240.

Asioli, A., 1996. High-resolution foraminifera biostratigraphy in the central Adriatic basin during the last deglaciation: a contribution to the Paliclas Project. In: Guilizzoni, P., Oldfield, F.L. (Eds.), Palaeoenvironmental analysis of Italian crater lake and Adriatic sediments (PALICLAS project). Mem. Istit. It. Idrob., 55, 197-217.

Asioli A., Trincardi F., Lowe J.J., Oldfield F. 1999. Short-term climate change durino the Last Glacial-Holocene transition: comparison between Mediterranean records and Grip event stratigraphy. Journal of Quaternary Science, 14, 373-381.

Asioli A., Trincardi, F., Lowe, J. J., Ariztegui, D., Langone, L., Oldfield, F. 2001. Sub-millennial climatic oscillations in the Central Adriatic during the last deglaciation: paleoceanographic implications. Quaternary Science Reviews, 20, 33-53.

Baztan, J., Berne, S., Olivet, J., Rabineau, M., Aslanian, D., Gaudin, M., Rehault, J. P., Canals, M. 2005. Axial incision; the key to understand submarine canyon evolution (in the western Gulf of Lion). Marine and Petroleum Geology, 22, 805-826

Bertotti, G., Casolari, E., Picotti, V. 1999. The Gargano Promontory; a Neogene contraction belt within the Adriatic Plate. Terra Nova, 11-4168-173.

Bignami, F., Salusti, E., Schiarini, S. 1990. Observations on a bottom vein of dense water in the Southern Adriaticand Ionian Seas. Journal of Geophysical Research, 95, 7249-7259.

Calanchi N., Cattaneo A., Dinelli E., Gasparotto G., Lucchini F. 1998. Tephra layer in Late Quaternary sediments of the Central Adriatic Sea. Marine Geology, 149, 191-209.

Capotondi L., Borsetti A. M., Morigi C. 1999. Foraminiferal ecozone, a high resolution proxy for the late Quaternari biochronology in the central Mediterranean Sea. Marine Geology, 153, 253-274.

Carlson, P. R. and Karl, H.A. 1988. Development of large submarine canyons in the Bering Sea, indicated by morphologic, seismic, and sedimentologic characteristics. GSA Bulletin, 100, 10, 1594-1615.

Cattaneo, A. and Trincardi, F. 1999. The late-Quaternary transgressive record in the Adriatic Epicontinental Sea: basin widening and facies partitioning. In: Bergman K., Snedden J. (Eds.), Isolated shallow marine sand bodies: sequence stratigraphic analysis and sedimentologic interpretation. SEPM, Spec. Publ., 64, 127-146.

Cattaneo, A., Correggiari, A., Langone, L., Trincardi, F. 2003. The late-Holocene Gargano subaqueous delta, Adriatic shelf: Sediment pathways and supply fluctuations. Marine Geology, 193, 61-91.

Colantoni, P. and Gallignani, P. 1978. Quateranry evolution of the continental shelf off the coast of Bari (South Adriatic Sea): shallow seismic, sedimentological and faunal evidences. Geologie Mediterraneenne, V (3), 327-338.

Colantoni P., Noto P., Taviani M. 1975. Prime datazioni assolute di una fauna fossile a *Pseudamussium septemradiatum* dragata nel basso Adriatico. Giornale di Geologia (s. 2a) 40, 133-140.

Colantoni, P., Tramontana, M., Tedeschi, R. 1990. Contributo alla conoscenza dell'avampaese apulo: struttura del Golfo di Manfredonia (Adriatico meridionale): Giornale di Geologia, 52 (1-2), 19-32.

Cushman-Roisin, B., Gacic, M., Poulain, P. M. & Artegiani, A. (eds) 2001. Physical oceanography of the Adriatic Sea: Past, present and future. pp. 304.Artegiani, A., Azzolini, R., Salusti, E. 1989. On dense water in the Adriatic Sea. Oceanologica Acta, 12, 151-160.

Cutshall, N.H., Larsen, I.L., Olsen, C.R., Nittrouer, C.A., DeMaster, D.J. 1986. Columbia River sediment in Quinault Canyon, Washington – Evidence from artificial radionuclides. Marine Geology, 71, 125-136.

Daly, R,A., 1936. Origin of submarine canyons. Am. Jour. Sc., 31, 401-420.

de Alteriis, G. 1995. Different foreland basins in Italy; examples from the central and southern Adriatic Sea. Tectonophysics, 252, 1-4, 349-373.

de Alteriis, G., Aiello, G. 1993. Stratigraphy and tectonics offshore of Puglia (Italy, southern Adriatic Sea). Marine Geology, 113, 3-4, 233-253.

Doglioni, C., Mongelli, F., Pieri, P., 1994. The Puglia uplift (SE Italy): an anomaly in the foreland of the Apennine subduction due to buckling of a thick continental lithosphere. Tectonics, 13, 1309-1321.

Doglioni, C., Harabaglia, P., Martinelli, G., Mongelli, F., Zito, G. 1996. A geodynamic model of the Southern Apennines accretionary prism. Terra Nova, 8, 540-547.

Droz, L., and Bellaiche, G., 1985, Rhone deep-sea fan: morpho-structure and growth pattern: AAPG Bulletin, v. 69, p. 460-479.

Fairbanks, R.G. 1989. A 17,000 year glacio-eustatic sea level record: influence of glacial melting rates on the Younger Dryas event and deep-ocean circulation. Nature, 342, 637–642.

Farre, J.A., MecGregor, B.A., Ryan, W.B.F., Robb, J.M. 1983. Breaching the shelfbreak: passage from youthful to mature phase in submarine canyon evolution. In: Stanley D.J., Moore T.G. (Eds.), The shelfbreak: critical interface on continental margins SEPM, Spec. Publ., 33, 25-39.

Faugères, J. C., Stox, D. A. V., Imbert, P., Viana, A. 1999. Seismic features diagnostic of contourite drifts. Marine Geology, 162, 1-38.

Field, M.E., and Gardner, J.A. 1990. Pliocene-Pleistocene growth of the Rio Ebro margin, northeast Spain: A prograding-slope model: Geological Society of America Bulletin, v. 102, p. 721-733.

Gallignani, P. 1982, Recent sedimentation processes on the Calabrian continental shelf and slope (Tyrrhenian Sea, Italy): Oceanologica Acta, 5, 493-500.

Galloway, W.E. 1998. Siliciclastic slope and base-of-slope depositional systems: Component facies, stratigraphic architecture, and classification. AAPG Bulletin, 82-4, 569-595.

Galloway, W.E., Dingus, W.F., Paige, R.E. 1991. Seismic and depositional facies of Paleocene-Eocene Wilcox Group submarine canyon fills, Northwest Gulf Coast, U.S.A. In: Weimer P., Link M.H. (Eds.), Seismic facies and sedimentary processes of submarine fans and turbidite systems. Springer-Verlag, 247-271.

Kolla, V. and Perlmutter, M.A. 1993. Timing of turbidite sedimentation on the Mississippi fan: American Association of Petroleum Geologists Bullettin, 77, 1129-1141.

Kulm, L.D. and Suess, E. 1990. Relationship between carbonate deposits and fluid venting: Oregon accretionary prism. J. Geophys. Res. 95-B6, 8899–8915.

Jorissen, F.J., Asioli, A., Borsetti, A.M., Capotondi, L., de Visser, J.P., Hilgen, F.J., Rohling, E.J., van der Borg, K., Vergnaud-Grazzini, C., Zachariasse, W.J. 1993. Late Quaternary central Mediterranean biochronology. Marine Micropalaeontology, 21, 169-189.

Lascaratos, A., Roether, W., Nittis, K. & Klein, B. 1999. Recent changes in deep water formation and spreading in the eastern Mediterranean Sea: a review. Progress in Oceanography. 44, 5–36.

Le Bas, T.P. , Mason D.C. & Millard N.W. 1995. TOBI Image Processing - The State of the Art. IEEE Journal of Oceanic Engineering, 20, 85-93.

Lowe, J.J., Blockley, S., Trincardi, F., Asioli, A., Cattaneo, A., Matthews, I.P. Pollard, Wulf, S., in press. Age modelling of late Quaternary marine sequences in the Adriatic: towards improved precision and accuracy using volcanic event stratigraphy. Continental Shelf Research.

Malatesta, A. and Zarlenga, F. 1986. Northern guests in the Pleistocene Mediterranean Sea. Geologica Romana, 25, 91-154.

Manca, B. B., Kovacevic, V., Gacic, M., Viezzoli, D. 2002. Dense water formation in the Southern Adriatic Sea and interaction with the Ionian Sea in the period 1997-1999. Journal of Marine System, 33-34, 133-154.

McAdoo, B.G., Orange, D.L., Screaton, E., Lee, H., Kayen, R. 1997. Slope basins, headless canyons, and submarine palaeoseismology of the Cascadia accretionary complex. Basin Research, 9, 313-324.

Migeon, S., Savoye, B., Zanella, E., Mulder, T., Faugères, J.C., Weber, O. 2001. Detailed seismic-re£ection and sedimentare study of turbidite sediment waves on the Var Sedimentare Ridge (SE France): Significance for sediment transport and deposition and for the mechanisms of sedimentwave construction. Marine and Petroleum Geology, 18, 179-208.

Minisini, D., Trincardi, F., Asioli, A. 2006. Evidences of slope instability in the South Adriatic Margin. Natural Hazards and Earth System Sciences, 6, 1, 1-20.

Mutti, 1985. Turbidite systems and their relations to depositional sequences. In: G.G. Zuffa (Eds.) Provenance of arenites. NATO ASI Series. Reidel Publishing, Holland: 65-93.

Myers, P. G., Haines, K., Rohling E. J. 1998. Modeling the paleocirculation of the Mediterranean: the last glacial maximum and the Holocene with emphasis on the formation of Sapropel S1. Paleoceanography, 13-6, 586-606.

Normark, W.R. 1970. Growth patterns of deep sea fans. AAPG Bulletin, 54, 2170-2195.

Normark, W.R., and Piper, D.J.W. 1991, Initiation processes and flow evolution of turbidity currents: implications for the depositional record, in Osborne, R.H., ed., From Shoreline to Abyss: SEPM Special Publication, 46, 207-230.

Normark, W.R., Posamantier, H.W., Mutti, E. 1993. Turbidite systems: state of the art and future directions. Reviews of Geophysics, 31, 91-116.

Palanques, A., Alonso, B., Farràn, M. 1994. Progradation and retreat of the Valencia fanlobes controlled by sea-level changes during the Plio-Pleistocene (northwestern Mediterranean). Marine Geology, 117, 195-205.

Piper, D.J.W. and Savoye, B. 1993. Processes of late Quaternary turbidity current flow and deposition on the Var deep-sea fan, north-west Mediterranean Sea: Sedimentology, 40, 557-582.

Ori, G.G., Roveri M., Vannoni, F. 1986. Plio-Pleistocene sedimentation in the Apenninic-Adriatic foredeep (Central Adriatic sea, Italy). In: Allen, P.A. & Homewood, P. (Eds.) Foreland Basins. IAS Spec. Publ. 8, 183-198.

Orlic, M., Gicic, M., La Violette, P.E. 1992. The currents and circulation of the Adriatic Sea. Oceanologica Acta, 15, 109-122.

Ortolani, F. and Pagliuca, S. 1987. Tettonica transpressiva nel Gargano e rapporti con le Catene Appenninica e Dinarica. Mem. Soc. Geol. It., 38, 205-224.

Pinardi, N. and Masetti, E. 2000. Variability of the large scale general circulation of the Mediterranean Sea from observations and modelling: a review. Palaeogeography, Palaeoclimatology, Palaeoecology, 158, 153–173.

Ricci Lucchi F. 1986. The Oligocene to Recent foreland basins of the Northen Apennines. In: Allen P., Homewood P. (Eds.), Foreland basins. IAS, Spec. Publ., 8, 105-139.

Ridente, D. and Trincardi, F. 2002. Eustatic and tectonic control on deposition and lateral variability of Quaternary regressive sequences in the Adriatic basin. Marine Geology, 184, 273-293.

Ridente, D. and Trincardi, F. 2005. Pleistocene "muddy" forced-regression deposits on the Adriatic shelf: a comparison with prodelta deposits of the late Holocene highstand mud wedge. Marine Geology, 222-223, 213-233.

Ridente D. and Trincardi F. 2006. Propagation of shallow folds and faults in late Pleistocene and Holocene shelf-slope deposits, central and South Adriatic margin (Italy). Basin Research, 18-2, 171-188.

Rohling, E. J. 1994. Review and new aspects concerning the formation of eastern Mediterranean sapropels. Marine Geology, 122, 1–28.

Rohling, E. J., Jorissen, F. J., de Stigter, H. C. 1997. 200 year interruption of Holocene sapropel formation in the Adriatic Sea. Journal of Micropalaeontology, 16-. 2, 97-108.

Rohling, E. J. and Hilgen F.J. 1991. The eastern Mediterranean climate at times of sapropel formation: A review. GEOL. MIN. 70- 3, 253-264.

Ross, W.C., Halliwell, B.A., May, J.A., Watts, D.E., Syvitski, J.P.M. 1994. Slope readjustment: a new model for the development of submarine fans and aprons: Geology, 22, 511-514.

Roussenov, V., Stanev, E., Artale, V., Pinardi, N. 1995. A seasonal model of the Mediterranean Sea general circulation. Journal of Geophysical Research, 100- C7, 13,515-13,538.

Royden, L.E., Patacca, E., Scandone, P. 1987. Segmentation and configuration of subducted lithosphere in Italy: an important control on thrust-belt and foredeep-basin evolution. Geology, 15, 714-717.

Schwartz, H., J. Sample, K. D. Weberling, D. Minisini, and J. C. Moore 2003. An ancient linked fluid migration system: cold-seep deposits and sandstone intrusions in the Panoche Hills, California, USA. Geo-Marine Letters, 23, 3-4, 340-350.

Shepard, F.P. 1933. Canyons beneath the Seas. Scientific Monthly, 37, 31-39.

Shepard, F.P. 1981. Submarine canyons: multiple causes and long-time persistence. AAPG Bulletin, 65-6, 1062-1077.

Shepard F.P. and Dill, R.F. 1966. Submarine canyons and other sea valleys. Rand McNally & Co., Chicago, 381 pp.

Siani G., Paterne M., Michel E., Sulpizio R., Sbrana A., Arnold M., Haddad G. 2001. Mediterranean Sea surface radiocarbon reservoir age changes since the Last Glacial Maximum. Science, 294, 1917-1920.

Stow, D.A.V., Faugères, J.C., Pudsey, C.J., Viana, A.R. 2002. Bottom currents, contourites and deep-sea sediment drifts; current state-of-the-art. In: Stow, D. A. V., Pudsey C. J., Howe J. A., Faugères J. C. & Viana A. Deep-water contourite systems: modern drifts and ancient series, seismic and sedimentary characteristics. Geological Society, London, Memoirs, 22, 191-208.

Taviani, M. 1978. Associazioni a molluschi pleistoceniche-attuali dragate nel Basso Adriatico. Bollettino di Zoologia, 45, 297-306.

Taviani, M., Freiwald, A., Zibrowius, H. 2005. Deep-coral growth in the Mediterranean Sea: an overview. In Freiwald, A., Roberts, M. (Eds.), Deep-water Corals & Ecosystems Springer-Verlag, 137-156.

Tramontana, M., Morelli, D., Colantoni, P. 1995. Tettonica plio-quaternaria del sistema sud-garganico (settore orientale) nel quadro evolutivo dell'Adriatico centro meridionale. Studi Geologici Camerti, 2, 467-473.

Trincardi, F. and Correggiari, A. 2000. Quaternary forced-regression deposits in the Adriatic basin and the record of composite sea-level cycles. In: Hunt D., Gawthorpe R. (Eds.), Depositional Response to Forced Regression. Geol. Soc., Spec. Publ., 172, 245-269.

Trincardi F., Correggiari A., Field M. E., Normark W. R. 1995. Turbidite deposition from multiple sediment sources: Quaternary Paola Basin (Eastern Tyrrhenian Sea). Journal of Sedimentary Research, 65 B, 469-483.

Trincardi, F., Asioli, A., Cattaneo, A., Correggiari, A., Langone, L. 1996. Stratigraphy of the late-Quaternary deposits in the Central Adriatic basin and the record of short-term climatic events. In: Guilizzoni, P., Oldfield, F.L. (Eds.), Palaeoenvironmental analysis of Italian crater lake and Adriatic sediments (PALICLAS project). Mem. Istit. It. Idrob., 55, 39-64.

Trincardi, F., Cattaneo, A., Correggiari, A., Ridente, D. 2004. Evidence of soft-sediment deformation, fluid escape, sediment failure and regional weak layers within the late-Quaternary mud deposits of the Adriatic Sea. Marine Geology, 213, 91-119.

Twichell, D.C and Roberts, D.G., 1982. Morphology, distribution, and development of submarine canyons on the United States Atlantic continental slope between Husdon and Baltimore Canyons. Geology, 10, 408-412.

Verdicchio, G. and Trincardi, F., in press. Short-distance variability in abyssal bed-forms along the Southwestern Adriatic Margin (Central Mediterranean). Marine Geology.

Verdicchio, G., Trincardi, F., Asioli, A., in press. Mediterranean bottom-current deposits: an example from the Southwestern Adriatic Margin. In Viana, A.R., Rebesco, M. (Eds.) Economic and palaeoceanographic importance of Contourite. Geol. Soc. Spec. Pub.

Vergnaud-Grazzini, C., Ryan, B. F., Cita, M. B. 1977. Stable isotopic fractionation, climatic change and episodic stagnation in the Eastern Mediterranean during the late Quaternary, Marine Micropaleontology, 2, 353-370.

Vilibic, I. and Orlic M. 2002. Adriatic water masses, their rates of formation and transport through the Otranto Strait. Deep-Sea Research I, 49, 1321–1340.

Weimer, P. 1991. Seismic facies, characteristics, and variations in channel evolution, Mississippi fan (Plio-Pleistocene), Gulf of Mexico, in Weimer, P., and Link, M.H., eds., Seismic Facies and Sedimentary Processes of Submarine Fans and Turbidite Systems: New York, Springer-Verlag, p. 323-347.

Wust, G. 1961. On the vertical circulation of the Mediterranean Sea. Journal of Geophysical Research, 66, 321-327.

FIGURE 1

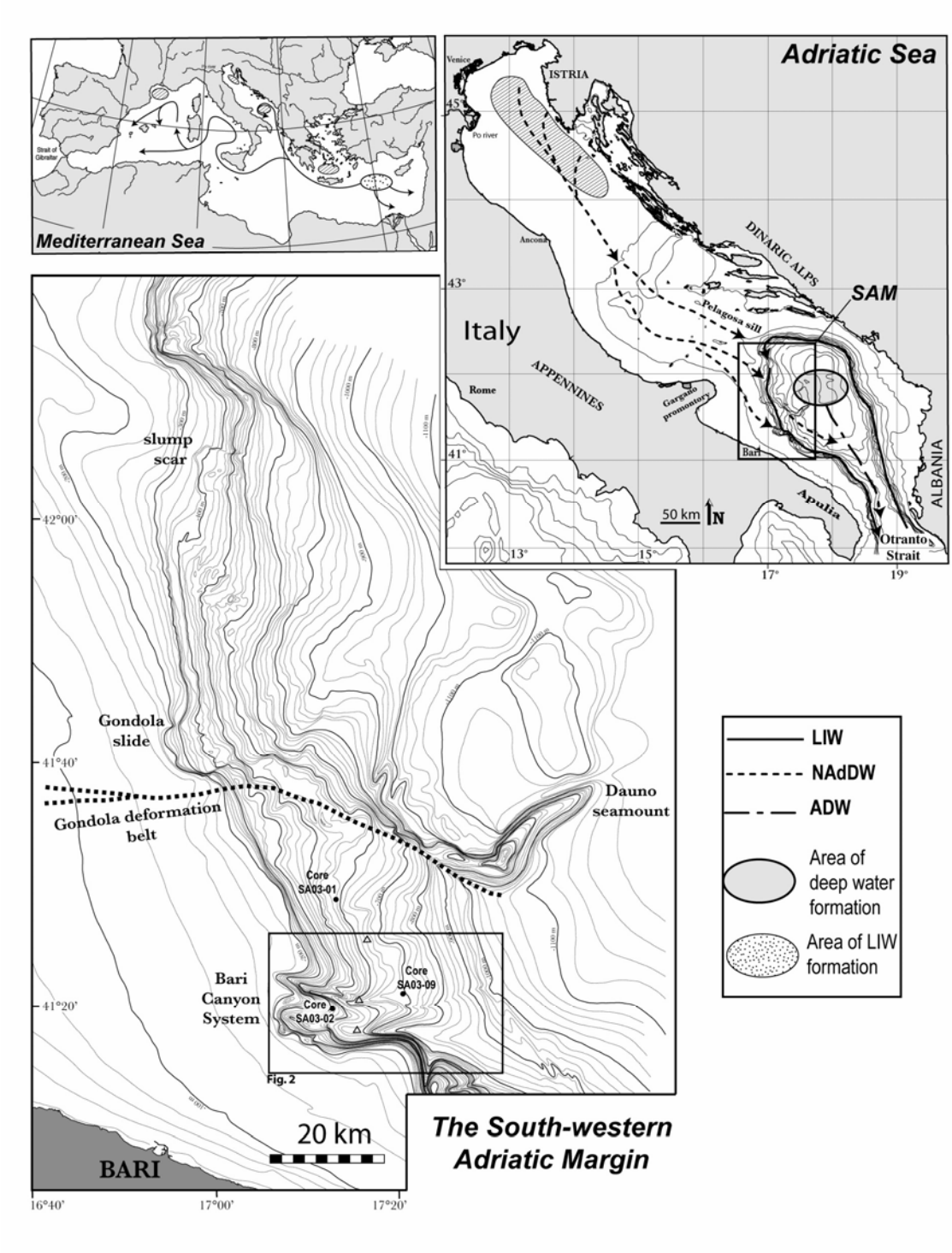
Mediterranean Sea
Strait of Gibraltar
Adriatic Sea
Venice
ISTRIA
Po river
Ancona
DINARIC ALPS
SAM
Pelagosa sill
Italy
APPENNINES
Rome
Gargano promontory
Bari
Apulia
ALBANIA
Otranto Strait
50 km
N
42°00'
41°40'
41°20'
13°
15°
17°
19°
slump scar
Gondola slide
Gondola deformation belt
Dauno seamount
Core SA03-01
Core SA03-09
Core SA03-02
Bari Canyon System
Fig. 2
20 km
BARI
16°40'
17°00'
17°20'
LIW
NAdDW
ADW
Area of deep water formation
Area of LIW formation
The South-western Adriatic Margin

FIGURE 2

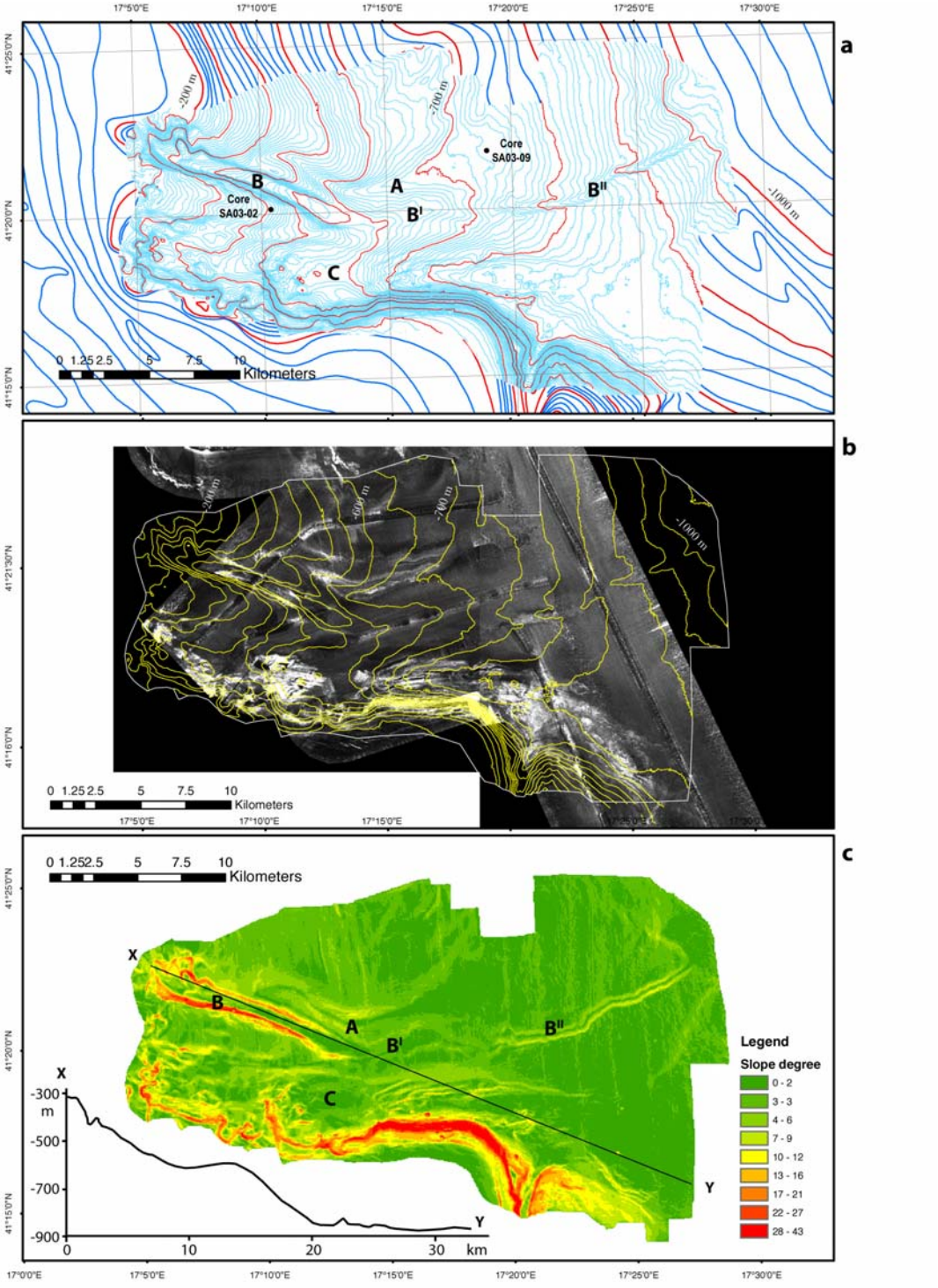

Figure 2

FIGURE 3

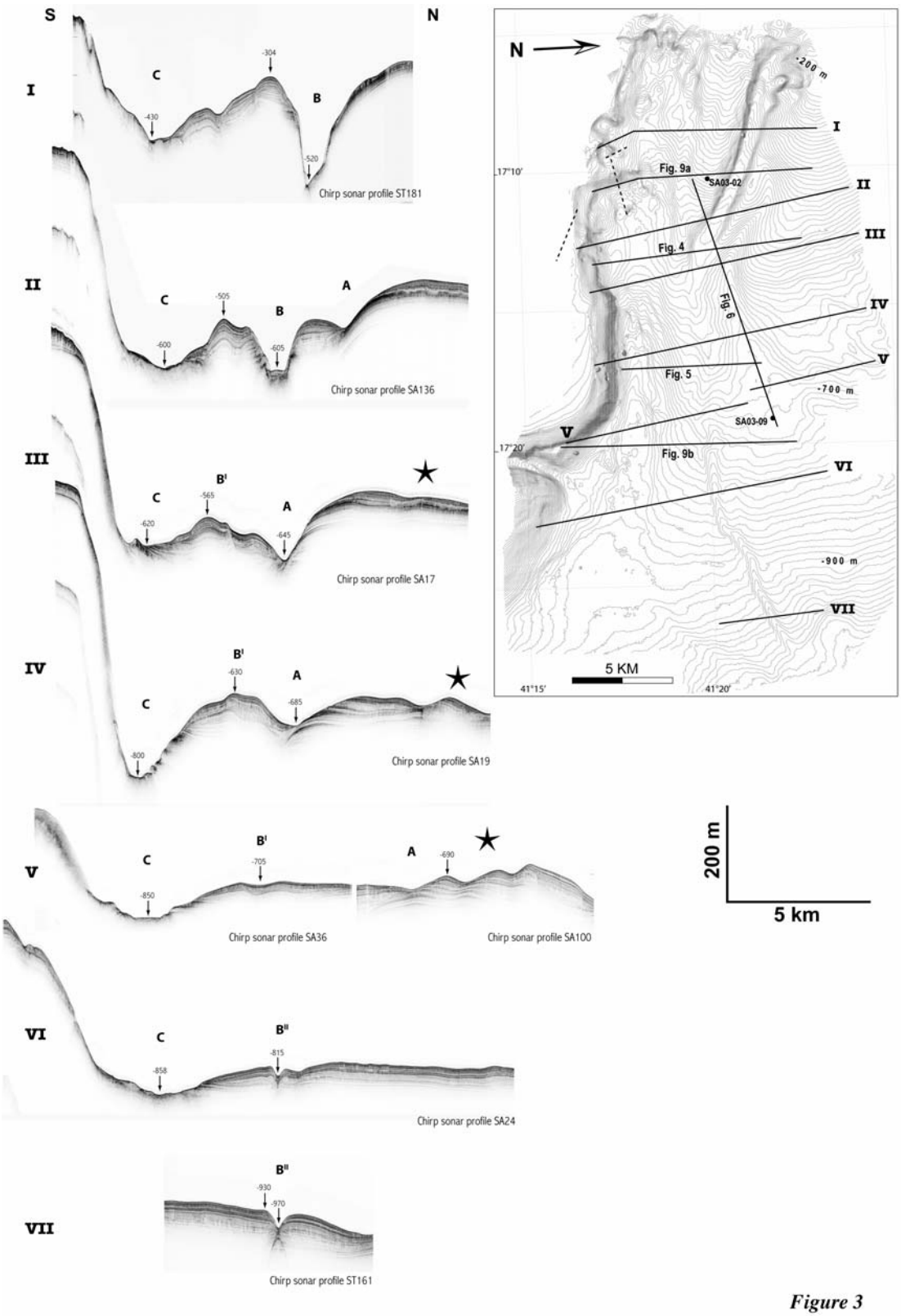

Figure 3

FIGURE 4

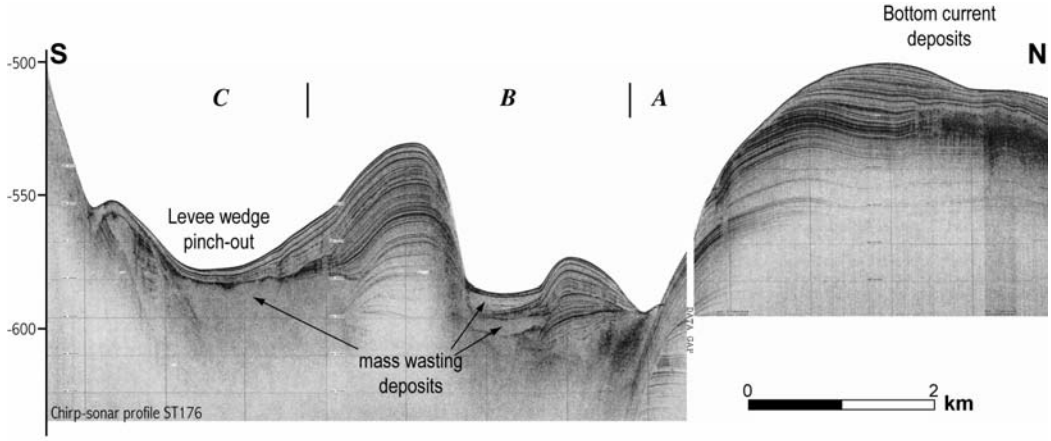

Figure 4

FIGURE 5

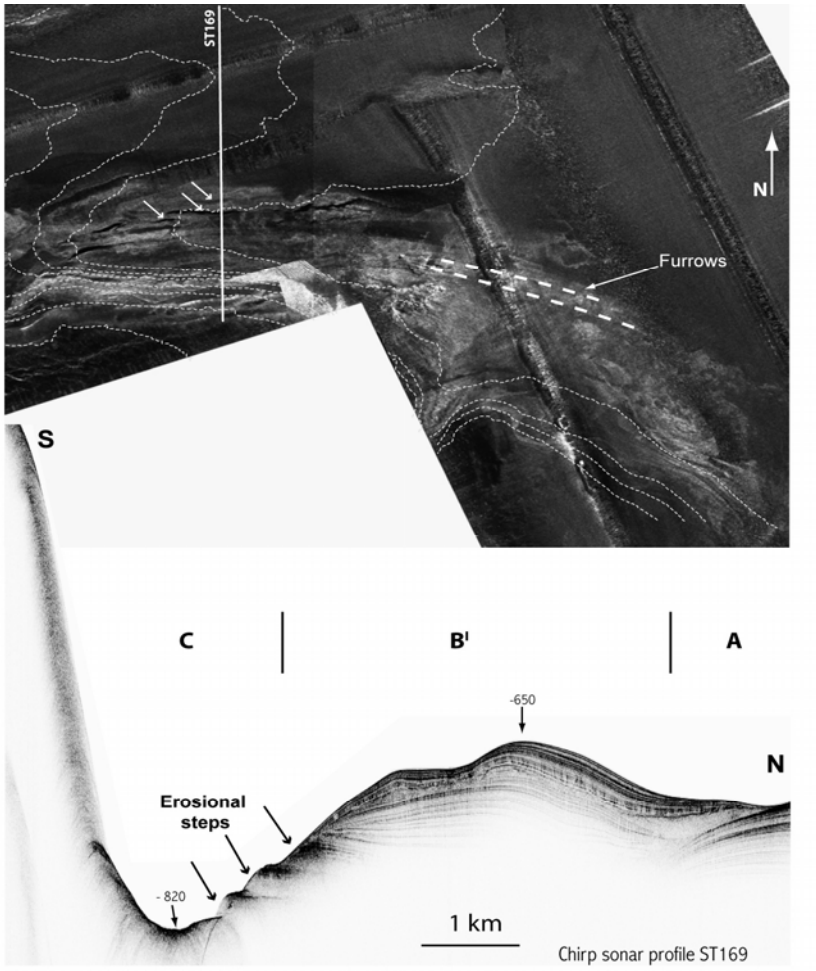

FIGURE 6

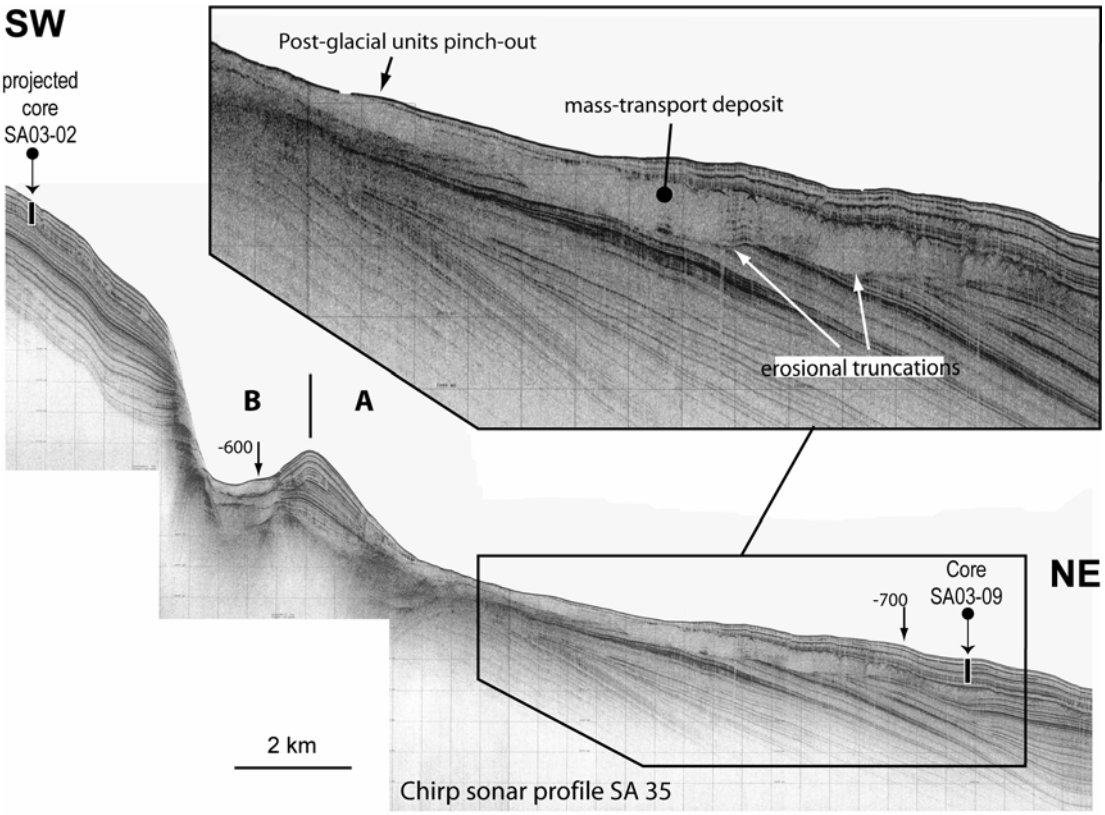

Figure 7

FIGURE 7/1

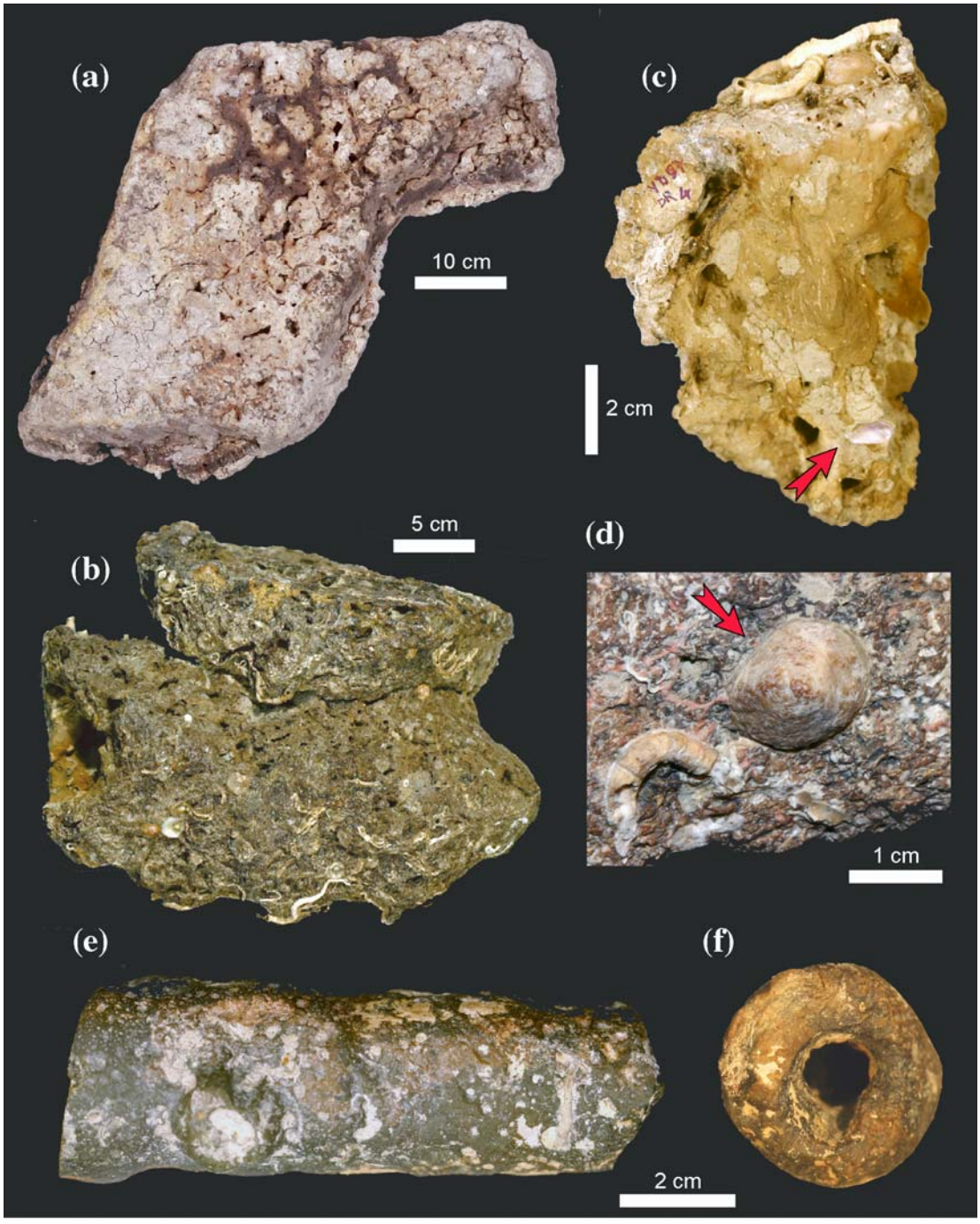

Figure 7/1

FIGURE 7/2

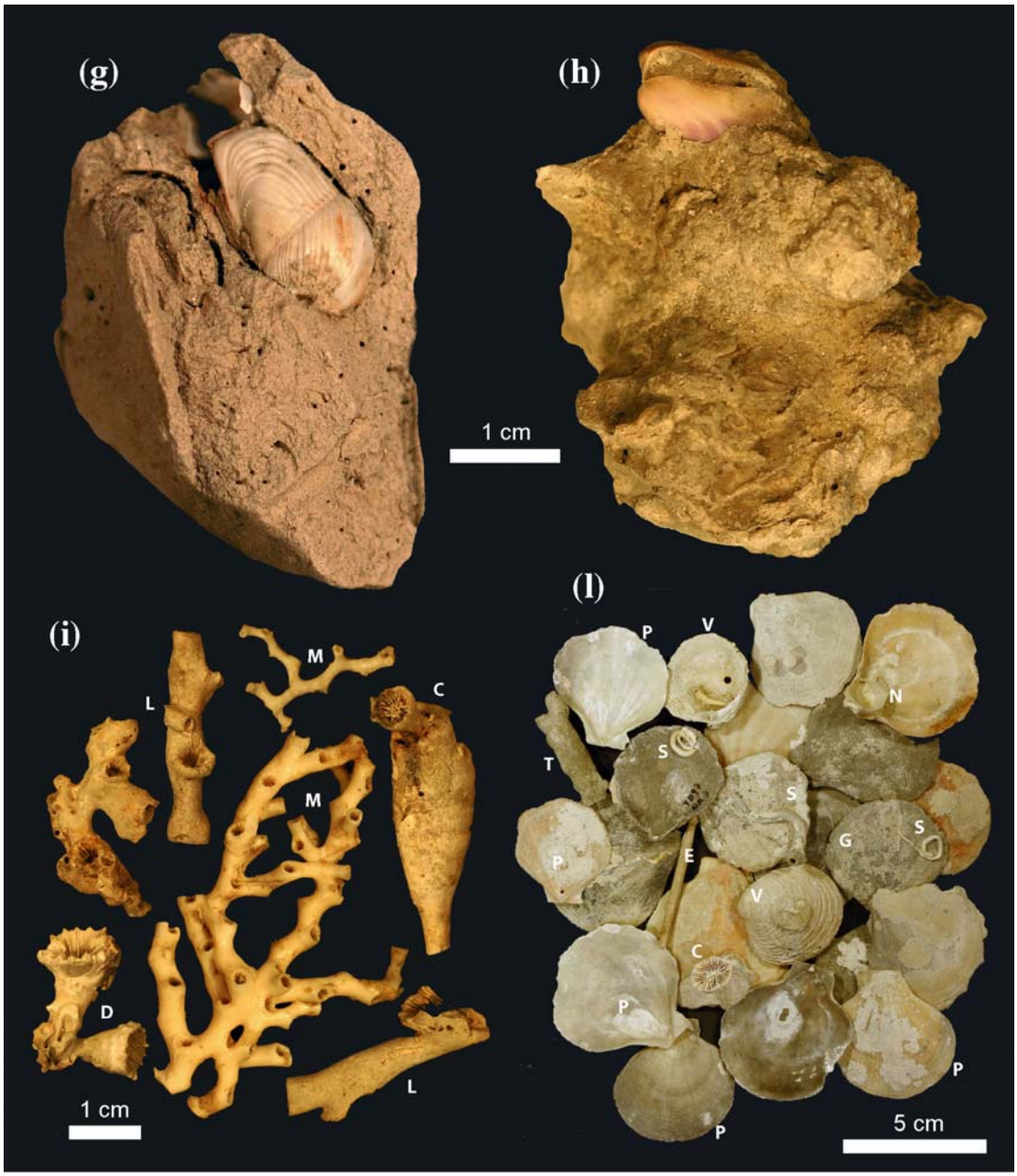

Figure 7/2

FIGURE 8

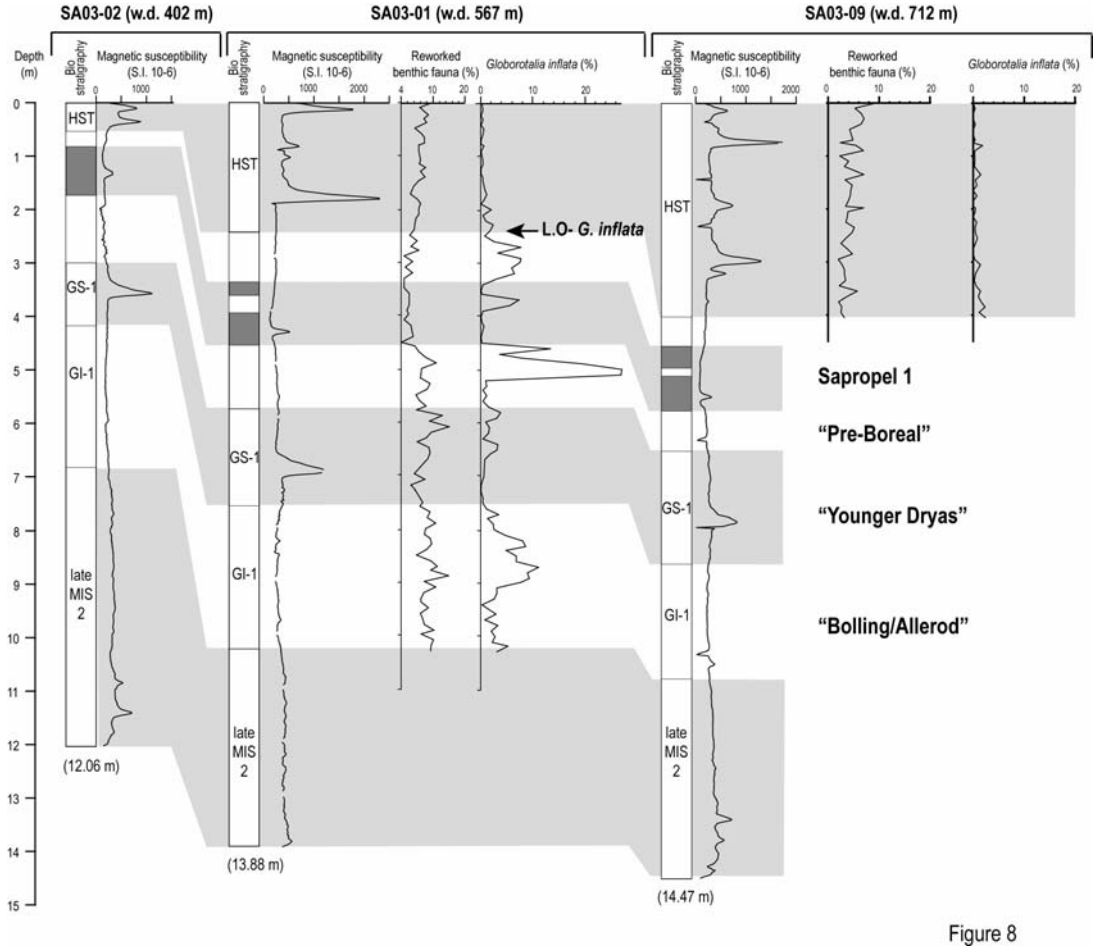

Figure 8

FIGURE 9

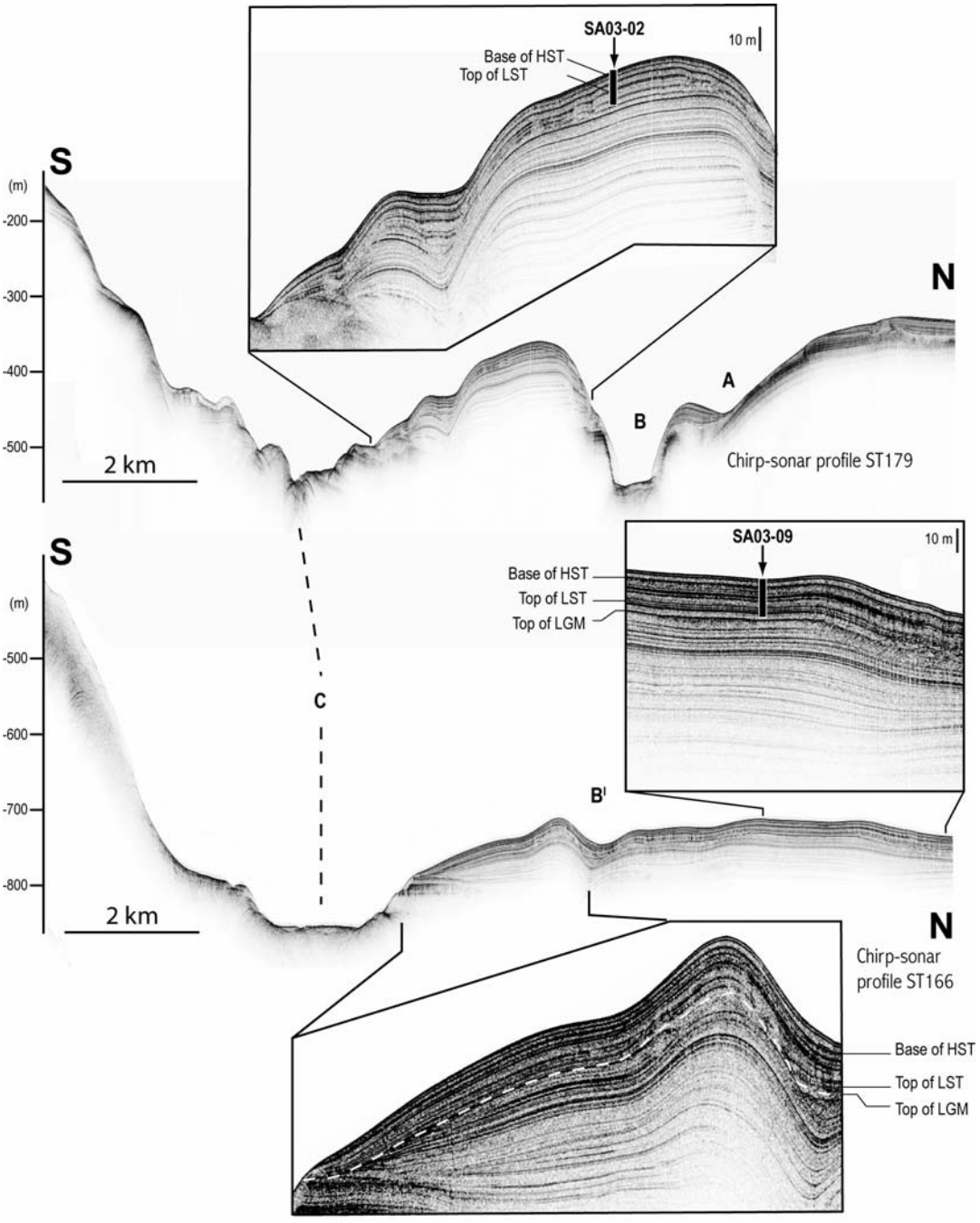

Figure 9

FIGURE 10

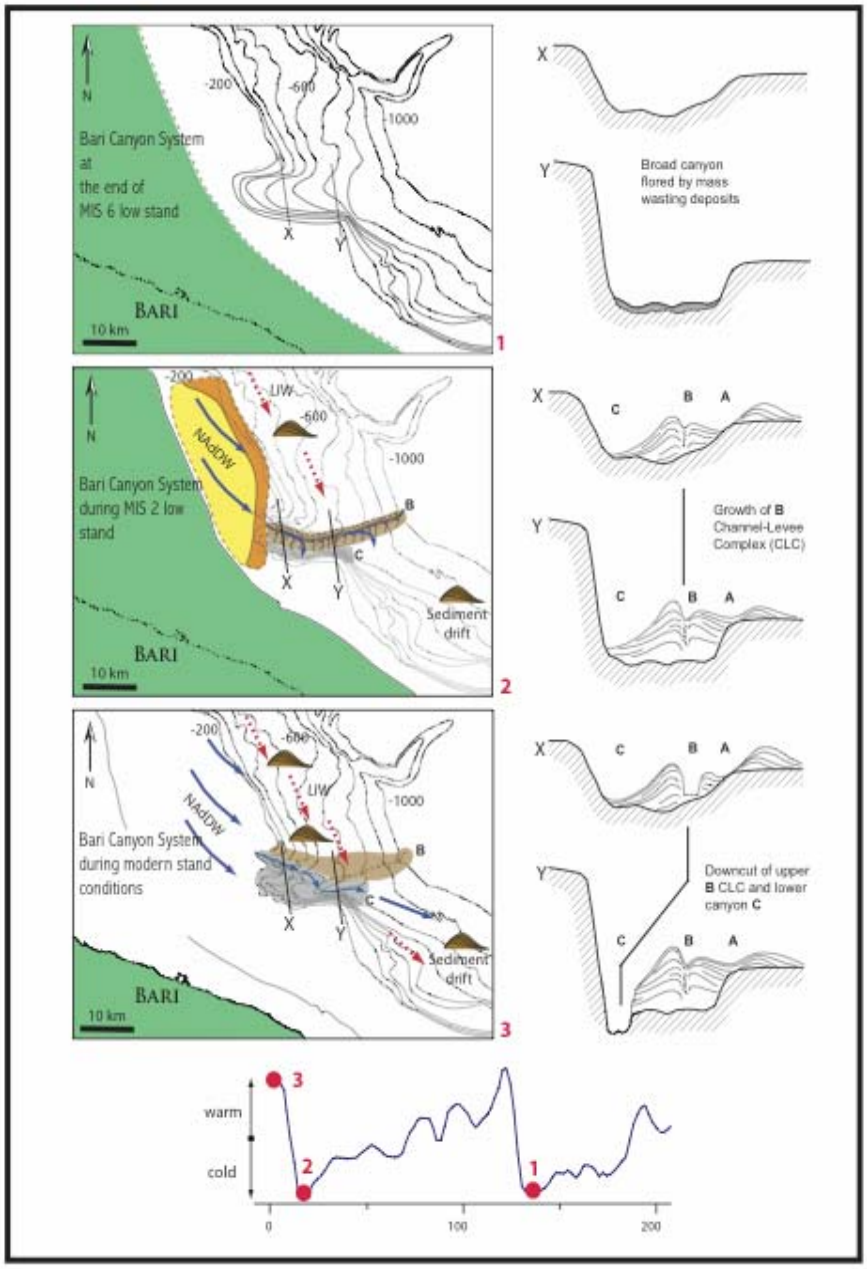

Figure 10

FIGURE 11

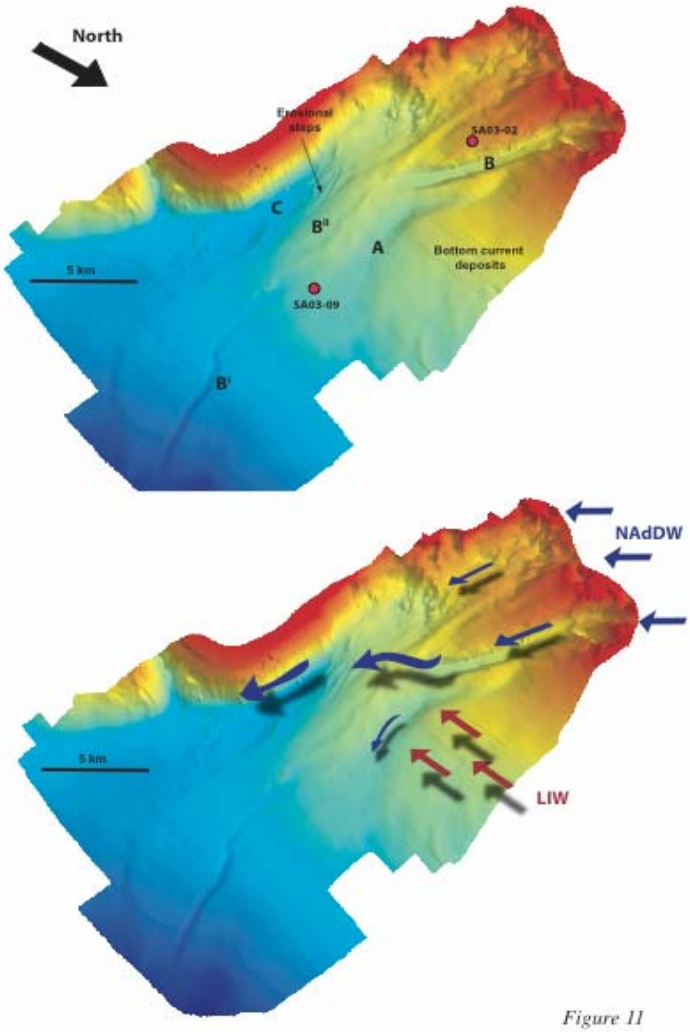

Figure 11

TABLE 1

TABLE

Cruise/Station	Lat N (start)	Lat N (end)	Long E (start)	Long E (end)	DEPTH m	GEAR
YD97-DR2	41° 18' 55	41° 19.0'	17° 05' 21	17° 05 '14	334	Dredge
YD97-DR3	41° 18' 51	41° 19' 13	17° 05' 27	17° 04° 47	316/246	Dredge
YD97-DR4	41° 18' 06	41° 17' 41	17° 11' 43	17° 09' 33	585/348	Dredge
YD97-DR5	41° 17' 41		17° 09' 32		347	Dredge
MAI 2-97 St A 4, even 109	41° 19' 02		17° 04' 95		250	Box corer
Ad 70/14	41° 22.2' N	41° 23.0' N	17° 05.6' E	17° 05.7' E	320/198	Dredge
Ad 70/29	41° 17.9'	41° 16.0'	17° 10.9'	17° 10.6'	300/180	Dredge

CHAPTER 4

This chapter consists of an article titled “ Morphologic variability of exposed mass-transport deposits on the Eastern slope of Gela Basin (Sicily Channel).” by Minisini D., Asioli A., Canu M., Trincardi F., Foglini F., accepted in “Basin Research”.

Title

MORPHOLOGIC VARIABILITY OF EXPOSED MASS-TRANSPORT DEPOSITS ON THE EASTERN SLOPE OF GELA BASIN (SICILY CHANNEL).

Short running title

Mass-transport deposits in Gela basin

Authors

Daniel Minisini, Istituto di Scienze del Mare, ISMAR-CNR, Via Gobetti 101, 40129 Bologna, Italy and

Dipartimento Scienze della Terra e Geologico-Ambientali, Univ. di Bologna, Via Zamboni 67, 40126 Bologna, Italy

Alessandra Asioli, Istituto di Geoscienze e Georisorse, IGG-CNR, C.so Garibaldi 37, 35137 Padova, Italy.

Marcello Canu, SnamProgetti, Via Toniolo 1, 61032 Fano, Italy.

Fabio Trincardi, Istituto di Scienze del Mare, ISMAR-CNR, Via Gobetti 101, 40129 Bologna, Italy.

Federica Foglini, Istituto di Scienze del Mare, ISMAR-CNR, Via Gobetti 101, 40129 Bologna, Italy.

Author to whom proofs/offprints requests should be directed:

Daniel Minisini,

Ismar-CNR, Via Gobetti 101, 40129 Bologna, Italy.

E-mail: daniel.minisini@ismar.cnr.it

ABSTRACT

The NE portion of Gela Basin in the Sicily Channel is affected by multiple slope failures originated during the late-Quaternary. Basin sequences show evidence of stacked acoustically-transparent and/or chaotic units, characterised by irregular upper surfaces, interpreted as mass-transport deposits. The seafloor morphology also shows evidence of both old, partially buried, as well as recent slide products. Two recent slides exposed at seafloor, only 6 km apart (Twin Slides), are similar in geomorphological parameters, age and multistage evolution. Multistage failure of Twin Slides evolved from mud flows, derived from the extensive failure of less consolidated post-glacial units, to localized slides (second stage of failure) affecting older and more consolidated materials. Although Twin Slides are very close to each other and have similar runout and fall height, they produced very dissimilar organization of the displaced masses, likely reflecting the distinct source units affected by failures. Integrating geophysical, sedimentological, structural and paleontological data, a detailed investigation was conducted to determine the size and internal geometry of this mass-transport complex, to explain the differentiated product and to shed light on its predisposing factors, triggers and timing.

A. INTRODUCTION

Many studies on submarine mass transport analysed extremely extensive and voluminous slide complexes (*e.g.*, Saharan Slide, Embley 1976; Storegga Slide, Bugge et al., 1988; Grand Banks Slide, Piper et al., 1988; Hawaiian Slides, Moore et al., 1994; Papua New-Guinea Slide, Synolakis et al., 2002) both because they are intriguing topographic features dominating the seascape of ocean margins and because they can have sudden, catastrophic and largely unpredictable consequences for coastal regions and human infrastructures. These giant mass-transport features commonly record multiple phases of failure and result in rather thick and complex deposits within which it proves difficult define the internal structure. More recent studies have focused on smaller-scale mass-transport features that can be defined at higher resolution, complementing the studies of giant slide complexes, thus enhancing the knowledge on transport processes, trigger mechanisms and timing of failure (*e.g.*, Canals et al., 2004; Schnellmann et al., 2005; Lee, 2005). However, even relatively small slide deposits often reveal multiple events making more difficult to evaluate the succession of processes and recurrence interval of failures. The advent of swath bathymetry and 3D seismic data increasingly document the wide variety in morphology and internal geometry of mass-transport deposits on continental margins (Locat & Lee, 2002; Posamentier & Kolla, 2003; Lee, 2005). By studying markedly different mass-transport deposits of similar age and comparable run out and volume, it is possible to discern the actual factors that determine these differences and to better understand the role of transport mechanisms.

The flanks of Gela Basin, in the Sicily Channel (Central Mediterranean) are recurrently impacted by failure through the Quaternary (Fig. 1). The seafloor

morphology shows evidence both of old, partially buried, and recent, typically exposed, slide scars and represents therefore an ideal site to discuss the origin of failures and their products (Fig. 2). The study focuses on mass-transport complexes that cover few squared kilometres and show relatively modest volume and extent compared to other slides on modern margins reported to be 2 or 3 orders of magnitude larger. However, the modest volume involved in the Gela Basin failures allows analyse with extreme accuracy the geometry, geomorphology and stratigraphy of the source units and of the resulting slide complexes. In particular, a detailed investigation using multibeam bathymetry, Chirp-sonar profiles and sediment cores determine failure phases of two recent exposed slides (called Twin Slides hereafter), confined by pre-existing antiforms and characterized by comparable run-out, fall height and age but markedly distinct organization of the resulting mass-transport deposit (Fig. 2).

A. GEOLOGICAL SETTING

Gela Basin is the most recent (Plio-Quaternary) foredeep of the Maghrebian fold-and-thrust belt and is filled with as much as 2.5 km of shallowing-upward marine deposits. In the north, the foredeep basin is loaded by Gela nappe, an accretionary *melange* that represents the southernmost compressive element of the Maghrebian fold-and-thrust belt (Argnani, 1990) (Fig. 1). The study area is north of the Sicily Channel rift zone that originated from oblique extension and created relatively deep pull-apart basins (Colantoni, 1974; Finetti, 1984). This rifting phase began in late-Miocene times and lasted through the Quaternary (Grasso, 1993).
Karstified breccias resting on Lower-Pliocene Trubi marls outcrop on the mainland northeast of the study area and record a phase of uplift during mid-Pliocene to Quaternary times affecting the entire southern rim of the Hyblean Plateau (Gardiner et al., 1993). This uplift nourished the westward-dipping Quaternary progradational wedges observed on the western flank of the Malta Plateau (Gardiner et al., 1993). The late-Pleistocene was characterized by intense vertical movements in the entire Sicily Channel (Catalano et al., 1993).

To the east, Gela Basin is bounded by the Malta Plateau which is the seaward counterpart of the Hyblean Plateau on mainland Sicily (Fig. 1). The Hyblean Plateau consists of Meso-Cenozoic carbonate rocks and volcanic deposits. The western limit of the Malta Plateau is a structural lineament that trends NNW-SSE and is accompanied by active faulting and deformation; stacked progradational deposits of Quaternary age on the western portion of the Malta Plateau have reduced thickness and appear separated by closely-spaced unconformities suggesting low subsidence rates (Gardiner et al., 1993; Max et al., 1993).

On the northern and western sides, Gela Basin is affected by tectonic deformation and by the emplacement of mass-transport deposits of large volume. One of the most extensive mass-transport deposits is the Gela Slide which occurs immediately above the tip of Gela nappe and covers 1500 km^2 (Trincardi & Argnani, 1990). This slide occurred around 600 ky BP, based on correlations to well sites reported in Di Stefano et al. (1993). Evidence of recent slope instability comes from seismic-reflection surveys in the southern portion of Gela Basin (Gardiner et al., 1993; Di Stefano et al., 1993).

Quaternary sediment accumulation rates in Gela Basin derive from ODP Site 963 on the northwestern side of Gela Basin in 470 m water depth (Fig. 1). The upper part of the section accumulated at an average rate up to 225 mm/ky (Emeis et al., 1996) and records the last deglaciation in 8 m of undisturbed sediment (Sprovieri et al., 2003). In the upper 100 m of section the ODP well encountered six graded ash layers and two intervals (35 m and 150 m below seafloor) characterized by a sharp decrease in shear strength corresponding to abrupt increases in porosity and water content (Emeis et al., 1996). This information cannot yet be precisely correlated to the study area but provides evidence of potential surfaces or sedimentary packages that can behave as weak planes and favour mass-failure processes.

In Gela Basin, instrumental and historical series (USGS data-base, http://neic.usgs.gov/neis/epic/epic.html) indicate a relatively low seismicity, if compared to other Mediterranean areas. However, since 1970 at least 7 epicenters between 2.8 and 4.2M where registered just in the area of the Twin Slides (Fig. 1) and may indicate a significant seismic frequency if extrapolated to longer intervals.

A. METHODS

The data set for this study has been collected during four cruises on board R/V Odin Finder (2000) and R/V Urania (2003, 2004 and 2005). The Chirp-sonar profiles use a 2-7 kHz sweep-modulated band width, equivalent to a 3.5 kHz profiler fired from 16 hull-mounted transducers and a 500-2000 msec recording length, depending on water depth. High-resolution bathymetric data derive from a 50-kHz Simrad EM-300 and a

RESON 8160 multibeam. A 30-kHz TOBI side-scan-sonar mosaic, processed at the "National Oceanographic Center, Southampton", offers information on seafloor back-scatter and morphology. Track-line positioning was based on D-GPS navigation, with an accuracy of circa 10 m, and transformed to geographic coordinates referred to the ED-50 datum. Five sediment cores were collected using a gravity corer. Sediment sub-samples for micropaleontology are 2 cm thick, at an average distance of 10 cm in each core. The sediment was dried at 50°C, soaked in water and then washed through a 0.063 mm mesh sieve. For the quantitative analysis each washed sample was split in aliquots (using a Jones-microsplitter) and counted up to 300 specimens both for the planktic and for benthic assemblages. This allows obtain also the concentration of the planktic and benthic foraminifera. Foraminifera appear generally well preserved and no dissolution trace is detectable at the optical stereomicroscope. The foraminifera-based eco-biostratigraphy relies on identification of (temporary) disappearance and (re-)occurrence of planktic species. In addition, variations in relative abundance of different planktic species allow identification of paleoenvironmental changes already defined in Central Mediterranean (Jorissen et al., 1993, Capotondi et al., 1999; Sbaffi et al., 2001; Asioli et al., 2001) and Sicily Channel (Vergnaud-Grazzini et al., 1988; Asioli et al., 2002; Sprovieri et al., 2003). AMS ^{14}C dating was conducted on 12 samples of planktic foraminifera sieved through a 0.180 mm mesh and cleaned with ultrasonic bath (Tab. 2).

A. RESULTS

B. **Late-Quaternary deposits**

The late-Quaternary depositional sequence of Gela Basin includes, from top to bottom (Fig. 3): 1) a progradational wedge that originated on the shelf since the modern sea level was attained, about 5,5 ky BP, as observed on many other Mediterranean margins (*e.g.*, Cattaneo et al., 2003; Labaune et al., 2005), 2) a faintly stratified transgressive drape that accumulated during the phases of drowning of the continental shelf driven by the post-glacial sea-level rise (information on the timing of deposition and short-term supply fluctuations during this interval is summarized in Cattaneo & Trincardi, 1999) and 3) a progradational wedge that formed in the upper-slope region during the last falling sea level leading to the glacial low stand. On the shelf and upper slope, down to 170 m water depth, this latter progradational wedge is cut by a pronounced erosional surface (ES1) that originated through subaerial exposure during the last-glacial sea-level lowstand and subsequent submarine erosion (Fig. 7). As observed on most Mediterranean margins (Tesson et al., 1990; Trincardi & Field, 1992; Ridente & Trincardi, 2002), this unconformity truncates older progradational deposits and the units above it include a combination of transgressive and high-stand marine deposits. Surface ES1 appears sharp and irregular due to the erosion of sediment units with variable strength (Fig. 7), as supported by Max et al. (1993) for the western Malta Plateau, where four unconformities with the same character as ES1 were identified and attributed to 100 ky sea-level low stands. The erosions generated by these surfaces expose over-consolidated materials (Skempto*n*, 1970). Toward south-west, ES1 cuts progressively older units that are likely more consolidated; in fact, moving north-westward along the contours, the ES1 surface becomes smoother and conformable, indicating that the underlying sediment did not undergo subaerial erosion and likely remained normal-consolidated (Fig. 7). Surface ES1 becomes conformable also toward the basin, representing the base of a drift unit, but can still be traced as a key reflector thus providing a clue for preliminary age assignments of the slope and basin sequences (Fig. 4). The basal marine onlap below the ES1 surface marks the base of the last glacial progradational wedge (Fig. 4A).

B. Seafloor morphology

The continental slopes of Gela Basin show evidence of widespread and recurrent mass failure events. Slide products from recent failures are obvious on bathymetric data (Fig. 2). In some cases, also older slide features, buried by younger deposits, are discernable on the bathymetry; however, they show reduced seafloor expressions as a result of the degradation of marginal headscarps, the infilling of sediment, the draping of the areas with rough topography and the overriding of successive mass-transport deposits (Fig. 2). Stacked failed masses occur also deeper in the stratigraphic section, on the lower slope and basin floor, and are commonly separated by draped units (Fig. 5). The edges of some of the buried failed masses generate on the seafloor prominent linear scarps up to 10 m in relief (white lines in Fig. 2).
Two sub-rounded scarps with a relief exceeding 100 m and dips up to 27° represent the source regions of two recent mass failures (Twin Slides: Northern and Southern) characterised by bathymetric bulges at the base of the slope and representing the main focus of this study. The upper-slope area between the two scarps defines a crescent-shape step, steeper (8°) than the surrounding area (3°); this depression reflects the buried headscarp of an older slide (termed Father Slide) that extends further southeast of the main study area and affected the progradational wedge formed during sea-level low stand (Fig. 2 and 4B).

West of the main study area, well-layered units are commonly disrupted by subvertical artefacts, accompanied by amplitude anomalies (Fig. 2 and 4); these features can be ascribed to fluid escapes where amplitude anomalies represent variable scattering and absorption of the acoustic signal probably due to a dense distribution of fractures that channelize fluids, as observed elsewhere by Gay et al. (2003) and Riedle et al. (2006). Where fluid-escape structures are recorded on seismic profiles, the overlaying seafloor appears irregular with local subrounded depressions interpreted as pockmarks (Fig. 2 and 4).

East of the main study area the slope veers to a north-south direction and presents a set of gullies generating a highly irregular seafloor morphology with steep erosional slopes exceeding 10° (Fig. 2). The gullies, up to 6-7 km long and 100 m deep, gradually disappear downslope where the gradients are lower and mass-transport deposits have accumulated (Fig. 5A). The eastern sector is also characterized by sediment drifts and slope-parallel moats up to 18 m deep, located just shallower than the gully heads, along the 200 m contour (Fig. 2 and 6). The growth of the drift deposits and moats are attributed to the peculiar spatial pattern of the local bottom currents. Bottom currents seem to be still active as suggested by the erosional upslope side of the moats. Drift deposits show growth faults resulting from differential compaction in rapidly-deposited units (as noted, among others, by Kenyon, 1987) and, on the downslope side, these sediment drifts are locally affected by mass failure of variable extent (Fig. 6).

B. **Syndepositional tectonic deformation**

Faulting occurs in the shelf-edge sub-parallel to the slope with reflector offsets on the order of 5 m; the main faulting activity occurred before the last sea-level rise, as post-glacial deposits appear to seal most of the faults that affect the last glacial progradational units (Fig. 3). A set of closely-spaced extensional faults (in the order of 100 m) occurs beneath Father Slide scar (Fig. 7). This set of faults can be traced into the evacuation zone of the Southern Twin Slide, also defining a local relief within the slide scar (Fig. 2 and 10A). Additional evidence of vertical offsets surrounds the headscarps of the Twin Slides, but it is not clear whether they are tectonic faults or failure planes related to successive slide events (Fig. 4A).

Folding occurs on the upper slope and particularly at the shelf edge, where several small-scale anticlines affect Quaternary units, especially in the eastern sector (Fig. 2). Folding occurred before the deposition of the late-Pleistocene and Holocene units that tend to onlap and smooth their morphologic expression. Antiforms related to pre-existing structural highs laterally confine the heads and upper portions of the Twin Slides (Fig. 2 and 8).

B. **Twin Slides**

Swath bathymetry data of the area show two exposed mass-transport deposits which emanated from two distinct slide scars on the north-eastern continental slope of Gela Basin (Fig. 2). Twin Slides have rounded headwalls composed of several smaller individual scarps, between 200 m and 500 m water depth. The slide headwalls dip around 16° and locally become as much as 27°, while, at the base of the slope, the displaced masses dip 1.5°-4.5°. The volume of sediment involved in each slide is calculated by multiplying each source area (5,7 km^2 Northern Slide; 3,6 km^2 Southern

Slide) by the average height of the failed section that is estimated restoring the regional slope to its pre-failure configuration (*ca*. 100 m). Therefore, the combined volume of the two slides is in the order of 1 km^3. The runouts of Northern and Southern Slides are 11,7 and 10,4 km, respectively. Maximum collapse heights, taken from the shallowest headscarp to the deepest area reached by the lobes, are 490 and 550 m (Tab. 1).

Twin Slides	**headwall water depth (m)**	**headwall length (km)**	**maximum headwall height (m)**	**evacuation area (km^2)**	**evacuated volume (km^3)**	**accumulation area (km^2)**
Northern	230	8.5	250	5.7	0.57	15.5
Southern	200	6.3	290	3.6	0.36	14.4

Twin Slides	**(H) total fall height (m)**	**(R) runout distance (km)**	**H/R ratio**	**maximum thickness of failed masses (m)**	**average slope steepness of failed masses**
Northern	490	11,7	0.0418	100	2.5°
Southern	550	10,4	0.0528	30	3.5°

Tab. 1. Geomorphological parameters of Twin Slides

The lateral extent of the Twin Slides reflects the pre-failure stratigraphy or the physical confinement of local bulges and antiforms that control the evacuation and accumulation areas. Northern Slide is located on the edge of the buried and irregular Father Slide scar (Fig 2) and affects planar, well-layered sediment units. Southern

Slide occupies a depressed sinformal area confined by two antiforms (Fig. 10A). Both accumulation zones of Twin Slides are partly confined by local seafloor bulges.

The accumulation zone of Northern Slide presents a morphologic bulge at the seafloor extending 7 km downslope and 1,5 km in width (Fig. 2 and 9A). Mapping of the topographic bulge displays an arcuate upslope-concave front down to 700 m water depth with a typical relief of 12 m above the adjacent seafloor. This bulge is the expression of a failed mass that extensively remolded pre-existing mass-transport deposits, as documented by the Chirp-sonar profiles (Fig. 10C) and by the swath bathymetry images of the modern seafloor (Fig. 2). The chaotic-transparent unit characterizing the subsurface of this bulge thins basinward and allow define an undisturbed reflector 75 m below the seafloor in 630 m water depth **(**Fig. 11), just basinward of the restored maximum run out of a pre-existing blocky slide deposit imaged on swath bathymetry (Fig. 2). The appearance of the 75 m-deep reflector coincides with the occurrence of arcuate parallel ridges at the seafloor, clearly imaged also on side-scan sonar mosaics (Fig. 9B). The spacing between these ridges is about 200 m and becomes tighter basinward, where it decreases to about 50 m. At 700 m water depth, chaotic-transparent facies end abruptly the deep-reaching deformation of the slope sediment and grade into a wedge-shaped transparent deposit where pressure ridges disappear at seafloor (Fig. 11).

The accumulation zone of the Southern Slide consists of large blocks that exceed 10 m in relief and appear up to 800 m long and 150 m wide (Fig. 2 and 9A). Typically the largest blocks are not randomly distributed but appear rather elongated along the direction of downslope transport. Blocks are separated from each other on the order of 50-100 m and are likely composed of consolidated sediment. The maximum runout distance of these blocks is 9,1 km; their size decreases downslope and the largest

elongated blocks occupy the central part of the slide deposit; no outrunner blocks were detected suggesting that uniform values of seafloor friction characterize the entire slide area.

The observation of a dissimilar organisation of the failed deposits of Twin Slides together with the study of regional seismic-stratigraphic correlations indicates that the source areas of Twin Slides affected different stratigraphic units, although the headscarps are only 6 km apart. Both slides involve the progradational deposits that formed since the last interglacial (Eemian) (Fig. 3). However, seismic-stratigraphic correlations across the upper slope suggest that Northern Slide emanated from younger and less consolidated units, while the Southern Slide involved older and likely more consolidated deposits within the same progradational sequence (Fig. 10A). Moreover, deposition likely occurred at increasing rates at progressively lower sea level, thus enhancing underconsolidation of the younger units in the progradational wedge. An acoustically-transparent facies with a smooth upper surface thinly draped appears beneath Twin Slides (Fig. 10C – 1st stage of failure) and extends further basinward (Fig. 2) suggesting a multistage evolution of the mass-transport complex.

B. **Sediment cores and stratigraphic data**

Biostratigraphic analysis of five sediment cores (Fig. 2), accompanied by 12 AMS ^{14}C dates (Tab. 2), allow: 1) litho- and chrono-stratigraphic correlations between the failure areas and the adjacent slope; 2) estimation of lateral variations in sediment-accumulation rates within the late-Quaternary deposits; 3) determination of the ages

of Holocene failure in the Twin Slide areas. In core P9 the following intervals were recognized, from bottom to top (Fig. 12):

1. cm 770-620. The last glacial maximum is characterized by the typical cold-water planktonic association (Pujol & Vergnaud Grazzini, 1995 and references therein), composed of *Neogloboquadrina pachyderma*, *Globorotalia scitula*, *Globigerina quinqueloba*, and *Globigerina bulloides*. The benthonic association is largely dominated by infaunal species adapted to low-oxygen conditions; this association includes: *Brizalina dilatata*, *Brizalina alata*, *Brizalina aenariensis* and *Bolivina albatrossi*. Forms typical of higher oxygen levels appear in low frequencies (*Cassidulina laevigata carinata*, *Hyalinea balthica*). This interval can be referred to GS2 (Greenland Stadial 2 defined in Bjorck et al., 1998; Asioli et al., 1999).

2. cm 620-510. This is a complex interval characterized at the base by the abrupt increase of *Globigerinoides ex gr. ruber* that reaches a relative abundance greater than 70 %, followed by a discontinuous decrease and a secondary peak before the complete disappearance of this species at the top of the interval; other species indicative of warm-surface waters are (in lower frequencies): *Orbulina, Globigerina rubescens* and *Globigerinoides tenellus*. *Globorotalia inflata* and *Globorotalia truncatulinoides* appear in this interval. This rapid warming of surficial waters likely reflects an increased seasonal contrast (*G. inflata*), not evident in interval 1. The benthonic association is dominated by *B. dilatata*, but species indicative of increasing availability of oxygen (*Gyroidinoides* spp) and of organic matter (*Uvigerina mediterranea*) are present. This interval can be referred to GI 1 (Greenland

Interstadial 1 of Bjorck et al., 1998; Asioli et al., 1999) and corresponds to the Bolling-Allerod interval of Mangerud et al. (1974).

3. cm 510-440. A cold reversal during the overall post-glacial warming trend is indicated by a typical cold-water assemblage: *N. pachyderma*, *G. bulloides*, *G. quinqueloba*, *G. scitula*, as observed in other Mediterranean regions; the relative abundance of *G. truncatulinoides* and *G. inflata* diminishes dramatically compared to interval 2; *G. ex gr. ruber* is almost absent with the exception of a moderate increase in the uppermost part of the interval. The benthonic association indicates a decrease of the oxygen concentration in the bottom waters, as well indicated by the increase of *Bolivina* spp and *Brizalina* spp (note the peak of *B. albatrossi*), while the persistence of *C. laevigata carinata* along with *H. balthica* and *Cibicidoides pachyderma* records intervals of relative increase of oxygen levels during parts of the year. This cold interval corresponds to GS 1 (Greenland Stadial of Bjorck et al., 1998; Asioli et al., 1999) and to the Younger Dryas defined by Mangerud et al. (1974).

4. cm 440-370. A new and substantial increase of *G. ex gr. ruber* occurs, as observed in other Mediterranean cores (Capotondi et al., 1999; Asioli et al., 2001). A similar trend is also shown by *G. inflata* and *G. truncatulinoides*. These elements are indicative of increased deep-water ventilation. The substantial decrease of *N. pachyderma* and *G. quinqueloba* reflects also the increase of surface water temperatures accompanied by increased seasonal contrasts. The benthonic association show substantial similarities to that of the underlying GI 1 interval. This interval can be referred to the Pre-Boreal of Mangerud et al. (1974).

5. cm 370-160. Highest frequency of *G. ex gr. ruber, G. aequilateralis, G. praecalida, G. rubescens* and *G. tenellus*. *Orbulina* increases in frequency compared to the underlying interval. This interval, characterized by benthonic associations indicative of limited oxygen availability, is the equivalent of Sapropel S1, a distinctive feature of the Holocene Mediterranean stratigraphy, recording the last episode of water stagnation and increased surface water productivity. This interval likely reflects a change in the hydrological balance, at the scale of the entire Mediterranean basin, and contains a break during which ocean bottom ventilation was re-established as indicated (cm 230-305) by the occurrence of *G. truncatulinoides* and *G. inflata*, the abundance of *G. sacculifer* that testifies an increased seasonal contrast and the occurrence of *H. balthica* and *C. pachyderma* that testify a substantial re-oxygenation of bottom waters. This break was recognized elsewhere in the Mediterranean region (Rholing et al., 1997; Ariztegui et al., 2000). The lower part of the Sapropel S1 (S1a of Rohling et al., 1997) is characterised by very weak seasonal contrast and decreased water turbidity (peak of the simbiont-bearing species *G. sacculifer*; Ariztegui et al., 2000). In this core the minimum concentration of benthonic foraminifera of Sapropel S1a reflects a relative abundance of deep infaunal species (*Praeglobobulimina* and *Chilostomella oolina*).

6. cm 160-0. Re-appearence of *G. truncatulinoides*, progressive increase of *G. inflata*, and consistent occurrence of species indicative of warm surface waters (*G. ex gr. ruber, Orbulina, G. aequilateralis, G. praecalida, G. rubescens* and *G. tenellus*). A substantial decrease of *G. inflata* (around 100 cm) marks the timing of maximum flooding of the margin at the end of the late-Quaternary sea-level rise, as observed on other Mediterranean margins (Asioli, 1996; Trincardi et al., 1996; Correggiari et al.,

2001). A pronounced peak of *G. sacculifer* between 70 and 90 cm, records a late-Holocene relatively drier interval with more oligotrophic surface likely occurring during the Bronze age. The benthonic association reflects intervals of substantial increase of the organic-matter flux (*Uvigerina* spp, *B. marginata*), and consequent decrease in the oxygen content within the bottom waters, alternated to intervals of increased oxygenation (*C. laevigata carinata*, *H. balthica*, *C. pachyderma*).

# Lab.	Sample	Material	^{14}C yr BP	±	Cal age ranges
CAMS # 75685	P08 cm 309-312	mixed planktic forams	7920	50	8158 - 8451
CAMS # 75686	P08 cm 342-347	mixed planktic forams	9750	50	10363 - 10711
CAMS # 75687	P08 cm 409-412	mixed planktic forams	9570	60	10198 - 10519
CAMS # 75688	P08 cm 434-439	mixed planktic forams	10440	40	11195 - 11734
CAMS # 75689	P09 cm 79 - 82	*G. inflata*	3540	40	3190 - 3517
CAMS # 75690	P09 cm 109-112	mixed planktic forams	4280	40	4116 - 4486
CAMS # 75691	P09 cm 189-192	mixed planktic forams	6040	40	6260 - 6539
CAMS # 75692	P09 cm 259-262	mixed planktic forams	7700	40	7957 - 8256
POZ # 16158	P09 cm 377-378	mixed planktic forams	9340	120	9668 - 10406
POZ # 16159	P09 cm 397-398	mixed planktic forams	9910	110	10506 - 11108
CAMS # 75693	P09 cm 519-522	mixed planktic forams	10870	40	12009 - 12407
CAMS # 75694	P09 cm 609-612	mixed planktic forams	12460	40	13721 - 13996

Tab. 2. AMS 14-C and calibrated ages in years BP 2Δ. based on planktic foraminifera. Calibration is based on Calib 5.0.2 Radiocarbon Calibration Program on line (Stuiver, M., and Reimer, P.J., 1993, Radiocarbon, 35, 215-230) (marine sample = 100%, Calibration data set: Marine04 ^{14}C according to Hughen et al., 2004). The ΔR (reservoir) was selected from the Calib 5.0.2 database for the Sicily Channel. The calculated weighted mean ΔR value is 71 with a standard deviation of 50.

The same climato-stratigraphic events defined in reference core P9 were recognized also in the other cores documenting that the sediment thickness accumulated during each stratigraphic interval varied substantially, depending on the core location, the distance from sediment sources and the effects of oceanographic circulation (Fig. 13). Core P8, retrieved on the outer-shelf, shows a very expanded Pre-Boreal interval resting on a hiatus surface where the entire GI-1 (Bolling/Allerod) and GS-1 (Younger Dryas) intervals are missing. The same core reached the MOIS 2 (Marine Oxygen Isotope Stage 2), including the last glacial maximum, and the top of the underlying MOIS 3, separated by a marked discontinuity interpreted as the core equivalent of the regional erosional unconformity that originated during last glacial sea-level low stand (ES1 in Fig. 4A). Core P3, retrieved on the lower slope, just outside the slide area, reached the top of MOIS 3 but no hiatus occurs between MOIS 2 and MOIS 3, even if core P3 displays lower accumulation rates compared to core P9. Therefore, the surface between MOIS 2 and MOIS 3 is here interpreted as the correlative conformity of ES1. Twelve dates were obtained for critical stratigraphic intervals through AMS ^{14}C determinations (Tab. 2 and Fig. 13). The ages obtained confirm the interpretation based on the micropaleontological study. The cores collected in the Gela Basin have rather uniform muddy lithology. Two exceptions are: core P4 and core P7 (Fig. 2). Core P4, basinward of the Northern Twin Slide, reached a thinly buried acoustically-transparent unit that correlates with 1st stage of failure of Figure 11; this core includes a level with rip-up mud clasts and vegetal remains overlain by thin muddy and silty layers, thus suggesting a mud-flow deposit overlaid by turbidites. Core P7 reached over-consolidated stiff deposits overlain by late-Holocene mud and ascribed to a large slumped mass that indented Northern Slide scar.

A. **DISCUSSION**

B. **Stages of failure**

The basin-wide Father Slide may have occurred during an interval of high tectonic activity documented by the closely-spaced faults beneath and adjacent to its scar (Fig. 7 and 14). This tectonic activity may relate to the intense vertical movements that affected the entire Sicily Channel during the Late-Pleistocene and reported in Catalano et al. (1993). In particular, seismic-stratigraphic correlations document that Father Slide scar cross cuts the base of the last glacial wedge and therefore occurred during the last-glacial low stand and is partially filled by late-glacial onlapping units and post-glacial sediment-drift deposits (Fig. 8).

The lower extensive transparent unit beneath the Twin Slides is interpreted as a mud-flow deposit recording a first stage of failure based on morphologic, seismic-stratigraphic evidence and sediment cores (Fig. 10C and 13). In the Southern Slide area this deposit pinches out against the base of the slope in a water depth that is at least 100 m shallower than the base of the slide scar. This evidence implies that failure took place in two distinct stages. During the first stage, the mudflow spread laterally along the slope base; during the second stage, further down-cutting of the slide scar resulted in large slide blocks of less runout that characterise the modern seafloor (Fig. 14). In Northern Slide, organization of second-stage mass-transport deposit suggests the occurrence of two distinct failure events whose time gap is geologically speaking negligible: a blocky slide and a slump that remoulded layered

seafloor units and the underlaying first-stage mud-flow deposit (Fig. 2, 10C and 14). On both Twin Slides, down-cutting of second stage of failure was related to retrogressive failure and downslope-eroding mass transport, as documented on initiation of other mass-wasting events (*e.g.*, Galloway et al., 1991; Pratson et al., 1994; Pratson & Coakley, 1996).

B. **Time constraint**

Based on the dated cores in the study area, estimated sediment accumulation rates during the late-Quaternary post-glacial interval are in the order of 300 mm/ky and are consistent with data from ODP site 963 (Emeis et al., 1996; Sprovieri et al., 2003) on the north-western side of Gela Basin (Fig. 13). If Twin Slides were relatively old (last glacial maximum or older) such sediment flux would result in the progressive burial of the slide scars and in the smoothing of their sharp edges. The evidence of clearly marked scars and the lack of detectable drapes on extensive proximal portions of mass-transport deposits suggest that the Twin Slides are very recent (late Holocene) features (Fig. 9A).

The Twin Slide scars clearly cut ES1 and its correlative conformity as well as the overlying Holocene drape, indicating that failures occurred during the modern sea level high stand, probably during very recent times (Fig. 4A). Seismic-stratigraphic correlations document also that the first-stage mud-flow deposit is coeval in both areas later impacted by the Twin Slides (Fig. 10B,C). Biostratigraphic and magnetic-susceptibility correlations to cores retrieved from adjacent undeformed regions suggest that the mud flow deposited during the formation of Sapropel S1a, about 8,5 Cal. ky BP (Fig. 13). In core P4 this interval is affected by the presence of mud balls, vegetal remains and recycled foraminifera species from slightly older beds.

B. **Coefficient of friction and remoulding of seafloor**

The apparent coefficient of friction in both Twin Slides (estimated by the ratio of maximum collapse height and runout distance – Lipman et al., 1988) is higher than in

most known large-scale submarine mass-transport deposits and it is almost included in the field of subaerial slides (Fig. 15). It is likely that remoulding of seafloor sediment implied loss of momentum and decreased runout, as documented by the highly erosional base of the mass-transport deposits and the lack of outrunner blocks (Fig. 9A and 10C). Physical factors that may have led to rework the seafloor sediment include load-induced dewatering and shear stress, exerted by the downslope-moving mass, as suggested on other continental margins (*e.g.*, Prior et al., 1984; Trincardi & Normark, 1989); a possible additional factor in Gela Basin is the lateral confinement by antiforms that forced downslope movement along a confined path minimising lateral spreading (Fig. 8). On the other hand, the first-stage mud-flow deposit (MF in Fig. 15) presents a coefficient of friction similar to most submarine mass-transport deposits. This mud flow involved dominantly the post-glacial units laying above ES1, more surficial and less compacted compared to deeper sediment units mobilized by Twin Slides (Fig. 14). Where the post-glacial deposits are organized in sediment drifts, they achieve significant thicknesses that, when mobilized, provide sufficient material for the generation of extensive mud-flow deposits (Fig. 2). The mobilization of material with distinct apparent coefficients of friction well compares with the results of McAdoo et al. (2000) and Huhnerback & Masson (2004) who generalize that failures of softer material travel further than failures involving stiffer, more consolidated sediment.

B. ***Twin Slides***

In Gela Basin, where gradients are relatively low, as in the western area, slopes are affected by extensive fluid escape from thick buried mass-transport deposits (Fig.

5B). Where gradients are relatively high, as in the eastern area, recurrent failure prevents accumulation of thick unstable deposits, and thus generates only relatively small mass-transport deposits with low erosional capability (Fig. 5A and 6). Potential slopes for voluminous slides capable of remoulding the seafloor present thick deposits of fine-grained sediment (Klaucke & Cochonat, 1999) and slope gradients that can sustain this weight until oversteepening leads to failure. This is the case of the central area where the Twin Slides occur.

C. *Distinct source units, distinct failed masses.* Twin Slides are only 6 km apart, have comparable volumes, depths and headscarps, are coeval and follow a common first stage of failure. Northern Slide affected well-layered sediment units and slid on a 70 m-deep glide plane (Fig. 4A) mobilizing a thick section whose movement remoulded the pre-existing seafloor and produced pressure ridges, distally (Fig. 9B). Southern Slide affected a faulted unit, older and likely more consolidated compared to the evacuation zone of Northern Slide (Fig. 10A and 14) and generated a 30 m-thick blocky mass-transport deposit (Fig. 10C). The blocks likely reflect the over-consolidation of this faulted unit, partially eroded during the last sea-level falling stage; the base of Northern Slide scar does not reach this older faulted unit that becomes progressively more deeply buried toward north-west (Fig. 10A). Hence, the dip of the underlying sequences is a key element controlling the mechanical properties of the failed units and determining the distinct organization of the resulting deposits (Fig. 10 B).

C. *Processes.* The combined seafloor morphology and seismic stratigraphy suggest that the topographic bulge of Northern Slide resulted from a slumped mass that moved maintaining a high shear strength. A similar process has been proposed in

other large- and small-scale mass-transport deposits (Schnellmann et al., 2005; Cartwright et al., 2005). The slumped mass impacted onto the middle slope at the main drop in slope splitting its kinetical energy into a vertical, load vector and a horizontal, shear vector (Fig. 16). Loading and bulldozing of basin floor sediment in the direction of movement generated an embricated thrust system with associated pressure ridges at the seafloor. The progressively decreasing spacing and relief of the pressure ridges towards the tip of the deposit suggests that the thrusts formed through progressively thinner sediment slices overriding the seafloor ahead and partially dissipating their energy (Fig. 16). Fluid escape features that pervasively dissect the sediment involved in the thrust system likely facilitated the formation of the thrusts. The mass movement froze, forming the bulge tip, when the most basinward thrust reached a pre-existing antiform (Fig. 11). Beyond the bulge tip deformation is reduced evidencing the low kinetic energy left in the distal part of the downslope moving mass to overcome friction forces. Thrust systems associated with failure deposits are widely recognized in the literature. *Marr et al.* (2001) describe imbricate sediment slices forming in laboratory mass-transport experiments; Shanmugam et al. (1988), document duplex-like features in outcrops of Arkansas attributed to mass-transport processes; Posamentier & Kolla (2003), mentioned pressure ridges as indicative of thrust faults within submarine debris-flow deposits; Martinez et al. (2005), Lastras et al. (2006) and Moscardelli et al. (2006), described compressional features in slump complexes similar to those observed in Gela Basin.

The overconsolidated source unit of Southern Slide displays closely-spaced faults whose average distance compares to the width of the largest slide blocks in the proximal depositional area suggesting that block disintegration during the first phase of transport was minimal (Fig. 16). The blocks scoured the seafloor down to the lower

slope creating irregular incisions and mobilizing seafloor sediment thereby increasing the volume of the mobilized material (Fig. 10C). Through their basinward movement, the blocks underwent progressive deformation that reduced their internal shear strength, favouring their partial disintegration (Fig. 16). Similar examples of block disintegration into mass flow come from several other slope settings (*e.g.*, Prior et al., 1982; Hampton et al., 1996; Lastras et al., 2002). Southern Slide affected simultaneously also a thick depocenter infilling the scar of the older Father Slide scar, likely less consolidated than the faulted unit below (Fig. 10B). This younger material spread around the rafted blocks partially smoothing the topography and suggesting a relatively low shear strength (as noted also by Boe et al., 2000, in the North Sea). A similar double component of the failed material (*i.e.*, basal flow derived from the sequence infilling of Father Slide scar and rafted blocks derived from over-consolidated units below) was recognized on other continental slopes by Gee et al. (1999) and Lastras et al. (2005).

B. Failures and sea level

It is possible that the deeper mass-failure deposits of the study area are correlative to the most recent failure masses observed east of Gela Slide and attributed to debris-flow processes driven by slope readjustment (Trincardi & Argnani, 1990). This correlation would indicate a phase of generalized slope instability affecting the entire Gela Basin and provide an indirect measure of the largest potential impact of mass-failure processes in the area. Comparable thick and basin-wide mass-failure deposits are documented during the last sea-level low stand in the Western African margin (Rothwell et al., 1992), in the Central Adriatic basin (Trincardi et al., 2004), in the

SW-Iberian margin (Lebreiro et al., 1997), in the Western Mediterranean (Rothwell et al., 1998; 2000), and in the South Adriatic margin (Minisini et al., 2006).

Since the last-glacial low stand, several mass-transport deposits accumulated in Gela Basin (*i.e.*, Father Slide, during last-glacial interval; extensive mud flow, ca. 8,5 ky BP; Twin Slides in very recent times - Fig. 14) evidencing the high recurrence of failure along the margin and suggesting a complex relationship among failures and sea-level change. Sequence stratigraphic models assumed that margin failure dominates during sea-level falls and low stands (*eg*., Posamentier & Vail, 1988), but increasing dating of Quaternary slides and improved dating precision and accuracy suggest that frequent failure characterises also intervals of rapid sea-level rise (*e.g.*, Weaver & Kuijpers, 1983; Bugge et al., 1988; Trincardi et al., 2003). It is possible that rapid sea-level rises of large magnitude (in the order of 100 m) bring about a significant build up of pore pressure. For instance, the 8,5-ky mud flow in the study area may coincide with a melt-water pulse successive to Melt Water Pulse 1b, interval of high rate of relative sea-level rise during the last deglaciation (Fairbanks, 1989; Bard et al., 1996). Our findings in Gela Basin confirm that repeated generations of failure may occur during intervals of relative sea-level rise and high stand, although their extent is typically more reduced compared to mass-failure events occurred during the last-glacial low stand.

B. **Predisposing factors and triggers**

C. *Pre-existing slide scars*: the occurrence of large slide scars in the upper slope define areas of markedly increased slope gradient (Fig. 2) and facilitate the temporary deposition of local sediment depocenters during and after the last glacial maximum. The presence of depocenters on high slope gradient increases the likelihood of sediment failures in the area.

C. *Sedimentation rates:* relatively high rates of sediment accumulations characterised the study area through the Quaternary (Emeis et al., 1996; Sprovieri et al., 2003; Fig. 13). Rapid accumulation of fine-grained low-permeability sediment can result in a buildup of overpressure and undercompaction favouring instability (Cartwright, 1994; Klaucke & Cochonat, 1999; Masson et al. 2002). Geologically-rapid releases of pore fluids from geopressured compartments can be a factor leading to increased sediment instability. The extensive occurrence of buried mass-failure deposits may act as an overpressured unit for the rapidly-accumulating overlying glacial and postglacial deposits, thus originating weak layers that may represent a key factor for sediment instability. Testing this hypothesis and the role of potential weak layers located in deeper stratigraphic levels, however, requires long cores and geotechnical investigations as well as deeper-penetration seismic surveys.

C. *Weak layers:* ODP Site 963, positioned on the northwestern side of Gela Basin in 470 m water depth, encountered two layers characterised by a sharp decrease in shear strength 35 m and 150 m below the seafloor associated with an abrupt increase in porosity and water content (Emeis et al., 1996). The occurrence of this relatively-shallow and several other potential weak layers (including five thick ash layers in the

first 100 m) cannot yet be precisely correlated to the study area. However, if one or more of such relatively-shallow potential weak layers correlates to the study area, it may occur in deeper subsurface levels and extend to areas of greater bathymetric gradients and therefore favour mass failure of the overlying and otherwise stable stratigraphic units (Fig. 8B).

C. *Gas-charged sediments:* seismic-reflection profiles provide local evidence of acoustic masking possibly induced by bubble-phase gas in the sediment column (Fig. 5B). High sediment accumulation rates in the area may have been accompanied by high production/accumulation of organic matter resulting in the production of biogenic gas. If present, the expansive pressure of bubble-phase gas can reduce the shear strength in the sediment while disrupting the sediment structures, as observed among others by Prior et al. (1982) and Sultan et al. (2004).

C. *Tectonic factors:* faults and anticlines influenced the location of failures; in particular, the suite of faults beneath the scar of Father Slide provides a set of closely-spaced mechanical discontinuities (Fig. 7), and anticlines crests partially confine the Twin Slides and other small-scale collapses in the eastern sector (Fig. 2). It seems that such faults and folds have been active during the late-Quaternary even though additional deeper-penetration seismic-reflection data are required to map such faults and understand their origin and activity.

C. Triggers: *the relevance of seismicity on the instability of submarine slopes has been widely recognized (*e.g.*, Prior & Coleman, 1984; Edwards et al., 1993; Keefer, 1994; Hasiotis et al., 2002; Imbo et al., 2003). Earthquakes have two main effects on slope sediments: 1) they generate horizontal and vertical acceleration stresses, producing cyclic loading on the deposits and leading to the degradation of the sediment stiffness; 2) they increase the pore pressure in the sediment reducing its shear strength (Hampton et al., 1978; Duperret et al., 1995; Sultan et al., 2004).*

*The continental margin of Gela Basin is in a seismically active region seaward of Gela nappe, a compressive element of the Maghrebian fold-and-thrust belt (Argnani, 1990), and north of the Sicily Channel rift zone (Finetti, 1984; Catalano et al., 1993; Max et al., 1993). In Gela Basin, the contemporaneous Twin Slides and the evidence of multiple sets of mass-transport deposits at several stratigraphic levels (Fig. 8B and 10C) require a recurrent trigger. In this case, seismicity is the most plausible trigger mechanism (*e.g.*, Syvitski & Schafer, 1996; Schnellmann et al., 2002). It is conceivable that the multiple phases of failure reflect repeated seismic shocks affecting the upper slope and outer shelf in Gela*

*Basin. Instrumental and historical series indicate a reduced seismicity of the area compared to other Mediterranean areas (Fig. 1, http://neic.usgs.gov/neis/epic/epic.html). However, knowledge of the historical seismicity may not take full account of the maximum possible earthquake magnitude and spatial distribution of the epicenters for a variety of reasons: 1) past epicenters located at sea are exceedingly difficult to infer; 2) the distribution of historical earthquake onland is biased by the location of ancient settlements; 3) the interval for which observational data are available may not include the extreme events for any given seismogenetic feature. Indeed, the epicenters registered in the area in the last few decades (*i.e., *2 shocks up to 4.2M, since 1970) would represent a significant frequency of seismic shocks if extrapolated to longer intervals. If the entire post-LGM interval is considered, 60 shocks in 1000 years would lead to some 2000 shocks during the post-glacial interval.*

A. **CONCLUSIONS**

Based on the seafloor morphology, seismic stratigraphy and core data available in Gela Basin, the following points are key:

1) The margin of Gela Basin underwent repeated and widespread failures during the last glacial-interglacial cycle as suggested by several stacked mass-transport deposits and numerous paleoscars of variable size. The largest basin-wide failure affected the margin during the last-glacial low stand (Father Slide); coeval failures affected the slope during the Holocene (Twin Slides).

2) Both Twin Slides occurred at least in two successive failure stages clearly affecting the late-Pleistocene and Holocene depositional units: the first mobilized the recently-deposited drape of the post-glacial depositional sequence and occurred close to the break in the formation of Sapropel S1, 8,5 Cal. ky BP; the second stage involved older (last glacial) more lithified materials and resulted in the formation of frontal thrusts (Northern Twin Slide) and slide blocks (Southern Twin Slide) which underwent limited run-out compared to the previous event. The evidence of clearly marked scars and the lack of detectable drapes on extensive proximal portions of the associated mass-transport deposits suggest that the Twin Slides are very recent.

3) Even if Twin Slides occurred very close to each other, with similar runout and fall height, they appear rather dissimilar in geomorphology and architecture of the resulting mass-transport deposits. This marked differentiation reflects the distinct stratigraphic units affected by failure: Northern Slide emanated from younger and less consolidated progradational units while Southern Slide involved older deposits, possibly more consolidated, from progradational units deposited during the last two glacial cycles. Therefore, the margin architecture is important not only in defining the location of potential weak layers but also in dictating which units can be mobilised.

4) Seismicity is the most plausible trigger for failures considering the multiple sets of coeval mass-transport deposits in the area and instrumental series of earthquakes registered just in the area of Twin Slides.

Acknowledgements: We thank G. Lastras, N. Mitchel and W. R. Normark for their precious reviews and comments on this paper. We also thank ISMAR colleagues and the NOC TOBI Team, Southampton, for their work and Michaele Kashgarian (Centre

for Accelerator Mass Spectrometry, Livermore, CA) and Thomasz Goslar (Poznan Radiocarbon Laboratory, Poland) who run the AMS 14C samples. EU-funded projects EUROSTRATAFORM (EVK3-CT-2002-00079), “EASSS III-TOBI side-scan sonar” (HPRICT199900047), and HERMES (G0CE-CT200551112341) supported this research. This is ISMAR (CNR) – Bologna contribution number 1512.

A. **FIGURE CAPTIONS**

Fig. 1. Location of the Gela Basin in the Sicily Channel, Central Mediterranean (bathymetric contour intervals are every 100 m – from GEBCO data base). Land topography derives from SRTM data base. Open circles are historical earthquakes recorded since 1970 (USGS data base), with diameter proportional to four ranges of magnitude (up to 2.8, 3.2, 4.2, 5.3, respectively). Solid circles represent earthquakes of unknown magnitude. The hand indicates the multibeam swath bathymetry shown in Fig. 2.

Fig. 2. Above: multibeam shaded relief of the study area in Gela Basin (artificial sun angle from NW, red is 180 m, dark blue is 1000 m); black lines locate Chirp-sonar profiles and white circles locate sediment cores shown in the following figures; the central sector of the map shows two prominent exposed slides (Twin Slides). Below: bathymetric map (contours every 20 m) with outline of main mass-transport depoits discussed in the text and isopach contours (in ms) of Twin Slide complex. Northern Twin Slide forms lateral ramps where it overrides a pre-existing mass-transport deposit; Southern Twin Slide shows larger blocks and a smoother seaward transition.

Fig. 3. Chirp-sonar profile showing the late-Quaternary depositional sequence in Gela Basin; the pronounced erosional unconformity ES1 formed during last sea-level low stand driven by 100 ky-glacial cycles. The deposits beneath ES1 record a prolonged interval of sea-level fall and low stand. Faults and gentle folds are sealed by post-glacial deposits.

Fig. 4. Chirp-sonar profiles (location on Fig. 2) showing (A) Northern Slide scar cutting through last-glacial and post-glacial units, dated through sampled cores; upslope of the slide scar minor reflector offsets can be observed (arrows); note the landward pinchout of the last glacial wedge where erosional surface (ES1) truncates deposits recording the last sea level fall**.** (B) Father Slide scar filled by 60 m-thick deposits including (lower portion) repeated mass transport deposits and (upper portion) a post-glacial sediment drift migrating upslope above surface ES1.

Fig. 5. Chirp-sonar profiles (location in Fig. 2) showing (A) stacked mass-transport deposits which tend to fill and smooth pre-existing seafloor irregularities; good acoustic penetration shows flat tops and conformable bases suggesting mud flow origin; the deepest mass-transport deposit (open circles) represents a basin-wide unit ubiquitous beneath the basin. (B) Well-layered units disrupted by subvertical artefacts ascribed to fluid escape and rooted into a buried failed mass; note depression (pockmark) and irregular seafloor where fluid escape is more intense.

Fig. 6. Chirp-sonar profile across the eastern slope of Gela Basin showing mounded sediment drift deposits between 190 m and 340 m water depth; growth faults occur where the drift deposit is thickest; the seafloor erosion of the upslope side of the moat suggests a recent activity of bottom currents. Buried and exposed, mass-transport features, affect the downslope side of the drift deposit. Profile location is in Fig. 2.

Fig. 7. Chirp-sonar profile showing that Southern Slide cuts the fill of Father Slide scar (profile location in Fig. 2). The unit affected by closely spaced faults beneath

Father Slide is mobilised only by Southern Twin Slide because further north the unit is more deeply buried.

Fig. 8. Chirp-sonar profile (located on Fig. 2) crossing the evacuation zones of Southern (A) and Northern (B, left) Slides; (A) in-situ relief associated with the faulted progradational unit beneath Father Slide scar (see also Fig. 7); (B) two close and coeval mass-transport deposits (highlighted in black) that slid along a common glide plane; note fluid-escape structures rooted on top of these buried failed masses and absent beyond the extent of these mass-transport deposits; these slope-parallel profiles document that both Twin Slides are laterally confined by antiforms.

Fig. 9. (A) Swath bathymetry of Twin Slides showing similar evacuation zones but significantly dissimilar organization of failed masses; multibeam bathymetry has vertical exaggeration of 10x, artificial sun angle is from N, red is 180 m, dark blue is 1000 m water depth; AA' and BB' show location of sketch profiles in Fig. 10B. (B) TOBI side-scan sonar image documents the distribution of pressure ridges in Northern Slide and blocky deposits in Southern Slide.

Fig. 10. (A) Slope parallel Chirp-sonar profile (location in Fig. 2) showing regional stratigraphic setting with deposits of last falling stage becoming progressively younger and likely less consolidated toward northwest (left); note differential deposition and erosion of post-last glacial sediment units above regional unconformity ES1. (B) Simplified sketch of geomorphology and stratigraphy along AA' and BB' key sections crosscutting the Twin Slide area (location on Figs. 2 and 12). (C) Chirp-sonar profile showing stacked acoustically-transparent deposits and a thinly draped

mud-flow deposit (1st stage of failure), remobilized by more recent slide deposits (2nd stage of failure), characterized by exposed reliefs with diffraction hyperbolae and erosional bases. The 2nd stage of failure led to the time-equivalent Northern and Southern Twin Slides. Reflectors overlaying acoustically-transparent deposits appear disturbed by closely spaced vertical artefacts that indicate possible fluid escape. The bulge in the centre of the image reflects a pre-existing relief inherited from a buried mass-transport deposit to the NW (left).

Fig. 11. Chirp-sonar profile (location in Fig. 2) showing the base of Northern Slide along its distal accumulation zone; the diffraction hyperbolae at the seafloor correspond to pressure ridges seen on TOBI mosaics (see Fig. 9B); a gentle antiform occurs beyond the tip of the slide deposit and fluid escape structures affect the layered units that bury older mass-transport deposits**.**

Fig. 12. Quantitative biostratigraphic diagrams from core P9, retrieved in 609 m water depth between, and just outside, Northern and Southern Twin Slides (location on Fig. 2). Main planktic (upper chart) and benthic (lower chart) foraminifera species trace the most significant stratigraphic intervals, consistent with the 8 available AMS ^{14}C dates; abundances are expressed in percentage; first top column represents concentration (number of specimens per gram of dry sediment).

Fig. 13. Core correlations, relying on magnetic-susceptibility wiggle matching and biostratigraphic determinations, provide information on the relative timing of the mass-failure events in the area. LH: late Holocene; Gs peak: G. sacculifer Bronze Age peak; mfs: maximum flooding surface (marking the end of the last post glacial sea-

level rise); S1: Sapropel 1 (including also break in sapropel deposition, a diagnostic stratigraphic character recognised in many Mediterranean cores); PB: pre-Boreal; GS-1: Glacial Stadial 1; GI-1: Glacial Interstadial 1. ES 1 (lower dashed line) coincides with the hiatus on P8 (core retrieved on the upper slope) and becomes conformable on P3 (core retrieved in the basin). Dates from AMS ^{14}C analyses are positioned by red circles. Upper dashed line indicates timing of the 1st stage of failure (mud-flow event).

Fig. 14. Simplified stratigraphic scheme of main stages of failure in the central sector of Gela Basin. The last stage is differentiated in two schemes: the upper one shows location of main cores along Northern Slide; the lower one shows how Southern Slide mobilizes older units beneath Father Slide scar, that are deeply buried in Northern Slide. Thicknesses of mass-transport features and stratigraphic units are not in scale.

Fig. 15. Logaritmic diagram showing the maximum runout distance versus the maximum height (modified from Lipman et al., 1988 and Trincardi & Normark, 1989). Black dots represent examples from the Mediterranean base-of-slope regions. The deposits of Northern (N) and Southern (S) Slides indicate low apparent coefficients of friction, compared both to the mud-flow deposit (MF) and to other known cases of submarine slides on continental margins.

Fig. 16. Simplified cartoon showing mass-transport processes of Twin Slides. An embricated thrust system with associated pressure ridges formed in Northern Slide while blocky deposits surrounded by less consolidated material characterise Southern Slide. The succession of events in each slide has no detailed chronological constraints and no implication is assumed on the possibility of correlating failure phases between the two slides.

A. REFERENCES

ARGNANI, A. (1990) The strait of Sicily Rift Zone: foreland deformation related to the evolution of a back-arc basin. *Journal of Geodynamics*, **12**, 311-331.

ARIZTEGUI, D., ASIOLI, A., LOWE, J.J., TRINCARDI, F., VIGLIOTTI, L., TAMBURINI, F., CHONDROGIANNI, C., ACCORSI, C. A., BANDINI MAZZANTI, M., MERCURI, A.M., van der KAARS, S., MCKENZIE, J.A. & OLDFIELD, F. (2000) Palaeoclimate and the formation of sapropel S1; inferences from late Quaternary lacustrine and marine sequences in the central Mediterranean region. *Palaeogeography, Palaeoclimatology, Palaeoecology*, **158**, 215-240.

ASIOLI, A. (1996) High resolution foraminifera biostratigraphy in the Central Adriatic basin during the last deglaciation: a contribution to the PALICLAS Project. In: *Palaeoenvironmental Analysis of Italian Crater Lake and Adriatic Sediments*, (Ed. by F. Oldfield and P. Guilizzoni), *Memorie dell'Istituto Italiano di Idrobiologia*, **55**, 197–218.

ASIOLI, A., TRINCARDI F., LOWE J.J., & OLDFIELD F. (1999) Short-term climate changes during the Last Glacial-Holocene transition: comparison between Mediterranean records and the GRIP event stratigraphy. *Journal of Quaternary Science*, **14**, 373-381.

ASIOLI, A., TRINCARDI, F., LOWE, J.J., ARIZTEGUI, D., LANGONE, L. & OLDFIELD, F. (2001) Sub-millennial climatic oscillations in the Central Adriatic during the last deglaciation: paleoceanographic implications. *Quaternary Science Reviews*, **20**, 33-53.

ASIOLI A., TRINCARDI F., CONSOLARO C., ARIZTEGUI D. & CANU M. (2002) High resolution paleoceanographic record for the last deglaciation in the Central Mediterranean: integration with the sequence stratigraphy to detect major intervals of the sea-level rise. EMMM'2002 Congress (Environmental Micropaleontology, Microbiology and Meiobenthology), September 1-6, Vienna, Austria, 45-46.

BARD, E., HAMELIN, B., ARNOLD, M., MONTAGGIONI, L., CABIOCH, G., FAURE, G. & ROUGERIE, F. (1996) Deglacial sea-level record from Tahiti corals and the timing of global meltwater discharge. *Nature*, **382**, 241-244.

BJÖRCK, S., WALKER, M.J.C., CWYNAR, L., JOHNSEN, S., KNUDSEN, K.L. LOWE, J.J. WOHLFARTH, B. & INTIMATE Members (1998) An event stratigraphy for the Last Termination in the North Atlantic region based on the Greenland ice-core record: a proposal by the INTIMATE group. *Journal of Quaternary Science*, **13**, 283-292.

BOE, R., HOVLAND, M., INSTANES, A., RISE, L. & VASSHUS, S. (2000) Submarine slidescars and mass movements in Karmsundet and Skudenesfjorden, southwestern Norway: morphology and evolution. *Marine Geology*, **167**, 147-165.

BUGGE, T., BALDERSON, R.H. & KENYON, N. (1988) The Storegga slide. Philos. *Trans. Royal Soc. London*, **325**, 357-388.

CANALS, M., LASTRAS, G., URGELES, R., CASAMOR, J.L., MIENERT, J., CATTANEO, A., DE BATIST, M., HEFLIDASON, H., IMBO, Y., LABERG, J.S., LOCAT, J., LONG, D., LONGVA, O., MASSON, D.G., SULTAN, N., TRINCARDI, F. & BRYN, P. (2004) Slope failure dynamics and impacts from seafloor and shallow sub-seafloor geophysical data: case studies from the COSTA Project. *Marine Geology*, **213(1-4)**, 9-72.

CAPOTONDI, L., BORSETTI, A.M. & MORIGI, C. (1999) Foraminiferal ecozones, a high resolution proxy for the late Quaternary biochronology in the central Mediterranean Sea. *Marine Geology*, **153**, 253-274.

CARTWRIGHT, J., FREY-MARTINEZ, J. & JAMES, D. (2005) Frontal confined versus frontally emergent submarine landslides: a 3D seismic characterisation. *2nd. International Conference on Submarine Mass Movements and Their Consequences*, Oslo, Norway, September 5-7, p. 24-25.

CARTWRIGHT, J.A. (1994) Episodic basin-wide fluid expulsion from geopressured shale sequences in the North Sea basin. *Geology*, **22**, 447-450.

CATALANO, R., INFUSO, S. & SULLI, A. (1993) The Pelagian foreland and its northward foredeep. Plio-Pleistocene structural evolution. In:. *UNESCO technical Reports in Marine Sciences* (Ed. by Max M.D. and Colantoni P.), **58**, 37-42.

CATTANEO, A. & TRINCARDI, F. (1999) The Late-Quaternary transgressive record in the Adriatic epicontinental sea: basin widening and facies partitioning, In: Isolated Shallow Marine Sand Bodies: Sequence Startigraphic Analysis and Sedimentological interpretation (Ed. by K. Bergman and J. Snedden), *SEPM Special Publication*, 64, 127-146.

CATTANEO, A., CORREGGIARI, A., LANGONE, L. & TRINCARDI, F. (2003) The late-Holocene Gargano subaqueous delta, Adriatic shelf: Sediment pathways and supply fluctuations. *Marine Geology*, **193**, 61-91.

COLANTONI, P. (1974). Note sulla geologia marina sul Canale di Sicilia. *Giornale di Geologia*, **40**, 181-207.

CORREGGIARI, A., TRINCARDI, F., LANGONE, L. & ROVERI, M. (2001) Styles of failure in heavily-sedimented highstand prodelta wedges on the Adriatic shelf. *Journal of Sedimentary Research*, **71**, 218-236.

DI STEFANO, E., INFUSO, S. & SCARANTINO, S. (1993) Plio-Pleistocene sequence stratigraphy of southwestern offshore Sicily from well logs and seismic sections in a high-resolution calcareous plankton biostratigraphic framework. In:.

UNESCO technical Reports in Marine Sciences (Ed. by Max M.D. and Colantoni P.), **58,** 105-110.

DUPERRET, A., BOURGOIS, J., LAGABRIELLE, Y. & SUESS, E. (1995) Slope instabilities at an active continental margin; large-scale polyphase submarine slides along the northern Peruvian margin, between 5 degrees S and 6 degrees S. *Marine Geology*, **122(4)**, 303-328.

EDWARDS, B.D., LEE, H.J. & FIELD, M.F. (1993) Seismically induced mudflow in Santa Barbara Basin, California. In: *Submarine Landslides: Selected Studies in the U.S. Exclusive Economic Zone* (Ed. by Schwab W.C., Lee H.J. and Twichell D.C.) USGS Bull., **vol. B-2002**, Washington D.C., 167-175.

EMBLEY, R.W. (1976) New evidence for occurrence of debris flow deposits in the deep sea. *Geology*, **4**, 371-374.

EMEIS, K.C., ROBERTSON, A.H.F., RICHER C., et al., (1996) 4. Site 963, *Proceedings of the ODP*, Initial Reports, **160**, 55-84.

FAIRBANKS, R.G. (1989) A 17,000 year glacio-eustatic sea level record: influence of glacial melting rates on the younger Dryas event and deep-ocean circulation. *Nature*, **342**, 637-642.

FINETTI, I. (1984) Geophysical studies of the Sicily Channel rift zone. *Bollettino di Geofisica Teorica e Applicata*, **26**, 3-28.

GALLOWAY, W.E., DINGUS, W.F.& PAIGE, R.E. (1991) Seismic and depositional facies of Paleocene-Eocene Wilcox Group submarine canyon fills, Northwest Gulf Coast, U.S.A. In: *Seismic facies and sedimentary processes of submarine fans and turbidite systems* (Ed. by P. Weimer and M.H. Link), 247-271, Springer-Verlag, Berlin.

GARDINER, W., GRASSO, M. & SEDGELEY, D. (1993) Plio-Pleistocene stratigraphy and fault movement of the Malta Platform. In:. *UNESCO technical Reports in Marine Sciences* (Ed. by Max M.D. and Colantoni P.), **58**, 111-116.

GAY, A., LOPEZ M., COCHONAT P., SULTAN N., CAUQUIL E. & BRIGAUD F. (2003) Sinuous pockmark belt as indicator of a shallow buried turbiditic channel on the lower slope of the Congo Basin, West African Margin. In: *Subsurface Sediment Mobilization* (Ed. by Van Rensbergen P., Hillis R.R., Maltman A. J., and Morley C. K.) Geological Society of London Special Publication **216**,, 173-189.

GEE, M.J.R., MASSON, D.G., WATTS, A.B. & ALLEN, P.A. (1999) The Saharan debris flow: an insight into the mechanics of long runout submarine debris flows. *Sedimentology*, **46**, 317-335.

GRASSO, M. (1993) Pleistocene structures along the Ionian side of the Hyblean Plateau (SE Sicily): implications for the tectonic evolution of the Malta Escarpment. In:. *UNESCO technical Reports in Marine Sciences* (Ed. by Max M.D. and Colantoni P.), **58**, 49-55.

HAMPTON, M.A., LEE, H.J. & LOCAT, J. (1996) Submarine landslides. *Reviews of Geophysics*, **34**, 33-59.

HAMPTON, M.A., BOUMA, A.H., CARLSON, P.R., MOLNIA, B.F., CLUKEY, E.C. & SANGREY D.A. (1978) Quantitative study of slope instability in the Gulf of Alaska. *10th Annual Offshore Technology Conference (OTC), 4*, 2307-2318.

HASIOTIS, T., PAPATHEODOROU, G., BOUCKOVALAS, G., CORBAU, C. & FERENTINOS G. (2002) Earthquake-induced coastal sediment instabilities in the western Gulf of Corinth, Greece. *Marine Geology*, **186(3-4)**, 319-335.

HUEHNERBACH, V. & MASSON, D.G. (2004) Landslides in the North Atlantic and its adjacent seas; an analysis of their morphology, setting and behaviour. *Marine Geology*, **213(1-4)**, 343-362.

HUGHEN K.A., BAILLIE M.G.L., BARD E. et al. (2004). Marine04 Marine Radiocarbon Age Calibration, 0-28 Cal kyr B.P. *Radiocarbon*, **46**, 1059-1086.

IMBO,Y., DE BATIST, M., CANALS, M., PRIETO, M.J. & BARAZA J. (2003) The GEBRA slide: a submarine slide on the Trinity Peninsula Margin, Antarctica. *Marine Geology*, **193**(3-4), 235-252.

JORISSEN, F. J., ASIOLI, A., BORSETTI A. M., CAPOTONDI L., DE VISSER J. P., HILGEN F. J., ROHLING E. J., VAN DER BORG K., VERGNAUD-GRAZZINI C. & ZACHARIASSE W. J., (1993) Late Quaternary Central Mediterranean biochronology. *Marine Micropaleontology*, **21**, 169-189.

KEEFER, D.K. (1994) The importance of earthquake-induced landslides to long-term slope erosion and slope-failure hazards in seismically active regions. *Geomorphology*, **10**, 265-284.

KENYON, N.H. (1987) Mass-wasting on the continental slope of northwest Europe. *Marine Geology*, **74**, 57-77.

KLAUCKE, I. & COCHONAT, P. (1999) Analysis of past seafloor failures on the continental slope off Nice (SE France). *Geo-Marine Letters*, **19-4**, 245-253.

LABAUNEA, C., JOUETB, G., BERNEB, S., GENSOUSA, B., TESSONA, M. & DELPEINTB, A. (2005) Seismic stratigraphy of the Deglacial deposits of the Rhône prodelta and of the adjacent shelf . *Marine Geology*, **222-223**, 299-311.

LASTRAS, G., CANALS, M., HUGHES CLARKE, J.E., MORENO, A., DE BATIST, M., MASSON, D.G. & COCHONAT P. (2002) Seafloor imagery from the BIG'95 debris flow, western Mediterranean. *Geology*, **30**(10), 871-874.

LASTRAS, G., DE BLASIO, F.V., CANALS, M. & ELVERHOI, A. (2005) Conceptual and numerical modeling of the BIG'95 debris flow, western Mediterranean Sea. *Journal of Sedimentary Research*, **75(5)**, 784-797.

LASTRAS, G., CANALS, M., AMBLAS, D., IVANOV, M., DENNIELOU, B., DROZ, L., AKHMETZHANOV, A. & TTR-14 LEG 3 SHIPBOARD SCIENTIFIC PARTY (2006) Eivissa slides, western Mediterranean Sea: morphology and processes. *Geo-Marine Letters*, **26(4)**, 225-233.

LEE, H.J. (2005) Undersea landslides: extent and significance in the Pacific Ocean, an update. *Natural Hazards and Earth System Sciences*, **5**, 877-892.

LEBREIRO, S.M., McCAVE, N. & WEAVER, P.P.E (1997) Late quaternary turbidite emplacement on the Horseshoe Abyssal Plain (Iberian margin). *Journal of Sedimentary Research*, **67**, 856-870.

LIPMAN, P.W., NORMARK, W.R., MOORE, J.G., WILSON, J.B. & GUTMACHER, C.E. (1988) The giant submarine Alika debris slide, Mauna Loa, Hawaii. *Journal of Geophysical Research*, **93**, 4279-4299.

LOCAT, J. & LEE, H.J. (2002) Submarine landslides: advances and challenges. *Can. Geotech. J.*, **39**, 193-212.

MANGERUD, J., ANDERSEN, S.T., BERGLUND, B.E & DONNER, J.J. (1974) Quaternary stratigraphy of Norden, a proposal for terminology and classification. *Boreas*, **3**,109-127.

MARR, J.G., HARFF, P.A., SHANMUGAM, G. & PARKER G. (2001) Experiments on subaqueous sand gravity flows; the role of clay and water content in flow dynamics and depositional structures. *GSA Bulletin*, **113**(11), 1377-1386.

MARTINEZ, J., CARTWRIGHT, J. & HALL, B. (2005) 3D seismic interpretation of slump complexes: examples from the continental margin of Israel. *Basin research*, **17**, 83-108.

MASSON, D.G., WATTS, A.B., GEE, M.J.R., URGELES, R., MITCHELL, N.C., LE BAS, T.P. & CANALS M. (2002) Slope failures on the flanks of the western Canary Islands. *Earth-Science Reviews*, **57**, 1-35.

MAX, M.D., KRISTENSEN, A. & MICHELOZZI, E. (1993) Small-scale Plio-Quaternary sequence stratigraphy and shallow geology of the west-central Malta Plateau. In:. *UNESCO technical Reports in Marine Sciences* (Ed. by M.D. Max and P. Colantoni), **58**, 117-122.

McADOO, B.G., PRATSON, L.F., & ORANGE, D.L. (2000) Submarine landslide morphology, US continental slope. *Marine Geology*, **169**, 103-136.

MINISINI, D., TRINCARDI, F. & ASIOLI, A. (2006) Evidence of slope instability in the Southwestern Adriatic Margin. *Natural Hazards and Earth System Sciences*, **6-1**, 1-20.

MOORE, D.G., CURRAY, J.R. & EMMEL, F.J. (1976) Large submarine slide (olistostrome) associated with Sunda Arc subduction zone, Northeast Indian Ocean. *Marine Geology*, **21**, 211-226.

MOSCARDELLI, L., WOOD, L., & MANN P. (2006) Mass-transport complexes and associated processes in the offshore area of Trinidad and Venezuela. *AAPG Bulletin,* **90**(7), 1059-1088.

PIPER, D.J.W., SHOR, A.N., & HUGHES CLARKE, J.E. (1988) The 1929 Grand Banks earthquake, slump and turbidity current. In: *Sedimentological Consequences of Convulsive Geologic Events* (Ed. by H.E. Clifton) Geological Society of America, Special Paper **229**, 77–92.

POSAMENTIER, H.W. & VAIL, P.R. (1988) Eustatic control on clastic deposition,II-sequence and systems trast models. In: *Sea-Level Changes- An integrated Approach* (Ed. by C.K. Wilgus, B.S. Hastings, C.G.St.C. Kendall et al.) Society of Economic Paleontologists and Mineralogists, Spec.Publ., **42**, 125-154.

POSAMENTIER, H.W. & KOLLA, V. (2003) Seismic geomorphology and stratigraphy of depositional elements in deep-water settings. *Journal of Sedimentary Research*, **73-3**, 367-388.

PRATSON, L.F. & COAKLEY, B.J. (1996) A model for the headward erosion of submarine canyons induced by downslope-eroding sediment flows, *GSA Bulletin*, **108**, 225-234.

PRATSON, L.F., RYAN, W.B.F., MOUNTAIN, G.S. & TWICHELL, D.C. (1994) Submarine canyon initiation by downslope-eroding sediment flows: Evidence in late Cenozoic strata on the New Jersey continental slope. *GSA Bulletin*, **106**, 395-412.

PRIOR, D.B., BORNHOLD, B.D., COLEMAN, J.M. & BRYANT, W.R. (1982) Morphology of a submarine slide, Kitimat Arm, British Columbia. *Geology*, **10**, 588-592.

PRIOR, D.B., BORNHOLD, B.D. & JOHNS, B.D. (1984) Depositional characteristics of a submarine debris flow. *Journal of Geology,* **92**, 707-727.

PRIOR, D.B. & COLEMAN, J.M. (1984) Submarine slope instability. In: Slope Instability (Ed. by Brundsen D. and Prior D.B.), Wiley, Chichester, NewYork, 419-455.

PUJOL, C. & VERGNAUD GRAZZINI, C. (1995) Distribution patterns of live planktic foraminifers as related to regional hydrography and productive systems of the Mediterranean Sea. *Marine Micropaleontology,* **25**, 187-217.

RIEDEL, M., NOVOSEL, I., SPENCE, G.D., HYNDMAN, R.D., CHAPMAN, R.N., SOLEM, R.C. & LEWIS, T. (2006) Geophysical and geochemical signatures associated with gas hydrate-related venting in the northern Cascadia margin. *GSA Bulletin*, **118**, 23-38.

RIDENTE, D. & TRINCARDI, F. (2002) Eustatic and tectonic control on deposition and lateral variability of Quaternary regressive sequences in the Adriatic basin. *Marine Geology*, **184**, 273-293.

ROHLING, E.J., JORISSEN, F.J. & DE STIGTER, H.C (1997) 200 Year interruption of Holocene sapropel formation in the Adriatic Sea. *Journal of Micropalaeontology*, **16**, 97-108.

ROTHWELL, R.G., PEARCE, T.J. & WEAVER, P.P.E. (1992) Late quaternary evolution of the Madeira Abyssal Plain, Canay Basin, NE Atlantic. *Basin Research*, **4**, 103-131.

ROTHWELL, R.G., THOMSON, J. & KÄHLER, G. (1998) Low-sea-level emplacement of a very large Late Pleistocene 'megaturbidite' in the western Mediterranean Sea. *Nature*, **392**, 377-380.

ROTHWELL, R.G., REEDER, M.S., ANASTASAKIS, G., STOW, D.A.V., THOMSON, J. & KAEHLER, G. (2000) Low sea-level stand emplacement of megaturbidites in the western and eastern Mediterranean Sea. *Sedimentary Geology*, **135**, 75-88.

SBAFFI, L., WEZEL F. C., KALLEL N., PATERNE M., CACHO I., ZIVERI P. & SHAKLETON N. (2001) Response of the pelagic environment to paleoclimatic changes in the central Mediterranean Sea during the late Quaternary. *Marine Geology*, **178**, 39-62.

SCHNELLMANN, M., ANSELMETTI, F.S., GIARDINI, D., MCKENZIE, J.A. & WARD S.N. (2002) Prehistoric earthquake history revealed by lacustrine slump deposits. *Geology*, **30**(12), 1131-1134.

SCHNELLMANN, M., ANSELMETTI, F., GIARDINI, D. & McKENZIE, J.A. (2005) Mass movement-induced fold-and-thrust belt structures in unconsolidated sediments in Lake Lucerne (Switzerland). *Sedimentology*, **52**, 271-289.

SHANMUGAM, G., MOIOLA R.J. & SALES J.K. (1988) Duplex-like structures in submarine fan channels, Ouachita Mountains, Arkansas. *Geology*, **16(3)**, 229-232.

SKEMPTON, A.W. (1970) The consolidation of clays by gravitational compaction. *Quart. Jour. Geol. Soc.*, **125**, 373-411.

SPROVIERI, R., DI STEFANO, E., INCARBONA, A. & GARGANO, M.E. (2003) A high resolution record of the last deglaciation in the Sicily Channel based on foraminifera and calcareous nannafossil quantitative distribution. *Palaeogeography, Palaeoclimatology, Palaeoecology*, **2002**, 119-142.

STUIVER, M. & REIMER, P.J. (1993) Extended 14C data base and revised CALIB 3.0 14C age calibration program. *Radiocarbon*, **35**, 215-230.

SULTAN, N., COCHONAT, P., CANALS, M., CATTANEO, A., DENNIELOU, B., HAFLIDASON, H., LABERG, J.S., LONG, D., MIENERT, J., TRINCARDI, F., URGELES, R., VORREN, T.O. & WILSON, C. (2004) Triggering mechanisms of slope instability processes and sediment failures on continental margins; a geotechnical approach. *Marine Geology*, **213(1-4)**, 291-321.

SYNOLAKIS, C.E., BARDET, J.P., BORRERO, J.C., DAVIES, H.L., OKAL, E.A., SILVER, E.A., SWEET, S. & TAPPIN, D.R. (2002) The slump origin of the 1998 Papua New Guinea tsunami. *Proceedings - Royal Society, Mathematical, Physical and Engineering Sciences*, **458**, 763-789.

SYVITSKI, J.P.M. & SCHAFER, C.T. (1996) Evidence for an earthquake-triggered basin collapse in Saguenay Fjord, Canada. *Sedimentary Geology*, **104(1-4)**, 127-153.

TESSON, M., GENSOUS, B., ALLEN, G.P. & RAVENNE, C.H. (1990) Late Quaternary deltaic lowstand wedges on the Rhone continental shelf, France. *Marine Geology*, **91**, 325-332.

TRINCARDI, F. & ARGNANI, A. (1990) Gela submarine slide: a major basin-wide event in the Plio-Quaternary foredeep of Sicily. *Geo-Marine Letters*, **10**, 13-21.

TRINCARDI, F. & FIELD, M. E. (1992) Collapse and flow of lowstand shelf-margin deposits: an example from the Eastern Tyrrhenian, Italy. *Marine Geology*, **105**, 77-94.

TRINCARDI, F. & NORMARK, W.R. (1989) Suvero Pleistocene slide, Paola basin, Southern Italy. *Marine and Petroleum Geology*, **6**, 324-335.

TRINCARDI, F., CATTANEO, A., ASIOLI A., CORREGGIARI, A. & LANGONE, L. (1996) Stratigraphy of the late-Quaternary deposits in the central Adriatic basin and the record of short-term climatic events. *Memorie Istituto Italiano di Idrobiologia*, **55**, 39-70.

TRINCARDI, F., CATTANEO, A., CORREGGIARI, A., MONGARDI, S., BREDA, A., & ASIOLI, A. (2003) Submarine slides during sea level rise: two exemples from the eastern Tyrrhenian margin. In: *Submarine Mass Movements and their Consequences* (Ed. by Locat J. and Mienert J.) Kluver Acad. Publ., Dordrecth, The Netherlands, 469-478.

TRINCARDI, F., CATTANEO, A., CORREGGIARI, A. & RIDENTE, D. (2004) Evidence of soft sediment deformation, fluid escape, sediment failure and regional weak layers within the late Quaternary mud deposits of the Adriatic Sea. *Marine Geology*, **213**, 91-120.

VERGNAUD-GRAZZINI, C., BORSETTI, A.M., CATI, F., COLANTONI, P., D'ONOFRIO, S., SALIEGE, J.F., SARTORI, R. & TAMPIERI, R. (1988) Paleoceanographic record of the last deglaciation in the Strait of Sicily. *Marine Micropaleontology*, **13 (1)**, 1-22.

WEAVER, P.P.E. & KUIJPERS, A. (1983) Climatic control of turbidite deposition on the Madeira abyssal plain. *Nature*, **306**, 360-363.

FIGURE 1

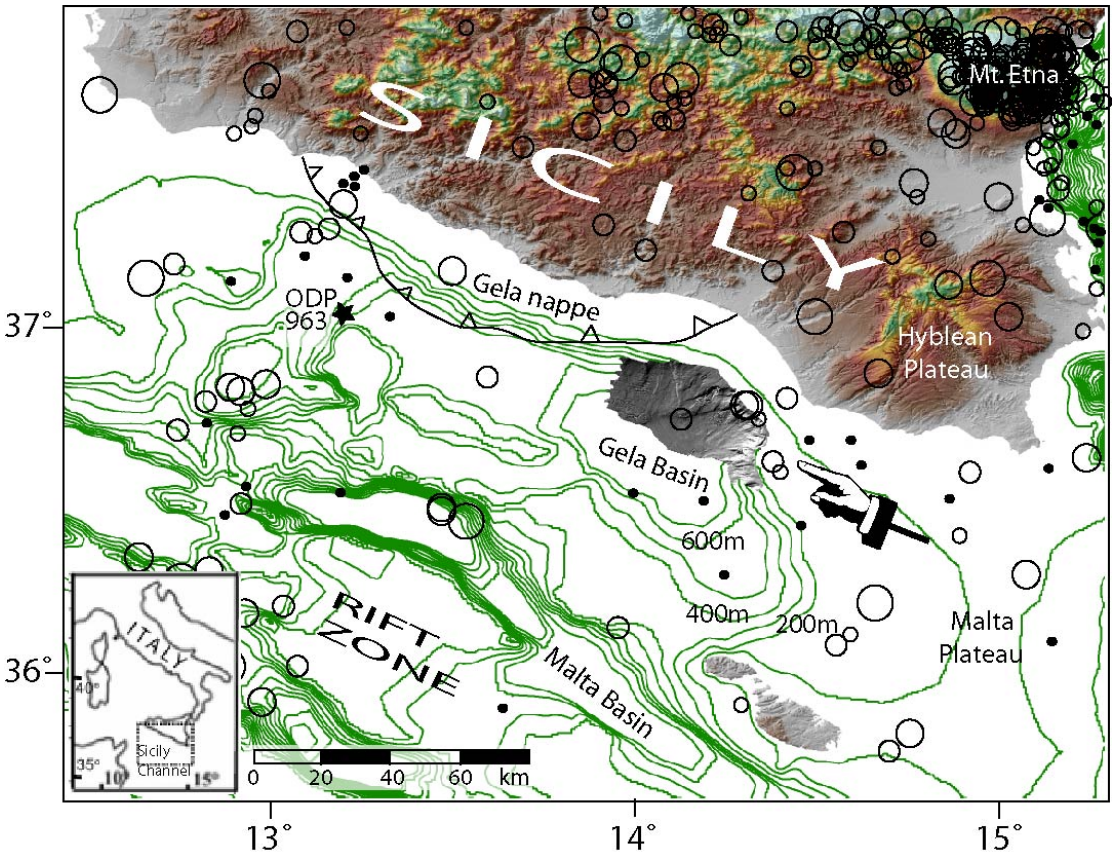
SICILY
Mt. Etna
Gela nappe
ODP
963
Hyblean
Plateau
Gela Basin
600m
400m
200m
Malta
Plateau
RIFT
ZONE
Malta Basin
ITALY
Sicily
Channel
0
20
40
60
km
37°
36°
13°
14°
15°

FIGURE 2

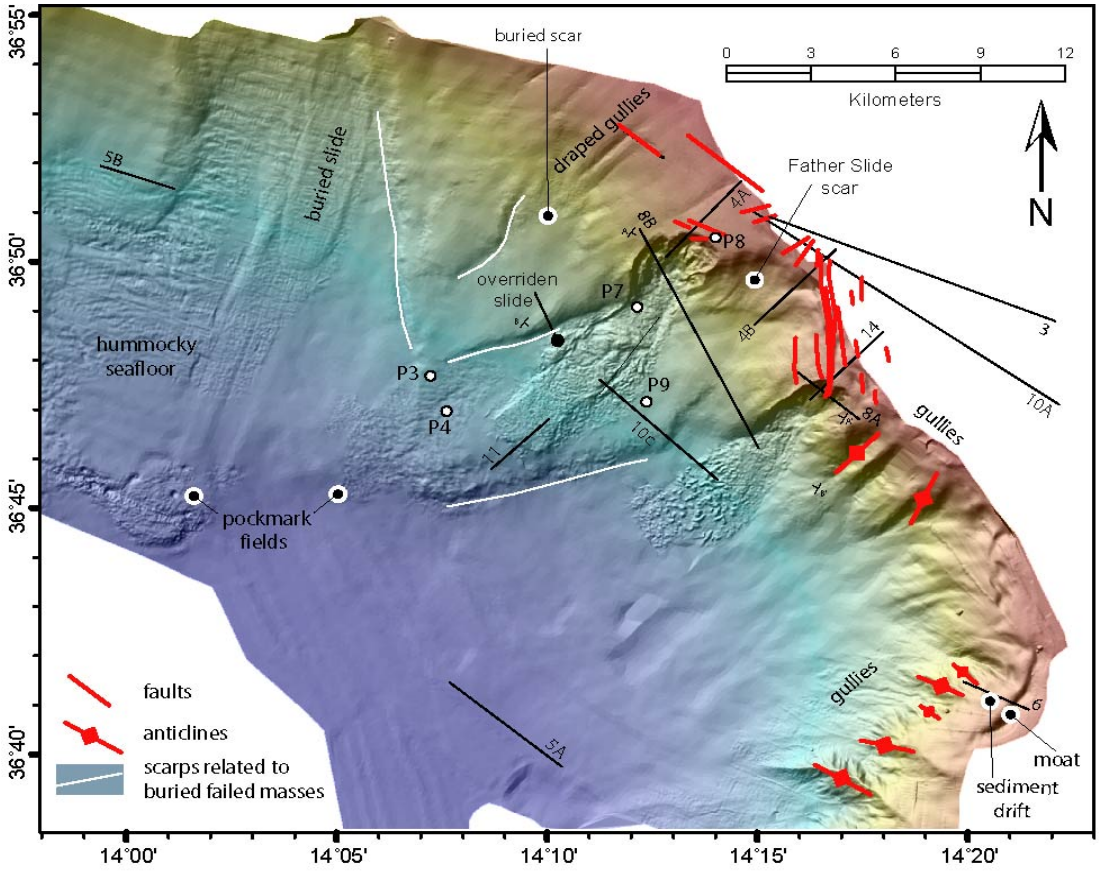
buried scar
draped gullies
buried slide
Father Slide scar
overriden slide
hummocky seafloor
P3
P4
P7
P8
P9
pockmark fields
gullies
gullies
moat
sediment drift
faults
anticlines
scarps related to buried failed masses
Kilometers
0 3 6 9 12
N
36°55'
36°50'
36°45'
36°40'
14°00'
14°05'
14°10'
14°15'
14°20'

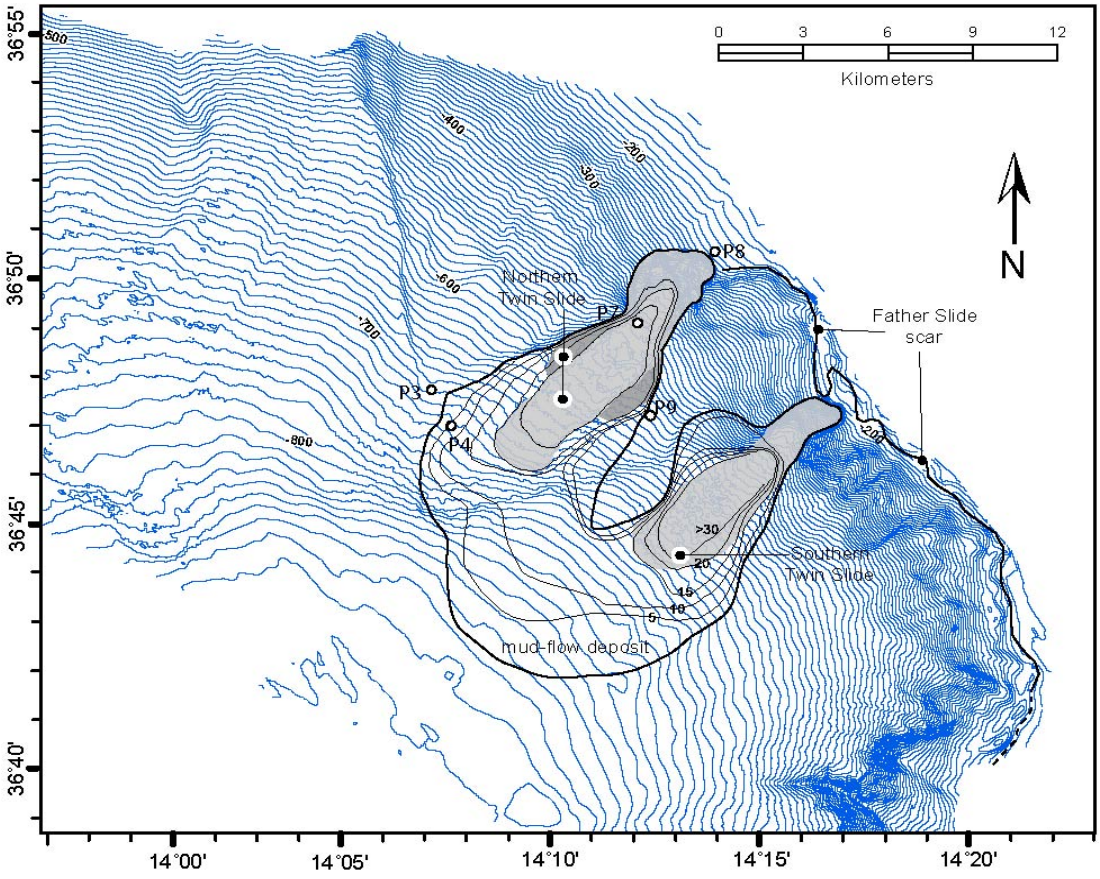
Northern Twin Slide
Father Slide scar
Southern Twin Slide
mud-flow deposit
P3
P4
P7
P8
P9
-500
-400
-300
-200
-600
-700
-800
-900
>30
20
15
10
5
Kilometers
0 3 6 9 12
N
36°55'
36°50'
36°45'
36°40'
14°00'
14°05'
14°10'
14°15'
14°20'

FIGURE 3

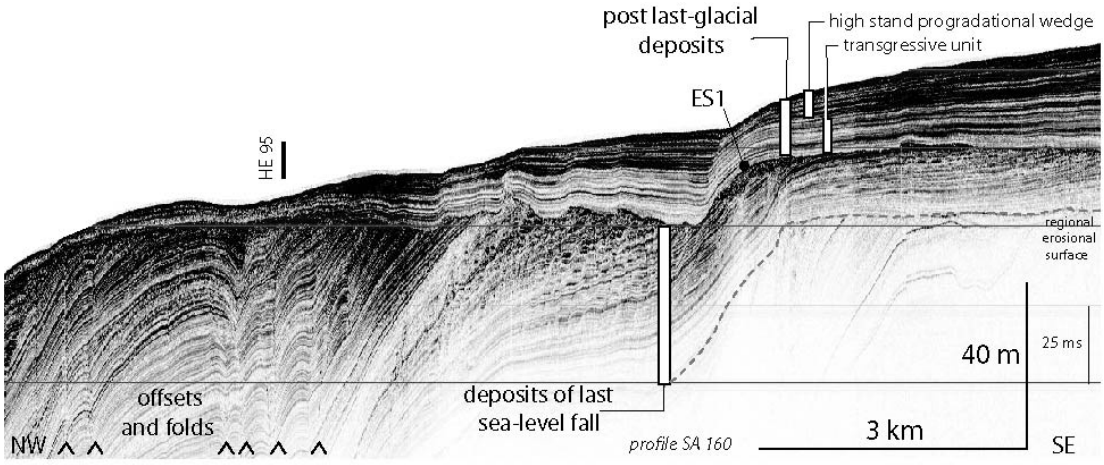
post last-glacial deposits
high stand progradational wedge
transgressive unit
ES1
HE 95
regional erosional surface
40 m
25 ms
offsets and folds
deposits of last sea-level fall
profile SA 160
3 km
NW
SE

FIGURE 4

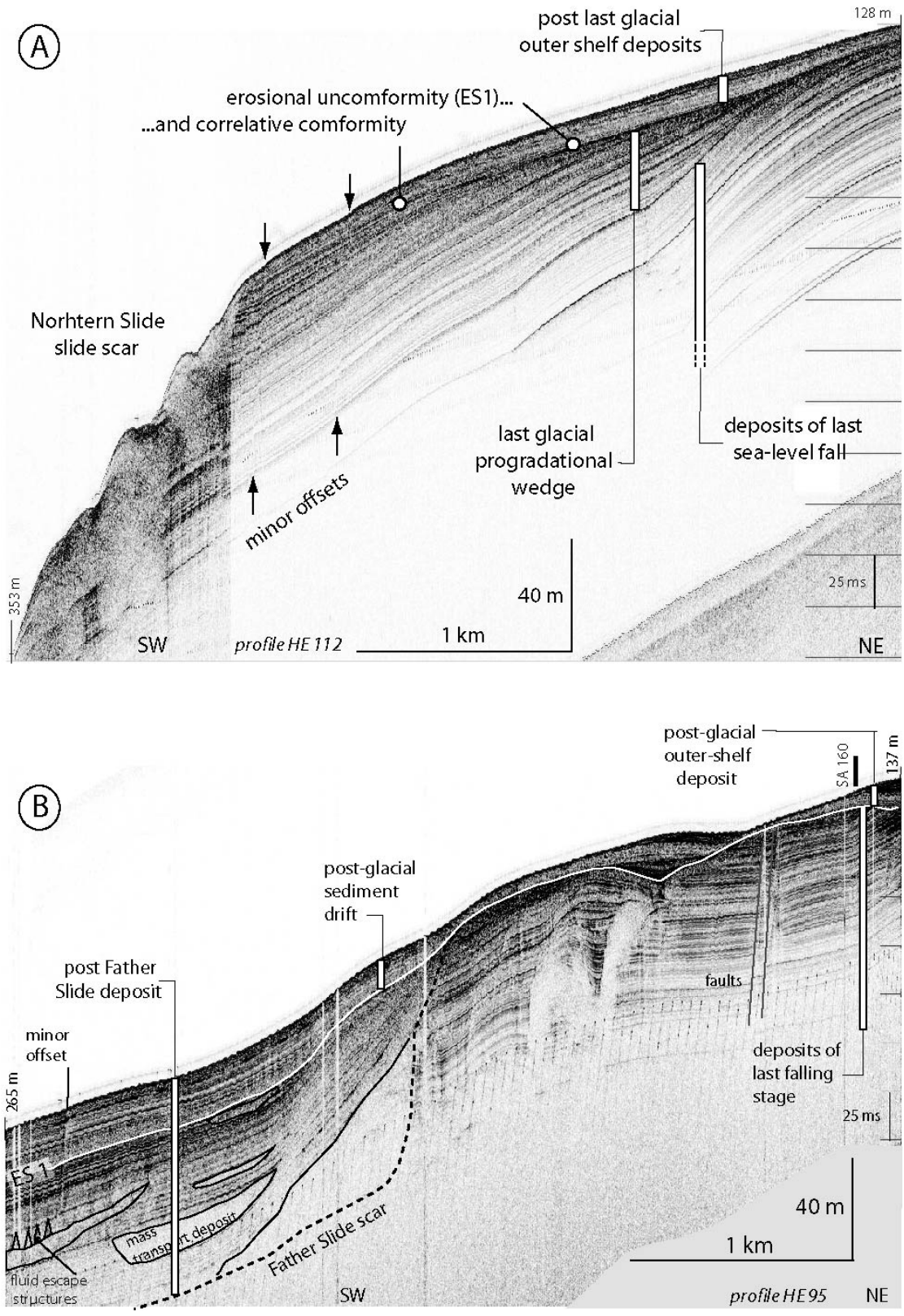
A
post last glacial
outer shelf deposits
128 m
erosional uncomformity (ES1)...
...and correlative comformity
Norhtern Slide
slide scar
minor offsets
last glacial
progradational
wedge
deposits of last
sea-level fall
353 m
SW
profile HE 112
40 m
1 km
25 ms
NE
B
post-glacial
outer-shelf
deposit
SA 160
137 m
post-glacial
sediment
drift
post Father
Slide deposit
faults
minor
offset
deposits of
last falling
stage
265 m
25 ms
ES 1
mass
transport deposit
Father Slide scar
40 m
1 km
fluid escape
structures
SW
profile HE95
NE

FIGURE 5

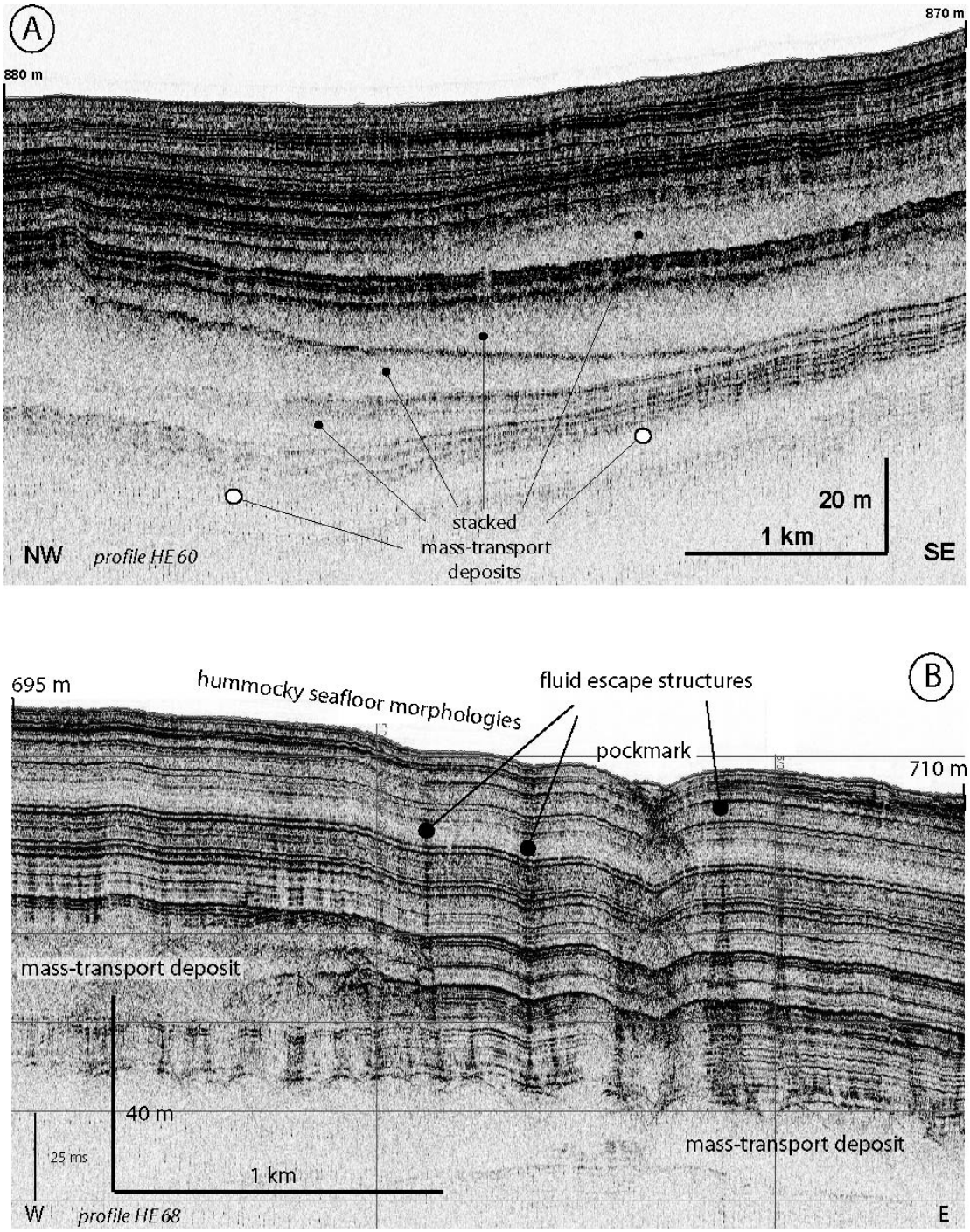
A
870 m
880 m
stacked
mass-transport
deposits
20 m
1 km
NW
profile HE60
SE
695 m
hummocky seafloor morphologies
fluid escape structures
B
pockmark
710 m
mass-transport deposit
40 m
25 ms
1 km
mass-transport deposit
W
profile HE68
E

FIGURE 6

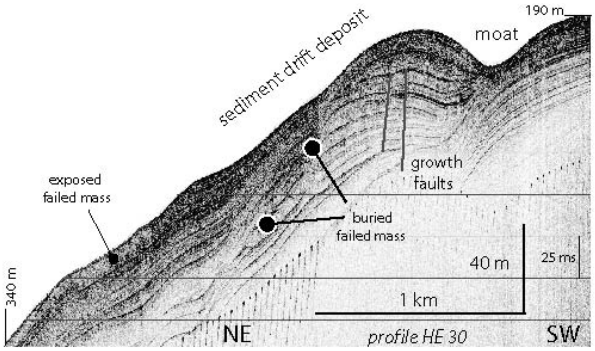
190 m
moat
sediment drift deposit
growth faults
exposed failed mass
buried failed mass
40 m
25 ms
340 m
1 km
NE
profile HE 30
SW

FIGURE 7

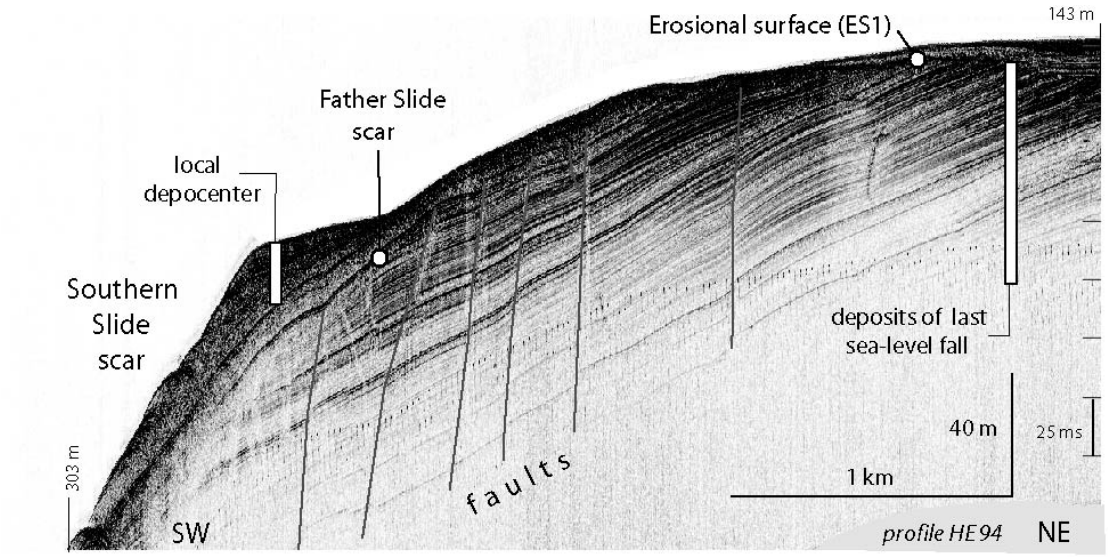
Erosional surface (ES1)
143 m
Father Slide
scar
local
depocenter
Southern
Slide
scar
deposits of last
sea-level fall
40 m
25 ms
1 km
303 m
faults
SW
profile HE94
NE

FIGURE 8

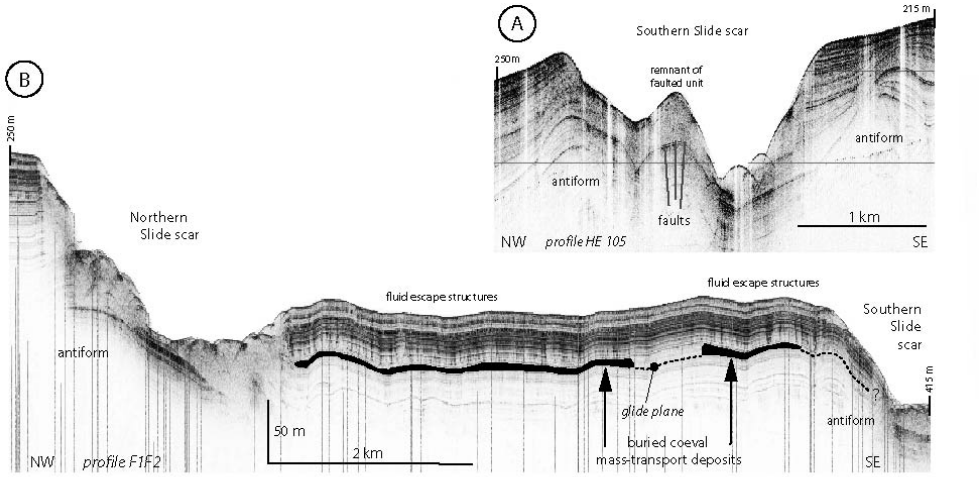
A
Southern Slide scar
215 m
250m
remnant of faulted unit
antiform
antiform
faults
1 km
NW
profile HE 105
SE
B
250 m
Northern Slide scar
fluid escape structures
fluid escape structures
Southern Slide scar
antiform
415 m
glide plane
buried coeval mass-transport deposits
antiform
50 m
2 km
NW
profile F1F2
SE

FIGURE 9

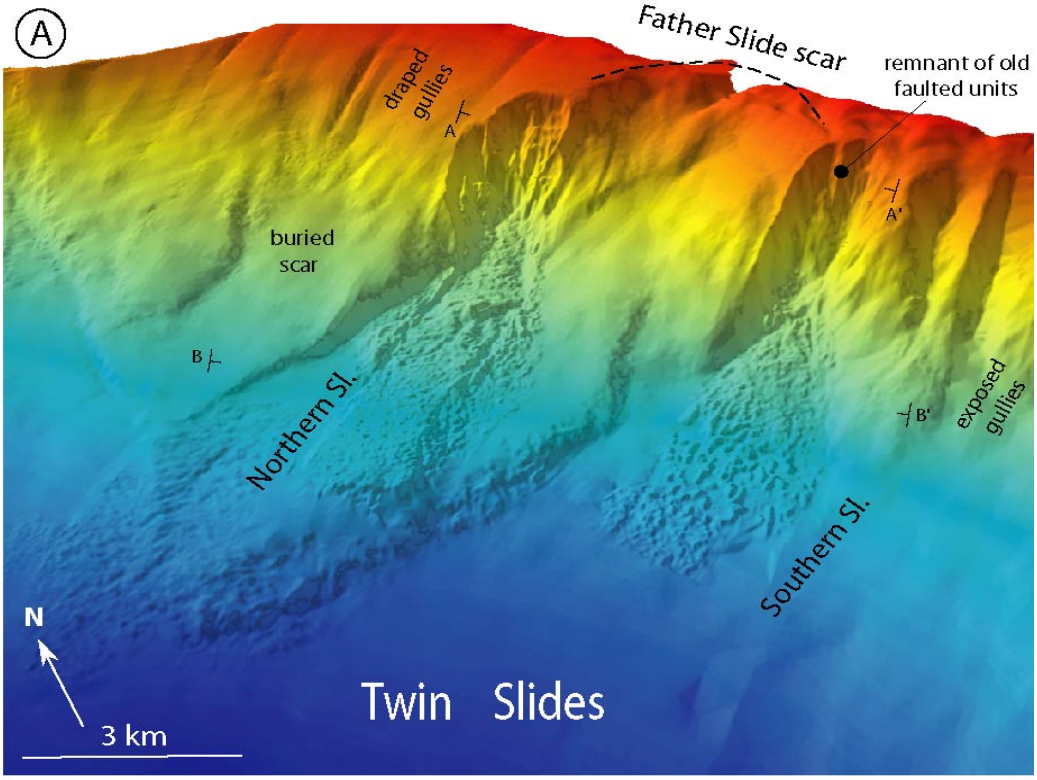
A
Father Slide scar
remnant of old faulted units
draped gullies
A
A'
buried scar
B
Northern Sl.
B'
exposed gullies
Southern Sl.
N
3 km
Twin Slides

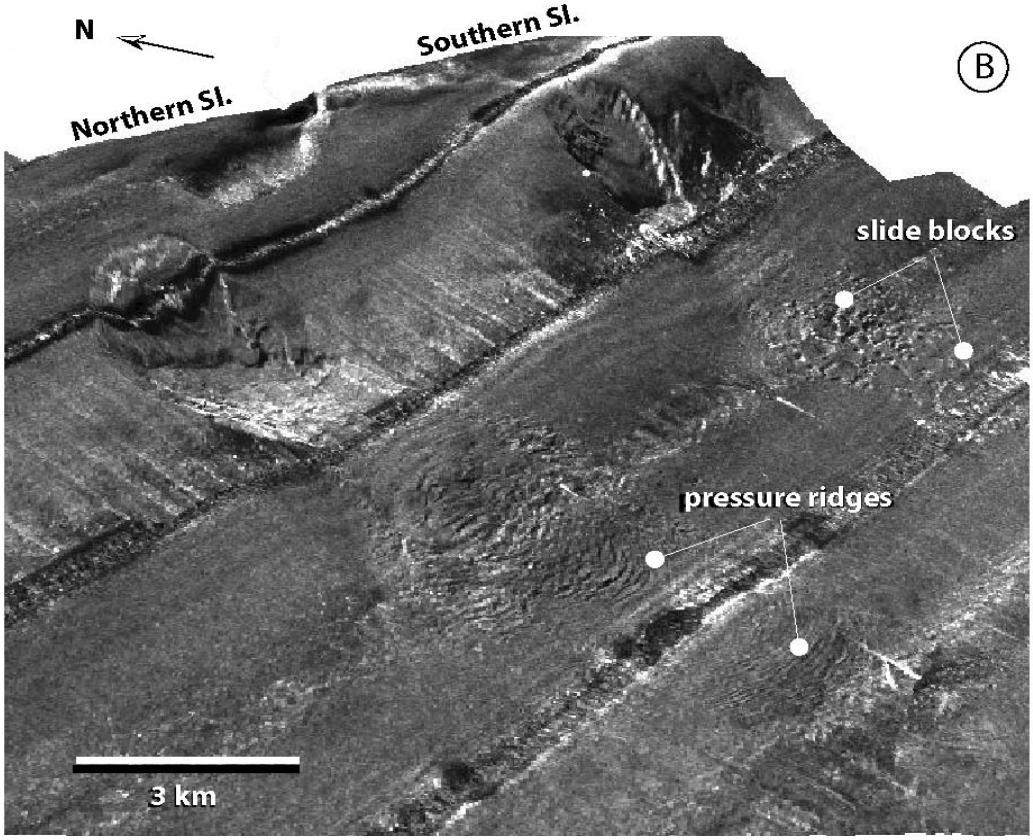
N
Southern Sl.
Northern Sl.
B
slide blocks
pressure ridges
3 km

FIGURE 10

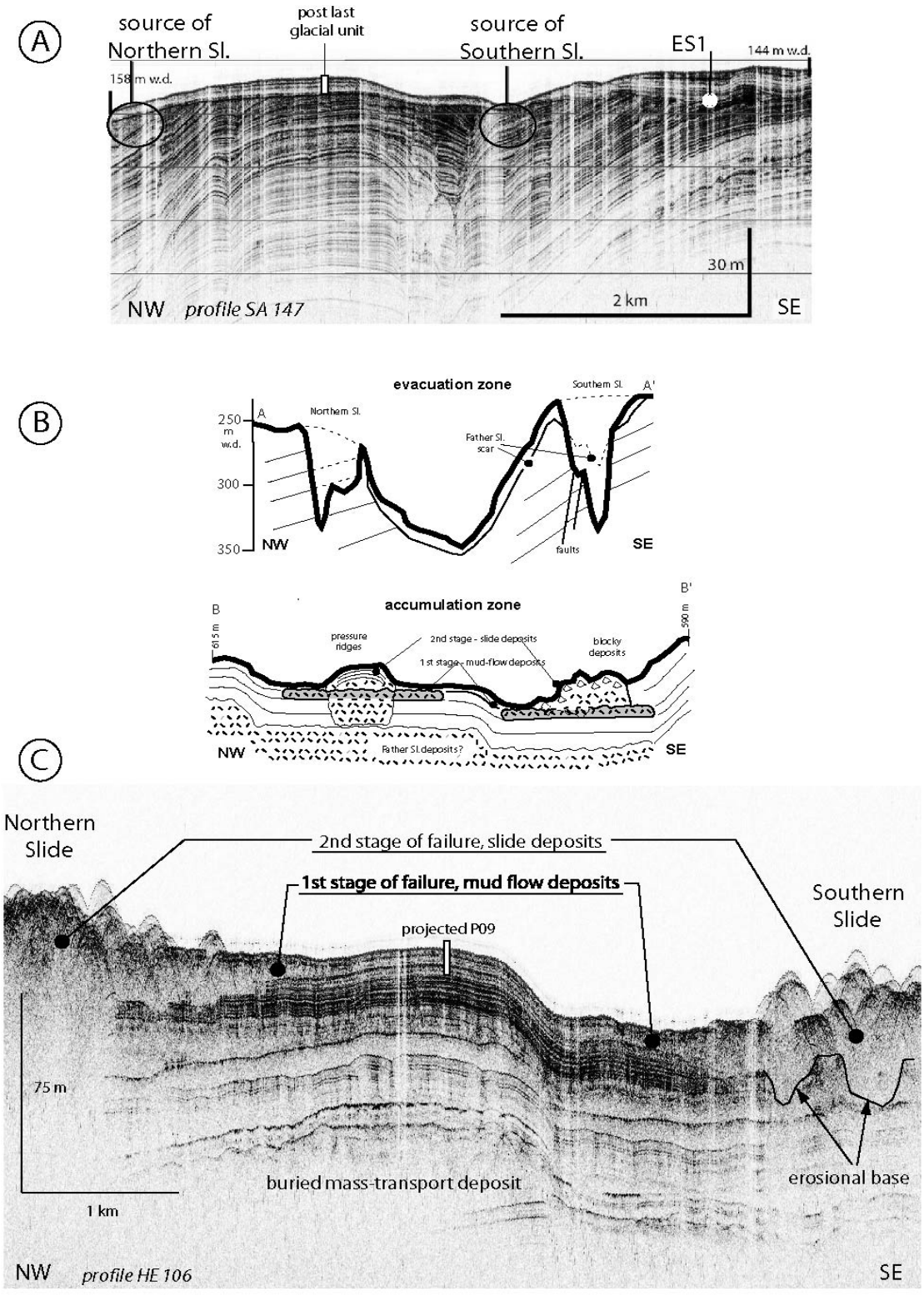
A
source of Northern Sl.
post last glacial unit
source of Southern Sl.
ES1
144 m w.d.
158 m w.d.
30 m
2 km
NW
profile SA 147
SE
B
evacuation zone
Southern Sl.
A'
A
Northern Sl.
250 m w.d.
300
350
Father Sl. scar
faults
NW
SE
accumulation zone
B
B'
615 m
590 m
pressure ridges
2nd stage - slide deposits
1st stage - mud-flow deposits
blocky deposits
Father Sl. deposits?
NW
SE
C
Northern Slide
2nd stage of failure, slide deposits
1st stage of failure, mud flow deposits
projected P09
Southern Slide
75 m
1 km
buried mass-transport deposit
erosional base
NW
profile HE 106
SE

FIGURE 11

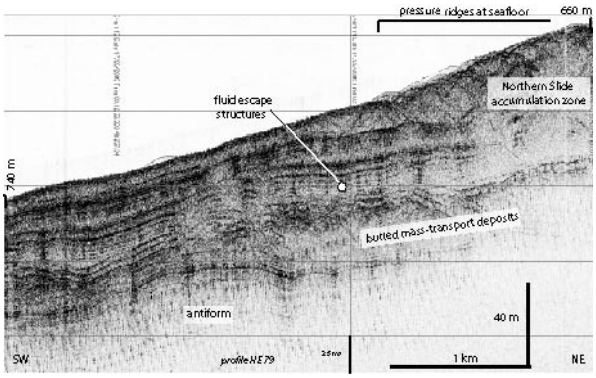
pressure ridges at seafloor
650 m
Northern Slide
accumulation zone
fluid escape
structures
740 m
buried mass-transport deposits
antiform
40 m
SW
profile NE79
1 km
NE

FIGURE 12

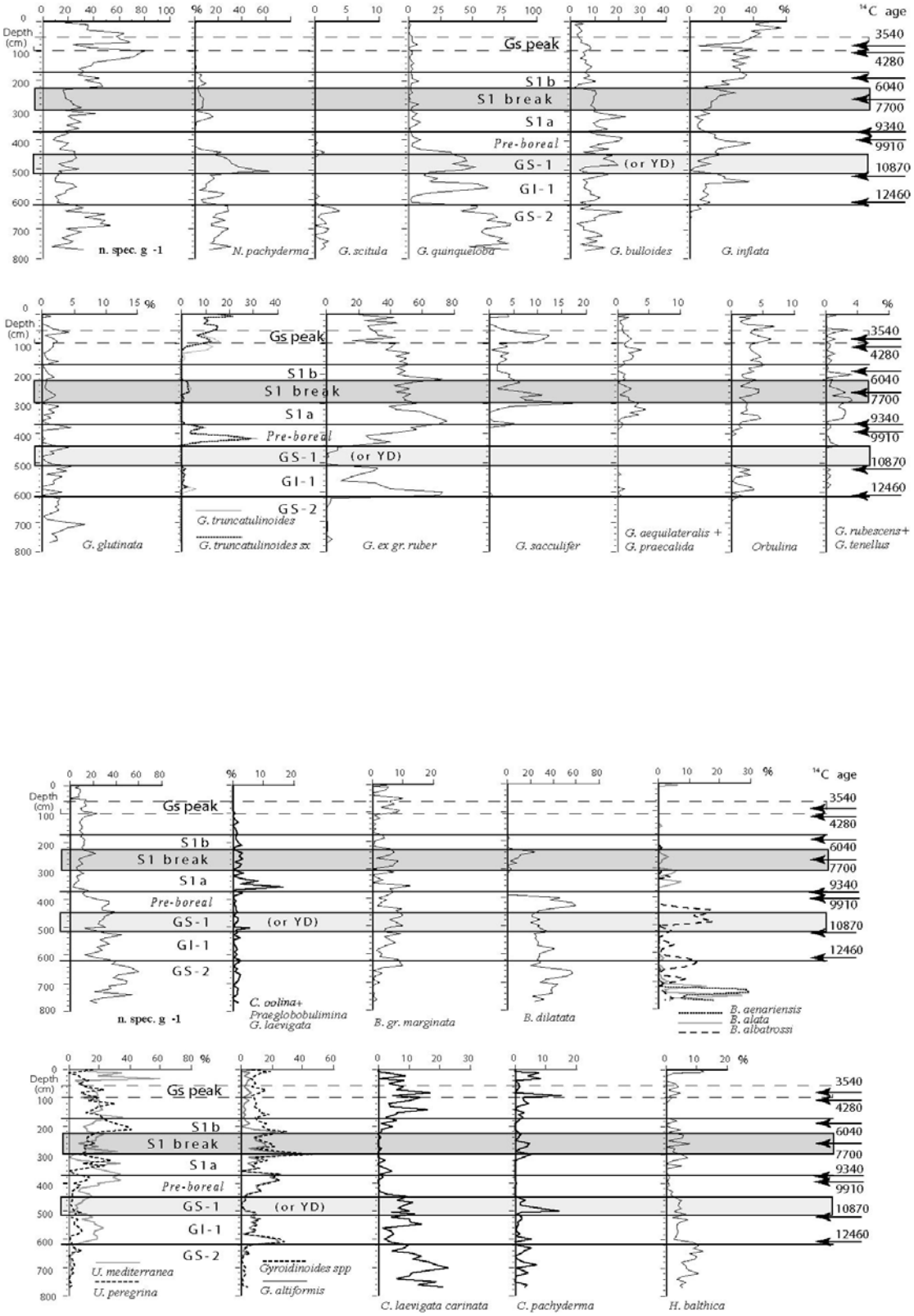
Depth (cm)
Gs peak
S1b
S1 break
S1a
Pre-boreal
GS-1
(or YD)
GI-1
GS-2
14C age
3540
4280
6040
7700
9340
9910
10870
12460
n. spec. g -1
N. pachyderma
G. scitula
G. quinqueloba
G. bulloides
G. inflata
G. glutinata
G. truncatulinoides
G. truncatulinoides sx
G. ex gr. ruber
G. sacculifer
G. aequilateralis + G. praecalida
Orbulina
G. rubescens+ G. tenellus
C. oolina+ Praeglobobulimina G. laevigata
B. gr. marginata
B. dilatata
B. aenariensis
B. alata
B. albatrossi
U. mediterranea
U. peregrina
Gyroidinoides spp
G. altiformis
C. laevigata carinata
C. pachyderma
H. balthica

FIGURE 13

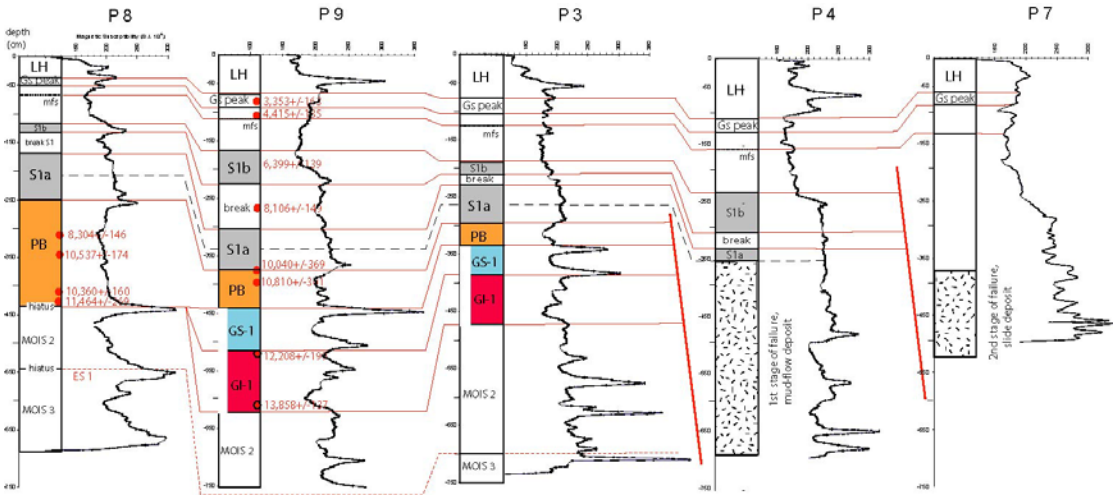
P8
P9
P3
P4
P7
depth (cm)
LH
Gs peak
mfs
S1b
break S1
S1a
PB
hiatus
MOIS 2
MOIS 3
ES 1
break
GS-1
GI-1
1st stage of failure, mudflow deposit
2nd stage of failure, slide deposit

FIGURE 14

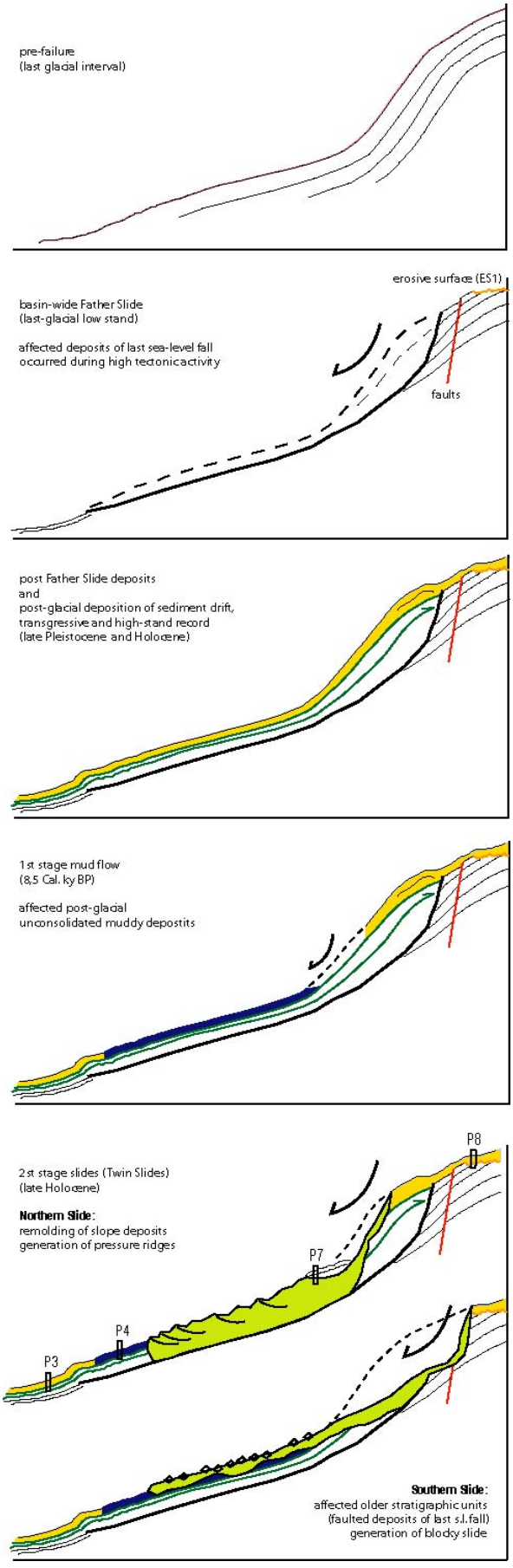
pre-failure
(last glacial interval)
erosive surface (ES1)
basin-wide Father Slide
(last-glacial low stand)
affected deposits of last sea-level fall
occurred during high tectonic activity
faults
post Father Slide deposits
and
post-glacial deposition of sediment drift,
transgressive and high-stand record
(late Pleistocene and Holocene)
1st stage mud flow
(8,5 Cal. ky BP)
affected post-glacial
unconsolidated muddy depostits
2st stage slides (Twin Slides)
(late Holocene)
Northern Slide:
remolding of slope deposits
generation of pressure ridges
P8
P7
P4
P3
Southern Slide:
affected older stratigraphic units
(faulted deposits of last s.l.fall)
generation of blocky slide

FIGURE 15

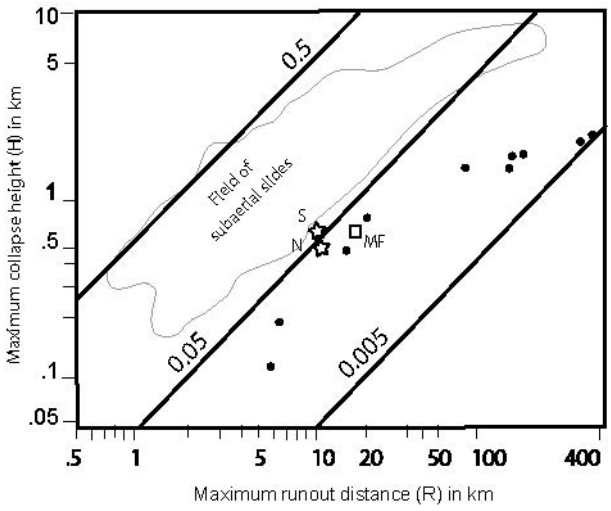

FIGURE 16

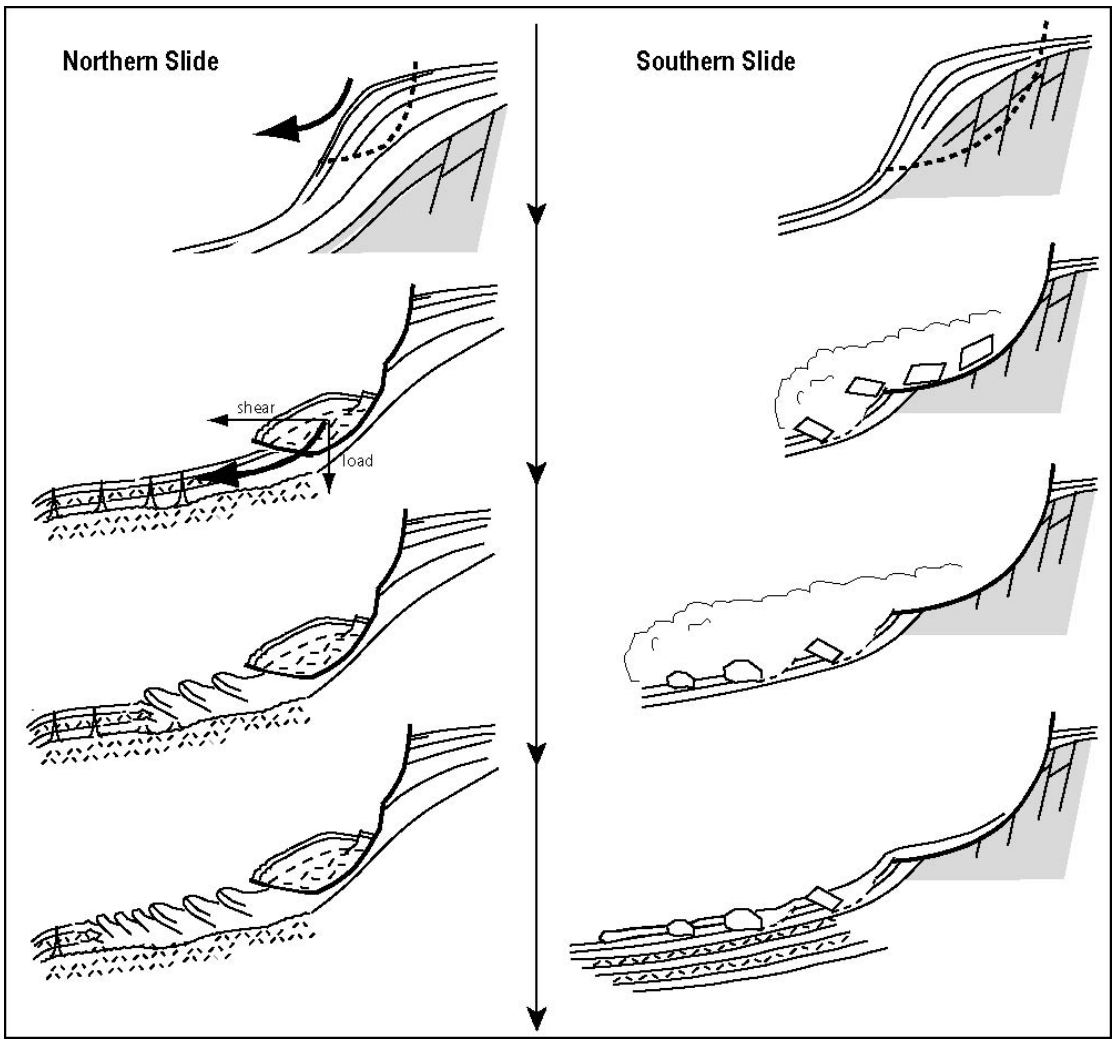

CHAPTER 5

This chapter consists of an article titled “Recent high frequency of sediment failures in Gela Basin (Sicily Channel), predisposing factors and possible future scenarios” by Minisini D. and Trincardi F., submitted to “Journal of Geophysical Research”.

High frequency of failures on the continental slope of Gela Basin (Sicily Channel), predisposing factors and possible future scenarios

Minisini D.[1-2] and Trincardi F. [1]

1 - ISMAR-CNR, Via Gobetti, 101, 40129 Bologna, Italy

2 - Dipartimento Scienze della Terra e Geologico-Ambientali, Università di Bologna, Via Zamboni 67, 40126 Bologna, Italy

ABSTRACT

Combination of seismic stratigraphy and seafloor geomorphology documents multiple slide scars and mass-transport deposits, buried and exposed, that shaped the continental slope of Gela Basin, Central Mediterranean. The very high resolution of geophysical data provides clues to: 1) reconstruct successive phases of failure stressing on the same location, 2) associate specific stratigraphic surfaces to glide planes, 3) analyze regional setting and indicate best place where to study mass wasting frequency. In particular, we recognized five failure phases since the Last Glacial Maximum, and determined a failure return interval of *ca*. 3 ky, two orders of magnitude higher compared to the best known oceanic margins.

1. INTRODUCTION

Most slides occur in a succession of multi-events [e.g., *Mulder and Cochonat*, 1996] and recognition of successive phases of failure is critical when they: 1) occur very close to each other in time, 2) enlarge the head region hampering a precise definition of the previous headscarps, 3) remobilize mass-transport deposits produced during the previous phases, 4) affect small volumes of material in each successive phase (0.01 to 0.1 km^3) posing a practical problem in their identification and correlation. In all these cases morphologic and stratigraphic reconstructions are complementary keys to understand, respectively, the cross-cutting relationship among successive headscarps and the stratal relationships among overlapping failed masses. The flanks of Gela Basin , in the Sicily Channel (Central Mediterranean) are recurrently impacted by failure through the Quaternary and are therefore an ideal site where to apply these reconstructions (Fig. 1). Basin sequences show evidence of stacked acoustically-transparent and/or chaotic deposits, characterised by irregular upper surfaces, interpreted to have resulted from mass-transport events; also the seafloor morphology displays both old, partially buried, and recent slide products. Using multibeam bathymetry, Chirp-sonar records and recovered sediment samples a detailed investigation was conducted to determine the geomorphological parameters and the internal geometry of these mass-transport complexes and to shed light on the stages, timing and frequency of failure events. In particular, examination of continental slope sediment sequences provides a novel approach to the study of failure frequency and produces a more coherent set of data on failed-deposits provenance than investigations of basin plains. This approach is suitable for instabilities of well-

defined slope areas and their consequent geohazard risk assessment rather than for basin-scale studies.

2. GENERAL SETTING

Gela Basin is the most recent (Plio-Quaternary) foredeep of the Maghrebian fold-and-thrust belt, loaded in the northwest by Gela nappe, an accretionary melange that represents the southernmost compressive element of this belt [*Argnani*, 1990] (Fig. 1). This foredeep basin is north of the Sicily Channel rift zone that originated from oblique extension and created relatively deep pull-apart basins [*Finetti*, 1984]. This extensional phase onset in late-Miocene to early Pliocene and lasted through the Quaternary [*Grasso*, 1993].

Karstified breccias resting on Lower-Pliocene marls outcrop on the mainland north-east of the study area and record a phase of uplift during mid-Pliocene to Quaternary times affecting the entire southern rim of the Hyblean Plateau [*Gardiner et al.*, 1993]. This uplift nourished the westward-dipping Quaternary progradational wedges observed on the western flank of the Malta plateau, seaward counterpart of the Hyblean Plateau [*Gardiner et al*., 1993].

Gela Basin is affected by shallowly active sub-vertical deformation and faulting [*Gardiner et al.,* 1993; *Max et al.,* 1993]. The fill of Gela Basin is dominated by mass-transport deposits of variable volume; evidence of recent and exposed slide deposits comes from seismic surveys along the northern and eastern margin [*Gardiner et al*., 1993; *Max et al.,* 1993; *Minisini et al*., 2006a; *Minisini et al*., subm.]. The Gela Basin area shows evidence of gas-charged sediment, small-scale mud volcanoes

[*Holland et al., 2004*], subrounded pockmarks at seafloor and vertical paths of fluid escape that obliterate the stratigraphic record [*Max et al*., 1993; *Minisini et al.*, subm.]. The upper slope includes drift deposits and associated moats [*Minisini et al.*, subm.]; similar bottom-current deposits characterize Mediterranean regions resulting in areas where sediment accumulation rates are greater than 1800 mm/ky [*Verdicchio et al.*, 2007]. According to *Lermusiaux and Robinson* [2001], the study area in Gela Basin is affected by a subsurface cyclonic gyre that flows along slope and is consistent with the formation of the observed sediment drifts and moats.

3. METHODS

The data set for this study has been collected by ISMAR-CNR (Bologna) during three cruises on board R/V Odin Finder (2000) and R/V Urania (2004 and 2005). The Chirp-sonar profiles use a 2-7 kHz sweep-modulated band width, equivalent to a 3.5 kHz profiler, and have a recording length up to 1500 msec, depending on water depth. High-resolution swath bathymetry data derives from a 50-kHz EM-300 and RESON 8160 multibeam. Sediment cores discussed in *Minisini et al*. [subm.] were collected using a piston corer with variable barrel lengths (5-20 m). Track-line positioning was based on D-GPS navigation, assuring a position accuracy of circa 10 m, and transformed to geographic coordinates referred to the ED-50 datum.

4. SEAFLOOR MORPHOLOGY

Most of the northern and eastern slopes of Gela Basin show evidence of mass-transport deposits exposed at seafloor with local slope of 27°. The continental slope unaffected by mass-wasting features records an average dip of 3°. Two slide complexes from recent failures (termed Twin Slides) are obvious on bathymetric data forming subrounded scars on the slope and basinward topographic bulges (Fig. 2). Paleo-slides, shallowly buried by younger deposits, show more reduced seafloor expressions but are still discerned on the bathymetry (Fig. 2). In particular: the lower slope shows elongated reliefs corresponding to buried failed masses of variable thickness and relief (Fig. 2); the western upper slope shows few NE-SW small-scale linear depressions, between 2.5 and 5 km in length, related to erosional gullies draped by recent deposits; some of these buried gullies converge into a broad concave-upward depression related to a paleo-scar; the upper slope between the Twin Slides exhibits a broad crescent-shape step extending eastward inherited from a larger buried slide feature (termed Father Slide); the eastern slope, veering to a more north-south direction, presents a set of gullies and major incisions that gradually disappears downslope where the gradients decrease and mass-transport deposits accumulate. The eastern sector is characterized also by the presence of sediment drifts, and associated slope-parallel moats, located along the 200 m contour, just shallower than gully heads (Fig. 2). Small-scale anticlines affect Quaternary units of the shelf edge and upper slope and laterally confine the heads and accumulation zones of several slides, including the Twin Slides.

5. STRATIGRAPHY

Two shelf-wide erosional unconformities are recognized in the study area: ES1, down to -170 m water depth (Fig. 3A), and ES2, a deeper erosional unconformity detected in the outer shelf and upper slope region but no longer detected basinward where the overlaying deposit is exceedingly thick (Fig. 4). Both surfaces have a combined origin: subaerial exposure of the shelf at sea-level low stands and rapid transgressive drowning during sea-level rises driven by 100 ky eustatic cycles, as observed on most Mediterranean margins [e.g., *Tesson et al*., 1988; *Trincardi and Field*, 1991; *Trincardi and Correggiari*, 2000; *Ridente and Trincardi*, 2002]. Therefore, the deposits between surfaces ES1 and ES2 are comprised between the end of MIS6 and the end of MIS2 lowstands. A paleo-valley complex, pre-dating ES2 formation, occurs in the area and affected successive fill geometry of sediment units (Fig. 3C, 5). The depositional sequence between ES1 and ES2 represents a progradational wedge dipping WSW-ward and formed during the drop of sea level during glacial times since MIS6 (Fig. 3D); prominent features in this sequence are: 1) a basin-wide mass-transport deposit and its broad paleo-slide scar (Father Slide) (Fig. 3C), 2) several stacked mass-transport deposits of variable extent above it, 3) a marine onlap surface marking the base of the last glacial (MIS2) progradational wedge, as documented by core P8 that reached the units beneath this onlap surface recovering sediment of MIS3 (Fig. 3A). A lenticular progradational unit at the shelf-edge with erosional base, steep internal clinoforms and a likely sandy or coarser-grain sediment, as suggested by the seaward lost of acoustic-signal penetration, resembles outer shelf ridges documented elsewhere in the Mediterranean and referred to the Last Glacial Maximum low stand

[e.g., *Trincardi and Field,* 1991*, Hernandez Molina et al.,* 2000*, Tesson et al.,* 2002] (Fig. 4).

Surface ES1 appears sharp and irregular due to the erosion of sediment units with variable strength (Fig. 5), as supported by *Max et al*. [1993] for the western Malta Plateau, where four unconformities with the same character as ES1 were identified and attributed to 100 ky sea-level low stands. The erosion generating ES1 exposed over-consolidated materials compared to what expected for not-eroded seafloor sediment [*Skempton*, 1970]. To the northwest the units beneath ES1 become gradually younger, and therefore it is likely that they also become; also, moving NW-ward along the contours, the ES1 surface becomes smoother and conformable, indicating that the sediment beneath it did not undergo subaerial erosion and likely remained normal-consolidated (Fig. 6A). Surface ES1 becomes conformable toward the basin (Fig. 3A) but can still be traced as a key reflector providing a clue for preliminary age assignments of the slope and basin sequences (Fig. 6).

On the outer shelf, the units overlaying ES1 include from bottom to top: 1) a faintly reflective drape that accumulated during the post-glacial sea-level rise and 2) a progradational wedge formed since about 5,5 ky BP when the modern sea level was attained [*Minisini et al*., subm.] (Fig. 3D). On the upper slope, these units combine into a deglacial sediment drift with a mounded morphology and an associated erosional moat (Fig. 3D, 7B). Immediately landward of Twin Slides headscarps, the inferred age of ES1 (ca. 18 ky at 120-130 m w.d.) and the thickness of overlaying units define a sediment accumulation rate in the order of 500-270 mm/ky (Fig. 3A, 9m/18ky; Fig. 3B, 5m/18ky), consistent with analyses of cores retrieved in the study area [*Minisini et al*., subm.] and with data from ODP site 963 on the NW side of Gela Basin [*Emeis et al.*, 1996].

6. MASS-TRANSPORT DEPOSITS

Above erosive surface ES2, deposits characterised by transparent to chaotic seismic facies with irregular tops document repeated mass-transport events separated by intervals of more draped deposition (Fig. 3D, 7).

6.1. Father Slide

A basinwide mass-transport complex is ubiquitous beneath the basinfloor and lower slope (Fig. 8A). Part of this basinwide mass-transport deposit can be traced into the Father Slide scarp that dissects thick progradational units at the shelf break and extends further SE of the study area (Fig. 2, 3C, 3D). At the headscarp, Father Slide presents acoustic-transparent facies with sharp and steep-sided reflector truncations (Fig. 6A), suggesting that failure affected consolidated masses with high shear strength; similar elements were tentatively assigned to catastrophic erosion followed by deposition by Fulthorpe & James (2004) in the "enigmatic" facies of the New Jersey outer shelf. The displaced mass of Father Slide filled Gela Basin with deposits that, when draped and loaded by rapidly-deposited younger sediment, may have compacted and released fluids, possibly predisposing further instability along the margin (Fig. 9A).

6.2. Minor failures

Above this basinwide mass-transport complex a stack of multiple but thinner mass-transport deposits displays acoustically-transparent facies, flat tops, and a tendency to fill and smoothen the pre-existing seafloor irregularities; this evidence together with the good penetration of the acoustic signal suggests that the deposits likely originated

as mass flows (Fig. 8A, 8B), as also suggested on several other mass-transport complexes [e.g., *Hampton et al.,* 1996]; also, the lack of clear headscarp regions suggests a failure mechanism subject to disintegration rather than to rigid rupture [e.g., *Mulder & Cochonat, 1996*]. Core P4 reached the most shallowly buried of these acoustically-transparent units (Fig. 8B) and recovered rip-up mud clasts and vegetal remains overlain by thin muddy or silty layers, thus suggesting a mud-flow deposit overlain by thin turbidites. Well-layered units intermingle with these acoustic-transparent units and present closely-spaced vertical artifacts or wipe outs that indicate possible fluid escape structures (Fig. 8A); in this view, the amplitude anomalies would represent variable scattering and absorption of the acoustic signal probably due to a dense distribution of fractures that channelize fluids [*Guy et al., 2003*; *Riedle et al, 2006*]; commonly fluid escape features root into pre-existing buried mass-transport deposits (Fig. 9). Where fluid-escape structures reach the seafloor the topography appears irregular with local subrounded depressions and hummocky seafloor morphologies (Fig. 2). In particular, a field of pockmarks with a typical 100 m spacing occurs atop of a distal mass-transport deposit overlaid by fluid-escape structures. Chirp-sonar profiles document craters more than 10 meters deep and few hundred meters in diameter without any sediment drape. This evidence of fluid–escape structures reaching the seafloor and the lack of infill within the pockmarks suggests that fluid escape may still be active at present.

6.3. Twin Slides

Twin Slides are two exposed mass-transport deposits whose internal structure, external geomorphology and runout distance indicate a more rigid movement with

respect to the underlying mass-flow deposits [*Minisini et al., subm*.] (Fig. 2, 3A, 3B). Southern Twin Slide consists of a debris-avalanche deposit Southern Twin Slide consists of a debris-avalanche deposit (*sensu* Lee et al., 2007) and presents erosional features at its base (Fig. 8A, 10) that resemble the giant striations documented, at the base of slide complexes offshore Borneo [*Posamentier and Kolla*, 2003], offshore Angola [*Gee et al.,* 2005] and offshore Venezuela and Trinidad [*Moscardelli et al.* 2006]: these studies interpret the striations as basal erosional scours ploughed by downslope-moving cohesive blocks. Northern Twin Slide represents a debris-avalanche deposit overriden by a slump deposit (*sensu* Lee et al., 2007); the latter failure produced an isolated oval slide mass more than 1 km wide at the main drop in slope (in *ca*. 500 m w.d.) between the concave-upward evacuation zone and the irregular accumulation zone (Fig. 11). This slumped mass displays a smooth top and a shape remarkably similar to the pronounced indentation within the composite slide scar, suggesting that a reduced downslope movement of this block (>0,1 km^3) did not produce disintegration. The instantaneous movement of such a block in the upper slope area may have triggered tsunami waves [e.g., *Watts et al*., 2005]. Individual blocks with similar characteristics but considerably larger in volume are described by *Hasegawa and Kanamori* [1987], *Schwab et al*. [1993], and *Duperret et al.* [1995]. An acoustically stratified unit up to 6 m thick is detected on the upper part of the slumped block and was recovered by core P7. Biostratigraphy indicates that at least part of this stratified unit remained in its original stratigraphic order; such peculiarity was observed also in the Bassein Slide in the NE Indian Ocean [*Moore et al., 1976*] and the Sahara debris-flow deposits [*Gee et al., 2006*]. The foram assemblages of core P7 differs from that of other cores in comparable water depth but outside the slide deposit; in particular, some benthic foram species (e.g., *Melonis, Valvulinaria*) are

very abundant and typical of much shallower environment with respect to its recovery water depth. The presence of subvertical offsets on this stratigraphic unit further suggests that it moved as part of the slumped mass; in fact, extensional structures upslope and compressional structures downslope, likely developed during the slumping movement. Compressional structures propagated in the accumulation zone generating a thrust system with pressure ridges at seafloor [*Minisini et al*., subm.] (Fig**.** 11).

Both Twin Slides deposits appear few km downslope of their evacuation zones implying limited movement compared to other documented exemples of mass-transport deposits that travelled tens of km, particularly where hydroplaning is hypothesized [e.g., *Mohrig et al.*, 1998; *Elverhoi et al.*, 2005; and references therein]. It seems that, in the case of the Twin Slides, the failed material did not lubricate the basal surface of the larger coherent masses. Therefore, rapid freezing limited their downslope movement. This interpretation is supported by: 1) the relatively short runout of the mass-transport deposits as discussed by *Mohrig et al*. [1998], 2) the limited fan-shaped spreading of the failed masses along the lower slope, as suggested by *Posamentier and Kolla*, [2003], 3) the reduced stretching, and absence of a detached head, within mass-transport deposits in the accumulation zones [*Elverhoi et al*., 2000], 4) the evidence of erosional bases with scours that indicate direct incision operated by the failed material and negligible basal fluid layer during downslope movement [*Gee et al*., 2006].

The relationship between total fall height and runout distance of Twin Slides (0.041: Twin Northern Slide, 0.052: Twin Southern Slide - *Minisini et al.*, subm.) recalls values of subaerial landslides, thus remarking their reduced downslope mobility. Slides that have this character were suggested to involve failed masses that were not

saturated with fluids [*Legros et al.*, 2002]. In the study area this interpretation is consistent with: 1) the steep and deep-seated headscarps downcutting overconsolidated units; 2) the compact volumes of failed material, suggesting minimal disintegration during transport and 3) the maintainance of discrete internal shear strength and cohesion. Also *McAdoo et al.* [2000] and *Huhnerback and Masson* [2004] hypothesize that failures consisting of stiffer material travel less than failures involving softer, less consolidated sediment.

7. FAILURE PHASES AND TIMING

Seismic-stratigraphic correlations document that Father Slide scar cross-cut the base of the last glacial wedge and therefore post-dates the Last Glacial Maximum (LGM) (Fig. 12, 13). Within the paleoscar of Father Slide rapid sediment deposition and minor but repeated failures (subject to mass flow) took place since the LGM (Fig. 8A, 12). The high sediment accumulation rate resulted in the rapid burial of each of these mass-flow deposits increasing their pore pressure and enhancing fluid expulsion, as observed elsewhere by other authors [*Cartwright*, 1994; *Klaucke et Cochonat*, 1999; *Masson et al*., 2002], thus leading to repeated failure events (Fig. 13). The uppermost of these minor stacked mass-transport deposits occurred about 8,5 ky BP from at least two evacuation zones and affected the post-glacial rapidly-deposited units laying above the last glacial unconformity (ES1) and its correlative conformity [*Minisini et al*., subm.] (Fig. 8). Twin Slides occurred during the modern sea level high stand and probably during very recent times, as indicated by their deep-seated scars clearly

down cutting the last glacial unconformity ES1 or its correlative conformity as well as the overlying post-glacial unit (Fig. 3A, 3B). Both Twin Slides events cannibalized part of the pre-existing mass-transport deposits (Fig. 8A, 13).

8. FREQUENCY OF FAILURES AND ASSOCIATED BIASES

In Gela Basin at least five minor mass-transport deposits are stacked between the top of Father Slide and the Twin Slides exposed on the modern seafloor (Fig. 8)**.** Because all these five deposits are recorded together exclusively in the area where the Twin Slides accumulated, we infer that they also came from the upper slope adjacent to the Twin Slides. Moving basinward the frequency of failures would be biased by: the stacking of mass-transport deposits with distinct provenance from the irregular continental slope and by the lack of failures occurring in the upper slope or having short runout. For this reason, the five mass-transport deposits are taken in consideration where their runout overlap. Both further downslope or upslope, some of the failed deposits are missing: in a case because of shorter runouts (Fig. 8B), in the other because considering areas unaffected by failure (Fig. 5). Calculating the average recurrence time of failures through studies of mass-transport deposits in the basin plain may bias their local return interval as indirectly showed by Weaver (2003) that documented a failure return interval of tens of ky in the Madeira Abyssal Plain and calculated a return interval of 3 My in the associated upper continental slope; the discrepancy evidences the collector function acted by the basin plain that recorded mass-transport deposits with distinct provenances from throughout the Canary Basin. This approach may be useful to study a relationship between failures and climatic

factors at basin scale but it may fail when the object of study is the slope, its stability and its geohazard risk assessment.

In Gela Basin, the timing of the considered five mass-transport deposits is constrained between the LGM (ca. 24-27 ky; occurrence of Father Slide) and 8,5 ky (dating of uppermost failed deposit), thus encompassing ca. 15-18 ky. In the lack of more precise age control on each mass-transport deposit, we subdivide evenly this time span by the number of failed masses in the stratigraphic record and obtain a return interval of *ca.* 3 ky. This value results two orders of magnitude higher with respect to studies inferring the recurrence of failures on the best known oceanic margins [e.g., *Weaver et al*., 2003; *Solheim et al*., 2005]. Despite most authors interpret the apparent cyclicity of mass-transport deposits as primary driven by Pleistocene high-frequency sea-level changes [e.g., *Weaver et al*., 1992; *Urgeles et al*., 1997; *Krastel et al*., 2001], the time constraints that encapsulate the stacked mass-transport deposits in Gela Basin suggest a much higher-frequency mechanism at work than sea level fluctuations alone.

9. MINOR SLOPE FAILURES: A POSITIVE FEEDBACK?

An intriguing observation in Gela Basin is the apparent regularity of the minor stacked mass-transport deposits and evenly layered units deposited after Father Slide (Fig. 8, 12). Deposition of failed masses generates an instantaneous load on sediment units at seafloor dramatically increasing their pore pressure, particularly where seafloor sediment is uncompacted. Alternatively, erosion and shearing generated by moving failed masses may lead to a drop in pore-pressure at the base of mass-

transport deposits where the underlying units are overpressured (Fig. 14). Both cases drive pore fluids to move toward, and to accumulate into, the overlaying chaotic mass-transport deposit, increasing its overpressure [e.g., *Masson et al*., 2002]. Further upward migration of pore fluids occurs where the failed mass is rapidly buried [e.g., *Trincardi et al*., 2004]. In the study area, this is the case where rapidly-deposited, and therefore undercompacted, sediment units accumulated on the slope above failed masses (Fig. 14) and resulting affected by fluid migration from the units beneath. This migration leads to sediment instability by increasing sediment overpressure, further increasing the likelihood of failure in the region. The role of fluid escape in favouring slope failure is evident in Chirp-sonar profiles (Fig. 9) showing the distinctive spacing, width and shape of subvertical acoustic anomalies on individual stratigraphic intervals that separate the mass-transport deposits. These structures suggest that fluid escape reaching the pre-existing seafloor stopped or reorganized each time a failed mass covered the basin (Fig. 14).

Following the initial failure, some landslides mobilize into flows whereas others undergo limited deformation [*Hampton et al.* 1996]. The mechanisms for mobilization into flows are not well understood but a longstanding hypothesis holds that a landslide evolution depends on the initial sediment porosity, the specific critical-state porosities achieved during shear deformation [*Schofield and Wroth*, 1968] and on the initial density state of the sediment [*Poulos et al.* 1985, *Lee et al.* 1991]. The initial state conditions depend on the porosity-effective stress ratio that a sediment assumes when strained; contractive sediment increases pore pressures when strained, and reduces the shear strength of the failed masses, resulting in mass flows rather than in movements of coherent material. Contractive behaviour well applies to the thin and widespread mass-transport deposits lacking clear headscarp regions, documented at several

stratigraphic levels on the Gela continental slope (Fig. 3C, 8, 12). Pore pressure of these mass-transport deposits likely increased through a rapid drop in sediment porosity during failure. Both porosity and pore pressure tend to decrease during failure but dissipation of pore pressure can rarely keep pace with sediment deformation [*Iverson et al.*, 1997; 2000]; therefore, the relatively faster drop in porosity results in an increased pore pressure greatly influencing landslide behavior. Hence, high porosity and low compaction likely characterized the failed units in Gela Basin but both disappeared after the initial failure, contributing to a pore pressure increase.

The combined effects of high pore-pressure gradient and rapid successive deposition likely triggered a positive feedback that enhanced the probability of recurrent mass-wasting through: 1) increasing pore-pressure gradients within slope sediment; 2) failed masses reaching the basin and loading rapidly-deposited fine-grained seafloor deposits; 3) low permeability of the resulting failed mass; 4) high sediment accumulation rate of the units overlaying and rapidly loading the mass-transport deposit and 5) upward migration of fluid flow potentially destabilizing the slope. The development of glide planes on elements of precursor slope failures (i.e., top of mass-transport deposit – see paragraph "11.1. Glide planes and stratigraphy") and the stacking pattern of mass-transport features recorded in the stratigraphic architecture emphasizes the preferential occurrence of slides in areas previously affected by slope instability.

10. SIGNIFICANCE OF DEEP-SEATED FAILURES

A distinctive internal structure and external geomorphology characterize the deep-

seated Twin Slides and Father Slide, respect to the minor slope failures that resulted from mass flows (Fig. 2, 10, 11). Had Twin Slides involved only mobile material with contractive behaviour, the resulting failed deposits would have been similar to the pre-exisitng layered stacked acoustically-transparent units (Fig. 8). The peculiar stratigraphic architecture of the failed units influenced significantly the distinctive characters of Twin Slides (including the occurrence of thrusts and pressure ridges, large blocks and associated erosional scours – *Minisini et al., subm*.), as probably occurred for a limited number of older mass-transport deposits that show significant morphological relief (even after burial and compaction) (Fig. 8).

Hence, we observe that seismic stratigraphy registers the stacking pattern of mass-transport deposits generated by multiple and successive minor failures having mass-flow mechanisms and negligible remoulding of the seafloor sediment. When failures are more deep-seated and affect more consolidated sediment units, the stratigraphic record of previous mass-transport deposits can be entirely cancelled by erosion and remoulding or remain undetected by acoustic signal that does not penetrate consolidated failed masses. As a consequence, a potential previous activity of frequent failures would be hampered, giving a different significance to the geohazard risks. A regional study of the stratigraphic record may help indicating if the failed area was previously affected by minor but more frequent failures. For instance, Father Slide, having a deep-seated evacuation area (Fig. 12), remolded a conspicuous section of stacked mass-transport deposits. Also Northern Twin Slide remoulded several pre-existing failed masses although mobilizing a reduced mass compared to Father Slide (Fig. 8A). In conclusion, the main slope readjustment takes place through larger and lower-frequency slides. A similar trend is documented in subaerial environments by *Hovius et al*. [1997] and is represented by the more general Poisson law used where

the probability of an event is low, but the number of opportunities for such occurrence is high.

11. PREDISPOSING FACTORS AND TRIGGERS

11.1. Glide planes and stratigraphy

The lithology close to the glide planes of failed masses is unknown; however, in Twin Slides marked seismic expression of these surfaces reflects a significant acoustic-impedance contrast, in turn, suggesting an abrupt physical change, as observed elsewhere by *Martinez et al*. [2005]. A major factor controlling the differences in the morphology between the Twin Slides resulted from the distinct stratigraphic rooting of the respective glide planes. Part of Southern Twin Slide failed along the shear plane previously followed by Father Slide (Fig. 3B). Northern Twin Slide moved on a basal shear surface atop a unit consisting of chaotic and likely remolded material and interpreted as a buried mass-transport deposit (Fig. 11B). It is likely that this older deposit maintained high pore pressure after it stopped, as suggested by fluid escape features emanating from its top and affecting the units above (Fig. 9A); this process has been documented elsewhere by *Masson et al*. [2002].

It is worth to note that shallowly buried glide planes occur on specific stratigraphic surfaces, as the marine onlap surface that acted as weak layer for part of Northern Slide (Fig. 3A) and the correlative conformity of ES1 on which several failed masses slid during distinct time intervals (Fig. 8B). These observations reflect the importance of pre-failure architecture of sedimentary bodies in understanding slope stability along continental margins. Key stratigraphic surfaces include erosional unconformities, paraconformities, onlap and downlap surfaces. In the Tyrrhenian Sea, Licosa Slide

documents the latter case in low-stand shelf margin deposits [*Trincardi and Field*, 1991]. It seems that these stratigraphic surfaces coincide with physical variations in sediment properties likely related to lithology, sediment accumulation rate, compaction and cementation, thus predisposing preferential planes of rupture when shallowly buried. Understanding the stratigraphy of submarine slide scars and associated failed deposits helps identify potential slip planes and areas that are more prone to failure.

11.2. Faults and weak layers influence

According to *Petley et al*. [2005], repeated seismic shocks induce proto-shear-surfaces and initial creep until shear stress starts to increase hyperbolically exceeding the shear strength of the material, causing a catastrophic acceleration to failure. In the study area, shear stress may have concentrated on sub-vertical faults (Fig. 7) and on bedding-parallel layers of mass-transport complexes (Fig. 8, 12) producing relatively small amounts of strain on these pre-existing discontinuities. The resulting breakdown of these discontinuities generated a consequent reduction of shear strength where failure was kinematically admissible. A predisposing factor for deep-seated slides may be represented by the combination of these subvertical shear zones and subhorizontal weak layers that facilitated the slope dissection affecting the upper slope up to the shelf-break, while across the shelf the influence of seafloor steepness, one of the main predisposing factors for failure, drops dramatically.

11.3. Tectonic elements

Both Twin Slides impacted the shoulders of the buried Father Slide headscarp (Fig. 12) generating a failure sequence similar to the “successive adjacent slides”

documented by *Mulder and Cochonat* [1996]. The location of the Twin Slides was influenced by the pre-existing margin stratigraphy and morphology. In addition, regional tectonic activity may have reduced the mass strength through locally increasing fracturation and by enhancing the seaward dip of discontinuities. Similar factors act also in subaerial slides, as documented by *Brideau et al.* [2005].

Southern Twin Slide locates at the intersection of growth faults along the mounded drift deposits (Fig. 12) and a deeper fault perpendicular to the slope (Fig. 15A). This slide impacted a pre-existing sinformal area confined by two antiforms perpendicular to the slope, that possibly constrained lateral propagations of the failure (Fig. 15A). Northern Slide occurred on a "high" (Fig. 15B) and the initial rupture developed at an inflection point where reflectors packages change from concave-upward to convex-upward and a steepening of the subsurface occurs, reflecting the ancient geomorphology of the margin; an antiform to the north confines failed masses and the basinward thrust system stopped at the edge of another pre-existing antiform (Fig. 2).

11.4. Sediment accumulation rate

Predisposing factors for failures include the high sediment accumulation rate (SAR) resulting in likely undercompacted sediment with excess pore pressures, as well documented elsewhere among others by *Klaucke et Cochonat* [1999] and *Masson et al*. [2002]. The study area presents sediment-drift deposits with high SAR both in the outer-shelf and upper-slope. SAR of 270-500 mm/ky characterizes the outer-shelf around Twin Slides (Fig. 3A, 3B). In the upper slope, the sediment units infilling Father Slide scar (ca. 60 m thick) display as well a high SAR (Fig. 3C): since these units post date LGM (ca. 24 ky), SAR results in the order of 2000-3000 mm/ky, that is a order of magnitude above the average of ODP site 963 [*Emeis et al., 1996*] and

collected cores on the outer-shelf in the study area [*Minisini et al., subm*.]. SAR in continental margins swept by along-slope bottom currents in the Central Mediterranean can reach 1850 mm/ky [*Verdicchio et al.,* 2007]; in the study area, the higher SAR value is biased by the stacked mass-transport deposits whose emplacements occurred instantaneously after failure.

In conclusion, a preferential setting for recurrent slope instability is determined by: 1) the conspicuous SAR favoured by the large embayment formed by Father Slide scar whose location, in turn, may reflect the underlaying paleo-incision complex (pre-dating ES2 -Eemian) (Fig. 5) and probably related to the loading effect of the parallel Gela nappe front (Fig. 1); 2) the steepness of Father Slide scar (Fig. 2); 3) the occurrence of weak layers typical of drift deposits [*e.g., Faugeres et al.,* 1999*; Bryn et al.,* 2005]. In addition, the presence of faults, either sealed or reaching the seafloor (Fig. 3A, 3B) and fluid escape features (Fig. 9) may have favoured the generation of weak planes for preferential ruptures and sliding determining the disintegrative mechanism of failures that gave shape to the stacking pattern of thin acoustically-transparent accumulation zones with conformable base (Fig. 8). The contemporaneity of Twin Slides events and the evidence of multiple sets of mass-transport deposits each set draped by a same stratigraphic level (Fig. 8) suggests the recurrent achievement of conditions favourable for failure and a recurrent trigger; in this case, seismicity is the most plausible trigger mechanism [e.g., *Syvitski and Schafer*, 1996; *Schnellmann et al*., 2002]. It is reasonable that the multiple phases of failures reflect repeated seismic shocks affecting the upper slope and outer shelf of the Gela margin.

Instrumental and historical series indicate that the seismicity of the area is small compared to other Mediterranean areas. However, the epicenters registered in the area in the last few decades (i.e. 2 shocks up to 4.2M, since 1970, http://neic.usgs.gov/neis/epic/epic.html, Fig. 1) would represent a significant frequency of seismic shocks if extrapolated to longer intervals. If the entire post-LGM interval is considered, 60 shocks in 1000 years would lead to some 2000 shocks during the post-glacial interval.

12. POSSIBLE FUTURE SCENARIOS

Based on geophysical data, the upper slope of the studied area coincides with a sector swept by bottom-current activity, both in the past and during present-day conditions. The bottom-current activity in the past is recorded since the last glacial interval by: 1) the paleo-incision complex, its fill and its internal erosional surfaces (Fig. 5), 2) the mounded drift deposits that overlay Father Slide scar (Fig. 3C, 12), 3) significant local reductions in the thickness of late Pleistocene and Holocene sediment units (Fig. 5). The modern activity of bottom currents is emphasized by: 1) drift deposits and related moat exposed at seafloor suggesting a flow path along the 200 m contour [*Minisini et al., subm.*] (Fig. 2), 2) local minor scours parallel to the slope, and 3) erosional areas of the seafloor that truncate reflectors of Holocene units (Fig. 5). These elements allow propose two end-member scenarios as future development for this study area affected by multiple and variable failure events. Depending on the role of sediment input and its distribution, the embayments of the deep-seated Twin Slides may: 1) act

as new collectors for the sediment carried by along-slope bottom currents, and re-edit the positive feedback of repeated minor failures; 2) capture part of the subsurface cyclonic gyre that flows along slope [*Lermusiaux et Robinson, 2001*] generating a conduit capable to channelize dense waters into a proto-canyon. Although the first scenario cannot be ruled out, the second hypothesis seems the most convincing because of the sediment units condensed or eroded between the headscarps of the Twin Slides that localize a preferential bottom current path, in particular along the southern part of the buried Father Slide scar (Fig 3). Therefore, we infer that the morphologic indentation of the Southern Twin Slide may capture part of the along-slope flows and drive them downslope, as suggested also by the presence of a minor erosional channel with chaotic seismic facies inside the evacuation zone. Furthermore, the Twin Slides area presents the key factors influencing a proto-canyon formation and recognized by several authors in a range of continental margins [e.g., *Farre et al.,* 1983; *Galloway et al.,* 1991; *Pratson and Coakley,* 1996]: 1) failure in the upper slope, 2) retrogressive indentations, 3) structural confinement of evacuated areas and, 4) capture of contour-parallel bottom currents. Biologic data integrate geophysical evidence of bottom current activity and lend weight to the hypothesis of the development of a proto-canyon; in fact, preliminary results of modern distribution of benthic foraminifera at the seafloor indicate significant differences between samples collected in the open slope and in the Southern Twin Slide. In particular, the samples of this slide scar lack living specimens and have a microfauna that presents a bad preservation state; downslope, superficial samples from the failed mass are dominated by organically cemented agglutinants in the living as well as in the total assemblage (with particularly high abundance of tubular agglutinant species) (Asioli, pers. comm.). Also these results seem to indicate that the Southern Twin Slide represents

an area somewhat affected by sediment transport in contrast with the open unfailed slope and the Northern Twin Slide areas.

13. CONCLUSIONS

Geomorphological, stratigraphic and sedimentological data support the following conclusions:

1) Conceptual problems arise when choosing the study area for failure recurrence: some basin sectors collect failed masses from distinct provenance (overestimation of recurrence), other basin sectors lack failed masses having short runout (underestimation of recurrence), while the upper slope may present areas unaffected by failure (underestimation of recurrence). In the study area, the lower slope presents five mass-transport deposits where their runout overlap. The return interval of these failures, that post-date the Last Glacial Maximum, results ca. 3 Ky, a value two orders of magnitude higher compared to the recurrence of failure on the best known continental margins.
2) The development of glide planes on elements of precursor slope failures (i.e., top of mass-transport deposits) and the stacking pattern of mass-transport features recorded in the stratigraphic architecture emphasizes the preferential occurrence of slides in areas previously affected by slope instability. The combined effects of high pore-pressure gradient and rapid deposition likely trigger a positive feedback that enhances the probability of recurrent mass-wasting.

3) Pre-failure stratigraphic architecture determine preferential failure planes, as the marine onlap surface at the base of the last glacial wedge and the base of the post-glacial units on which several failed masses slid during distinct time intervals. Understanding the stratigraphy of submarine slide scars and associated failed deposits helps to identify potential slip planes and define areas that are more prone to failure.
4) The embayment and the steepness of a paleo-slide, the high sediment accumulation rate resulting in a rapid recharge of meta-stable sediment, and the occurrence of weak layers determine a preferential setting for slope instability.
5) Stratigraphic, geomorphological and biological data suggest that Southern Twin Slide captures part of the along-slope currents and drive them downslope, hence catalizing headward erosion and generating preferential pathways that act as a proto-canyon.

FIGURE CAPTIONS

Fig. 1. Location of the Gela Basin in the Sicily Channel, Central Mediterranean Sea (bathymetric contour intervals are every 100 m, from GEBCO data base –onland image from SRTM data base). Circles are historical earthquakes recorded since 1970 (USGS data base), diameter of open circles represent four ranges of magnitude (up to 2.8, 3.2, 4.2, 5.3), solid circles represent earthquakes of unknown magnitude.

Fig. 2. Multibeam swath bathymetry and overlaying shaded relief of the study area in the Gela Basin (artificial sun angle from NW, red is 180 m, dark blue is 1000 m); central sector shows two evident slides exposed at the seafloor (Twin Slides).

Fig. 3. A) Northern Twin Slide scar cutting through the stratigraphic section from last glacial deposits to most surficial sediment units. Note the erosional surface ES1 that becomes conformable toward the basin and the onlap surface at the base of the last glacial progradational wedge. Post-glacial outer-shelf deposit records SAR of ca. 500 mm/ky. B) Southern Twin Slide cuts a local depocenter that lays on Father Slide scar; closely-spaced faults beneath Father Slide evacuation zone root beyond the acoustic signal penetration. Post-glacial outer-shelf deposits records SAR of ca. 270 mm/ky. C) Chirp-sonar profile showing 60 m-thick sedimentary unit overlaying the basinwide Father Slide scar that dissects thick sections of last-glacial deposits. Polygons are buried mass-transport deposits; locally they root fluid escape structures. D) Simplified stratigraphic scheme of the late-Quaternary deposits on the NE margin of the Gela Basin. ES are regional erosional surfaces and related conformities. Late-Quaternary depositional sequence in Gela Basin; the pronounced erosional uncomformities (ES1-ES2) fomed during last sea-level lowstands, associated with 100 ky-glacial cycles. Light gray area represents the maximum depth reached by Twin Slides failure planes (modified from *Minisini et al.*, subm.).

Fig. 4. Chirp-sonar profile showing two regional erosional surfaces (ES1 – ES2) and a lenticular progradational unit interpreted as an outer-shelf ridge referred to the Last Glacial Maximum.

Fig. 5. The Chirp-sonar profile, located upslope with respect to Father Slide, shows the regional stratigraphic setting with deposits of last falling stage that become progressively younger, and likely less consolidated, toward NW where ES1 appears smoother without the sharp steps shown in the SE sector. Note the buried incised valley complex and the truncated reflectors of the deglacial unit suggesting erosion of bottom-currents at present.

Fig. 6. Chirp-sonar profiles cross-cutting each other and showing deglacial drift and outer-shelf deposits accumulated during post-LGM sea-level rise and modern high stand. A) along slope, ES1 correlates from base of outer-shelf deposits to base of upper-slope sediment drift; this profile presents also the landward apex of Father Slide scar where acoustically-transparent facies are interpreted as in situ deformed blocks; these deformed units are constrained among faults rooted beyond the acoustic-signal penetration. B) across slope, no direct correlation of ES1 is observed.

Fig. 7. Simplified scheme of main failure complexes occurring above surface ES2 and affecting post-Eemian units; 1: Father Slide; 2: minor slope failures; 3: Twin Slides.

Fig. 8. Along-slope Chirp-sonar profiles showing a basinwide mass-transport complex ubiquitous beneath the basinfloor and lower slope; above it, a stack of multiple thinner mass-transport deposits interpreted as derived from mass flow events; intermingled well-layered units present several sets of fluid-escape structures. A) The concentration of stacked mass-transport deposits between Twin Slides represents a key area to study frequency of failures. Note that Twin Slides deposits are entrenched with surrounding stratified units and remoulded embedded pre-existing failed masses. B) Mass-transport deposits, both coeval and not, present the same glide planes. Core P4 dates the uppermost mass-flow deposit to 8,5 ky BP. Note that not all mass-transport deposits registered in A are present in B.

Fig. 9. Chirp-sonar profiles showing distinct families of fluid-escape structures rooted in distinct mass-transport deposits.

Fig. 10. Chirp-sonar profile showing distal accumulation zone of Southern Twin Slide; note erosional scours ploughed by downslope-moving cohesive blocks and the longer runout of mobile material with respect to the blocky deposit.

Fig. 11. A. Shaded relief of multibeam swath bathymetry; illumination from N evidences the slumped mass in the proximal accumulation zone of Northern Twin Slide and its peculiar shape similar to the indentation marked in the composite scar. B. Chirp-sonar profile along the Northern Twin Slide deposit showing from left to right: distal part of slumped mass, thrust system, appearance of glide plane, tip of mas-transport deposit.

Fig. 12. Chirp-sonar profile showing source units of Twin Slides and the stratigraphy among them.

Fig. 13. Schematic summary of main failure phases along the NE continental slope of Gela Basin.

Fig. 14. Simplified sketch of distinct cases of pore pressure increase on sediment units.

Fig. 15. A. Chirp-sonar profiles showing evacuation zones of Southern (A) and Northern (B) Twin Slide. A. sinformal area affected by a fault and confined by two antiforms. B. Topographic high subject to rupture where slope gradient increases basinward.

REFERENCES

Argnani, A. (1990), The strait of Sicily Rift Zone: foreland deformation related to the evolution of a back-arc basin, *Journal of Geodynamics, 12,* 311-331.

Asioli A., F. Trincardi, J.J. Lowe., and F. Oldfield (1999), Short-term climate changes during the Last Glacial-Holocene transition: comparison between Mediterranean records and the GRIP event stratigraphy, *Journal of Quaternary Science, 14*, 373-381.

Asioli A., F. Trincardi, J.J. Lowe., D. Ariztegui, L. Langone, and F. Oldfield (2001), Sub-millennial climatic oscillations in the Central Adriatic during the last deglaciation: paleoceanographic implications, *Quaternary Science Reviews, 20*, 33-53.

Boe, R., M. Hovland, A. Instanes, L. Rise, and S. Vasshus (2000), Submarine slidescars and mass movements in Karmsundet and Skudenesfjorden, southwestern Norway: morphology and evolution. *Marine Geology, 167*, 147-165.

Brideau, M.A., D. Stead, D. Kinakin, and K. Fecova (2005), Influence of tectonic structures on the Hope Slide, British Columbia, Canada, *Engineering Geology, 80*(3-4), 242-259.

Bryn, P., K. Berg, M.S. Stoker, H. Haflidason, and A. Solheim (2005), Contourites and their relevance for mass wasting along the mid-Norwegian margin, *Marine and Petroleum Geology, 22*(1-2), 85-96.

Bugge, T., Belderson R.H., and Kenyon N.H. (1988), The Storegga slide, *Royal Society (London), Philosophical Transactions, 325*, 357–388.

Cartwright, J.A. (1994), Episodic basin-wide fluid expulsion from geopressured shale sequences in the North Sea basin. *Geology*, 22, 447-450.

Catalano, R., S. Infuso, and A. Sulli (1993), The Pelagian foreland and its northward foredeep. Plio-Pleistocene structural evolution, in *UNESCO technical Reports in Marine Sciences, 58,* edited by M.D. Max and P. Colantoni, pp. 37-42.

Duperret, A., J. Bourgois, Y. Lagabrielle, and E. Suess (1995), Slope instabilities at an active continental margin; large-scale polyphase submarine slides along the northern Peruvian margin, between 5 degrees S and 6 degrees S, *Marine Geology, 122*(4), 303-328.

Edwards, B.D., H.J. Lee, and M.F. Field (1993), Seismically induced mudflow in Santa Barbara Basin, California, in *Submarine Landslides: Selected Studies in the U.S. Exclusive Economic Zone*, *USGS Bull.,* vol. B-2002, edited by W.C. Schwab, H.J. Lee and D.C. Twichell, , pp. 167-175, Washington D.C.

Elverhoi, A., C.B. Harbitz, D. Panagiotis, D. Mohrig, and G. Parker (2000), On the dynamics of subaqueous debris flows, *Oceanography, 13*(3), 109-117.

Elverhoi, A., D. Issler, F.V. Blasio, T. Ilstad, C.B. Harbitz, and P. Gauer (2005), Emerging insights into the dynamics of submarine debris flows, *Natural Hazards and Earth System Sciences, 5*(5), 633-648.

Embley, R.W. (1976), New evidence for occurrence of debris flow deposits in the deep sea, *Geology, 4*, 371-374.

Emeis, K.C., A.H.F. Robertson, C. Richer, and other 26 authors (1996), Site 963, *Proceedings of the ODP*, *Initial Reports, 160*, 55-84.

Farre, J.A., B.A. MecGregor, W.B.F. Ryan, and J.M. Robb (1983), Breaching the shelfbreak: passage from youthful to mature phase in submarine canyon evolution, in *The shelfbreak: critical interface on continental margins, SEPM, Spec. Publ.,* vol. 33, edited by D.J. Stanley and T.G. Moore, pp. 25-39.

Faugères, J. C., D.A.V. Stow, P. Imbert, and A. Viana (1999), Seismic features diagnostic of contourite drifts, *Marine Geology, 162*, 1-38.

Finetti, I. (1984), Geophysical studies of the Sicily Channel rift zone, *Bollettino di Geofisica Teorica e Applicata, 26*, 3-28.

Galloway, W.E., W.F. Dingus, and R.E. Paige (1991), Seismic and depositional facies of Paleocene-Eocene Wilcox Group submarine canyon fills, Northwest Gulf Coast, U.S.A, in *Seismic facies and sedimentary processes of submarine fans and turbidite systems*, edited by P. Weimer and M.H. Link, pp. 247-271, Springer-Verlag, Berlin.

Gardiner, W., M. Grasso, and D. Sedgeley (1993), Plio-Pleistocene stratigraphy and fault movement of the Malta Platform, in *UNESCO technical Reports in Marine Sciences, 58,* edited by M.D. Max and P. Colantoni, pp. 111-116.

Gee, M.J.R., D.G. Masson, A.B. Watts, and P.A. Allen (1999), The Saharan debris flow: an insight into the mechanics of long runout submarine debris flows. *Sedimentology, 46,* 317-335.

Gee, M.J.R., R.L. Gawthorpe, and J.S. Friedmann (2005), Giant striations at the base of a submarine landslide, *Marine Geology, 214*(1-3), 287-294.

Gee, M.J.R., R.L. Gawthorpe, and S.J. Friedmann (2006), Triggering and evolution of a giant submarine landslide, offshore Angola, revealed by 3D seismic stratigraphy and geomorphology, *Journal of Sedimentary Research, 76*(1), 9-19.
Geology, 33(2), 85-88.

Grasso, M. (1993), Pleistocene structures along the Ionian side of the Hyblean Plateau (SE Sicily): implications for the tectonic evolution of the Malta Escarpment, in *UNESCO technical Reports in Marine Sciences, 58,* edited by M.D. Max and P. Colantoni, pp. 49-55.

Haflidason, H., R. Lien, H.P. Sejrup, C.F. Forsberg, P. Bryn (2005), The dating and morphometry of the Storegga Slide, *Marine and Petroleum Geology, 22*(1-2), 123-136.

Hampton, M.A., A.H. Bouma, P.R. Carlson, B.F. Molnia, E.C. Clukey, and D.A. Sangrey (1978), Quantitative study of slope instability in the Gulf of Alaska, *10th Annual Offshore Technology Conference (OTC), 4*, 2307-2318.

Hampton, M.A, H.J. Lee, and J. Locat (1996), Submarine landslides, *Reviews of Geophysics, 34*(1), 33-59.

Hasegawa, H.S., and H. Kanamori (1987), Source mechanism of the magnitude 7.2 Grand Banks earthquake of November 18, 1929: double-couple or submarine landslide? *Bull. Seism. Soc.Am., 77*, 1984-2004.

Hasiotis, T., G. Papatheodorou, G. Bouckovalas, C. Corbau, and G. Ferentinos (2002), Earthquake-induced coastal sediment instabilities in the western Gulf of Corinth, Greece, *Marine Geology, 186*(3-4), 319-335.

Hernandez Molina, F.J., L.M. Fernandez Salas, F. Lobo, L. Somoza, V. Diaz del Rio, and J.M. Alveirinho Dias (2000), The infralittoral prograding wedge: a new large-scale progradational sedimentary body in shallow marine environments, *Geo-Marine Letters, 20*(2), 109-117.

Holland, C.W., G. Etiope, A.V. Milkov, E. Michelozzi, and P. Favali (2003) Mud volcanoes discovered offshore Sicily, *Marine Geology, 199*(1-2), 1-6.

Hovius, N., C.P. Stark, and P.A. Allen (1997), Sediment flux from a mountain belt derived by landslide mapping, *Geology, 25*(3), 231-234.

Huehnerbach, V., and D.G. Masson (2004), Landslides in the North Atlantic and its adjacent seas; an analysis of their morphology, setting and behaviour, *Marine Geology, 213*(1-4), 343-362.

Imbo,Y., M. De Batist, M. Canals, M.J. Prieto, and J. Baraza (2003), The gebra slide: a submarine slide on theTrinity Peninsula Margin, Antarctica, *Mar. Geol.,193*(3-4), 235-252.

Iverson, R.M, M.E. Reid, and R.G. LaHusen (1997), Debris-flow mobilization from landslides, *Annual Review of Earth and Planetary Sciences, 25*, 85-138.

Iverson, R.M., M.E. Reid, N.R. Iverson, R.G LaHusen, M. Logan, J.E. Mann, and D.L. Brien (2000), Acute sensitivity of landslide rates to initial soil porosity, *Science, 290*, 513-516.

Keefer, D.K. (1994), The importance of earthquake-induced landslides to long-term slope erosion and slope-failure hazards in seismically active regions, *Geomorphology, 10*, 265-284.

Klaucke, I. & Cochonat, P. (1999) Analysis of past seafloor failures on the continental slope off Nice (SE France). *Geo-Marine Letters*,19-4, 245-253.

Krastel, S., H.U. Schmincke, C.L. Jacobs, R. Rihm, T.P. Le Bas, and B. Alibes (2001), Submarine landslides around the Canary Islands, *Journal of Geophysical Research, B, Solid Earth and Planets, 106*(3), 3977-3997.

Lastras, G., M. Canals, J.E. Hughes Clarke, A. Moreno, M. De Batist, D.G. Masson, P. Cochonat (2002), Seafloor imagery from the BIG'95 debris flow, western Mediterranean, *Geology, 30*(10), 871-874.

Lastras, G., F.V. De Blasio, M. Canals, A. Elverhoi (2005), Conceptual and numerical modeling of the BIG'95 debris flow, western Mediterranean Sea, *Journal of Sedimentary Research, 75*(5), 784-797.

Lee, H.J. (2005), Undersea landslides: extent and significance in the Pacific Ocean, an update, *Natural Hazards and Earth System Sciences, 5*, 877-892.

Lee, H.J., J. Locat, P. Desgagnes, J.D. Parsons, B.G. McAdoo, D.L. Orange, P. Puig, F.L. Wong, P. Dartnell, and E. Boulanger (in press), Submarine Mass Movements on Continental Margins, in *Continental-Margin Sedimentation: from Sediment Transport to Sequence Stratigraphy*, *IAS special publication*, vol. 37, edited by C.A. Nittrouer, J.A. Austin, M.E. Field, J.H. Kravitz, J.P.M. Syvitski, and P.L. Wibergeds, Blackwell Publishing Ltd., Oxford.

Lee, H.J., W.C. Schwab, B.D. Edwards, and R.E. Kayen (1991), Quantitative controls on submarine slope failure morphology, *Mar. Geotech.*, *10*, 143-158.

Legros, F. (2002), The mobility of long-runout landslides, *Engineering Geology, 63*(3-4), 301-331.

Lermusiaux, P.F.J., and A.R. Robinson (2001), Features of dominant mesoscale variability, circulation patterns and dynamics in the Strait of Sicily, *Deep-Sea Research (Part I, Oceanographic Research Papers), 48*(9), 1953-1997.

Lindberg, B., J.S. Laberg, and T.O. Vorren (2004), The Nyk Slide; morphology, progression, and age of a partly buried submarine slide offshore northern Norway, *Marine Geology, 213*(1-4), 277-289.

Marr, J.G., P.A. Harff, G. Shanmugam, and G. Parker (2001), Experiments on subaqueous sand gravity flows; the role of clay and water content in flow dynamics and depositional structures, *GSA Bulletin, 113*(11), 1377-1386.

Martinez, J., J. Cartwright and B. Hall (2005), 3D seismic interpretation of slump complexes: examples from the continental margin of Israel, *Basin research, 17*, 83-108.

Masson, D.G., A.B. Watts, M.J.R. Gee, R. Urgeles, N.C. Mitchell, T.P. Le Bas, and M. Canals (2002), Slope failures on the flanks of the western Canary Islands, *Earth-Science Reviews, 57*, 1-35.

Max, M.D., A. Kristensen, and E. Michelozzi (1993), Small-scale Plio-Quaternary sequence stratigraphy and shallow geology of the west-central Malta Plateau, in

UNESCO technical Reports in Marine Sciences, 58, edited by M.D. Max and P. Colantoni, pp. 117-122.

McAdoo, B.G., L.F. Pratson, and D.L. Orange (2000), Submarine landslide morphology, US continental slope, *Marine Geology, 169*, 103-136.

Minisini, D., F. Trincardi and A. Asioli (2006), Evidence of slope instability in the Southwestern Adriatic Margin, *Natural Hazards and Earth System Sciences, 6-1*, 1-20.

Minisini, D., A. Asioli, F. Foglini and F. Trincardi (2006a), Widespread seafloor instability on Gela basin slopes (Sicily Channel), EGU Annual Meeting, Vienna, Austria, April 2-7.

Minisini, D., F. Trincardi, A. Asioli, M. Canu, and F. Foglini (submitted), Morphologic variability of exposed mass-transport deposits on the eastern slope of Gela Basin (Sicily Channel), *Basin Research*.

Mohrig, D., K.X. Whipple, M. Hondzo, C. Ellis, and G. Parker (1998), Hydroplaning subaqueous debris flows, *GSA Bulletin, 110-3*, 387-394.

Moore, D.G., J.R. Curray, and F.J. Emmel (1976), Large submarine slide (olistostrome) associated with Sunda Arc subduction zone, Northeast Indian Ocean, *Marine Geology, 21*, 211-226.

Moore, J.G., Normark W.R., and Holcomb R.T. (1994), Giant Hawaiian underwater landslides, *Science, 264*, 46-47.

Moscardelli, L., L. Wood, and P. Mann (2006), Mass-transport complexes and associated processes in the offshore area of Trinidad and Venezuela, *AAPG Bulletin, 90*(7), 1059-1088.

Mulder, T., and P. Cochonat (1996), Classification of offshore mass movements, *Journal of Sedimentary Research, 66*(1), 43-57.

Petley, D.N., T. Higuchi, D.J. Petley, M.H. Bulmer, and J. Carey (2005), Development of progressive landslide failure in cohesive materials, *Geology, 33*(3), 201-204.

Piper, D.J.W., P. Cochonat, and M. Morrison (1999), Sidescan sonar evidence for progressive evolution of submarine failure into a turbidity current: the 1929 Grand Bank event, *Sedimentology, 46*, 79-97.

Piper, D.J.W., Shor, A.N., and Hughes Clarke, J.E. (1988), The 1929 Grand Banks earthquake, slump and turbidity current, in *Sedimentological Consequences of Convulsive Geologic Events* edited by H.E. Clifton, Geological Society of America, Special Paper 229, pp. 77–92.

Posamentier, H.W., and V. Kolla, (2003), Seismic geomorphology and stratigraphy of depositional elements in deep-water settings. *Journal of Sedimentary Research, 73*(3), 367-388.

Poulos, S.G., G. Castro, and J.W. France (1985), Liquefaction evaluation procedure, *Jour. Geotech. Eng., ASCE*, *111*, 772-791.

Pratson, L.F., and B.J. Coakley(1996), A model for the headward erosion of submarine canyons induced by downslope-eroding sediment flows, *GSA Bulletin, 108*(2), 225-234.

Prior, D.B., and Coleman, J.M. (1984), Submarine slope instability. In: Slope Instability (Ed. by D. Brundsen & D.B. Prior), 419-455.Wiley, Chichester, NewYork.

Prior, D.B., B.D. Bornhold, J.M. Coleman, and W.R. Bryant (1982), Morphology of a submarine slide, Kitimat Arm, British Columbia, *Geology, 10*, 588-592.

Ridente, D., and F. Trincardi (2002), Eustatic and tectonic control on deposition and lateral variability of Quaternary regressive sequences in the Adriatic basin, *Marine Geology, 184*, 273-293.

Riedel, M., I. Novosel, G.D. Spence, R.D. Hyndman, R.N. Chapman, R.C. Solem, T. Lewis (2006), Geophysical and geochemical signatures associated with gas hydrate-related venting in the northern Cascadia margin, *GSA Bulletin, 118*(1-2), 23-38.

Schnellmann, M., F. Anselmetti, D. Giardini, and J.A. McKenzie (2005), Mass movement-induced fold-and-thrust belt structures in unconsolidated sediments in Lake Lucerne (Switzerland), *Sedimentology, 52*, 271-289.

Schnellmann, M., F.S. Anselmetti, D. Giardini, J.A. McKenzie, and S.N. Ward (2002), Prehistoric earthquake history revealed by lacustrine slump deposits, *Geology, 30*(12), 1131-1134.

Schofield, A.N., and C.P. Wroth (Eds.) (1968), *Critical State Soil Mechanics*, McGraw-Hill, New York.

Schwab W.C., H.J. Lee., and D.C. Twichell (Eds) (1993), *Submarine landslides: selected studies in the U.S. Exclusive Economic Zone*, USGS Bull., B-2002, Washington D.C.

Shanmugam, G, and Moiola, R.J. (1995), Reinterpretation of depositional processes in a classic flysch sequence (Pennsylvanian Jackfork Group), Ouachita Mountains, Arkansas and Oklahoma, *AAPG Bulletin, 79*(5), 672-695.

Shanmugam, G., R.J. Moiola, and J.K. Sales (1988), Duplex-like structures in submarine fan channels, Ouachita Mountains, Arkansas, *Geology, 16*(3), 229-232.

Skempton, A.W. (1970), The consolidation of clays by gravitational compaction, *Quart. Jour. Geol. Soc., 125*, 373-411.

Solheim, A., R. Bhasin, F.V. De Blasio, and other 22 authors (2005), International Centre for Geohazards (ICG): Assessment, prevention and mitigation of geohazards, *Norwegian Journal of Geology, 85*(1-2), 45-62.

Sprovieri, R., E. Di Stefano, A. Incarbona, and M.E. Gargano (2003), A high resolution record of the last deglaciation in the Sicily Channel based on foraminifera and calcareous nannafossil quantitative distribution, *Palaeogeography, Palaeoclimatology, Palaeoecology, 2002*, 119-142.

Sultan, N., P. Cochonat, M. Canals, A. Cattaneo, B. Dennielou, H. Haflidason, J.S. Laberg, D. Long, J. Mienert, F. Trincardi, R. Urgeles, T.O. Vorren, C. Wilson (2004), Triggering mechanisms of slope instability processes and sediment failures on continental margins; a geotechnical approach, *Marine Geology, 213*(1-4), 291-321.

Synolakis, C.E., J.P Bardet., J.C. Borrero, H.L. Davies, E.A. Okal, E.A.Silver, S. Sweet, and D.R. Tappin (2002), The slump origin of the 1998 Papua New Guinea tsunami, *Proceedings - Royal Society, Mathematical, Physical and Engineering Sciences, 458*, 763-789.

Syvitski, J.P.M., and C.T. Schafer (1996), Evidence for an earthquake-triggered basin collapse in Saguenay Fjord, Canada, *Sedimentary Geology, 104*(1-4), 127-153.

Tesson, M., B. Gensous, G.P. Allen, and C.H. Ravenne (1988), Late Quaternary deltaic lowstand wedges on the Rhone continental shelf, France, *Marine Geology, 91*, 325-332.

Tesson, M., H.W. Posamentier, and B. Gensous (2000), Stratigraphic organization of late Pleistocene deposits of the western part of the Golfe du Lion shelf (Languedoc shelf), western Mediterranean Sea, using high-resolution seismic and core data, *AAPG Bulletin*, *84*(1), 119-150.

Trincardi, F., and A. Correggiari (2000), Quaternary forced-regression deposits in the Adriatic basin and the record of composite sea-level cycles, in *Depositional Response to Forced Regression*, edited by D. Hunt and R. Gawthorpe, Geol. Soc. Spec. Publ., *172*, 245-269.

Trincardi, F., and M.E. Field (1991), Collapse and flow of lowstand shelf-margin deposits: An example from the eastern Tyrrhenian Sea, Italy, *Marine Geology, 105*, 77-94.

Trincardi, F., A. Cattaneo, A. Correggiari, and D. Ridente (2004), Evidence of soft sediment deformation, fluid escape, sediment failure and regional weak layers within the late Quaternary mud deposits of the Adriatic Sea, *Marine Geology, 213*, 91-120.

Urgeles, R., M. Canals, J. Baraza, B. Alonso, D. Masson (1997), The most recent megalandslides of the Canary Islands; El Golfo debris avalanche and Canary debris flow, West El Hierro Island, *Journal of Geophysical Research, B, Solid Earth and Planets, 102*(9), 20,305-20,323.

Verdicchio, G., F. Trincardi, and A. Asioli (in press), Mediterranean bottom-current deposits: an example from the Southwestern Adriatic Margin, in *Economic and palaeoceanographic importance of Contourite*, edited by A.R. Viana and M. Rebesco, Geol. Soc. Spec. Pub.

Watts, P., S.T. Grilli, D.R. Tappin, and G.J. Fryer (2005), Tsunami generation by submarine mass failure; II, Predictive equations and case studies, *Journal of Waterway, Port, Coastal and Ocean Engineering, 131*(6), 298-310.

Weaver, P.P.E., R.G. Rothwell, J. Ebbing, D. Gunn, and P.M. Hunter (1992), Correlation, frequency of emplacement and source directions of megaturbidites on the Madeira Abyssal Plain, *Marine Geology, 109*(1-2), 1-20.

Weaver, P.P.E. (2003), Northwest African continental margin; history of sediment accumulation, landslide deposits, and hiatuses as revealed by drilling the Madeira abyssal plain, *Paleoceanography, 18*(1), 9.1-9.12.

FIGURE 1

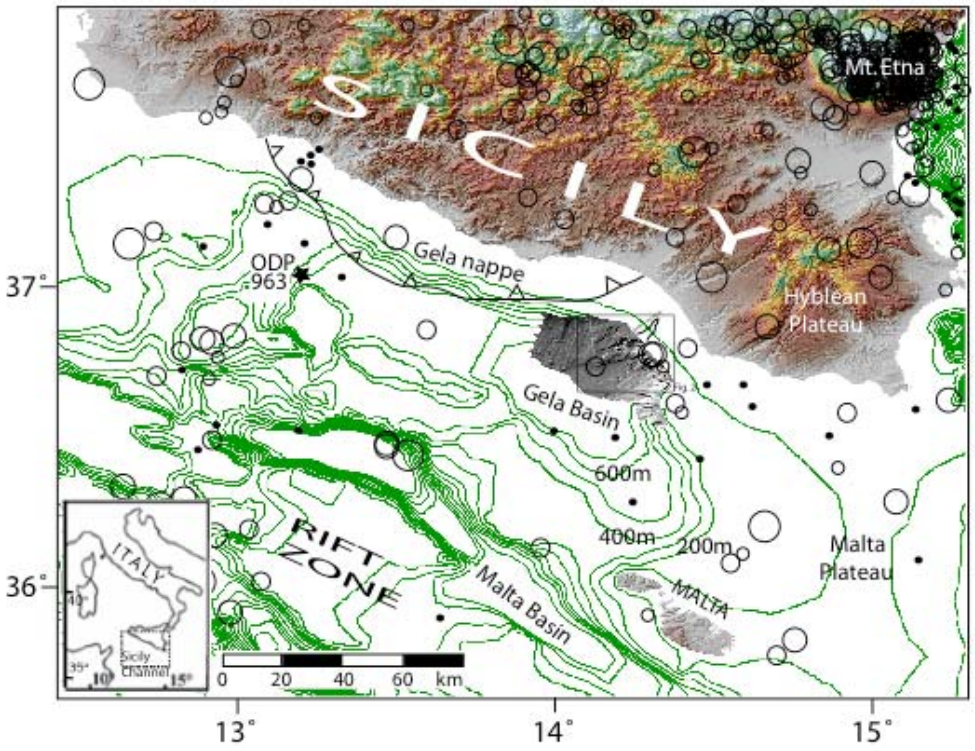
SICILY
Mt. Etna
Gela nappe
ODP
963
Hyblean
Plateau
Gela Basin
600m
400m
200m
Malta
Plateau
RIFT
ZONE
Malta Basin
MALTA
ITALY
Sicily
Channel
0 20 40 60 km
37°
36°
13°
14°
15°

FIGURE 2

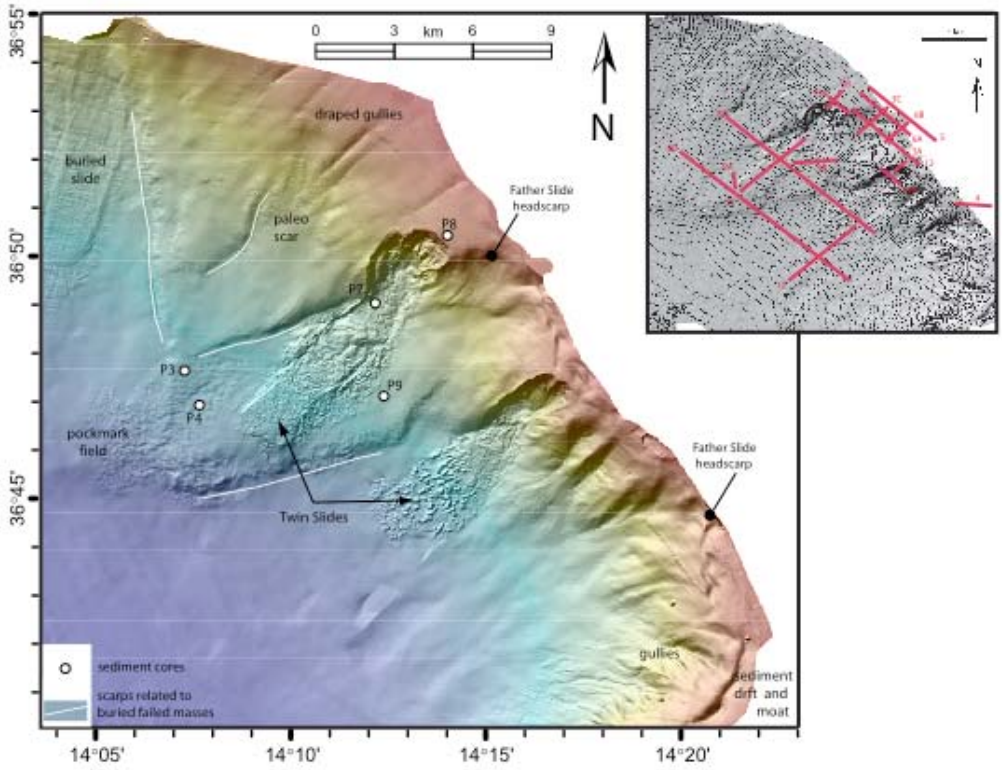
0
3
km
6
9
N
draped gullies
buried slide
paleo scar
Father Slide headscarp
P8
P7
P3
P9
P4
pockmark field
Twin Slides
Father Slide headscarp
gullies
sediment drift and moat
sediment cores
scarps related to buried failed masses
36°55'
36°50'
36°45'
14°05'
14°10'
14°15'
14°20'

FIGURE 3

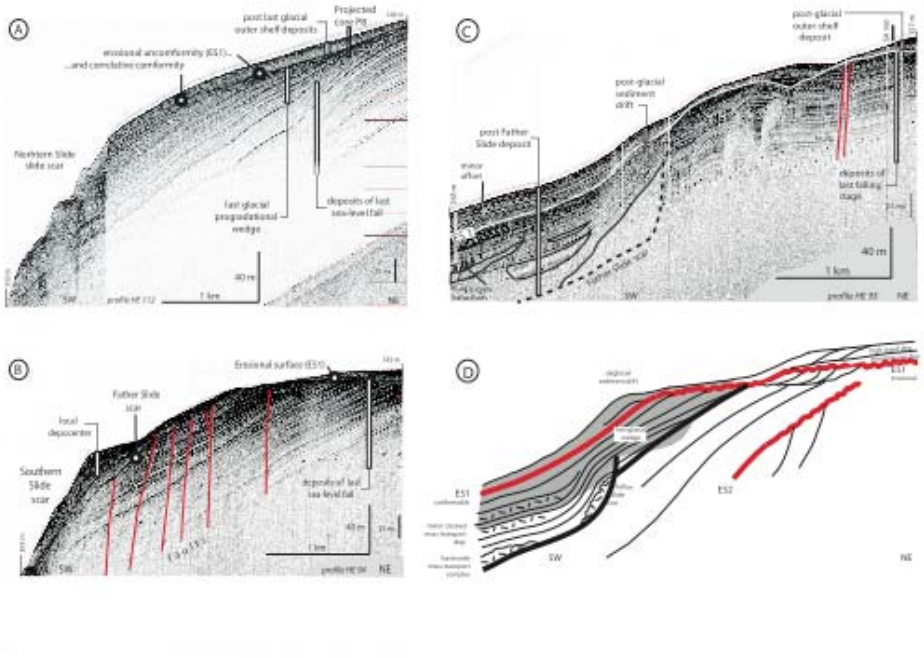
A
post-last glacial outer shelf deposits
Projected core Pit
erosional unconformity (ES1)...
...and correlative conformity
Northern Slide slide scar
last glacial progradational wedge
deposits of last sea-level fall
40 m
1 km
SW
NE
B
Erosional surface (ES1)
Father Slide scar
local depocenter
Southern Slide scar
deposits of last sea-level fall
40 m
1 km
SW
NE
C
post-glacial outer shelf deposit
post-glacial sediment drift
post Father Slide deposit
minor effluent
deposits of last falling stage
40 m
1 km
SW
NE
D
ES1
ES2
SW
NE

FIGURE 4

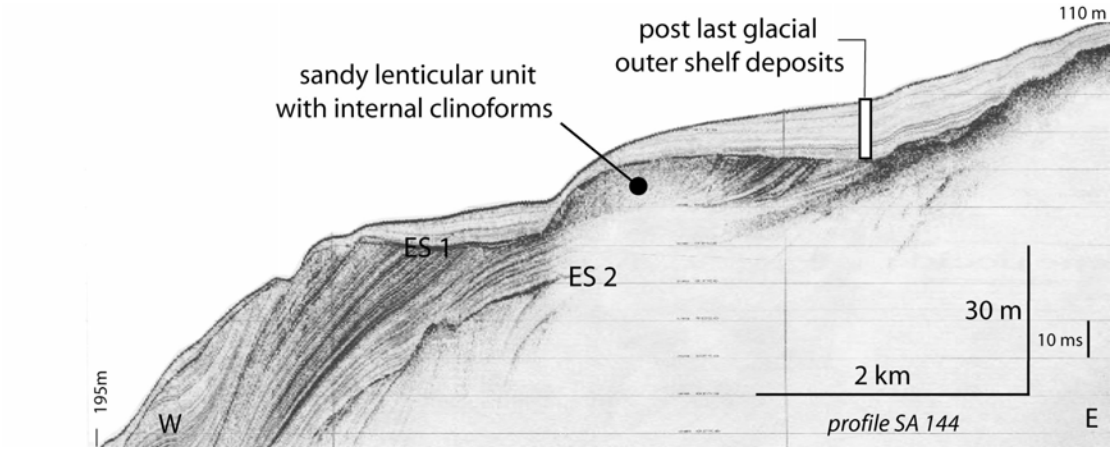

FIGURE 5

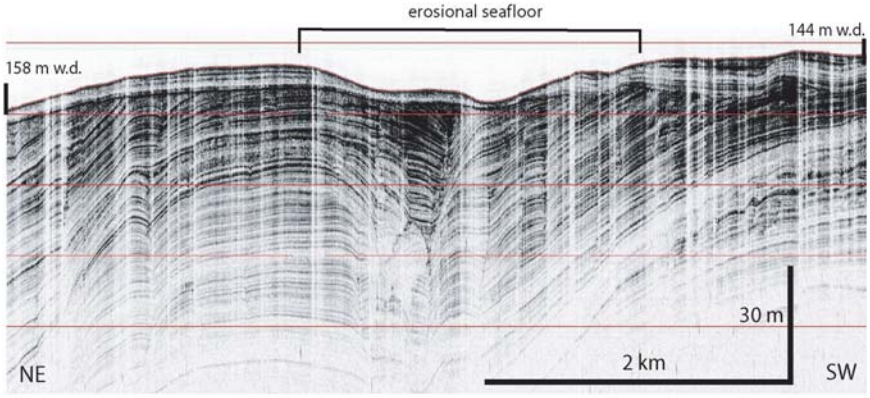

FIGURE 6

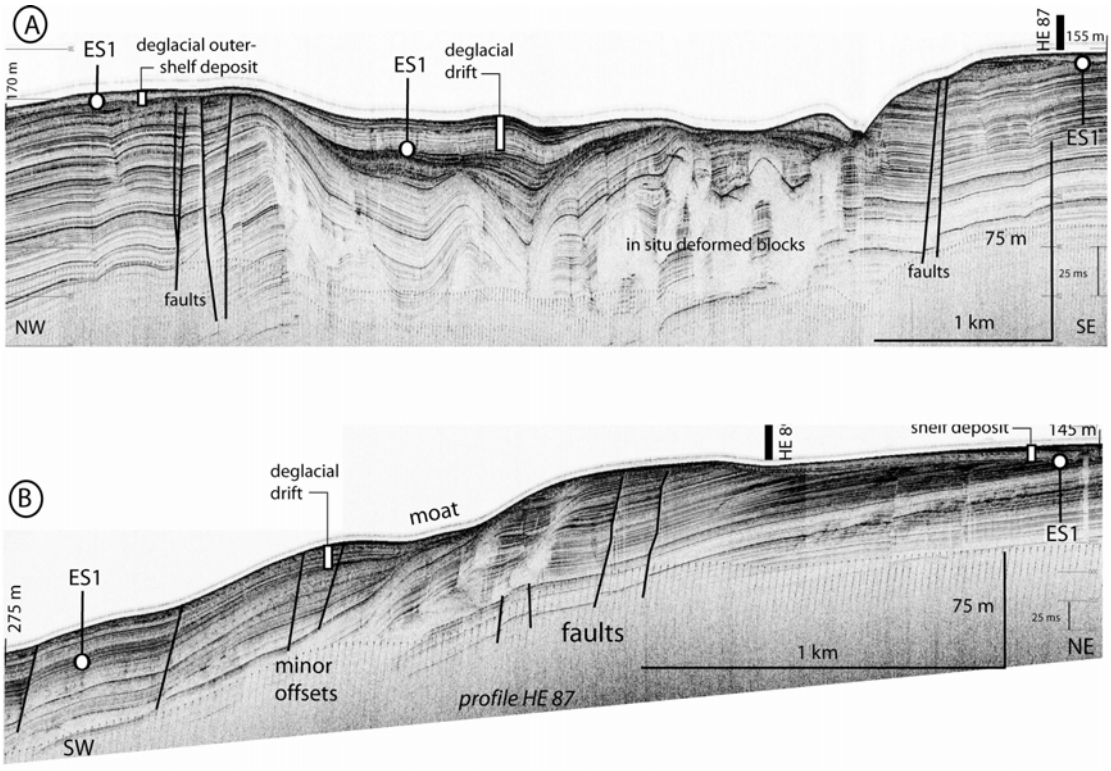

FIGURE 7

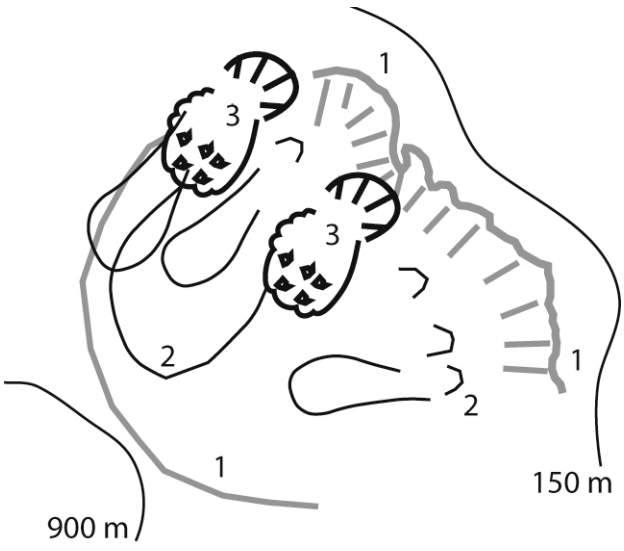

FIGURE 8

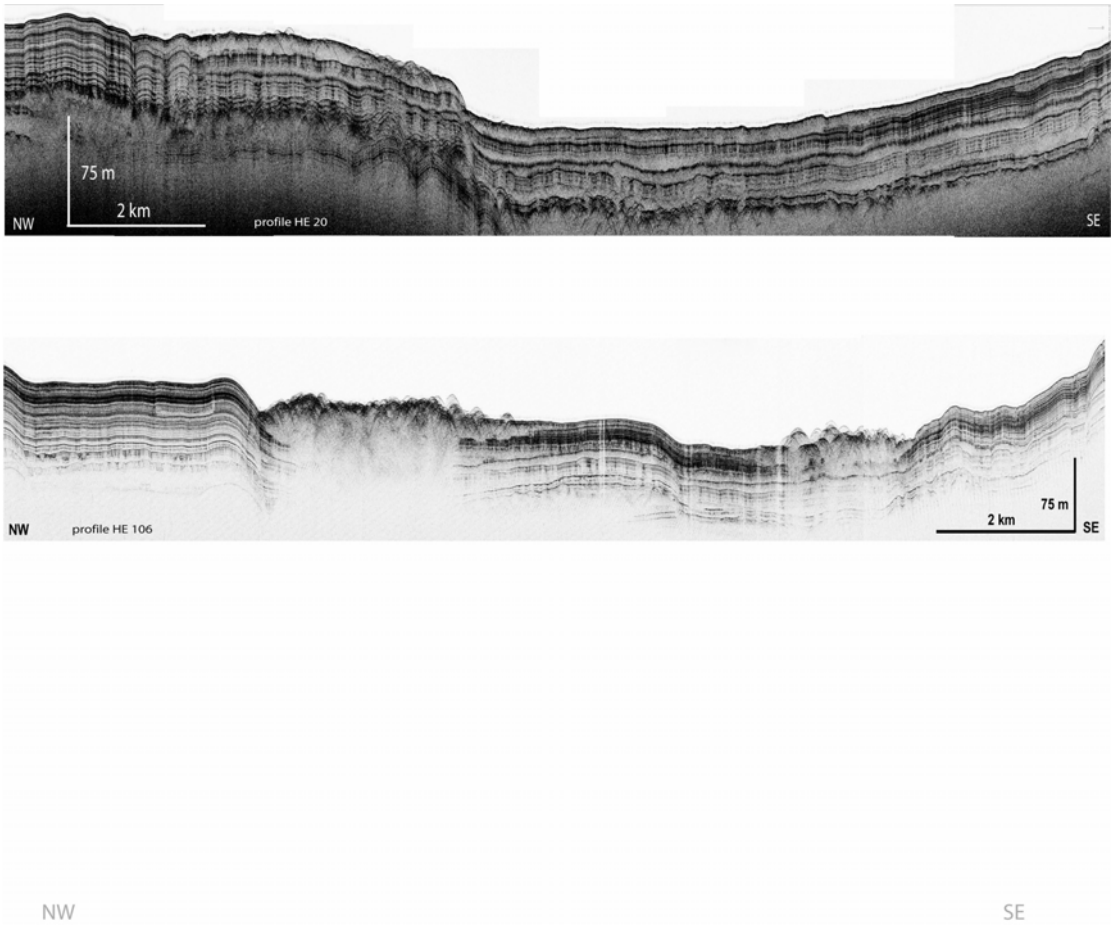

FIGURE 9

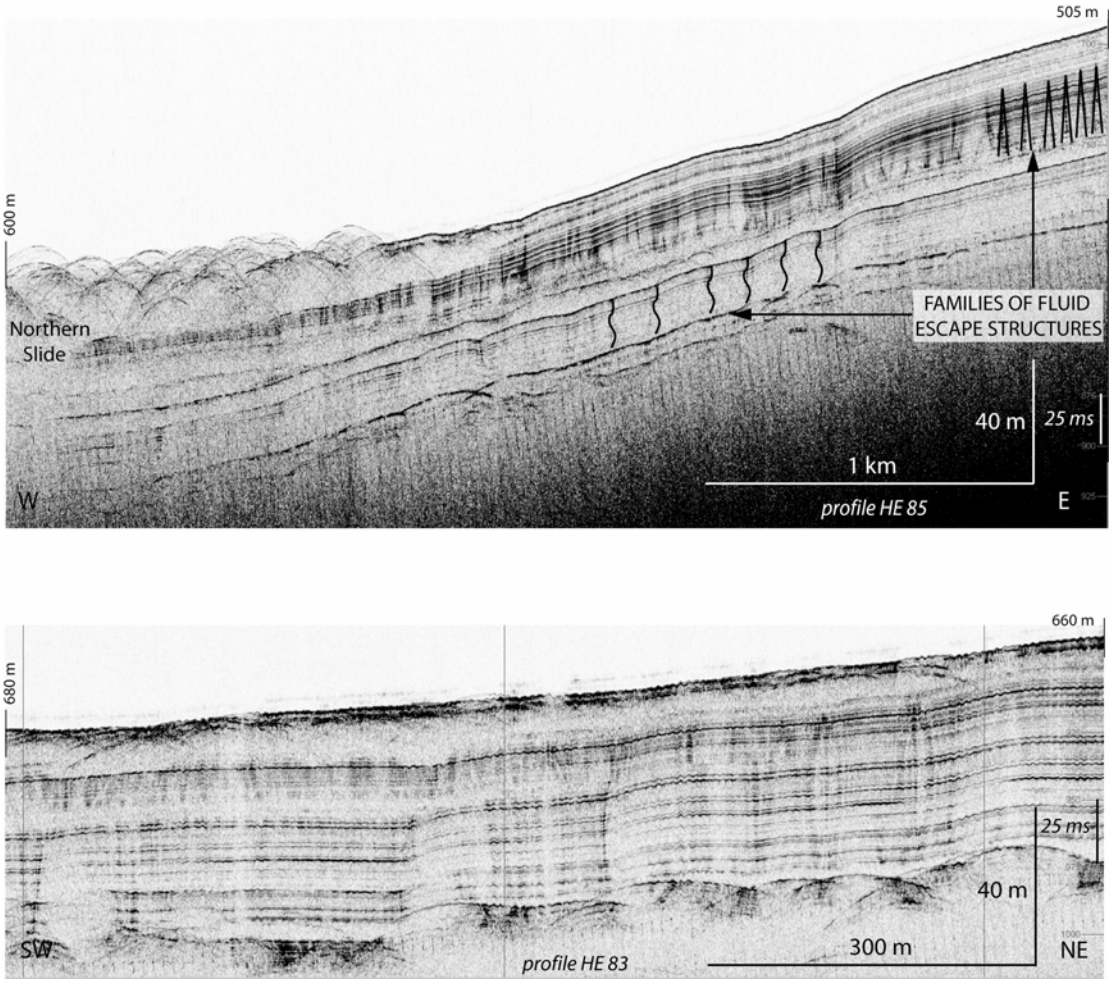

FIGURE 10

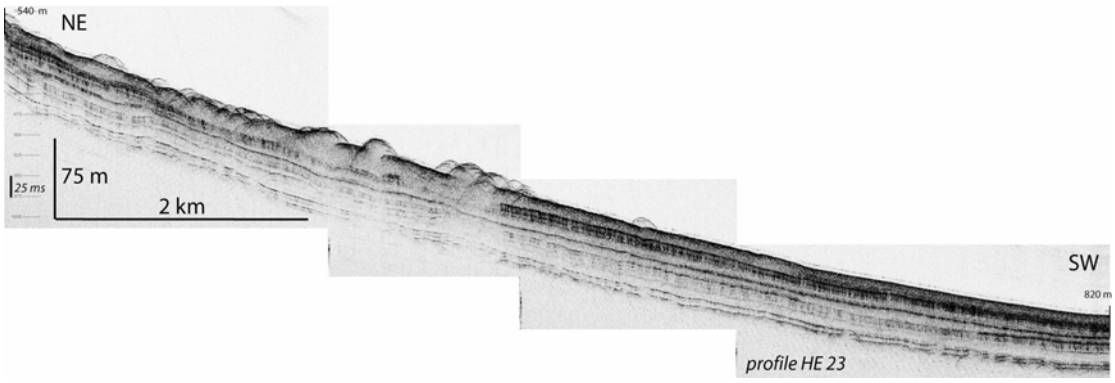

FIGURE 11

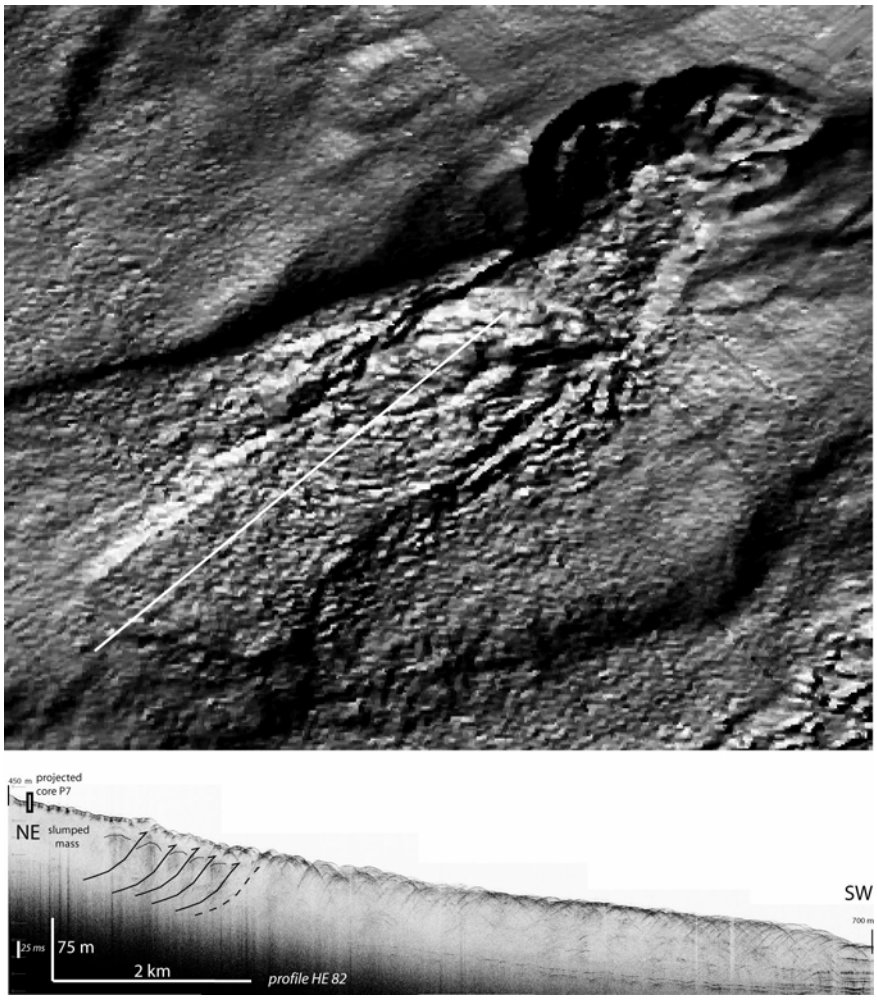

FIGURE 12

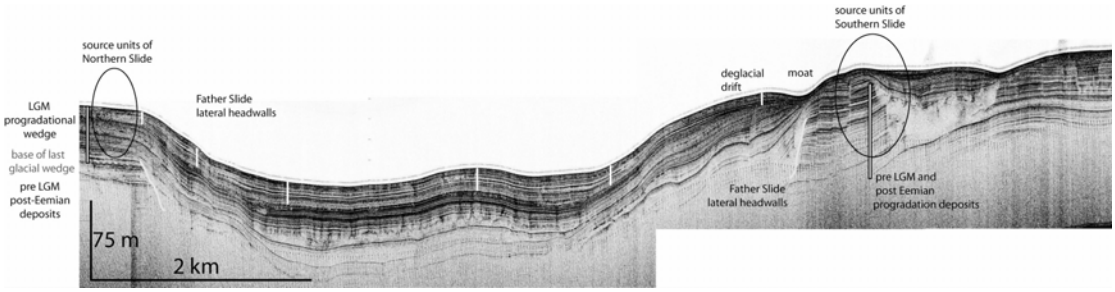

FIGURE 13

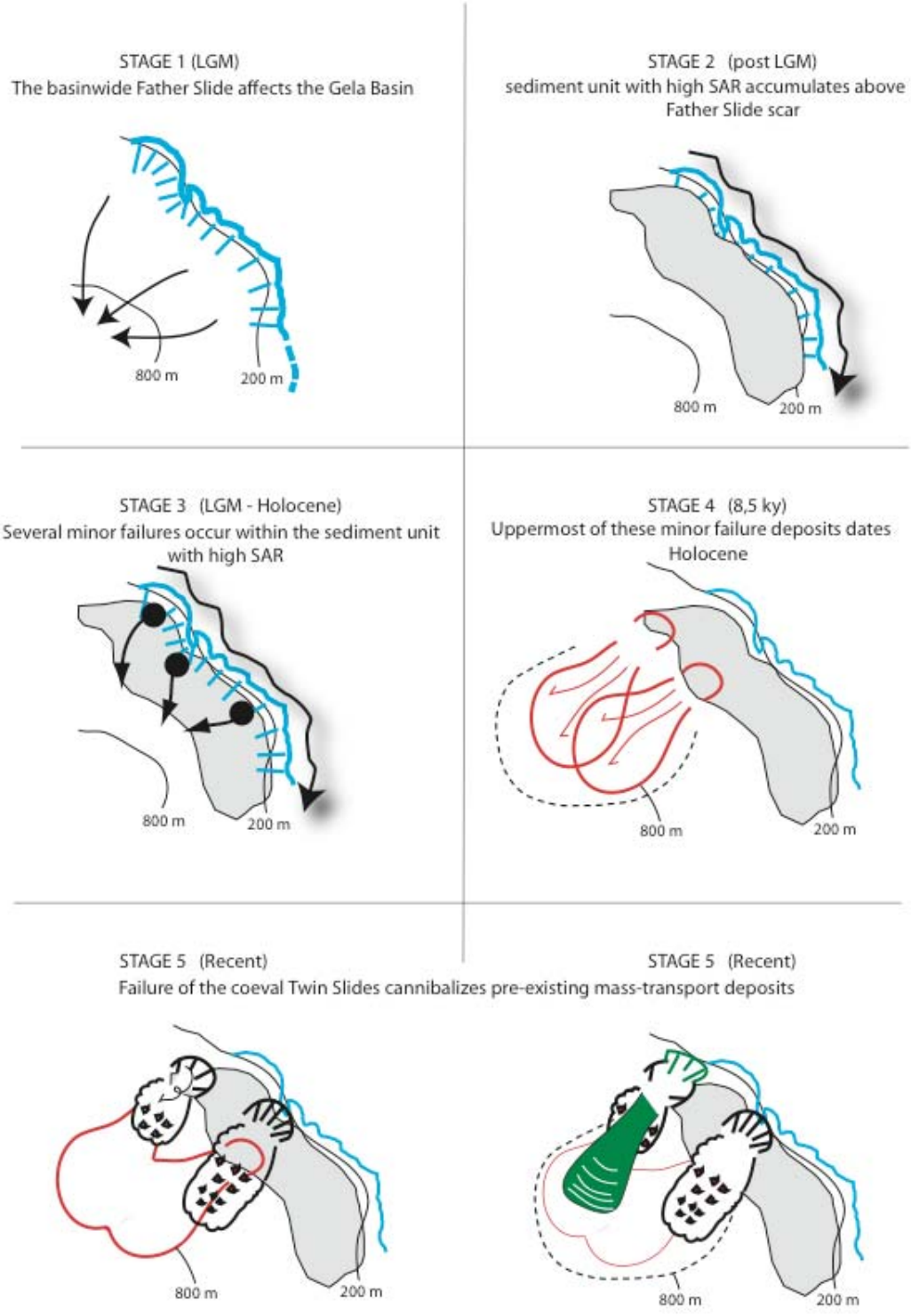
STAGE 1 (LGM)
The basinwide Father Slide affects the Gela Basin
800 m
200 m
STAGE 2 (post LGM)
sediment unit with high SAR accumulates above Father Slide scar
800 m
200 m
STAGE 3 (LGM - Holocene)
Several minor failures occur within the sediment unit with high SAR
800 m
200 m
STAGE 4 (8,5 ky)
Uppermost of these minor failure deposits dates Holocene
800 m
200 m
STAGE 5 (Recent)
Failure of the coeval Twin Slides cannibalizes pre-existing mass-transport deposits
800 m
200 m
800 m
200 m

FIGURE 14

FIGURE 15

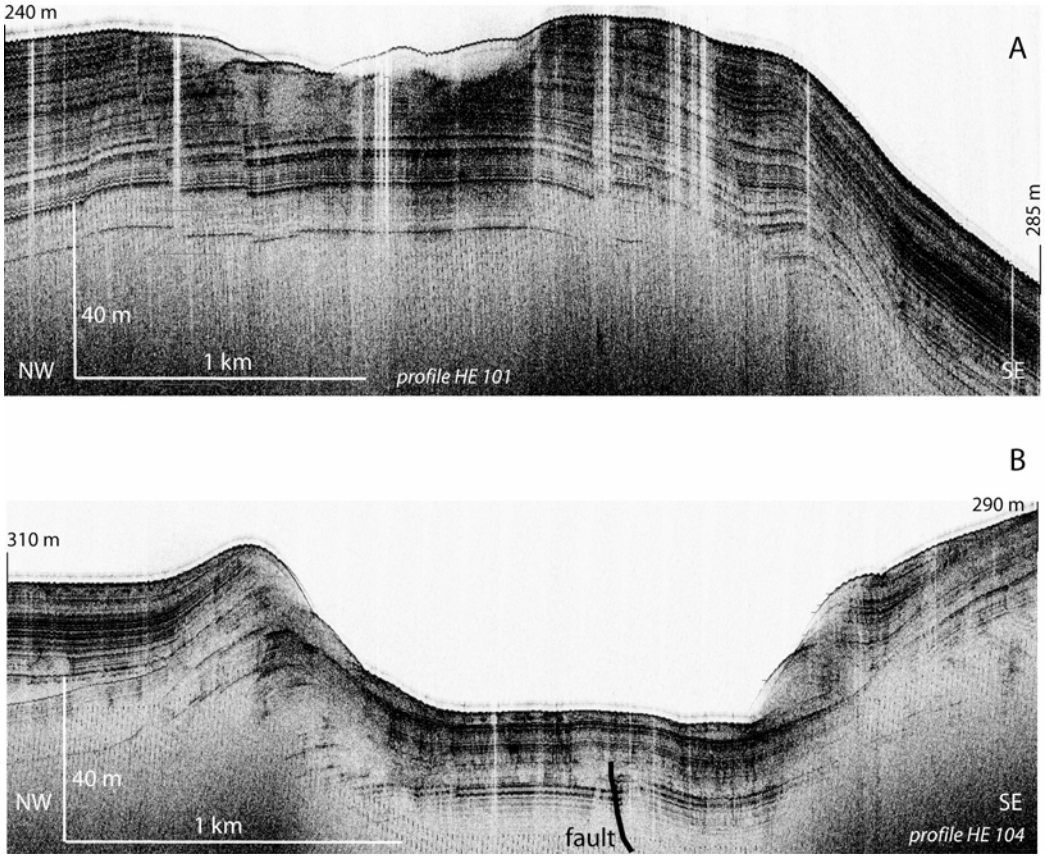

CHAPTER 6

This chapter consists of an article titled “An Early Paleocene Cold Seep System in the Panoche and Tumey Hills, Central California (United States)” by Minisini D. and Schwartz H., in press in “American Association of Petroleum Geologists - Memoir”.

16

Minisini, D., and H. Schwartz, 2006, An early Paleocene cold seep system in the Panoche and Tumey Hills, Central California, (United States), *in* A. Hurst and J. Cartwright, eds., Sand injectites: Implication for hydrogen exploration and production: AAPG Memoir 87, p. 1–13.

An Early Paleocene Cold Seep System in the Panoche and Tumey Hills, Central California (United States)

Daniel Minisini[1]

Ismar-CNR (Istituto di Scienze Marine–Consiglio Nazionale delle Ricerche), Bologna, Italy

Hilde Schwartz

Earth Sciences Department, University of California at Santa Cruz, Santa Cruz, California, U.S.A.

ABSTRACT

A paleoseep system consisting of hundreds of sand injectites and authigenic carbonate structures crops out in the Panoche and Tumey Hills, central California. This paleoseep system developed on the western margin of the Great Valley forearc basin and is contained within the uppermost, early Paleocene part of the dominantly siliciclastic Moreno Formation. It is 20 km (12 mi) long and is distributed over more than 700 m (2296 ft) of stratigraphic section. Injectites appear in the lower 600 m (1968 ft), thinning upward from 3 m (9.8 ft) to less than 1 cm (0.4 in.), and cooccur with the paleoseep carbonate structures in the uppermost 200 m (660 ft) of section. The paleoseep slab, mound, and concretionary carbonates are ^{13}C depleted (to −46‰ Vienna Peedee belemnite) and commonly contain pipelike structures and the remains of chemosynthetic macroinvertebrates, including tube worms and lucinid bivalves. Their diverse morphologies likely reflect different rates and styles of fluid flow, but most show a similar paragenesis beginning with biologic colonization and pervasive micrite authigenesis and concluding with sparite precipitation in vugs and conduits. The close stratigraphic and compositional associations of paleoseep carbonate structures with injectites suggest that they were contemporaneous, and that injectites controlled the location of the seeps. Variations in abundance, morphology, and geochemistry of the authigenic carbonates, fossils, and injectites across the outcrop area indicate considerable variability in seep venting rates locally, regionally, and over the nearly 2-Ma duration of the seep system. Thus, the Panoche and Tumey Hills locality offers a four-dimensional view of the nature and evolution of a large, injectite-driven, cold seep in a forearc setting.

[1]*Present address*: Dipartimento Scienze della Terra e Geologico-Ambientale, Universita di Bologna, Bologna, Italy.

DOI:_____

INTRODUCTION

Cold seeps occur where low-temperature fluids rich in predominantly methane and hydrogen sulfide flow from the sea floor. Authigenic carbonates commonly form in such environments and are the primary diagnostic features of ancient cold seeps (e.g., Beauchamp et al., 1989; Clari and Martire, 2000; Campbell et al., 2002). Distinctive features of ancient and modern cold seep carbonates include (1) occurrence as discrete masses of carbonate-rich rocks embedded in predominantly siliciclastic, carbonate-poor sediments; (2) ^{13}C depletion; (3) presence of botryoidal, splayed, or yellow calcite cements; (4) association with high-abundance, low-diversity chemotrophic biotic assemblages, which are absent in the surrounding rocks or sediments. Pathways for upward fluid migration at cold seeps are commonly controlled by submarine erosion or by faults (Moore et al., 1990; Paull et al., 1991; Ogawa et al., 1996; Eichhubl et al., 2000; Campbell et al., 2002).

In contrast, a carbonate-rich Paleocene paleoseep system in the Panoche and Tumey Hills (central California) appears to have been plumbed by an interconnected network of sandstone injectites (Schwartz et al., 2003a). The Panoche and Tumey Hills system is exposed for 20 km (12 mi) along strike and is 700 m (2296 ft) thick (Figures 1, 2). It offers three-dimensional views of the ancient sea floor and subsurface and a temporal dimension to the study of the seep system. It also allows for a more detailed analysis of fluid pathways than is possible at modern cold seeps because the resolution of geophysical data used to image the modern sea floor is larger in scale than the injectites exposed at this site. Thus, the Panoche and Tumey Hills locality represents one of the first opportunities to analyze a long-lived seep system at field-scale and to study the linkage between injectites and cold seep deposits.

The Panoche and Tumey Hills field area was studied through field mapping and analysis of approximately 50 kg of rock samples. Mapping established the scale of the system, distribution of injectites and cold seep deposits, and main morphologies and textures of the authigenic seep carbonates. Sample analyses, including petrography (80 thin sections), carbon and oxygen stable isotope analysis (70 samples), and x-ray diffraction (XRD) (20 samples), allowed us to identify paragenetic sequences and $\delta^{13}C$ trends across the field area.

GEOLOGIC SETTING

The Panoche and Tumey Hills are located on the western edge of the San Joaquin Valley in central California (United States) (Figure 1). The San Joaquin Valley is part of the Great Valley of California, a basin whose position roughly corresponds to that of a Late Jurassic to Oligocene forearc basin (Dickinson and Seely, 1979; Bartow, 1991).

The Panoche Hills and the Tumey Hills, the northern and southern parts of the study area, respectively, are composed of Upper Cretaceous and Tertiary strata that dip 35–50° east-northeast into the paleoforearc basin. The oldest units exposed are the Panoche Formation and the Moreno Formation, the latter being the uppermost local unit of the so-called Great Valley sequence (Ingersoll, 1979). The Moreno Formation, deposited from the middle Maastrichtian to late Danian, contains the paleoseep features described in this chapter. It is a predominantly fine-grained siliciclastic unit subdivided into four members (Payne, 1951): the Dosados Sandstone and Shale Member, the Tierra Loma Shale Member, the Marca Shale Member, and the Dos Palos Member (with the Cima Sandstone Lentil interbed) (Figure 2). In the study area, the three youngest members preserve a 700-m (2296-ft)-thick paleoseep system, representing sea-floor seepage over at least 2 Ma (Weberling, 2002; Schwartz et al., 2003b). The paleoseep system is characterized by a wide range of authigenic carbonate structures, most of which are contained within a main horizon, previously mapped as the Cima Sandstone Lentil (Payne, 1951) (Figure 2). They are linked to an underlying network of interconnected sand injectites whose likely source is the underlying upper Panoche Formation (Payne, 1951; Smyers and Peterson, 1971; Friedmann et al., 2002).

Faulting in the study area occurred after Moreno Formation deposition, during the late Cenozoic uplift of the Coast Ranges (Wentworth and Zoback, 1989). Therefore, injectite genesis is not directly related to tectonics. It was more likely the result of overpressure in the central basin and subsequent lateral fluid migration, with mobilization of sand intrusions and marginal seepage along the western edge of the Great Valley forearc during the early Paleocene (Schwartz et al., 2003a).

CARBONATE STRUCTURES

Carbonate structures in the Panoche and Tumey Hills crop out above an interconnected network of injectites for 20 km (12 mi) along strike (Figure 1). Previous studies mention these carbonates (e.g., Anderson and Pack, 1915; Payne, 1951; Dibblee, 1975; McGuire, 1988) but describe neither their morphology nor their distribution and avoid any hypothesis about their genesis.

Stratigraphically, the Panoche and Tumey Hills carbonates are most abundant in the 25–30-m (82–98-ft)-thick Cima Sandstone Lentil of the Dos Palos Member, a poorly indurated, very fine-grained sandstone. Isolated

carbonate bodies are also present in the underlying shale of the Dos Palos Member. Thus, carbonates occur in at least 200 m (660 ft) of the upper Moreno Formation stratigraphic section (Figure 2). The distribution of the carbonate structures in the field area is patchy, depending on both original patterns of formation and availability of outcrops (Figure 3). Exposures of the Cima Sandstone Lentil and Dos Palos Member are markedly better on south-facing slopes and along southward-draining creeks. Other areas are covered by colluvium and soil and, locally, by alluvium and landslides. In some areas, carbonate structures crop out continuously for hundreds of meters. In other regions, carbonates occur as dense to sparse isolated bodies (Figure 3). Virtually all of the carbonate structures are in place, as indicated by the incorporation of matrix sandstone and siltstone, lateral continuity of complexly shaped bodies, and the presence of well-preserved in-situ fossils (Schwartz et al., 2003a, b). The in-situ fossil biota, together with the uncompacted grains of siliciclastic sediment, suggest that these carbonates precipitated close to the sea floor. Contacts between carbonate structures and the encasing rocks vary from sharp to gradational over several centimeters. Late-stage, fracture-filling gypsum cement commonly borders carbonate-siliciclastic contacts or crosscuts both lithologies (Figure 4).

The Panoche and Tumey Hills carbonate body morphologies strongly resemble those found at modern cold seep deposits (e.g., Kulm and Suess, 1990; Roberts and Aharon, 1994; von Rad et al., 1996) and at other ancient seeps with associated methane-derived authigenic carbonate precipitated via microbially mediated methane oxidation (e.g., Terzi et al., 1994; Kauffman et al., 1996; Peckmann et al., 1999; Clari and Martire, 2000; Goedert et al., 2000).

Most of the Panoche and Tumey Hills carbonate structures are rich in irregular, interconnected vugs and conduits whose textures strongly resemble the microbially induced fabrics of Black Sea cold seep deposits (Luth et al., 1999). Wavy laminae around conduits and worm tubes and peloidal and clotted textures represent further evidence of microbial activity (Figure 5). In modern seep environments, these textures have been shown to form through microbial activity (Chafetz, 1986; Guo and Riding, 1992), and at several paleoseeps, their microbial origin was confirmed by biomarker analysis (e.g., Peckmann et al., 1999, 2002).

In addition to microbial fabrics, the Panoche and Tumey Hills carbonate structures typically exhibit patchy patterns of induration (from very high to moderate), color (from grayish to reddish brown), lithology (from calcarenite to micrite), and fossil abundance (from many to none). They can be grouped into three main morphologies: (1) mounds, (2) stratiform bodies, and (3) spheroidal to ellipsoidal concretions (Figure 6).

Mounds

Mounds are irregular bodies that are typically somewhat taller than they are wide. Their average height is 3 m (9.8 ft), and the width ranges between 0.5 and 6 m (1.6 and 19.6 ft). Most exhibit complex lithologies and fabrics, accompanied by mottled coloration. Mounds incorporate siliciclastic sediments from the encasing rocks and are carbonate cemented, ranging in texture from micrite to calcarenite. Carbonate cement-filled veins, as much as 2 cm (0.8 in.) wide, occur in virtually all of the mounds. Vuggy texture is common, and the pervasive interconnected mound cavities are either open or filled with carbonate cements and lithified sediment. Pipelike structures are preserved in many mounds; they are as much as 3 cm (1.2 in.) in diameter and several centimeters long (Figure 7A, B); they contain multiple phases of cement (Figure 7D) and, uncommonly, smaller freestanding tubes (Figure 7C). Some mounds consist of fine to coarse breccia, but generally, mounds are coherent structures with extremely well-cemented cores. Both induration and carbonate abundance decrease outward, upward, and downward from the mound cores. The bottom few centimeters of each mound is typically weakly cemented. Generally, the absence of carbonate cement defines the boundaries of the mounds.

Mounds are commonly fossiliferous: lucinid bivalves occur locally in mound cores, and tube worms are ubiquitous. Both bivalves and tube worms represent chemosynthetic species whose modern representatives colonize cold seeps and sulfide-rich marine environments (e.g., Sibuet and Olu, 1998). Worm tubes, found as isolated bodies or in clusters with no apparent preferred orientation, are distinguished from pipelike conduits by their more regularly circular to elliptical cross sections and their well-defined, uniformly thick carbonate rims (Schwartz et al., 2003a) (Figure 8). In some mounds, however, the morphologies of tubes and pipes converge, suggesting that some worm tubes acted as fluid conduits, and were ultimately infilled by seep-derived cements after the deaths of their original owners. Cook and Stakes (1995) noted such tube worm conduits in hydrothermal vent sulfide edifices at the Endeavour Segment of the Juan de Fuca Ridge. Some Panoche and Tumey Hills mounds with distinctively knobbly textures (Figure 9A, B) contain numerous tubes and/or pipelike structures with thick, authigenic carbonate overgrowths (Figure 9C) as much as 15 cm (6 in.) in diameter.

Stratiform Bodies

Stratiform carbonate bodies are tens of meters long and wide and 1–5 m (3.3–16 ft) thick. They occur at several levels in the Cima Sandstone Lentil, and their

contacts with the encasing rocks are sharp and irregular (Figure 6). Most of the carbonate stratiform bodies are grayish, micritic, well-indurated slabs and pavements, devoid of sedimentary structures. Slabs both pinch out as lenses and terminate abruptly laterally. Their upper boundaries are rather flat, whereas their lower boundaries are irregular; hence, slabs pinch and swell from 1 to 6 m (3.3–19 ft). In contrast, pavements are thinner and maintain relatively constant thickness across their area of exposure. Stratiform carbonate bodies are similar in texture, lithology, and fossil content to the mounds, but the uppermost slabs and pavements in the study area contain small gastropods, solitary corals, and wood fragments, in addition to bivalves and tube worms.

Locally, the lower stratiform carbonate contacts connect to elongate conduits (as much as 8 × 0.75 m [26 × 2.5 ft]) that penetrate the underlying Dos Palos Member (Figure 10A–C). The conduits exhibit the same lithologies and sharp contacts with the encasing rock as the overlying slabs. Closely spaced, irregularly shaped carbonate masses, with an average diameter of 30 cm (12 in.), underlie some slabs (as well as a few carbonate mounds). They tend to form vertically oriented clusters that are similar in scale and orientation to the conduits. The subslab and submound conduits and masses typically exhibit brecciated texture (Figure 10D).

In the northernmost Panoche and Tumey Hills, Cima Sandstone strata are pervasively carbonate cemented but do not contain obvious carbonate bodies. In this area, the lower Cima Sandstone preserves sedimentary structures, but the upper Cima is massive. Sedimentary structures include fining-upward sequences with (in order) sigmoidal ripples, climbing ripples, and parallel laminations, although in places, burrows, pipelike conduits, and fluid-escape structures obliterate the stratification. Isolated tube worm fossils are relatively common in the Cima Sandstone Lentil in this area, but remnants of other chemosynthetic organisms are uncommon.

Concretions

Spheroidal and ellipsoidal concretions are common in the Cima Sandstone Lentil and vary in dimension from several centimeters to 3 m (9.8 ft). The long axes of ellipsoidal masses are parallel to stratification (Figure 6). Concretion nuclei typically contain isolated tube worms, mollusks, or wood fragments, as well as abundant authigenic carbonate. As with mounds, carbonate content generally decreases from the centers to the outer edges of the concretions. Calcarenite concretions are especially well indurated.

A horizon of white, foliated carbonate concretions occurs lower in the section just below the Marca–Dos Palos contact. These concretions are regularly spaced across the field area, but crosscutting relationships suggest that the concretions predate sand injection and, thus, the formation of the overlying authigenic carbonates (see the section on Stable Isotopes for $\delta^{13}C$ values).

Minor Morphologies

Rare carbonate chimneys and doughnuts (sensu Kulm and Suess, 1990) also occur in the Panoche and Tumey Hills seep horizon, particularly in northern Tumey Hills, in the upper part of the Cima Sandstone Lentil (Figure 11). Where present, they are generally associated with concretions and, more uncommonly, with mounds. Carbonate chimneys and doughnuts differ from the above-described conduits: they are generally short and wide (to 1 m × 40 cm [3.3 ft × 15 in.]), isolated, and not overlain by slabs or mounds. Chimneys display a central hollow, suggestive of a relict conduit, which is typically visible on the upper surface of the structure. The sediments that surround and cover carbonate chimneys are well indurated and locally contain carbonate breccias near chimney bases.

Distribution

In this study, carbonate structures were mapped in detail on the Chounet ranch and Tumey Hills, 1:24,000, U.S. Geological Survey Topographic Quadrangles, using the 1:50,000 geologic map of Bartow (1996) for reference. Despite patchy distribution in the Panoche and Tumey Hills, seep carbonates are clearly identifiable for 20 km (12 mi) along strike (Figures 1, 12). In places, composite seep deposits are continuous across hundreds of meters, whereas elsewhere, they crop out as isolated or multiple structures (Figure 6). Most of the carbonates occur in the 25–30-m (82–98-ft)-thick Cima Sandstone Lentil, but isolated seep carbonate bodies also occur in the underlying Dos Palos Member, beginning several meters above the Marca–Dos Palos contact (Figure 2). Hence, cold seep carbonates bracket about 200 m (660 ft) of the local stratigraphic section. The first appearance of abundant seep carbonates occurs at the base of the Cima Sandstone Lentil in the form of both laterally extensive, irregular stratiform bodies and groups of mounds whose lower contacts typically intersect underlying conduits (Figure 3). The largest paleoseep mounds occur in the upper parts of the Cima Sandstone Lentil. Concretions are most common in the uppermost seep horizon between 8 and 30 m (26 and 98 ft) above the base of the Cima Sandstone Lentil. Slabs and pavements occur locally in the uppermost Cima Sandstone Lentil, but in such areas, they still represent the first stratigraphic occurrence of stratiform bodies (Figure 12).

The most morphologically diverse paleoseep deposits in the Panoche and Tumey Hills occur in the southern Panoche Hills and northern Tumey Hills; elsewhere, the paleoseep carbonates have less variety. The northern Panoche Hills seep horizon is characterized predominantly by pervasively carbonate-cemented sediment, and the southern Tumey Hills seep horizon is characterized predominantly by scattered mounds and concretions. Carbonate bodies are most abundant in the central part of the field area (southern Panoche Hills and northern Tumey Hills).

INJECTITES

Injectites appear stratigraphically below carbonate structures across the 20 km (12 mi) of exposure of the Panoche and Tumey Hills paleoseep (Figure 13). They consist of subhorizontal sills and subvertical to vertical dikes of fine-grained, whitish to reddish sandstone that is massive, well sorted, and poorly cemented (Weberling, 2002). Injectites crosscut the Moreno Formation from near its base up to the Dos Palos Member (Figure 2); most terminate 20–30 m (66–98 ft) below the main paleoseep horizon in the Cima Sandstone Lentil, but several thin dikes completely penetrate the carbonate-rich zone (Figure 14A). Injectites that propagate through the Dos Palos Member locally crosscut sediments that contain the lowermost paleoseep carbonate structures (Figure 14B), but higher in the stratigraphic section, injectites are typically overlain by carbonate structures. Thus, some injectites are stratigraphically higher than (and, therefore, younger than) adjacent paleoseep carbonates, assuming, from in-situ fossils and uncompacted sediment, that these carbonates formed close to the sea floor. Mazzini et al. (2003) recognized similar crosscutting relationships, indicating that injected sands postdated authigenic carbonate structures, in a paleoseep above a submarine oil reservoir.

Dikes are not continuously exposed throughout the Moreno section, and they are not uniform in scale: both length and width of dike exposures decrease proportionally upward in the section. In the Dosados and Tierra Loma Shale members, individual dikes are exposed for tens of meters, and thickness decreases from bottom to top, narrowing, on average, from 2–3 to 1 m (6.6–9.8 to 3.3 ft). Higher in the section, dikes are shorter, commonly cropping out across less than 10 m (33 ft) of section, and they exhibit decreasing thickness upward to an average width of 5 cm (2 in.) below the Cima Sandstone Lentil and an average width of 1 cm (0.4 in.) in the Cima Sandstone (Figure 14A).

In the Panoche and Tumey Hills, dikes and sills commonly crosscut one another or branch into two elements, forming a complex interconnected network (Figure 13B). Low in the section, where injectites are wider, interconnections are widely spaced; high in the section, where injectites are thinner, interconnections are denser. Thus, in places, the injectite network comprises tens of thin injectites in 100 m^2 (1076 ft^2). In the southern Tumey Hills, near the border of the study area, the Cima Sandstone Lentil pinches out (Bartow, 1996); here, the distance between injectites progressively increases, and injectite length and thickness are considerably less than elsewhere in the study area.

Near the Marca–Dos Palos contact, dikes intersect local zones of white, foliated, nonseep concretions (see the section on Concretions). Dikes do not crosscut these well-indurated concretions but divert around them, suggesting that the concretions acted as obstacles to injection pathways and are older than the seep system. In contrast, two 40-cm (16-in.)-wide, poorly indurated dikes in the Dos Palos Member in the northern Panoche Hills terminate directly below a well-cemented paleoseep carbonate concretion. In this case, the carbonate content of the dikes increases upward toward the center of the concretion, providing direct evidence of a genetic and temporal link between injectites and seep features. This link is reinforced by the work of Sample et al. (2001), who found that the isotope values of carbonate cements in some of these injectites fall within the range of typical seep carbonates (−21.12 to −5.54‰).

In the lower members of the Moreno Formation, dikes are better cemented than sills, but higher in the section, they become progressively more poorly cemented and more fractured. Sheets of gypsum, as much as 10 cm (4 in.) in width, border the contacts between injectites and surrounding shales (Figure 4B). Minor gypsum-filled fractures also crosscut both shales and sand intrusions, indicating late timing for this diagenetic phase.

STABLE ISOTOPES

Seventy Panoche and Tumey Hills samples were analyzed for $\delta^{13}C$ and $\delta^{18}O$ (relative to the Vienna Peedee belemnite [V-PDB]) standard at the University of California, Santa Cruz, stable isotope laboratory (Figure 15; Table 1), with a precision of better than 0.1‰. Authigenic carbonate and fossil samples were analyzed using materials hand drilled from the surfaces of polished blocks with precision of about 1 mm.

The white, foliated, spherical concretions just below the Dos Palos–Marca contact (described in the section on Concretions) have $\delta^{13}C$ values of 3‰, suggesting that their formation was not related to the Panoche and Tumey Hills paleoseep fluids. The $\delta^{13}C$ values of all other carbonate features along the stratigraphic section are consistent with precipitation at a methane seep. The $\delta^{13}C$ values of mounds, slabs, and

TABLE 1. Carbon and Oxygen Stable Isotope Results for Carbonates and Short Description of Samples; Samples Ordered from North to South; Dashed Line Separates Panoche Hills from Tumey Hills; Vertical Lines on the Left Indicate Samples from Same Specimen.

Sample Code	$\delta^{13}C_{PDB}$ *(V–PDB)*	$\delta^{18}O_{PDB}$ *(V–PDB)*	*Short Description*
δ FIRST	−7.22	−4.61	Carbonate structure: micrite
CL14 (er)	−15.81	−2.25	Carbonate structure encasing CL14: micrite
CL14	1.64	−1.08	Bivalve
CL15	−26.21	−1.01	Carbonate structure: micrite
M4 (er)	−36.14	−2.25	Carbonate structure encasing M4: micrite
M4 (yc)	−11.52	−2.04	Yellow calcite
M2A	−8.35	−3.16	Conduit core
M2	−18.64	1.89	Carbonate structure: micrite with microbial fabric
CC4	−31.74	−1.17	Carbonate structure: micrite
CL9 (er)	−23.80	−1.21	Carbonate structure encasing CL9: micrite
CL9	0.32	−0.95	Bivalve
CL10	−14.06	−4.65	Bivalve
CL6	−13.81	−2.00	Bivalve
TW33	−19.62	−4.09	Rim of conduit
M3	−19.72	−6.92	Carbonate structure: micrite
M1	−28.61	−0.92	Carbonate structure: micrite
δ 1	−27.31	−0.03	Carbonate structure: micrite
δ 2B	−25.16	−2.21	Carbonate structure: micrite
PH04_6 (er)	−25.25	2.96	Carbonate structure encasing PH04_6(ic): micrite
PH04_6 (ic)	−9.46	−1.55	Rim of conduit
PH04_2	−41.72	3.35	Carbonate structure: micrite
CL3	−2.61	−0.44	Bivalve
C2	−13.97	−4.29	Carbonate structure (concretion): micrite
7/3	−7.10	0.87	Base of carbonate structure: micrite
7/4	−46.26	0.05	Core of carbonate structure: micrite
7/5	−43.71	0.21	Top of carbonate structure: micrite
12C	−25.70	−3.47	Carbonate structure: micrite
12B	−25.27	−3.48	Carbonate structure encasing coral PH04_3C: micrite
PH04_3C	−1.06	−0.19	Coral internal mold
PH04_3D	−23.58	1.33	Carbonate structure: micrite with microbial fabric
PH04_5YM	−38.02	0.33	Carbonate structure encasing PH04_5Y: micrite
PH04_5Y	−19.09	−1.74	Yellow calcite
PH13_1A	−7.49	0.74	Wood fragment
PH02_3B	−29.36	0.04	Rim of conduit
PH02_3C	−6.77	−0.03	Infilling of conduit PH02_3B
PH02_3A	−6.88	−3.54	Bivalve internal mold
PH04_3LA	−17.12	−3.55	Bivalve
PH04_3LB	−16.34	−4.42	Bivalve
PH04_3LC	−20.56	−5.33	Bivalve
PH3_28_7	−19.75	0.44	Bivalve
CC9	−35.24	0.12	Carbonate structure: micrite
δ 10	−28.36	1.00	Carbonate structure: micrite
δ 12	−21.02	1.78	Carbonate structure: micrite
δ 13	−19.97	−0.53	Carbonate structure (concretion): micrite
δ 14	−17.01	−0.01	Carbonate structure (concretion): micrite
CL1	−6.77	0.23	Bivalve
CC8	−11.42	1.00	Carbonate structure (concretion): micrite

Table 1. (continued)

Sample Code	$\delta^{13}C_{PDB}$ *(V–PDB)*	$\delta^{18}O_{PDB}$ *(V–PDB)*	*Short Description*
δ 9B (er)	−27.49	−2.08	Carbonate structure encasing δ 9B: micrite
δ 9B (oc)	−19.15	−3.79	Outer rim of conduit
δ 9B (ic)	−18.00	−0.61	Inner rim of conduit
δ 9B (core)	2.65	0.07	Conduit core
Ci1	−20.61	−3.69	Carbonate structure: micrite
CC11	−14.44	0.38	Carbonate structure (concretion): micrite
TW30	−22.42	0.26	Inner rim of conduit
M20 (er)	−14.78	−2.36	Carbonate structure encasing M 20: micrite
M20 (ic)	−12.68	−3.42	Rim of conduit
TW23	−19.38	−0.12	Rim of conduit
TW27B	−44.87	0.34	Rim of conduit
THM6A	−12.99	0.50	Rim of conduit
THM6B	−21.63	2.48	Conduit core
M22	−21.71	−0.87	Carbonate structure: micrite
TW5 (er)	−11.74	0.37	Carbonate structure encasing TW5: micrite
TW5 (ic)	−19.03	−3.84	Rim of conduit
B4	3.03	−0.40	White foliated concretion in lower Dos Palos
W11	−7.41	−2.47	Wood fragment
TW29 (er)	−0.26	0.16	Carbonate structure encasing TW29: micrite
TW29 (oc)	−9.87	−4.98	Rim of conduit
TW29 (ic)	−9.46	0.60	Conduit core
TW28A	−6.70	0.42	Carbonate structure: micrite
δ LAST	0.55	−0.19	Carbonate structure: micrite

concretions in the Panoche and Tumey Hills paleoseep horizon overlap. Slabs and mounds have lighter average values but a wider range of $\delta^{13}C$ (−46 to −7‰) compared to isolated concretions, which range between −20 and −11‰ (Figure 15).

The $\delta^{18}O$ values of most of the Panoche and Tumey Hills seep materials are close to 0‰, with values ranging from −6.92 to 3.35‰. In the Panoche and Tumey Hills, 86% of all seep carbonate samples range between −4 and 2‰, and in the Tumey Hills, 83% of samples have values in between −3 and 0‰. Micrites from the Cima Sandstone Lentil record the heaviest $\delta^{18}O$ values, with most close to 0‰. Bivalve shells and fibrous and sparry cements in conduit rims have somewhat lighter values (Figure 15).

$\delta^{13}C$ values in the Panoche and Tumey Hills samples range from −46.26 (mound cores) to 2.65‰ (conduit infillings), but two-thirds of 29 samples drilled from the main micritic lithofacies show values between −46 and −20‰. These 29 samples collected across the 20 km (12 mi) of exposure indicate a consistent trend toward lighter carbon isotopic composition in the central part of the study area (Figure 16). The southernmost Tumey Hills paleoseep micrites, near the stratigraphic pinch-out of the Cima Sandstone Lentil (Bartow, 1996), record $\delta^{13}C$ values around 0‰. The northern Panoche Hills micrites, where the Moreno Formation is uncomformably overlain by the Laguna Seca Formation, have values heavier than those in the central paleoseep region but less than 0‰ (Figure 16).

All but one seep conduit display increasing $\delta^{13}C$ values from the edges toward the centers (e.g., external matrix = −27‰; infilling cement rim = −19‰; and infilling cement core = 2‰) (Figure 17), except in the peripheral area of the southern Tumey Hills, where conduit centers record lighter values than the surrounding carbonate structures (i.e., external matrix = −11‰; and infilling cement = −19‰) (Table 1). The $\delta^{13}C$ values of cement infilling are similar for all conduits, except for one anomalously light value of −44‰. Mollusks have $\delta^{13}C$ values between −18 and 0‰, similar to those of infilling cements. Two wood samples collected at the base of Cima Sandstone Lentil, 5 km (3 mi) apart, have the same $\delta^{13}C$ value (−7‰). Almost 70% of randomly collected samples from the lowest stratigraphic level of the abundant seep carbonates record values lighter than −15‰, and analysis of a mound base (−7‰), core (−46‰), and top (−43‰) shows a trend of $\delta^{13}C$ depletion upward.

PETROGRAPHY AND MINERALOGY

The texture and composition of the Panoche and Tumey Hills authigenic carbonates were examined using thin sections and XRD analysis. The dominant cement in the carbonates is magnesian calcite, with lesser amounts of dolomite and low magnesian calcite. Other diagenetic minerals in the carbonates include ferrous hydroxides (hematite), ferrous sulfides (pyrite), and sparse traces of barite.

In the Panoche and Tumey Hills, most of the seep fossils are associated with micrite that contains abundant silt and sand-size detritus derived from the host Cima Sandstone Lentil and preserves whole and fragmentary remains of tube worms, mollusks, radiolaria (Figure 18D), planktonic (Figure 18C) and benthonic foraminifera (Figure 18E), sponge spicules (Figure 18F), and wood (Figure 18G). In places, the micrite contains pyrite framboids (Figure 18I, J) and displays mottled pigmentation (Figure 18H). Vugs, voids, and conduits are common in the paleoseep micrites. Pipelike conduits (see Mounds section), now closed or almost closed by sediment or authigenic cements, are tubular features as much as 3 cm (1.2 in.) in diameter, which penetrate the matrix for as much as 30 cm (12 in.) (Figure 7). They are infilled with numerous diagenetic phases, the most volumetrically important of which is botryoidal or isopachous sparite. Both textures display undulose extinction in cross-polarized light. Calcite cement generally grew from the outer edges to the centers of conduits, incorporating inclusion bands in continuous calcite fibers. Most conduits were filled initially by fibrous calcite rim cements and later by blocky calcite pore-filling cements. Fibrous calcite and blocky calcite commonly maintain optical continuity. A late-stage, conduit-filling micrite containing peloids and some detritus commonly forms wavy laminae that encrust older sparite.

PARAGENESIS

Six phases of seep fluid-derived cementation were identified in the Panoche and Tumey Hills paleoseep carbonates (Figure 19). The earliest Panoche and Tumey Hills diagenetic phase is fossiliferous, detritus-rich micrite (phase 1) (Figure 19A). Most of the paleoseep fossils are associated with this early cement, indicating that authigenesis and biological colonization were coeval in the Panoche and Tumey Hills system, and that early cements formed close to the sea floor, at least within the zone of macroinvertebrate infaunal activity. The abundance of cement and the loose packing of micrite-cemented detrital grains indicate that the phase 1 micrite cemented uncompacted sediment. Phase 1 micrite was locally pervasive and produced well-indurated, erosion-resistant carbonate structures.

A corrosion event (phase 2a, b) (Figure 19B, C) formed vugs, veins, and pipe structures in the phase 1 micrite. The irregular corrosion surfaces are locally associated with microcrystalline pyrite (Figure 19C). Some conduit and tube worm walls show only local evidence of corrosion (Figure 19D) and pyrite precipitation, suggesting that seawater diluted the effects of reducing fluids in some places, whereas localized microbial activity fostered both corrosion and pyrite precipitation elsewhere.

A sparite phase (phase 3), only present locally, coats corroded conduit walls (Figure 19E). This minor phase appears dark yellow in plane polarized light but is not volumetrically significant. Fibrous calcite (phase 4) (Figure 19F) is the most volumetrically important cement in the seep horizon. This phase fills most of the larger open spaces, such as conduits and veins, and commonly replaces worm tubes. The uniform circularity and thickness of fibrous calcite cements around worm tubes suggests that their replacement occurred before or shortly after the deaths of the organisms. Zoned inclusion bands in phase 4 cements thus represent early multiple generations of cements (Clari and Martire, 2000), possibly related to variations in fluid composition. Such variations likely affected carbonate precipitation-dissolution and preservation-loss of organic matter (Peckmann et al., 1999) and, together with light $\delta^{13}C$ values and cementation of uncompacted sediment, provide evidence for the precocious diagenesis typical of cold-seep environments. Phase 5 (Figure 19G) consists of ubiquitous, pore-filling blocky calcite cement. This phase typically fills the centers of tubes, conduits, and vugs. Crystals are polygonal, larger toward the center and transparent in plane polarized light. Laminated peloidal micrite appears to be the final seep-derived cement (phase 6) (Figure 19H); it is predominantly associated with the terminal pore infillings, although in places, it is intercalated with layers of fibrous calcite or crystals of blocky calcite.

The early paragenetic sequence described above resembles those reported from many other paleoseep carbonates, including Cenozoic paleoseeps in western Washington state (Peckmann et al., 2002) and Mesozoic paleoseeps in the Great Valley forearc (Campbell et al., 2002), Canadian Arctic (Beauchamp et al., 1989), northern Japan (Hikida et al., 2003), the United States Western Interior (Kauffman et al., 1996), and Argentina (Gümez-Perez, 2003). Late-stage, postseepage diagenetic events in the Panoche and Tumey Hills carbonates include local recrystallization (especially of micrite to microsparite) and precipitation of gypsum, ferrous hydroxide (hematite), and ferrous sulfide (pyrite).

It is difficult to establish accurate stable isotope trends for the Panoche and Tumey Hills paragenetic sequence because of possible mixture among phases during hand drilling. Conduit-filling cements generally display a trend of increasing $\delta^{13}C$ values from the edges toward the center (i.e., external matrix = −27‰; infilling cement rim = −19‰; and infilling cement core = 2‰) (Figure 17) and fairly stable $\delta^{18}O$ values (i.e., external matrix = −2‰; infilling cement rim = −3‰; and infilling cement core = 0‰). Thus, with respect to cement paragenesis, $\delta^{18}O$ values were more or less constant during seepage, whereas $\delta^{13}C$ values increased over time.

The alternation of precipitation and dissolution events and precipitation of different carbonate phases and fabrics in the early Panoche and Tumey Hills cements likely reflects fluctuating rates of the reduced fluid flow through the shallow sea-floor sediments. This interplay probably also regulated bacterial activity, which, in turn, established strong chemical gradients that affected precipitation and dissolution of various mineral phases and fabrics (Clari and Martire, 2000).

The paragenetic sequence described above recurs in numerous carbonate mounds and stratiform bodies at many stratigraphic levels across the field area. Thus, it seemingly reflects a general pattern of seep development, implying that fluid sources and porewater evolution were similar during different seepage events.

DISCUSSION

The Panoche and Tumey Hills carbonate structures, exposed for 20 km (12 mi), represent one of numerous ancient seeps known from the Great Valley forearc (Campbell et al., 1993, 2002) and an interesting spatial-temporal link between the Jurassic–Cretaceous seeps of the Sacramento Valley (Campbell et al., 1993) and an Eocene seep in the southern San Joaquin Valley (Squires and Gring, 1996).

The $\delta^{13}C$ values of Panoche and Tumey Hills carbonates (60% between −42 and −20‰) reflect microbial oxidation of biogenic or thermogenic methane (Campbell et al., 2002). The less negative $\delta^{13}C$ values (30% between −20 and 2‰) suggest a carbon reservoir that is a mixture between marine organic matter and seawater bicarbonate. The lightest carbon isotope values occur in the central study area (the southern Panoche Hills and northern Tumey Hills), which is stratigraphically above the maximum concentration of injectites (Figure 16), where fluid flux was likely vigorous enough to inhibit seawater mixing. In peripheral areas and the upper parts of many mounds, $\delta^{13}C$ values tend to be heavier. At the margins of the fluid system, this was probably the result of comparatively slow seepage rates, increased mixing of seawater with seep fluids, and consequent increased participation of seawater carbon in the formation of carbonate cements.

In contrast, incremental increases in $\delta^{13}C$ stratigraphically, at the top of some mounds, may reflect a vertical decrease in the pressure and volume of ascending seep fluids and increased advection of seawater at the top of the system. Rim-to-core conduit cements also record progressively heavier $\delta^{13}C$ trends, which likely represent progressively decreasing seep discharge as fluid reservoirs emptied, allowing increasing influx of seawater during the last stages of cement precipitation. The narrowing of dikes upward in the stratigraphic section could also be interpreted as representing the progressive decrease of fluid pressure upward during injection. The stratigraphic termination of most dikes below the Cima Sandstone Lentil further suggests that ascending fluids were largely unable to hydrofracture overlying sediments above that point, and that fluids migrated in the porous sediment by intergranular flow above that level.

Cold seep deposits first appear just above the Marca–Dos Palos Member contact and bracket approximately 200 m (660 ft) of the local stratigraphic section. Average postcompaction sedimentation rates for the Dos Palos Member based on calcareous nannofossil, dinoflagellate, and planktonic foram biostratigraphy (summarized by McGuire, 1988) are approximately 10 cm/1000 yr (4 in./1000 yr), suggesting that the 200-m (660-ft)-thick seep zone represents at least 2 m.y. of seep activity (Schwartz et al., 2003a). The extraordinary longevity of the system is emphasized in regions where dikes are stratigraphically higher than the lowest seep deposits (Figure 14). In such areas, single outcrops record authigenic paleoseep carbonate precipitation and burial (in shale), followed by the successive propagation of injectites.

Patterns of carbonate morphology, distribution, and abundance in the Panoche and Tumey Hills suggest numerous seepage pulses and complex lithologic controls on seep flow patterns over the 2-m.y. duration of the system, possibly implying variations of fluid composition that remain unconstrained. In the main paleoseep horizon, contained within the Cima Sandstone Lentil, at least three different seepage pulses are apparent, each marked by distinctive carbonate volumes, distributions, and morphologies (Figure 12):

pulse A: laterally continuous slabs, laterally grouped mounds, and clustered concretions
pulse B: large- to medium-size mounds, scattered concretions, and chimneys
pulse C: scattered spheroidal and ellipsoidal concretions and medium-size mounds, local chimneys, and laterally extensive pavements

Pulse A

$\delta^{13}C$ analyses of slabs and the bases of clustered mounds in the Cima Sandstone Lentil generally have relatively heavy values (as much as 2‰), probably because of dilution of organic carbon sources by seawater. Slabs and clustered mounds have a range of carbon values that seem to represent a range of venting rates. Tabular, fossil-poor carbonate structures with gradational contacts with the encasing rocks probably formed in areas of diffuse, slow-venting, pavement-covered flat areas, whereas thicker slabs formed in local sea-floor depressions and thinned or pinched out laterally. Thick, fossiliferous slabs and clustered mounds with sharp contacts with the encasing rocks likely formed in areas of rapid venting; in these regions, carbonate morphology was probably controlled by both sea-floor morphology and rate of carbonate precipitation. Variability in fossil abundance and carbonate morphology and the highly irregular lower contact of the Cima Sandstone seep deposits suggests that seep venting rates varied regionally during phase A.

Pulse B

Phase B authigenic carbonates are typically strongly depleted in $\delta^{13}C$ (as much as −46‰) relative to pulse A carbonates, and we infer that most precipitated in areas where the upward flow of reduced fluids was focused instead of diffuse. The B seepage pulse formed many isolated, large mounds. Pipe-like structures in these mounds experienced fluid flow that was vigorous enough to cause precipitation of carbonate relatively free of silt and sand, and one of these recorded the highest infilling cement $\delta^{13}C$ value (−44‰) in the study area. Furthermore, pulse B carbonates are associated with abundant remains of chemosynthetic organisms, mainly concentrated in mound cores, and with sparse barite and pyrite precipitates.

Carbon isotope variation in an individual pulse B mound (samples 7-3, 7-4, and 7-5 in Table 1) suggests that early, basal cements (−7‰) formed from mixed carbon sources, whereas higher (later) cements formed from $\delta^{13}C$ depleted, seep-derived carbon (to −46‰). This pattern suggests that the later fluids were less diluted and, hence, faster flowing than those that contributed to the mound base. The later seep fluids also probably flowed through carbonate-cemented conduits incorporated into the bases of the carbonate structures (Figure 10). The uppermost mound micrites have a slightly heavier value (−43‰), perhaps signaling decreasing venting rate and increasing dilution of seep fluids by seawater over time. The terminal decrease in flux rate implied by the isotopic signature of pulse B may have resulted in the collapse and occlusion of major fluid conduits just before the end of seepage, as suggested by the presence of tilted blocks and breccias in some conduits (Figure 10D). Many phase B mound worm tubes are infilled by carbonate cements with light carbon isotopes, indicating that invertebrate structures were ultimately co-opted by seep fluids and enhanced the porosity of the system during this phase. Trends in isotopic composition in tube-infilling cements (e.g., Figure 9C) generally reflect decreasing seepage (increasing mixing of seep fluids with seawater) over time. Carbonate chimneys and doughnuts formed during the early part of phase B precipitation and are similar to carbonate structures are associated with focused flow in the northern Gulf of Mexico (Roberts and Aharon, 1994). In general, chimneys are encased in well-indurated basal sediments overlain by poorly indurated sediments that include angular carbonate clasts. These features suggest that the chimneys originated in regions of diffusive seepage and cementation (similar to some pulse A features), grew upward above the sea floor around focused flow paths, and finally collapsed and were eroded after venting ceased. A similar scenario for the origin of chimneys is proposed by Kulm and Suess (1990).

Pulse C

Seepage pulse C produced scattered, well-indurated spheroidal and ellipsoidal concretions, scattered mounds, and extensive carbonate pavements. The concretions typically have almost perfectly symmetrical forms and clearly defined edges, which probably reflects diffusion of bicarbonate outward from a small region of concentrated microbial activity (Coleman, 1993). The pavements are regionally extensive and, in many places, incorporate solitary coral and/or wood fossils; the latter suggests that these carbonates were exposed as hardgrounds during the final stages of seep activity.

The Cima Sandstone pulses A, B, and C represent a time series marked by changing styles of seepage with multiple carbonate morphotypes formed during each seepage event. The pulses are recorded in multiple outcrops, and particular morphotypes occur in multiple stratigraphic levels. Seep carbonates also occur in the lower Dos Palos Member, below the Cima Sandstone, generally as small- to medium-size mounds and concretions. Sea-floor geometry, lithologic variability, and changing sediment deposition rates and upward fluid flux were probably all important controls on the

emplacement of distinctive carbonate structures in the Panoche and Tumey Hills system. In-situ fossils indicate that most carbonates precipitated close to the sea floor, it is possible that some structures formed in the shallow subsurface, especially those with poorly preserved fauna, as in the case of some concretions.

The Cima Sandstone Lentil and associated cold seep deposits gradually pinch out in the southern part of the study area, suggesting that the southernmost Tumey Hills carbonates represent the true margin of the paleoseep field. However, the Cima Sandstone is cut out by a disconformable surface in the northern study area, and the presence in the northern Panoche Hills of abundant interconnected injectites and carbonates with light $\delta^{13}C$ signatures (Figure 16) suggests that the system originally extended further northward. Thus, future field and remote sensing studies could focus on the identification of injectites and paleoseep deposits in the Moreno Formation north of the present study area.

CONCLUSIONS

The Panoche and Tumey Hills paleoseep system was episodically fueled by fluids that reached the Paleocene sea floor along injectite pathways. At the sea floor, seep fluids supported complex ecosystems and promoted precipitation of carbonate mounds, stratiform bodies, concretions, and diffuse intergranular cements along more than 20 km (12 mi) of the western margin of the Great Valley forearc basin. Rates of fluid seepage and related precipitation of authigenic, methane-derived carbonate varied regionally and temporally, as illustrated by the varying fossil distribution and varying patterns in the volume, texture, and gross morphology of cements. Six recurring early paragenetic phases identify a typical pattern of seep initiation and development, implying that fluid sources and pore-water evolution were similar during each seepage event. Seepage persisted for nearly 2 m.y., but the duration of injectite activity is unclear. This site adds new early Paleocene data to the existing record of Jurassic to Eocene fluid expulsion in the Great Valley forearc and is a uniquely extensive and well-exposed example of a long-lived, injectite-driven paleoseep system.

ACKNOWLEDGMENTS

This work was supported in part by the Petroleum Research Fund (Grant 35329-AC2) and the University of California Energy Institute (Grant 19900-443759). We are indebted to Casey Moore for introducing us to the field area and for his ongoing encouragement and advice, and to Bruce Tanner and Steve Bohaty at University of California Santa Cruz for help with sample preparation and analysis. We also thank the U.S. Bureau of Land Management for permission to work in the Panoche Hills Wilderness Study Area and for access to aerial photography. This is Ismar-CNR (Istituto di Scienze Marine–Consiglio Nazionale delle Ricerche) contribution number 1454.

REFERENCES CITED

Anderson, R., and R. W. Pack, 1915, Geology and oil resources of the west border of the San Joaquin Valley north of Coalinga, California: U.S. Geological Survey Bulletin, v. 603, 220 p.

Bartow, J. A., 1991, The Cenozoic evolution of the San Joaquin Valley, California: U.S. Geological Survey Professional Paper 1501, 40 p.

Bartow, J. A., 1996, Geologic map of the west border of the San Joaquin Valley in the Panoche Creek–Cantua Creek area, Fresno and San Benito counties, California: U.S. Geological Survey Miscellaneous Investigations Series, Map I-2430, scale 1:50,000, 1 sheet.

Beauchamp, B., H. R. Krouse, J. C. Harrison, W. W. Nassichuk, and L. S. Eliuk, 1989, Cretaceous cold-seep communities and methane-derived carbonates in the Canadian Arctic: Science, v. 244, p. 53–56.

Campbell, K. A., C. Carlson, and D. J. Bottjer, 1993, Fossil cold seep limestones and associated chemosymbiotic macroinvertebrate faunas, Jurassic–Cretaceous, *in* S. A. Graham and D. R. Lowe, eds., Advances in the sedimentary geology of the Great Valley Group, Sacramento Valley, California: Pacific Section SEPM Fall Fieldtrip Guidebook, v. 73, p. 37–50.

Campbell, K. A., J. D. Farmer, and D. Des Marais, 2002, Ancient hydrocarbon seeps from the Mesozoic convergent margin of California: Carbonate geochemistry, fluids and paleoenvironments: Geofluids, v. 2, p. 63–94.

Chafetz, H. S., 1986, Marine peloids: A product of bacterially induced precipitation of calcite: Journal of Sedimentary Petrolology, v. 56, p. 812–817.

Clari, M., and L. Martire, 2000, Cold seep carbonates in the Tertiary of northwest Italy: Evidence of bacterial degradation of methane, *in* R. E. Riding and S. M. Awramik, eds., Microbial sediments: Berlin, Springer-Verlag, p. 261–269.

Coleman, M. L., 1993, Microbial processes; controls on the shape and composition of carbonate concretions: Marine Geology, v. 113, p. 127–140.

Cook, T. L., and D. S. Stakes, 1995, Biogeological mineralization in deep-sea hydrothermal deposits: Science, v. 267, p. 1975–1979.

Dibblee, T. W. Jr., 1975, Geologic maps of the ''Pacheco Pass,'' ''Hollister,'' ''Quien Sabe,'' ''Ortigalita Peak,'' ''San Benito,'' ''Panoche Valley,'' and ''Tumey Hills'' quadrangles; San Benito, Santa Clara, Merced, and Fresno counties, California: U.S. Geological Survey Open-file Report 75-0394, scale 1:62,500, 7 sheets.

Dickinson, W. R., and D. R. Seely, 1979, Structure and stratigraphy of forearc basins: AAPG Bulletin, v. 63, no. 1, p. 2–31.

Eichhubl, P. H., G. Greene, T. Naehr, and N. Maher, 2000, Structural control of fluid flow: Offshore fluid seepage in the Santa Barbara basin, California: Journal of Geochemical Exploration, v. 69–70, p. 545–549.

Friedmann, J., P. Vrolijk, X. Ying, A. Despanhe, G. Moir, and D. Mohrig, 2002, Quantitative analysis of sandstone intrusion networks, Panoche Hills, CA (abs.): AAPG Annual Meeting Program, v. 2002, p. 59.

Goedert, J. L., J. Peckmann, and J. Reitner, 2000, Worm tubes in an allochthonous cold-seep carbonate from lower Oligocene rocks of western Washington: Journal of Paleontology, v. 74, no. 6, p. 992–999.

Gómez-Pérez, I., 2003, An early Jurassic deep-water stromatolitic bioherm related to possible methane seepage (Los Molles Formation, Neuquén, Argentina): Palaeogeography, Palaeoclimatology, Palaeoecology, v. 201, p. 21–49.

Guo, L., and R. Riding, 1992, Aragonite laminae in hot water travertine crusts, Rapolano Terme, Italy: Sedimentology, v. 39, p. 106–1079.

Hikida, Y., S. Suzuki, Y. Togo, and A. Ijiri, 2003, An exceptionally well-preserved fossil seep community from the Cretaceous Yezo Group in the Nakagawa area, Hokkaido, northern Japan: Paleontological Research, v. 7, no. 4, p. 329–342.

Ingersoll, R. V., 1979, Paleogeography and paleotectonics of the late Mesozoic forearc basin of northern and central California, *in* D. G. Howell and K. A. McDougall, eds., Mesozoic paleogeography of the western United States: SEPM Pacific Coast Paleogeography Symposium 2, p. 471–482.

Kauffman, E. G., M. A. Arthur, B. Howe, and P. A. Scholle, 1996, Widespread venting of methane-rich fluids in Late Cretaceous (Campanian) submarine springs (Tepee Buttes), Western Interior seaway, U.S.A.: Geology, v. 24, no. 9, p. 799–802.

Kulm, L. D., and E. Suess, 1990, Relationship between carbonate deposits and fluid venting: Oregon accretionary prism: Journal of Geophysical Research, v. 95, p. 8899–8915.

Luth, C., U. Luth, A. V. Gebruk, and H. Thiel, 1999, Methane gas seeps along the oxic/anoxic gradient in the Black Sea: Manifestations, biogenic sediment compounds and preliminary results on benthic ecology: Marine Ecology, v. 20, no. 3–4, p. 221–249.

Mazzini, A., D. Duranti., R. Jonk, J. Parnell, B. T. Cronin, A. Hurst, and M. Quine, 2003, Palaeo-carbonate seep structures above an oil reservoir, Gryphon field, Tertiary, North Sea: Geo-Marine Letters, v. 23, p. 323–339.

McGuire, D. J., 1988, Stratigraphy, depositional history, and hydrocarbon source-rock potential of the Upper Cretaceous–lower Tertiary Moreno Formation, central San Joaquin basin, California: Ph.D. theses, Stanford University, California, 309 p.

Moore, D. M., D. Orange, and L. D. Kulm, 1990, Interrelationship of fluid venting and structural evolution: Alvin observations from the frontal accretionary prism, Oregon: Journal of Geophysical Research, v. 95, no. B6, p. 8795–8808.

Ogawa, Y., K. Fujioka, K. Fujikura, and Y. Iwabuchi, 1996, En echelon patterns of *Calyptogena* colonies in the Japan Trench: Geology, v. 24, no. 9, p. 807–810.

Paull, C. K., J. P., Chanton, C. S. Martens, P. D. Fullagar, A. C. Neumann, and J. A. Coston 1991, Seawater circulation through the flank of the Florida platform: Evidence and implications: Marine Geology, v. 102, p. 265–279.

Payne, M. B., 1951, Type Moreno Formation and overlying Eocene strata on the west side of the San Joaquin Valley, Fresno and Merced Counties: California Division of Mines and Geology Special Report 9, 29 p.

Peckmann, J., V. Thiel, W. Michaelis, P. Clari, C. Gaillard, L. Martire, and J. Reitner, 1999, Cold seep deposits of Beauvoisin (Oxfordian, southeastern France) and Marmorito (Miocene, northern Italy): Microbially induced authigenic carbonates: International Journal of Earth Science, v. 88, p. 60–75.

Peckmann, J., J. L. Goedert, V. Thiel, W. Michaelis, and J. Reitner, 2002, A comprehensive approach to the study of methane-seep deposits from the Lincoln Creek Formation, western Washington state, U.S.A.: Sedimentology, v. 49, p. 855–873.

Roberts, H. H., and P. Aharon, 1994, Hydrocarbon-derived carbonate buildups of the northern Gulf of Mexico: A review of submersible investigations: Geo-Marine Letters, v. 14, p. 135–148.

Sample, J., J. C. Moore, K. D. Weberling, H. Schwartz, and P. Vrolijk, 2001, Clastic intrusions and chemosynthetic paleocommunities in the Great Valley forearc, Panoche Hills, CA: Geochemistry of carbonates suggests biogenic and thermogenic input during early Tertiary subduction: American Geophysical Union Annual Fall Meeting, San Francisco, California, December 2001, v. 82, no. 47, p. 1341.

Schwartz, H., J. Sample, K. D. Weberling, D. Minisini, and J. C. Moore, 2003a, An ancient linked fluid migration system: Cold-seep deposits and sandstone intrusions in the Panoche Hills, California, U.S.A.: Geo-Marine Letters, v. 23, no. 3–4, p. 340–350.

Schwartz, H., D. Minisini, and J. Sample, 2003b, Early Paleocene cold seep deposits, western San Joaquin Valley, CA: II. Authigenic carbonates and long-lived, tube worm-dominated chemosynthetic ecosystems (abs.): Geological Society of America Abstracts with Programs, v. 35, no. 6, p. 381–382.

Sibuet, M., and K. Olu, 1998, Biogeography, biodiversity and fluid dependence of deep-sea cold-seep communities at active and passive margins: Deep-Sea Research II, v. 45, p. 517–567.

Smyers, N. B., and G. L. Peterson, 1971, Sandstone dikes and sills in the Moreno Shale, Panoche Hills, California: Geological Society of America Bulletin, v. 82, p. 3201–3208.

Squires, R. L., and M. P. Gring, 1996, Late Eocene chemosynthetic? bivalves from suspect cold seeps, Wagonwheel Mountain, central California: Journal of Paleontology, v. 70, no. 1, p. 63–73.

Terzi, C., P. Aharon, F. Ricci Lucchi, and G. B. Vai, 1994, Petrography and stable isotope aspects of cold-vent

activity imprinted on Miocene-age ''calcari a Lucina'' from Tuscan and Romagna Apennines, Italy: Geo-Marine Letters, v. 14, p. 177–184.

Von Rad, U., H. Rosch, U. Berner, G. Mebus, V. Marchig, and S. Hartmut, 1996, Authigenic carbonates derived from oxidized methane vented from the Makran accretionary prism off Pakistan: Marine Geology, v. 136, p. 55–77.

Weberling, K. D., 2002, Clastic intrusions and cold seeps in the Late Cretaceous–early Tertiary Great Valley forearc basin, Panoche Hills, CA: Structural context of a linked fluid system: Master's thesis, University of California, Santa Cruz, 48 p.

Wentworth, C. M., and M. D. Zoback, 1989, The style of late Cenozoic deformation at the eastern front of the California Coast Ranges: Tectonics, v. 8, no. 2, p. 237–246.

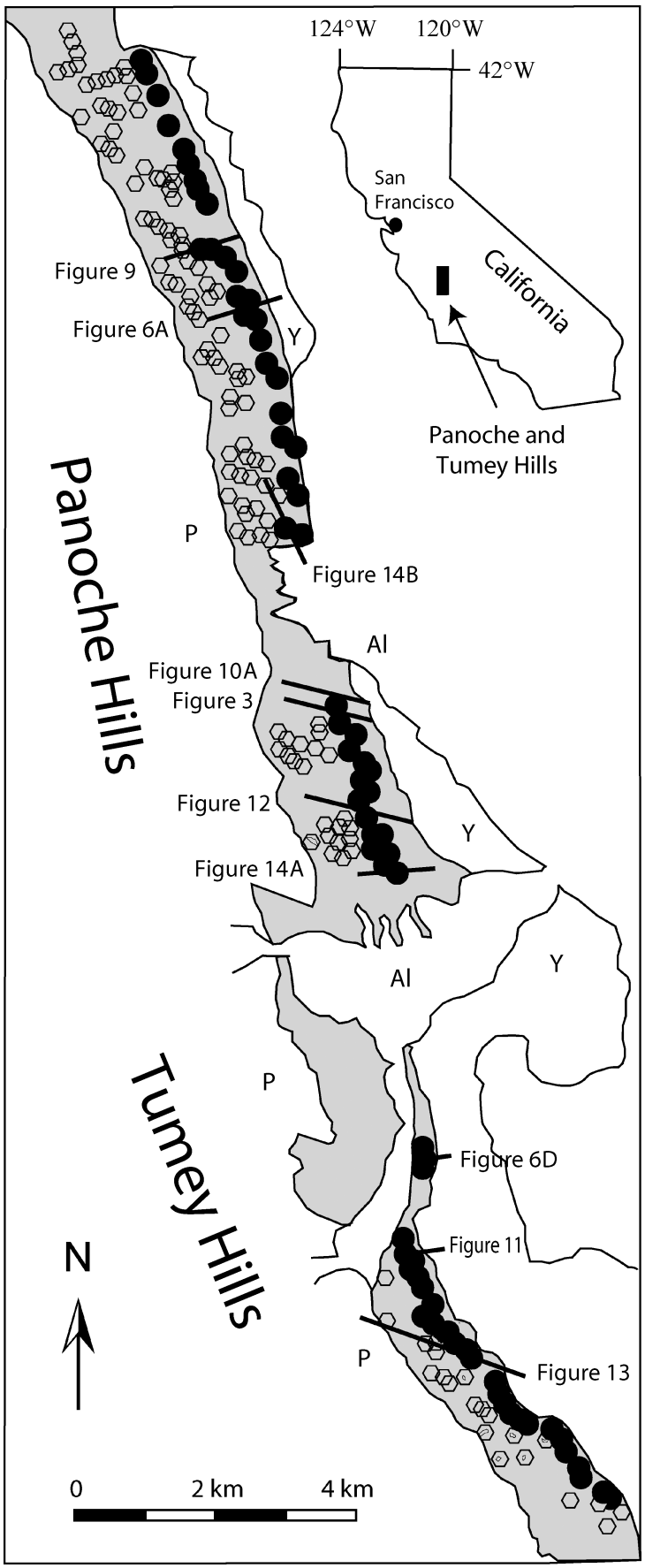

FIGURE 1. Geological setting of the Panoche and Tumey Hills and distribution of ancient cold seep carbonates (black circles) and underlying injectites (open hexagons). The gray pattern is the Moreno Formation. P = Panoche Formation; Al = Holocene alluvial deposits; Y = formations younger than the Moreno Formation.

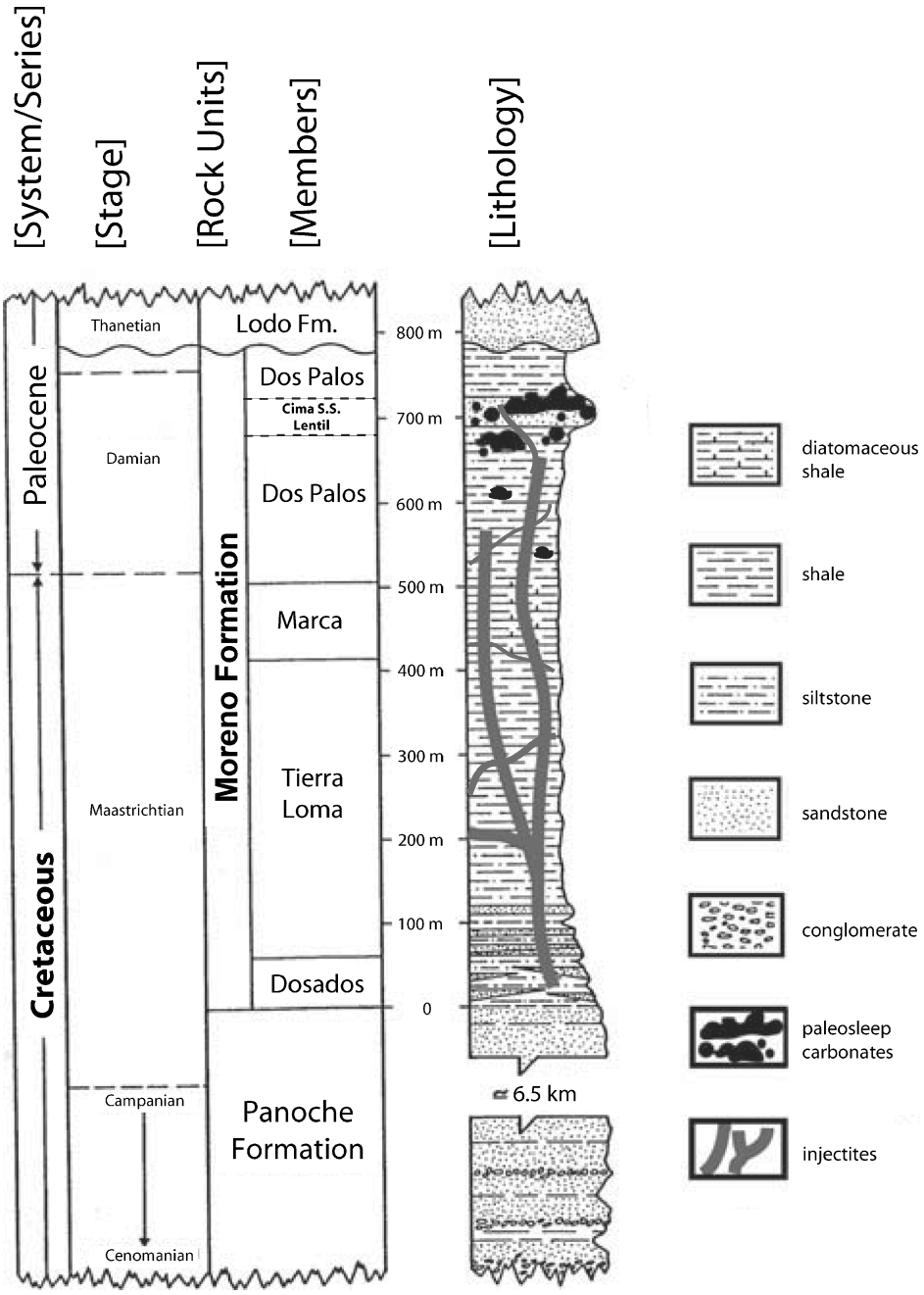

FIGURE 2. Stratigraphy of the Moreno Formation (modified from McGuire, 1988). Paleoseep carbonates occur from just above the Marca–Dos Palos Shale Member contact upward to the main paleoseep horizon in the Cima Sandstone Lentil.

FIGURE 3. Authigenic carbonates exposed in the Cima Sandstone Lentil in the central Panoche and Tumey Hills study area (location in Figure 1). Carbonate abundance and morphology vary considerably in this horizon: on the left, carbonate structures are exposed continuously for more than 100 m (330 ft); on the right, they are smaller and sparser; morphologies include stratiform, moundlike, and concretionary bodies.

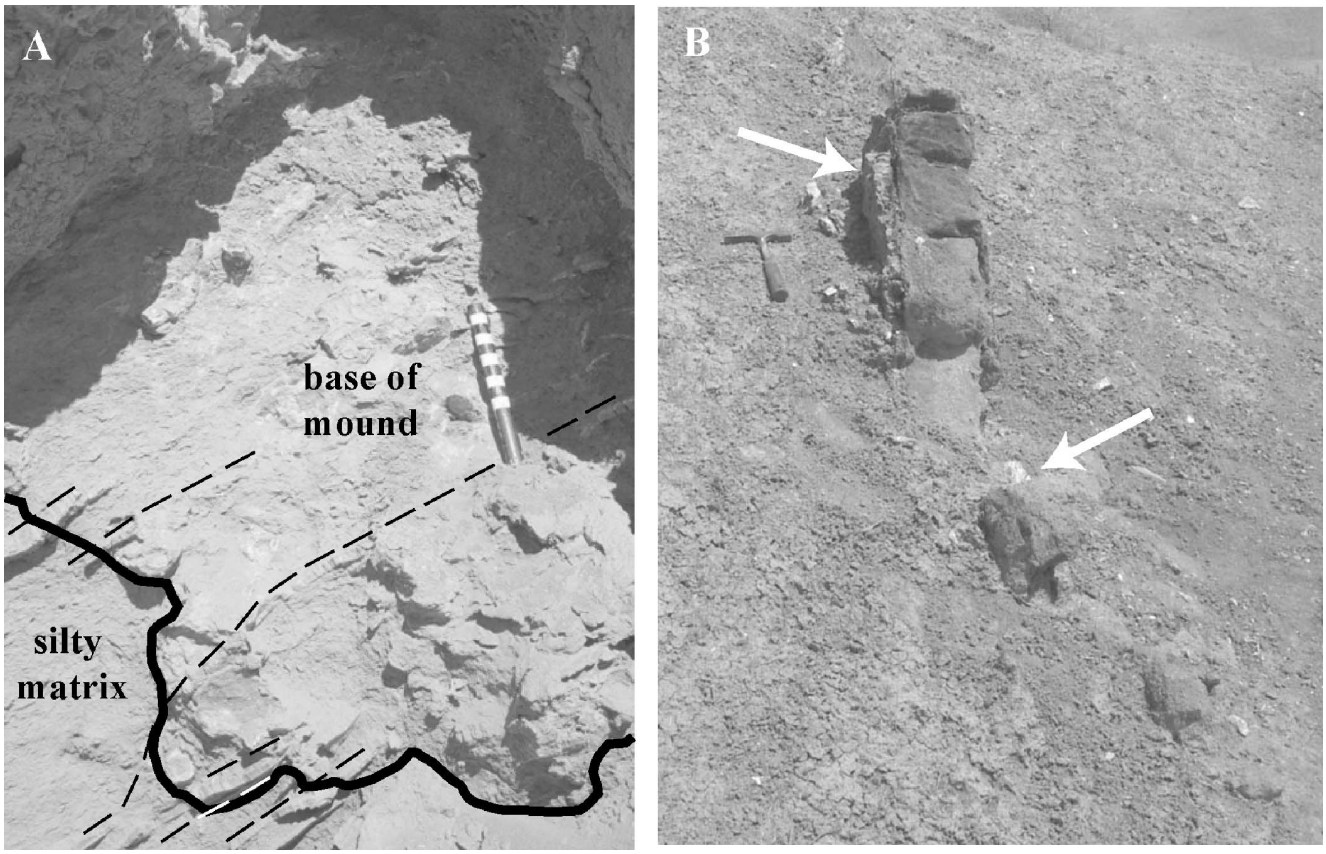

FIGURE 4. Late-stage, fracture-filling gypsum cement. (A) Gypsum veins (~1 cm [~0.4 in.] thick) crosscutting the contact between a paleoseep carbonate mound and the encasing silty matrix; the solid line delineates the sharp contact between authigenic carbonate and host rock, and the dashed lines trace gypsum veins; scale bar shows 1-cm increments; (B) gypsum veins (2–4 cm [0.8–1.5 in.] thick, see arrows) lining the margins of a sandstone dike.

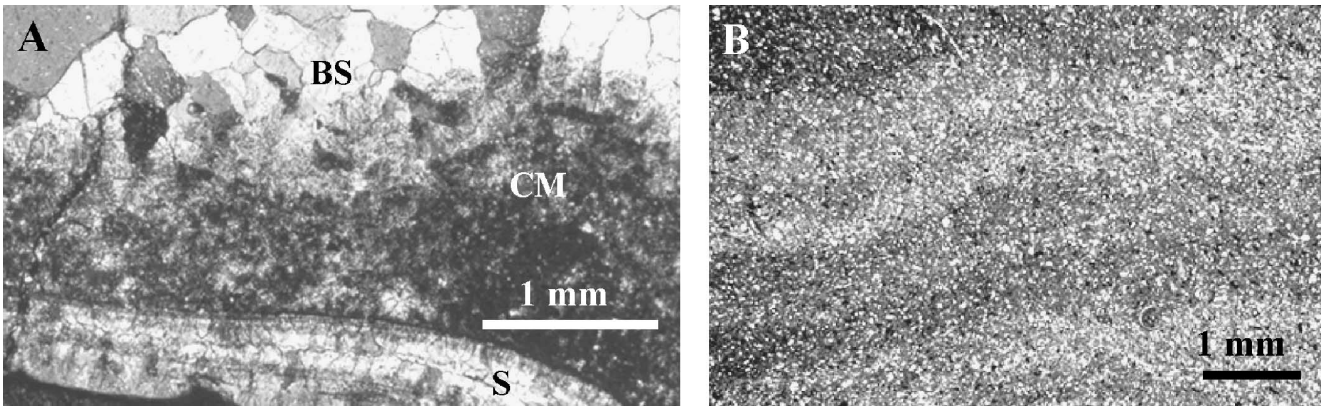

FIGURE 5. Plane light microscope images of microbial textures in Panoche and Tumey Hills carbonates. (A) Clotted micrites (CM) between shell material (S) and blocky calcite spar (BS); (B) wavy laminae around a spar-filled conduit.

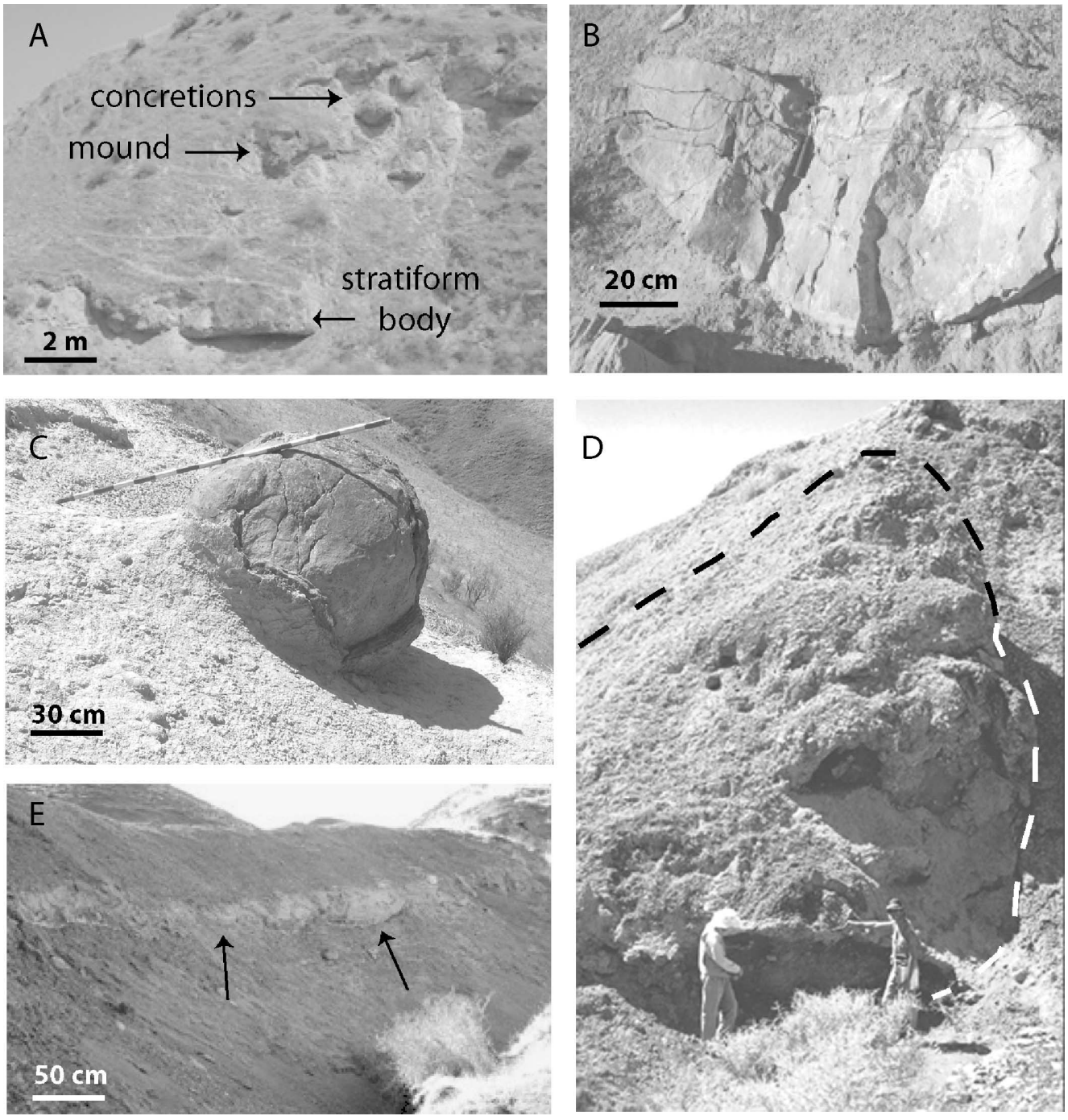

FIGURE 6. Authigenic paleoseep carbonates. (A) The three main morphologies of carbonate structures found in the study area, here co-occurring in the Panoche Hills (location in Figure 1); (B) an ellipsoidal concretion; (C) a spherical concretion; (D) the largest mound in the Panoche and Tumey Hills (~8 m [~26 ft] tall) (location in Figure 1); (E) a laterally continuous, pavementlike stratiform body.

FIGURE 7. Examples of pipelike structures. (A) Pipes in a basal mound in the Cima Sandstone Lentil, central field area; (B) pipe in the Cima Sandstone Lentil, northern Panoche Hills; (C) large pipe with smaller, freestanding tube inside (arrow); (D) pipe fragments in cross section, showing infilling cements.

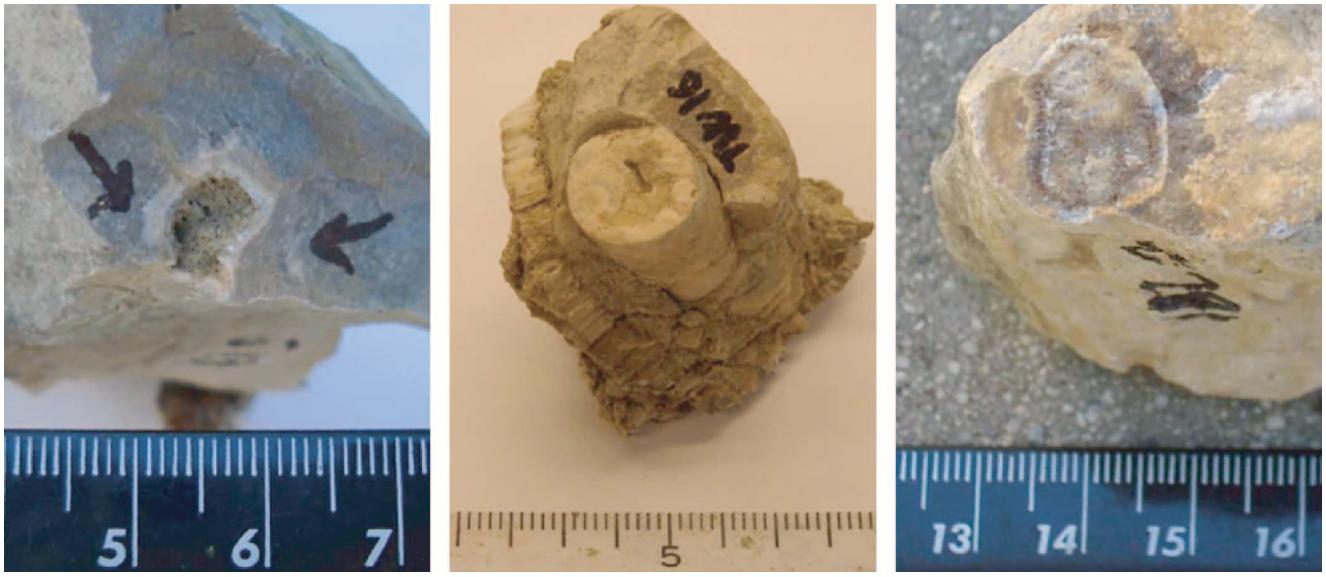

FIGURE 8. Tube worm vs. pipe morphology. (A) Cross section of an irregular, pipelike structure; (B) cross section of a circular structure and probable tube worm fossil; (C) intermediate morphology, suggesting that some worm tubes acted as fluid conduits.

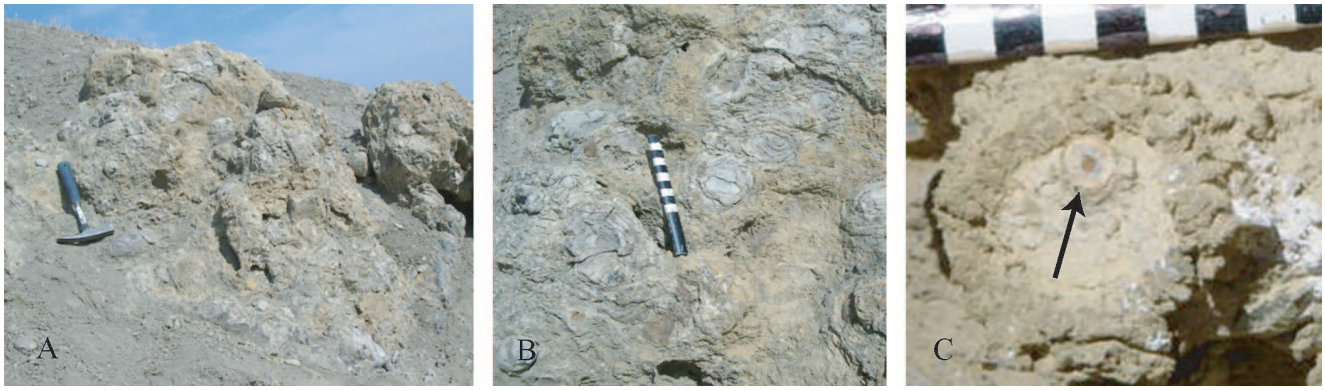

FIGURE 9. Knobbly mound textures and cement overgrowths on tubes and pipes (location in Figure 1). (A) Two small mounds with knobbly texture; (B) individual tubes and pipes and authigenic overgrowth on mound surface; (C) authigenic overgrowth around a probable worm tube (arrow).

FIGURE 10. Subslab and submound features in the Cima Sandstone Lentil. (A–C) Carbonate conduits (arrows) below stratiform and moundlike carbonates in the Cima Sandstone Lentil (location of A is in Figure 1); (D) brecciated texture of basal mound near conduit.

FIGURE 11. Carbonate chimneys in the Cima Sandstone Lentil (location in Figure 1).

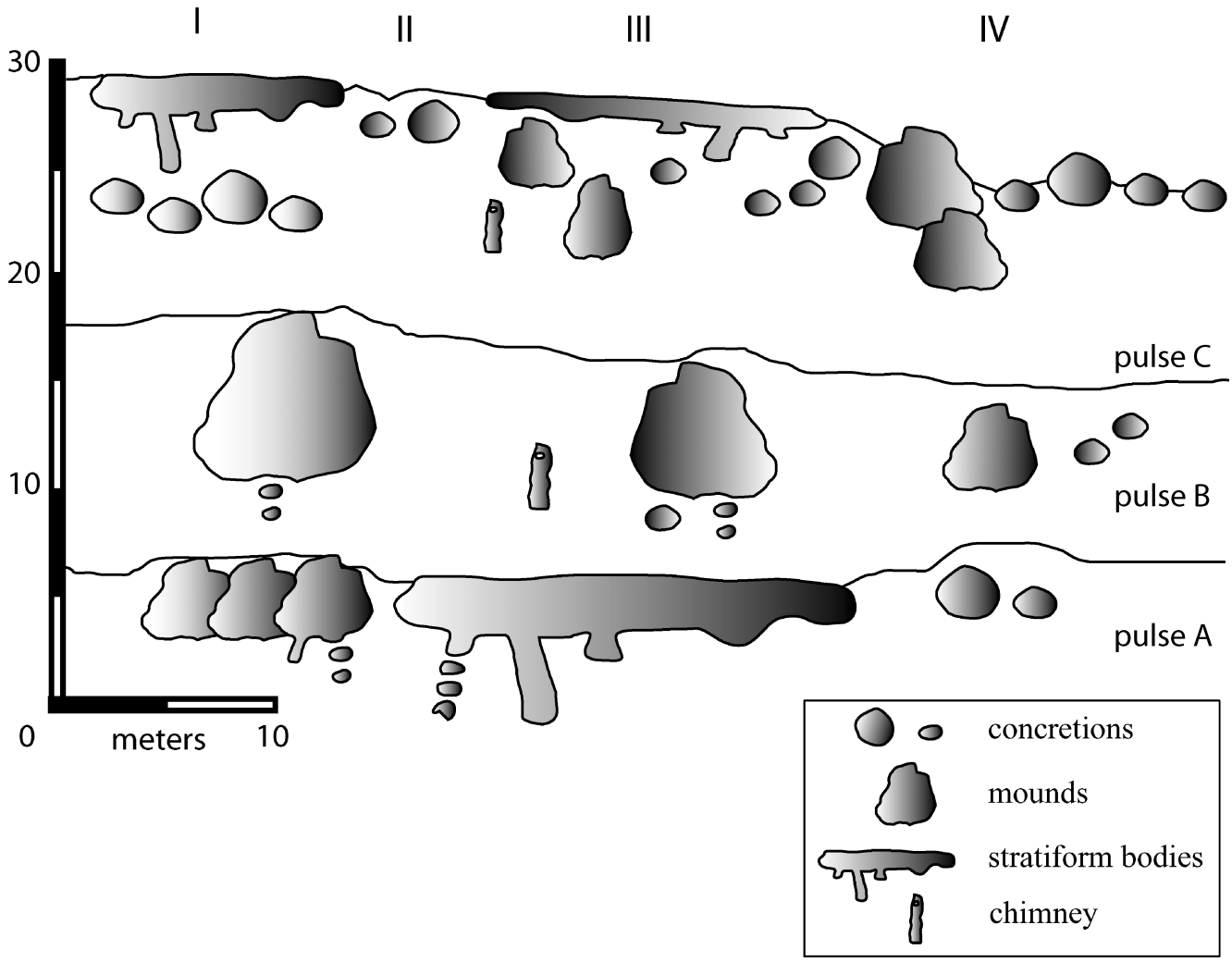

FIGURE 12. Idealized distribution of carbonate structures in the Cima Sandstone Lentil (see Figure 2) in the southern Panoche Hills (location in Figure 1). Horizontal lines represent approximate sea-floor positions. Pulse A formed stratiform bodies, laterally grouped mounds, and local concretions; pulse B produced the largest mounds, in conjunction with scattered concretions and chimneys; pulse C formed scattered mounds and concretions, local chimneys, and laterally extensive, dip slope-forming stratiform bodies. Distinctive vertical sequences are (from bottom to top): (I) mounds, concretions, and stratiform bodies; (II) stratiform bodies and concretions; (III) stratiform bodies, mounds and concretions, and stratiform bodies; (IV) mounds and concretions.

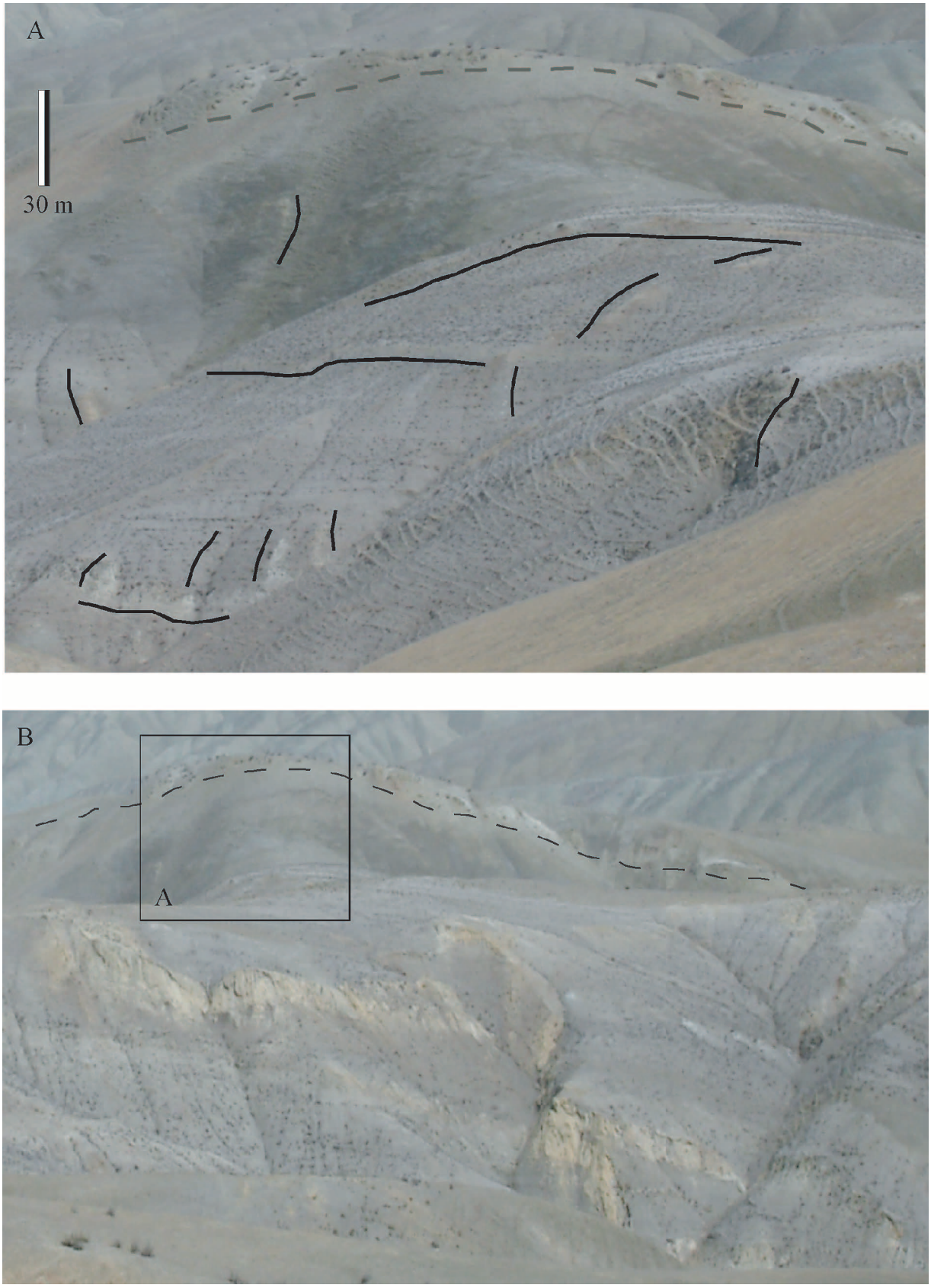

FIGURE 13. Dikes and sills close to the main paleoseep horizon (dashed line) in the Tumey Hills. (A) Injectite outcrops are highlighted by solid lines; (B) thicker dikes and sills lower in the section crosscut one another into a comformable stratigraphic sequence. View is to the east (location in Figure 1).

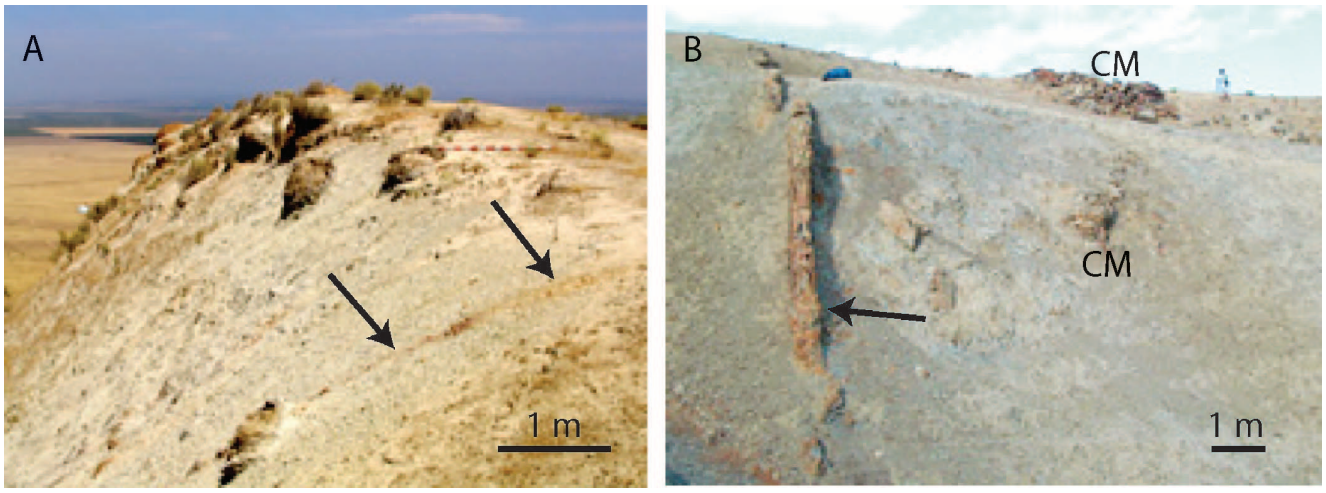

FIGURE 14. Injectites and paleoseep deposits (locations in Figure 1). (A) Thin sandstone dike (arrows) penetrating main seep deposit; carbonate mounds and concretions are in the foreground and background. Strata dip approximately 35° east (to right in photo); (B) thick sandstone dike (arrow) and adjacent paleoseep carbonate mounds (CM) in lower Dos Palos Shale Member. Regional dip is eastward (in the direction of view).

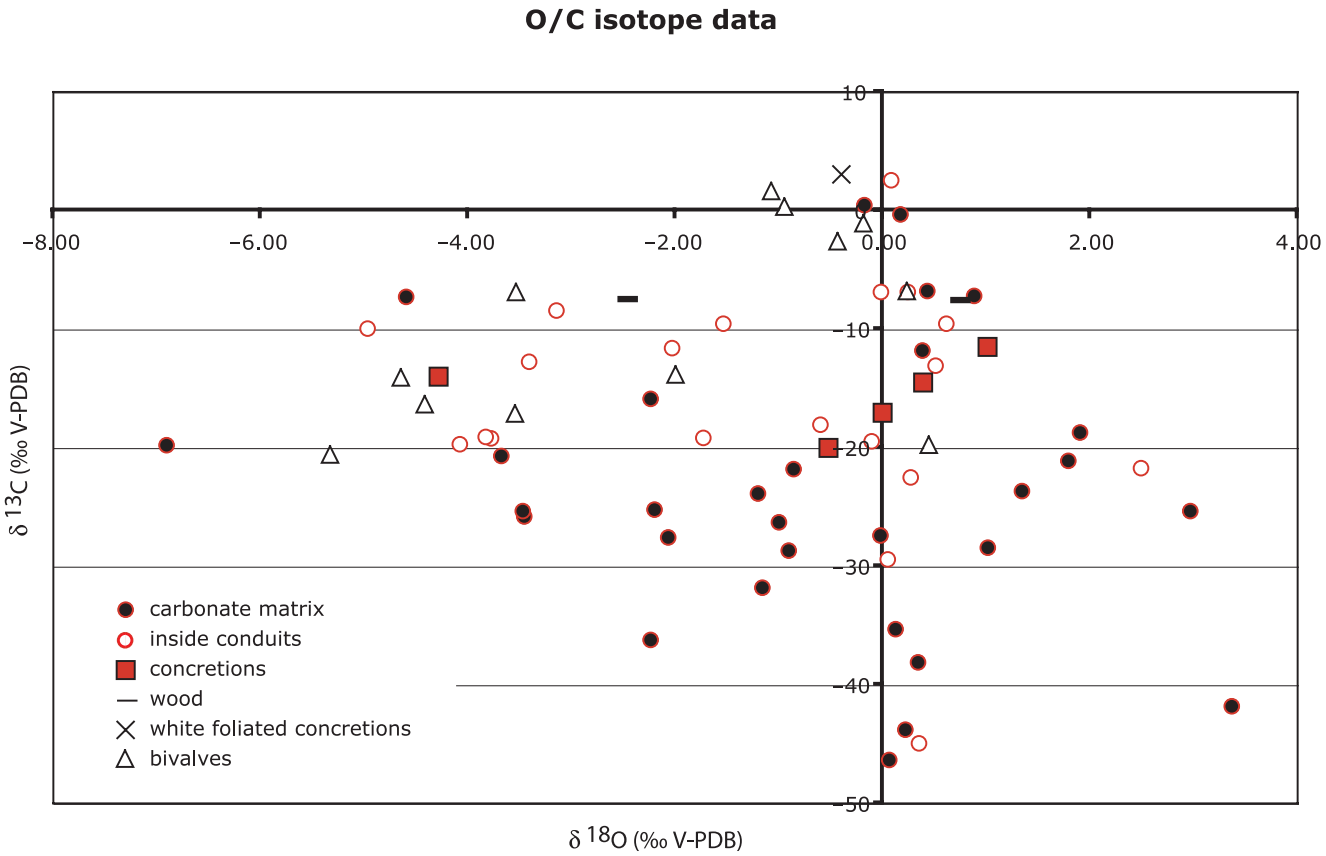

FIGURE 15. Carbon and oxygen isotopes in paleoseep carbonates and fossils in the Panoche and Tumey Hills.

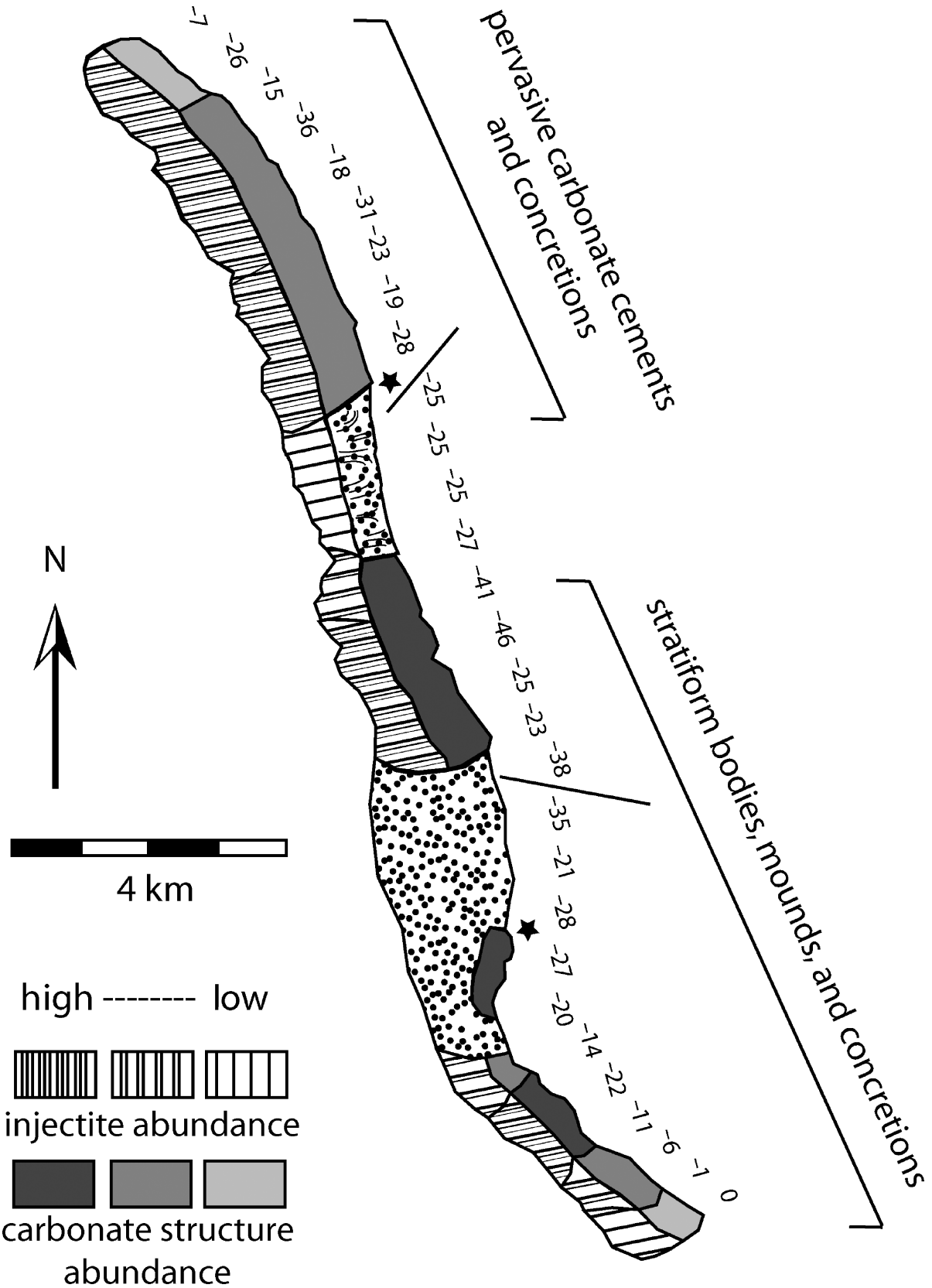

FIGURE 16. The study area of the Moreno Formation (gray in Figure 1; for comparison, stars indicate the location of Figures 6D, 14B in Figure 1) with distribution and abundance of injectites and carbonate structures (specifying morphotype distribution). Dotted areas represent alluvium-colluvium cover. Numbers show distribution of $\delta^{13}C$ values in micritic lithofacies of slabs and mounds (slashes represent areas covered by alluvium-colluvium).

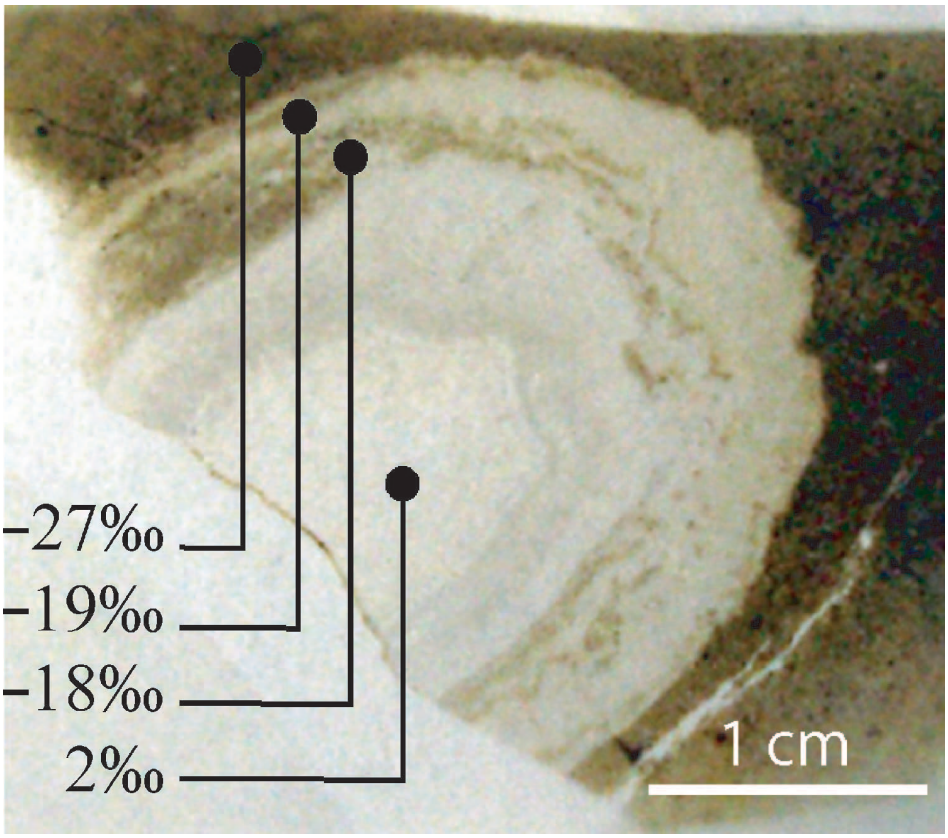

FIGURE 17. Thin section of probable worm tube showing $\delta^{13}C$ values of authigenic cements (sample δ9B, Table 1).

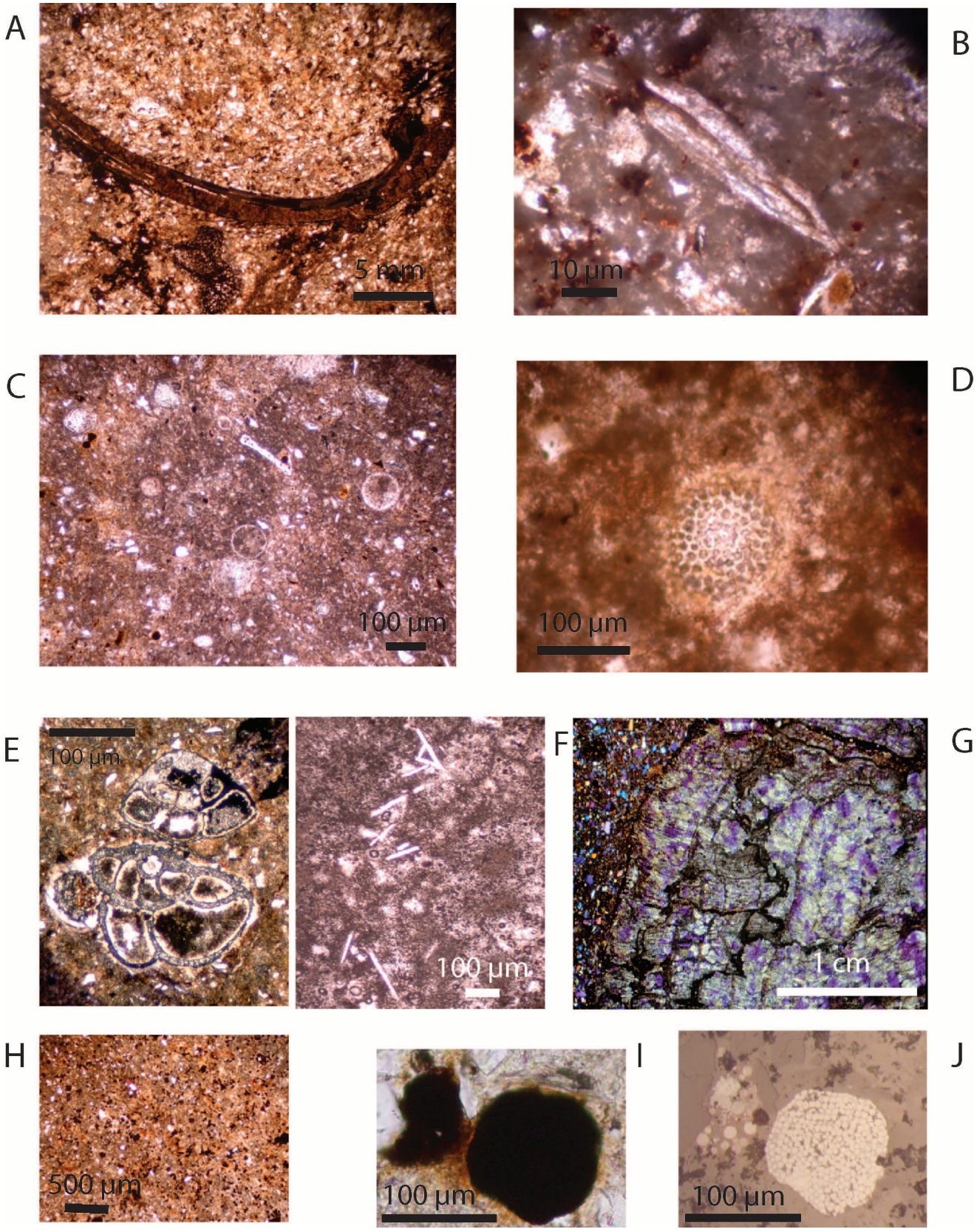

FIGURE 18. Reflected, plane light microscope images of fossils and other features associated with the micritic matrix: (A) bivalve in cross section; (B) mollusk bioclast; (C) planktonic foraminifera; (D) radiolaria; (E) benthonic foraminifera (Rotalidi); (F) sponge(?) spicules; (G) wood fragment; (H) mottled pigmentation; (I, J) pyrite framboids in reflected and transmitted light.

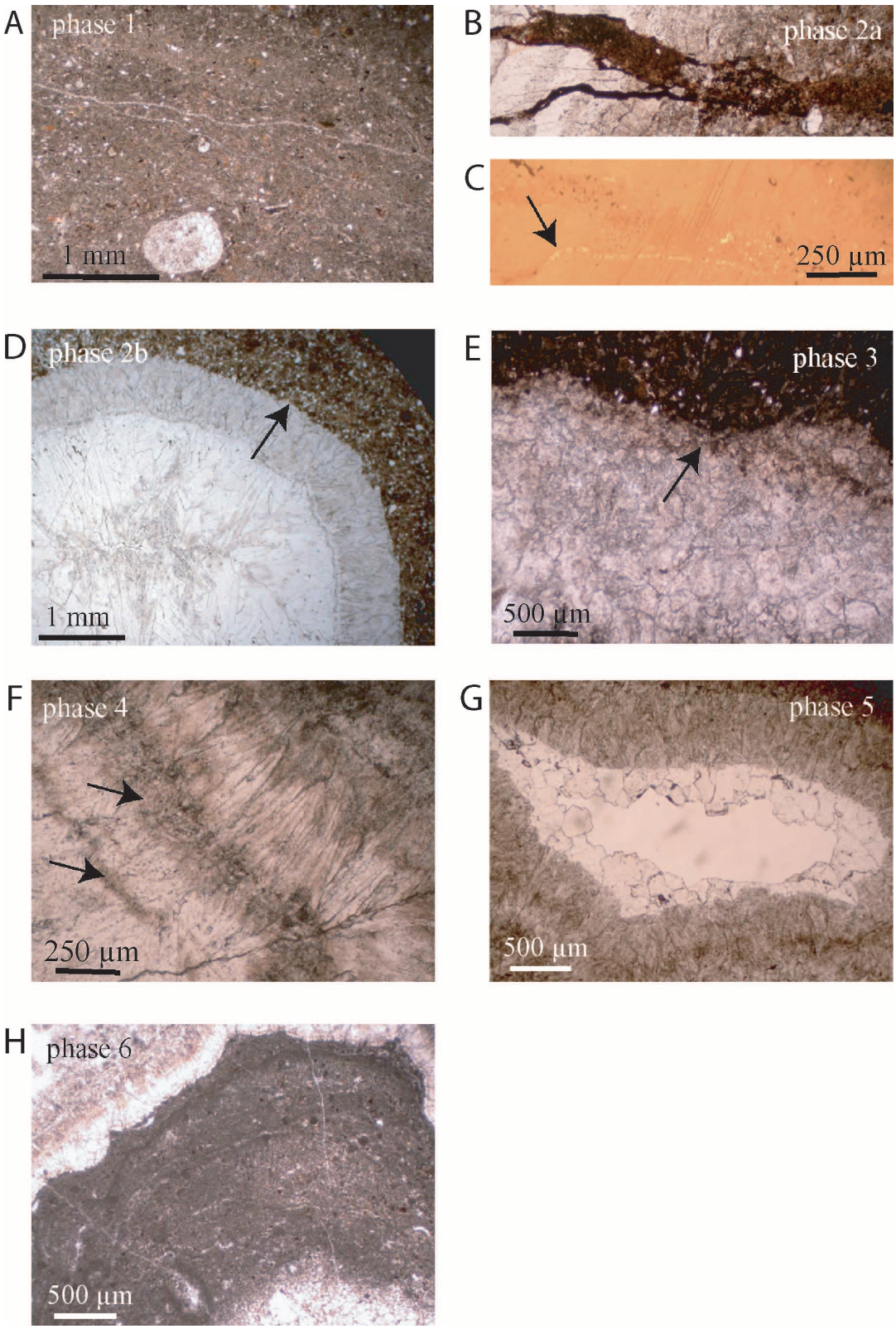

FIGURE 19. Reflected, plane light microscope images of the recurring paragenetic sequence in the Panoche and Tumey Hills carbonates. (A) Phase 1: fossiliferrous, detritus-rich micrite; (B) phase 2a: corrosion event; (C) phase 2a: same area under transmitted light; note the presence of microcrystalline pyrite (arrow); (D) phase 2b: corrosion of conduit wall (arrow); (E) phase 3: dark-yellow calcite; (F) phase 4: fibrous calcite (arrows indicate two zoned inclusion bands); (G) phase 5: blocky calcite; (H) phase 6: nondetrital laminated peloidal micrite. Phases 4 and 5 are present also in (D) toward the center.

CONCLUSIONS

Geomorphological, seismo-stratigraphic, sedimentological and biostratigraphic data support the following conclusions:

- Multiple slide scars and extensive, buried or exposed, mass transport deposits testify widespread and recurrent sediment failure on the SW-Adriatic Margin and SE-Sicilian Margin. These failures contributed to the shaping of the slope and filling of the basin, resulting in a characteristic stratigraphic and geomorphologic pattern.

- Distinctive failure styles range from in situ sediment deformation to sliding and mass transport with run out distances exceeding 50 km. Locally, dissimilar organisation of coeval failed deposits depends on the distinct units of the failed areas that, in turn, reflect the stratigraphic architecture of the margin.

- Most slides occur through a succession of multi-events. Morphologic and stratigraphic reconstructions are instrumental in understanding, respectively, the cross-cutting relationship among successive headscarps and the stratal relationships among overlapping failed masses. These combined reconstructions allow determination of possible sequences of failure phases and of their relative timing. Following this approach, four main phases of failure characterize the study area in the SE-Sicilian Margin and three in the SW-Adriatic Margin.

- The failures events and associated mass-transport deposits occurred during the last glacial cycle showing a varied relationship with changes in relative sea level (low stand –Gondola Slide; relative sea level rise –Gela mud flow; sea level high stand –Twin Slides in Gela Basin and a minor failure in SW-Adriatic Margin).

- Basinwide failures affect the margins during the last-glacial low stand. Where waxing of bottom currents prevented deposition, these old glacial mass-transport deposits are still exposed at seafloor. Beneath the basin floor, instead, failed

masses are buried by thick and layered units deposited since the Last Glacial Maximum. Proximal deposits resulting from large-scale collapses imply that multiple sources supplied, instantaneously, these basin-wide mass-transport deposits.

- Smaller and shorter runout mass-transport deposits took place during the sea level rise and modern high stand. However, even these young, relatively small and well defined slide deposits reveal successions of multiple events and, in many cases, imply more than one transport mechanism.

- The detection of morphologic or stratigraphic elements indicating possible incipient failure, together with evidence of seismic activity and tectonic deformation, suggest that large slope areas are still prone to failure in the SW-Adriatic and SE-Sicilian margins, as well as on other Mediterranean margins.

- The pre-failure stratigraphic architecture determines preferential failure planes (i.e., erosional unconformities, onlap and downlap surfaces). Understanding of the pre-slide margin stratigraphy examining submarine slide scars and associated failed deposits helps identify potential slip planes and areas that are more prone to failure.

- It is possible that some of the deepest-seated failures affecting the shelf edge or upper slope generated tsunami in the past, particularly if taking place during the last glacial interval when sea level was 120 m lower than today.

- Hard-grounds colonised by bivalves and deep-sea living corals occur where steep canyon walls or slide blocks are exposed at seafloor and impinged by bottom currents.

- Substantial seafloor remoulding occur during phases of failure, especially where the mass-transport deposits are confined by pre-existing antiforms.

- Rapidly buried mass-transport deposits release fluids that escape upward, favouring further sediment instability. Variable rates of fluid seepage and

episodic fueling of fluid migration systems, inferred from ancient subaerial outcrops, may trigger failure events.

- Mass failure acts as driving mechanism of submarine canyon inception when wide headscarps close to shore may capture density currents both at lowstands (when longshore drift dominates) and during highstands (when dense cold waters flush the incision) hence catalizing headward erosion and acting as preferential pathways to the deepest part of the basin.

- Interaction between mass wasting and bottom currents dominates along the studied slopes: a) mass-transport deposits create irregular seafloor morphologies where sediment waves develop, b) sediment drifts form within large slide evacuation areas, c) failure planes coincide with key surfaces within bottom-current deposits.

- The development of glide planes on elements of precursor slope failures (i.e., top of mass-transport deposits) and the stacking pattern of mass-transport features recorded in the stratigraphic architecture emphasize the preferential occurrence of slides in areas previously affected by slope instability. The embayment and the steepness of a paleo-slide, the high sediment accumulation rate resulting in a rapid recharge of meta-stable sediment, and the occurrence of weak layers determine a preferential setting for sliope instability. The combined effects of high pore-pressure gradient and rapid deposition likely trigger a positive feedback that enhances the probability of recurrent mass-wasting.

- Basin plains are the areas that collect most of the mass-transport deposits generated along the slope. However, in choosing the basin plain as the key study area for determining the recurrence of failure events, some concepts have to be considered: a) distinct provenance of mass-transport deposits and therefore recurrence from a single area could be biased by over-estimation, b) voluminous but rigid failures may stop before reaching the basin plain, in this case the recurrence would be under-estimated, c) variable trend of failure events (recurrence could be biased when increasing/decreasing failure frequency is simply averaged out).

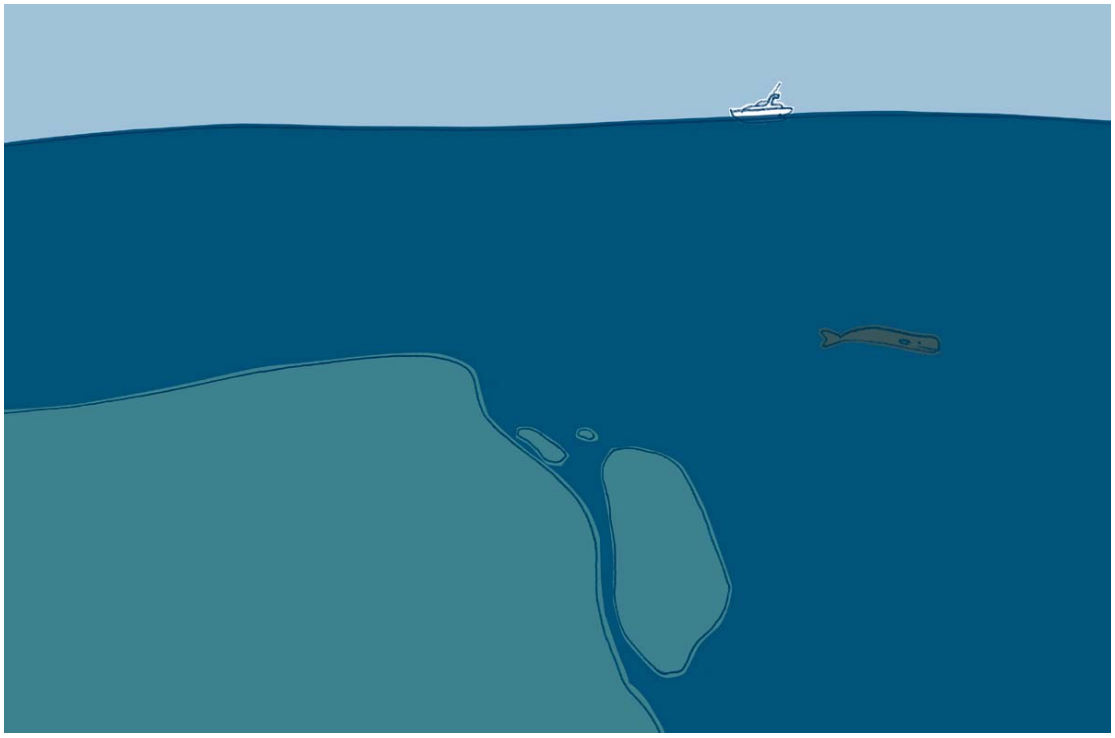

“Slide” drawn by artist Guido Scarabottolo for this Ph.D. thesis.